# Hydrogen dissociation on metal surfaces

Wijzenbroek, M.

# Hydrogen dissociation on metal surfaces

PROEFSCHRIFT

ter verkrijging van
de graad van Doctor aan de Universiteit Leiden,
op gezag van Rector Magnificus prof. mr. C. J. J. M. Stolker,
volgens besluit van het College voor Promoties
te verdedigen op donderdag 2 juni 2016
klokke 10:00 uur

door

Mark Wijzenbroek
geboren te Vlaardingen in 1988

# Promotiecommissie

| | |
|---|---|
| Promotor: | prof. dr. G. J. Kroes |
| Overige leden: | prof. dr. J. Brouwer |
| | prof. dr. M. T. M. Koper |
| | prof. dr. J. G. E. M. Fraaije |
| | prof. dr. A. Groß (Universität Ulm) |
| | dr. C. Díaz (Universidad Autónoma de Madrid) |
| | dr. L. B. F. Juurlink |
| | dr. J. Meyer |

The research described in this thesis was performed at the theoretical chemistry group of the Leiden Institute of Chemistry (Einsteinweg 55, 2333 CC, Leiden). This work was supported financially by the division Chemische Wetenschappen of the Nederlandse organisatie voor Wetenschappelijk Onderzoek (NWO-CW) and with computer time granted by the Physical Sciences division of NWO (NWO-EW). This work is part of the programme of BiG Grid, the Dutch e-Science Grid, which is financially supported by the Nederlandse Organisatie voor Wetenschappelijk Onderzoek (Netherlands Organisation for Scientific Research, NWO).

# Contents

# List of acronyms

| | |
|---|---|
| AIMD | *ab initio* molecular dynamics. |
| BOSS | Born–Oppenheimer static surface. |
| BtH | bridge-to-hollow. |
| CRP | corrugation reducing procedure. |
| CT | classical trajectory. |
| DFT | density functional theory. |
| DVR | discrete variable representation. |
| DW | Debye–Waller. |
| FBR | finite base representation. |
| FCC | face-centered cubic. |
| FFT | fast Fourier transform. |
| GGA | generalized gradient approximation. |
| HCP | hexagonal close packed. |
| HEG | homogeneous electron gas. |
| LDA | local density approximation. |
| meta-GGA | meta-generalized gradient approximation. |
| ML | monolayer. |
| MSO | modified surface oscillator. |

| | |
|---|---|
| NEB | nudged elastic band. |
| PAW | projector augmented wave. |
| PES | potential energy surface. |
| QCT | quasi-classical trajectory. |
| QD | quantum dynamics. |
| RMSE | root mean square error. |
| SCM | static corrugation model. |
| SM | surface mass. |
| SO | surface oscillator. |
| SRP | specific reaction parameter. |
| TD-DFT | time-dependent density functional theory. |
| TDWP | time-dependent wave packet. |
| TOF | time-of-flight. |
| TtB | top-to-bridge. |
| USPP | ultrasoft pseudopotential. |
| XC | exchange–correlation. |
| ZPE | zero-point energy. |

# List of symbols

**Coordinates of a diatomic molecule**

| | |
|---|---|
| $U$ | Lateral position of the center of mass of a diatomic molecule with respect to the surface (skewed coordinates). |
| $V$ | Lateral position of the center of mass of a diatomic molecule with respect to the surface (skewed coordinates). |
| $X$ | Lateral position of the center of mass of a diatomic molecule with respect to the surface (Cartesian coordinates). |
| $Y$ | Lateral position of the center of mass of a diatomic molecule with respect to the surface (Cartesian coordinates). |
| $Z$ | Distance of the center of mass of a diatomic molecule to the surface. |
| $\varphi$ | Azimuthal angle of a diatomic molecule. |
| $\vartheta$ | Polar angle of a diatomic molecule. |
| $\vec{r}$ | Collection of $U$, $V$, $Z$, $r$, $\vartheta$, $\varphi$. |
| $r$ | Bond length of a diatomic molecule. |

**Coordinates of an atom**

| | |
|---|---|
| $\vec{\rho}$ | Collection of $u$, $v$, $z$. |
| $u$ | Lateral position of an atom with respect to the surface (skewed coordinates). |

| | |
|---|---|
| $v$ | Lateral position of an atom with respect to the surface (skewed coordinates). |
| $z$ | Distance of an atom to the surface. |

**Corrugation reducing procedure**

| | |
|---|---|
| $I^{3D}$ | Three-dimensional interpolation function. |
| $I^{6D}$ | Six-dimensional interpolation function. |
| $V^{1D}$ | Repulsive pair potential used for the calculation of $I^{3D}$. |
| $V^{3D}$ | Three-dimensional potential energy surface. |
| $V^{6D}$ | Six-dimensional potential energy surface. |

**Density functional theory**

| | |
|---|---|
| $E_{XC}$ | Exchange–correlation functional. |
| $V_H$ | Hartree potential. |
| $V_{KS}$ | Kohn–Sham potential. |
| $V_{XC}$ | Exchange–correlation potential. |
| $V_{ext}$ | External potential. |
| $\epsilon_C$ | Correlation energy per particle. |
| $\epsilon_{XC}$ | Exchange–correlation energy per particle. |
| $\epsilon_X$ | Exchange energy per particle. |
| $n$ | Electron density. |

**Geometry of the surface**

| | |
|---|---|
| $\vec{q}_{id}$ | Collection of all surfaces degrees of freedom for an ideal surface. |
| $\vec{q}$ | Collection of all surface degrees of freedom. |
| $d_{a-b}$ | Distance between layers $a$ and $b$. |

**Initial conditions**

| | |
|---|---|
| $E_\perp$ | Perpendicular translational energy of a molecule. |
| $E_{rot}$ | Rotational energy of a molecule. |
| $E_{trans}$ | Translational energy of a molecule. |
| $E_{vib}$ | Vibrational energy of a molecule. |

| | |
|---|---|
| $E_{\parallel}$ | Parallel translational energy of a molecule. |
| $L$ | Magnitude of the angular momentum vector. |
| $T_{\mathrm{n}}$ | Nozzle temperature. |
| $T_{\mathrm{rot}}$ | Rotational temperature. |
| $T_{\mathrm{s}}$ | Surface temperature. |
| $\alpha$ | Width of the velocity distribution of a molecular beam. |
| $\varphi_i$ | Angle of incidence of the molecule (angle between the projection of the velocity vector on the ($U$, $V$) plane and the $U$ axis). |
| $\vartheta_L$ | Angle between the angular momentum vector and the surface normal. |
| $\vartheta_i$ | Angle of incidence of the molecule (angle between the velocity vector and the surface normal). |
| $v_0$ | Stream velocity of a molecular beam. |
| $v_i$ | Incident velocity of a molecule. |

**Observables**

| | |
|---|---|
| $A_0^{(2)}$ | Rotational quadrupole alignment parameter. |
| $P_{\mathrm{deg}}$ | Degeneracy averaged initial state-resolved reaction probability. |
| $P_{\mathrm{scat}}$ | State-to-state scattering probability. |
| $P_r$ | Fully initial state-resolved reaction probability. |
| $\chi_\nu$ | Vibrational efficacy. |

**Physical constants**

| | |
|---|---|
| $k_B$ | Boltzmann constant. |
| $\hbar$ | Reduced Planck constant. |

**Properties of the potential**

| | |
|---|---|
| $E_b$ | Height of a barrier. |
| $Z_b$ | $Z$ coordinate at a barrier. |
| $\xi$ | Energetic corrugation. |
| $r_b$ | $r$ coordinate at a barrier. |

**Quantum numbers**

| | |
|---|---|
| $J'$ | Final rotational quantum number of a diatomic molecule. |
| $J$ | Initial rotational quantum number of a diatomic molecule. |
| $\nu'$ | Final vibrational quantum number of a diatomic molecule. |
| $\nu$ | Initial vibrational quantum number of a diatomic molecule. |
| $m'_J$ | Final magnetic rotational quantum number of a diatomic molecule. |
| $m_J$ | Initial magnetic rotational quantum number of a diatomic molecule. |
| $m$ | A diffraction quantum number of a diatomic molecule interacting with a surface. |
| $n$ | A diffraction quantum number of a diatomic molecule interacting with a surface. |

**Reaction probability curve parameters**

| | |
|---|---|
| $A$ | Saturation value of a reaction probability curve. |
| $E_0$ | Dynamical barrier height. |
| $W$ | Width of a reaction probability curve. |

**Static corrugation model**

| | |
|---|---|
| $V_{\text{coup}}$ | Coupling potential. |
| $V_{\text{strain}}$ | Strain potential. |

CHAPTER 1

# Introduction

## 1.1 Reactions of molecules on surfaces

A large number of processes in chemistry and physics, both in everyday life and in industry, occur at a surface. Atoms and molecules can interact with a surface, but also light and heat can. Well known examples of surface chemistry in everyday life are for example the rusting (oxidation) of metals and the conversion of toxic exhaust gases of a car into less harmful gases. An example from physics is the transfer of heat through a surface, which is noticeable in everyday life by the air inside a house cooling down on a cold day, but also by a lake freezing over, which starts at the water–air surface and then continues downward.

Processes occurring at surfaces are also heavily used in industry. Probably the most famous industrial process making use of surface chemistry is the Haber–Bosch process,[1]

$$N_2 + 3\,H_2 \rightleftharpoons 2\,NH_3, \tag{1.1}$$

the process in which ammonia is synthesized, an important chemical in the production of fertilisers, which are needed in order to produce food for the world population. Another example of such a reaction is the methane steam reforming process,[2]

$$CH_4 + H_2O \rightleftharpoons 3\,H_2 + CO, \tag{1.2}$$

which is currently the most used method to produce hydrogen, for example for use in fuel cells.

In both of these processes, the metal surface acts as a catalyst, which lowers the barrier to reaction. The gas reactants such as $N_2$ or $CH_4$ are passed over the solid catalyst, on which they are then adsorbed and the reaction can then take place. For the Haber–Bosch process, commonly iron- or ruthenium-based catalysts are used, whereas for the methane steam reforming process commonly nickel-based catalysts are used.

Clearly, processes occurring at surfaces are important and it should therefore not come as a surprise that such processes are well studied, both from an experimental and a theoretical perspective. Many such processes are however rather complex. Often surfaces are not well-defined or rather rough, or the surface is polluted with atoms or molecules that had already been adsorbed on the surface, thus making

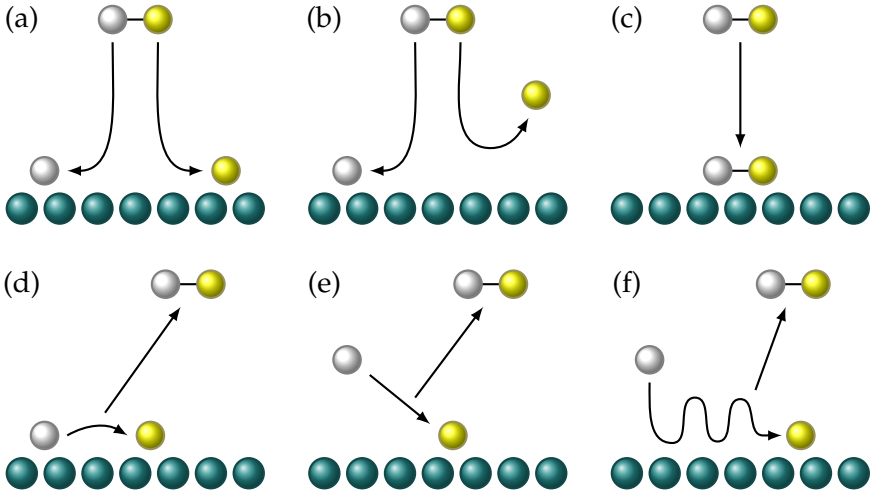


**Figure 1.1** Different mechanisms for molecule–surface reactions: (a) dissociative chemisorption, (b) abstraction, (c) molecular adsorption, (d) Langmuir–Hinshelwood, (e) Eley–Rideal and (f) the hot-atom mechanism.

it unclear what causes a particular process to occur. It is even possible that such pre-adsorbed particles block a particular process from occurring. Often therefore well-defined surfaces are used, and a large number of studies in the field of surface science consider clean, single crystal-cut surfaces. This reduces the complexity of the system considerably and makes it possible to understand, at the very least in a qualitative way, processes at surfaces.

Research on molecule–surface reactions has revealed various mechanisms, the most common mechanisms being shown in figure 1.1. Before any chemistry can occur on a surface, first the surface needs to be covered with some reactant, *i.e.*, atoms or molecules. The way to achieve this is by adsorbing this reactant on the surface. In figure 1.1(a) to (c), three mechanisms are shown for a molecule being adsorbed to the surface: dissociative chemisorption (a), in which a bond of the incoming molecule is broken and both fragments are adsorbed to the surface; abstraction (b), in which a bond of the incoming molecule is also broken but only one fragment is adsorbed to the surface while the other fragment bounces back into the gas phase; and molecular adsorption (c),

in which the molecule is adsorbed onto the surface as a whole, and no bond in the molecule is broken, either by chemisorption or physisorption.

It is also possible for molecules to combine with a fragment that is adsorbed on the surface and then dissociate. Three such mechanisms are shown in figure 1.1(d) to (f): Langmuir–Hinshelwood (d), in which two fragments that are adsorbed on the surface meet each other, form a new bond and dissociate; Eley–Rideal (e), in which a fragment coming in from the gas phase collides with an adsorbed fragment to form a new bond and the molecule formed in this way desorbs; and the hot-atom mechanism (f), in which a fragment from the gas phase collides with a surface, makes several bounces while it is not yet equilibrated with the surface, after which it collides with another adsorbed fragment on the surface, forming a new bond with this fragment, and the molecule formed in this way desorbs.

Of particular interest is the dissociative chemisorption mechanism, which is in many applications of molecule–surface reactions an elementary step in the reaction and can even be the rate-limiting step: for example, in the Haber–Bosch process, both $N_2$ and $H_2$ need to dissociate on the metal surface, and in this process $N_2$ dissociation is the rate-limiting step.[3]

## 1.2 Scattering of hydrogen from metal surfaces

As discussed above, an important step in many applications of molecule–surface reactions is the adsorption of (small) molecules on a metal surface. Understanding the scattering and adsorption of molecules on a surface is therefore often the first step to be studied for a chemical reaction occurring at a surface. An example of such a reaction is the scattering and adsorption of hydrogen molecules on a metal surface.

The scattering and adsorption of hydrogen molecules on a metal surface is a particularly interesting system to study. This is due to several reasons. A hydrogen molecule is a homonuclear diatomic molecule and thus it is the simplest system which can undergo dissociative chemisorption. Additionally, both thermal surface atom displacements due to phonons and electron–hole pair excitations, which can in principle oc-

cur, are expected to have a small effect on the dissociation of hydrogen on a metal surface.[4] For a discussion of these effects, and a detailed overview of theoretical results on $H_2$ dissociation on and scattering from metal surfaces, the reader is also referred to reviews on these topics, such as references 4–7.

For $H_2$ dissociation on Pt(111), it has been argued that electron–hole pair excitations should not play a large role in such a process.[8] For $H_2$ dissociation on Cu(111),[9,10] Cu(110)[11] and Ru(0001)[12] dynamical calculations have been performed in which non-adiabatic effects have been taken into account using electronic friction methods. No large non-adiabatic effects have been found in these calculations, suggesting that electron–hole pair excitations do not play a large role. Furthermore, for activated systems, the amount of energy exchanged between $H_2$ and the surface is not expected to be large,[13,14] due to the large mass mismatch between the $H_2$ molecule and a surface atom.[15,16]

By making these approximations it becomes computationally feasible to represent the potential energy surface (PES), as it only has six dimensions, as well as to perform many (quasi-)classical trajectory and quantum dynamics[4] calculations. This allows, for example, the effect the used electronic structure method has on the PES and through that on dynamical properties to be investigated.

### 1.2.1 The hydrogen molecule

Before the case of a hydrogen molecule interacting with a metal surface can be discussed, first the hydrogen molecule itself needs to be discussed. The hydrogen molecule is the simplest and lightest diatomic molecule (two electrons) that can be considered. A diatomic molecule in general has six degrees of freedom. Applying the rules of quantum mechanics to a diatomic molecule has several consequences. The vibrational motion (associated with one degree of freedom) of the molecule is quantised and is represented by the quantum number $v$ and has a particular vibrational zero-point energy (ZPE). The rotational motion (associated with two degrees of freedom) of the molecule is also quantised and is represented by the quantum numbers $J$ and $m_J$ (see figure 1.2). Translational motion (given by the three remaining degrees of freedom)

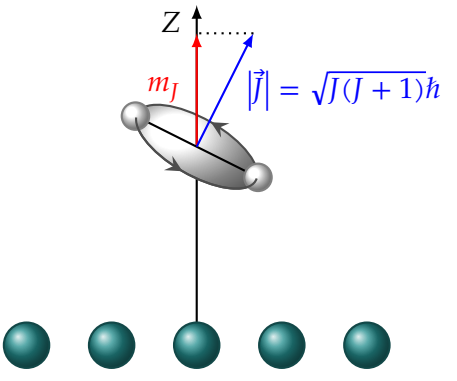


**Figure 1.2** The angular momentum vector $\vec{J}$ of the hydrogen molecule together with its projection ($m_J$) on the surface normal ($Z$), and the definition of its angular momentum quantum number $J$.

is not quantised in the gas phase. The molecule can therefore have any amount of initial translational energy ($E_{\text{trans}}$) with any arbitrary incidence direction.

### 1.2.2 Hydrogen interacting with a surface

When a hydrogen molecule approaches a surface, the PES becomes more complicated due to the interaction of $H_2$ with the metal surface. If the surface is considered to be frozen, the PES will depend on the six degrees of freedom of the $H_2$ molecule. As the molecule approaches the surface, the bond will stretch and, if enough energy is present, the molecule may overcome the barrier to dissociation, and as a result two individual H atoms are adsorbed on the surface. If not enough energy is present in the $H_2$ molecule to overcome the barrier to dissociation, it may scatter back or it may stick on the surface without the molecule dissociating.

In any collision of a molecule with a surface, energy can be redistributed over the molecule from one degree of freedom to another, or the molecule can lose energy to the surface. In figure 1.3 these possibilities are shown for scattering of a diatomic molecule from a metal surface. In principle, any combination of these processes can occur when a molecule scatters on a metal surface. If no energy is rearranged over the

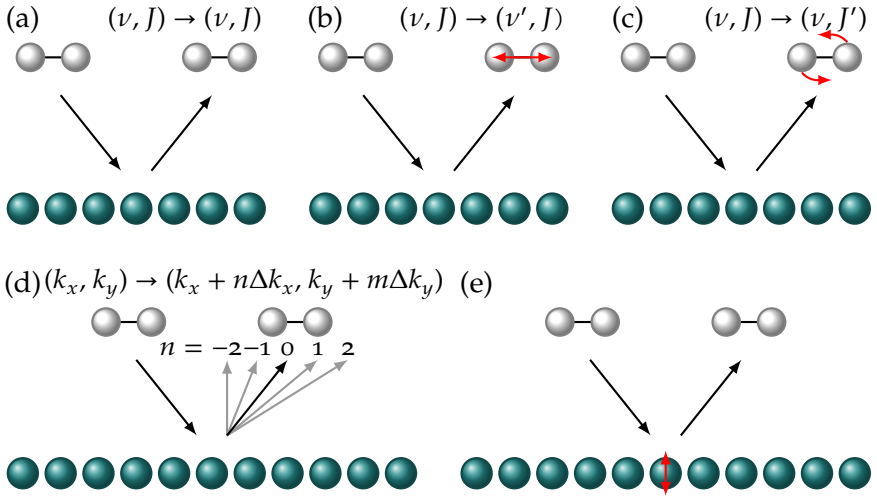


**Figure 1.3** Scattering of a diatomic molecule on a metal surface: (a) elastic scattering, (b) vibrationally inelastic scattering, (c) rotationally inelastic scattering, (d) diffraction and (e) excitation of phonons.

molecular degrees of freedom, it is called elastic scattering (a). If energy is transferred into the vibrational or rotational degrees of freedom of the $H_2$ molecule, it is called vibrational inelastic scattering (b) or rotational inelastic scattering (c), respectively. Near a surface the momentum parallel to the surface can only change in discrete amounts due to the periodic nature of such a surface. This process is called diffraction or diffractive scattering (d). The associated quantum numbers are $n$ and $m$, and the diffraction quanta are given by $\Delta k_x = 2\pi/L_x$ and $\Delta k_y = 2\pi/L_y$, respectively, with $L_x$ and $L_y$ the lengths of the surface unit cell. Finally, the molecule may also excite surface degrees of freedom, *i.e.*, phonons (e) and electron–hole pairs. It is noted that due to the quantisation of rotational, vibrational and parallel motion of the $H_2$ molecule, energy transfer from or into these degrees of freedom may only correspond to full energy quanta. For motion perpendicular to the surface, however, no such restrictions apply and any amount of energy can therefore be transferred into this degree of freedom. The surface degrees of freedom are in theory also quantised. Phonons show discrete states, and in electron–hole pair excitations electrons of the surface are excited into

another state. Electron–hole pair excitations are, however, in infinitely sized metals possible with infinitesimally small energy changes because the highest band occupied by electrons is only partly filled.

Depending on the precise interaction of $H_2$ with the surface, different potentials are obtained. It is therefore of interest to define several different types of $H_2$–surface systems. From a phenomenological point of view, it is interesting to define different types of $H_2$–surface systems based on the interactions and, in particular, the barrier heights found in the PES of such a system. Such a system can show activated (barrierless) or non-activated dissociation. There are, however, also systems falling in between these two extrema, such as $H_2$ dissociation on Ru(0001)[17,18] and Pt(111).[8,19] It is therefore illustrative to make a division in three types of systems, in order of increasing probability for reaction: strongly activated systems, weakly activated systems and non-activated systems. It is emphasized that this division is somewhat arbitrary, especially considering that the scale might be somewhat continuous, considering that the barrier heights for different systems are in general different, and as such no two systems are equivalent. The three "model" systems are now briefly discussed, and examples are given.

Strongly activated systems show late, high barriers to dissociation for all possible geometries and therefore show the least amount of reaction of all cases. Examples of these systems include $H_2$ dissociation on Cu(111),[20] Cu(110),[20] Cu(100),[20] Ag(111)[21] and Au(111).[21] Molecules that have an energy high enough to overcome the barrier react, whereas molecules that do not have an energy high enough to overcome the barrier scatter back into the gas phase. The reaction probability as a function of collision energy generally rises monotonically up to the saturation value, as the $H_2$ molecule, with increasing incidence energy, can overcome the barrier to dissociation for more reaction pathways. For Cu(111),[22] Cu(100)[23] and Ag(111),[24] the lowest barrier is found for the bridge site.

On the other side of the spectrum are the systems with non-activated dissociation, in which at least some of the reaction pathways show no barrier. Other reaction pathways show barriers that can be either early or late. Examples of these systems include $H_2$ dissociation on Pd(111),[25,26] Pd(100),[27] Ni(110),[27] Ni(100)[27] and V(111).[28] Often, not

all reaction pathways show barrierless dissociation, and the reaction probability still increases with increasing incidence energy. For low incidence energies, however, the reaction probability may also be increased due to the trapping of molecules in a well in the potential.[29,30] For Pd(111), barrierless dissociation is found for the top site.[30]

The weakly activated systems share properties with the strongly activated and the non-activated systems. No barrierless pathways are found, *i.e.*, dissociation is an activated process. Examples of these systems are $H_2$ dissociation on Ru(0001),[17,18] Rh(111),[31,32] Pt(111)[8,19] and Ni(111).[27] The PES only shows low barriers to dissociation and these are often early (far away from the surface), as found for Pt(111)[33] and Ru(0001).[17] As there is no barrierless dissociation, the reaction probability, as for the strongly activated systems, increases monotonically with increasing incidence energy. For Pt(111),[33] Ru(0001)[17] and Ni(111),[34] the lowest barrier is found for the top site.

### 1.2.3 Approximations and challenges

There are a number of approximations inherent to theoretical treatments of scattering of $H_2$ from metal surfaces and a number of challenges remain. First the approximations are considered. The three large approximations are:

- the ideal static surface approximation,
- the neglect of electron–hole pair excitations,
- the exchange–correlation (XC) functional used in density functional theory (DFT).

In the ideal static surface approximation, the surface atoms are assumed to be frozen in their ideal lattice positions (after the surface is allowed to relax), and as a result neither energy exchange between the molecule and the surface, nor the effect of the increased corrugation of the surface due to the surface temperature is considered. It is also not possible for the surface to undergo expansion due to the surface temperature, which can have a marked effect on the reaction dynamics.[35] Additionally, from experiments on $H_2$ and $D_2$ desorbing from Cu(111),

it is known that reaction probability curves broaden as a function of the surface temperature.[36,37]

The neglect of electron–hole pair excitations is the next approximation. When a molecule collides with a surface, it can excite electrons of the surface (*i.e.*, the Born–Oppenheimer[38] approximation does not hold). As crystals, due to their periodicity, exhibit a band structure and the highest occupied band in metals is only partly filled, for metal surfaces electronic excitations can occur with an infinitesimally small energy. This approximation thus seems dangerous for reactions of molecules on metal surfaces. For $H_2$ dissociation on metal surfaces however it has been argued[8] that electron–hole pair excitations do not have a large effect on reactive and non-reactive scattering. For $H_2$ dissociation on Cu(111),[9,10] Cu(110)[11] and Ru(0001)[12] electronic friction-based approaches have been used to study non-adiabatic effects in dynamical calculations. No large non-adiabatic effects have however been found in these calculations, suggesting that this approximation is not bad for reactions of $H_2$ and $D_2$ on metal surfaces.

The XC functionals used in DFT calculations on molecule–surface reactions are not exact and as the generation of the PES depends on the DFT calculations, the PES is therefore not exact. The approximations used in the construction of the XC functionals therefore also pose limits to the accuracy of a description of a molecule–surface reaction. For molecule–surface reactions, commonly generalized gradient approximation (GGA)[39,40] level functionals are used as these are readily available in many quantum chemistry software packages. The local density approximation (LDA)[41] does not work well for molecule–surface reactions,[42–44] as it tends to give barriers for activated processes that are significantly too low compared to experimental data. The levels of approximations for the XC functional are further described in section section 2.2.1.

Apart from the approximations given above, also challenges remain for molecules reacting on metal surfaces in general[45,46] which are not all immediately related to reactions of $H_2$ on a metal surface. One such challenge is the treatment of more complex systems. For example, the dissociation of $CH_4$ and its isotopologues on metal surfaces have recently been studied using *ab initio* molecular dynamics (AIMD) calcu-

lations,[47] and also the dissociation of $N_2$ on W(110) has recently been studied.[48] Although $N_2$ dissociation does not introduce any additional degrees of freedom, energy exchange with the surface is a more important process as the mass mismatch between a $N_2$ molecule and a metal atom is not as small as it is for a $H_2$ molecule with a metal atom. Additionally, whether electron–hole pair excitations might have a large effect on reaction of $N_2$ on W(110) and other metal surfaces remains a matter of debate.[11,45,49]

The surface can also be made more complex, for example by adding pre-adsorbed atoms or molecules to it or considering surface cuts which exhibit a lower symmetry and a larger unit cell, such as stepped surfaces. Adding pre-adsorbed atoms or molecules is rather interesting because these types of systems can be examples of the "poisoning" of a catalyst. Each of these changes makes a treatment using a static model more complex and as such the use of AIMD is an interesting approach.[50]

## 1.3 Scope and aim of this thesis

As discussed above, there are a number of commonly used approximations and limitations to theoretical descriptions of surface science. In this thesis, the main aim is to provide an improved description of $H_2$ dissociation on metal surfaces, and to better understand when and why the approximations discussed above fail. Predominantly the effect of the XC functional is considered (chapters 4 to 7), but attempts are also made to go beyond the ideal static surface approximation (chapters 3 and 7) and to include adsorbates on the metal surface (chapter 7).

In **chapter 2** the theory of the dynamical methods used in this thesis is described. Also an overview of DFT is given, as well as an overview of the interpolation method used for the PESs in the later chapters of this thesis, the corrugation reducing procedure (CRP).

In **chapter 3** a model is developed to describe surface temperature effects for the dissociation of $H_2$ and $D_2$ on Cu(111). In this model, in contrast to many models developed before, such as the (modified) surface oscillator (SO) models,[13,51–56] the goal is not to describe energy exchange, which may be expected to be a relatively small contribution to the dynamics because of the large mass mismatch between $H_2$ and Cu,

but instead to describe the effect of the surface becoming more corrugated by the displacement of Cu atoms with respect to their ideal lattice positions at a particular $T_s$.

In **chapter 4** the XC functional dependence of the dissociation of $H_2$ on Ru(0001) is investigated to investigate whether a functional can be found which can describe the dependence of reaction on the incidence energy as well as the probability for diffraction. Various XC functionals are tested, including the revTPSS meta-generalized gradient approximation (meta-GGA) and functionals containing vdW-DF[57] or vdW-DF2[58] correlation.

In **chapter 5** the XC functional dependence of the dissociation of $H_2$ on Pd(111) is investigated, in order to investigate whether a better functional, possibly using vdW-DF correlation, can be found to describe this system.

In **chapter 6** the differences between the SRP48 and optPBE-vdW-DF functionals are investigated using quasi-classical dynamics calculations on the dissociation of $H_2$ on Cu(111), Cu(100), Ru(0001) and Pt(111) surfaces, in order to investigate whether functionals with vdW-DF correlation, here represented by optPBE-vdW-DF, can in principle provide an improved description of $H_2$ dissociation on metal surfaces compared to ordinary GGA functionals, here represented by SRP48.

In **chapter 7** the dissociation of $D_2$ on CO-covered Ru(0001) is investigated using an AIMD approach, in which special attention is paid to the effects arising due to the motion of CO and the Ru atoms.

## 1.4 Main results

Throughout this thesis various $H_2$–surface systems are considered. The main results of each chapter are discussed here.

### Chapter 3: Static surface temperature effects on the dissociation of $H_2$ and $D_2$ on Cu(111)

In chapter 3, the surface temperature dependence of $H_2$ dissociation on Cu(111) is discussed using a static corrugation model, in which a pair potential is used to correct the PES for displacements of surface atoms.

In such a model energy exchange is not possible. The experimentally observed broadening[36] of the reaction probability as a function of incidence energy is attributed primarily to the displacement of surface atoms and can be described in at least a semi-quantitative way. The rotational quadrupole alignment parameter is decreased, especially at lower incidence energies, resulting in a better agreement with experimental data. For low surface temperatures, *i.e.*, at $T_s = 120\,\mathrm{K}$, which was used for the experimental molecular beam experiments, no large differences are observed with the ideal static surface calculations.

### Chapter 4: The effect of the exchange–correlation functional on $H_2$ dissociation on Ru(0001)

In chapter 4, various XC functionals are tested for their applicability to the dissociation of $H_2$ on Ru(0001). For this system the energetic corrugation is known to vary with the XC functional used.[17] It is found that XC functionals which contain vdW-DF or vdW-DF2 correlation give a PES with a higher energetic corrugation for a particular lowest barrier height than the purely semi-local XC functionals that have been tested. As a result of this higher energetic corrugation, the reaction probability curves are broader for these functionals and thus are in better agreement with the width of the reaction probability curve measured in experiments. The revTPSS meta-GGA functional does not give a large improvement over the "standard" GGA functionals, *e.g.* those containing PBE correlation, but the meta-GGA does give a lattice constant in good agreement with experiments, in contrast to the standard GGA functionals. The PBE-vdW-DF2 functional, which combines PBE exchange with vdW-DF2 correlation, and the PBE:RPBE(50:50)-vdW-DF functional, which combines 50% PBE and 50% RPBE exchange with vdW-DF correlation, both give a good overall agreement with the experimentally measured reaction probabilities. These functionals however do not give a good agreement for diffraction, as the computed diffraction probabilities are too large compared to the experimental values. It is not fully understood why this is the case. This may be related to the Debye–Waller extrapolation, which was done by the experimentalists to estimate diffraction probabilities for a 0 K surface. It is unclear whether this extra-

polation works well for this system.

### Chapter 5: Towards a specific reaction parameter density functional for reactive scattering of $H_2$ from Pd(111)



In chapter 5, four XC functionals are tested on the dissociation of $H_2$ on Pd(111), in order to determine whether a specific reaction parameter (SRP) functional can be found for this system. A comparison with experimental data is complicated by the amount of experimental data available, as three different molecular beam experiments have been carried out and all three show different results. The latest experiment is assumed to be the most accurate. The PBE-vdW-DF functional is found to give a good agreement with the experimentally measured sticking probabilities above a collision energy of 125 meV. Below this energy, neither quantum nor quasi-classical dynamics can reproduce the experimental sticking probabilities, as the "upturn" of reaction probabilities for low incidence energies does not occur. The agreement with the experimentally measured state-resolved reaction probabilities, which have been measured at incidence energies lower than 125 meV, is also not good due to the lack of the upturn. The agreement between quantum and quasi-classical dynamics is however rather good in general. A reason for the lack of the upturn could be a lack of pathways in which barrierless dissociation can occur. It is also possible that the lack of energy exchange between the molecule and the surface in the dynamical model is responsible for the poor agreement with experiment. Calculations[14,59] on the $H_2$/Pd(111) system suggest that at low collision energies energy exchange with the surface might lead to trapping, which can in turn promote reaction.

### Chapter 6: Performance of a non-local van der Waals density functional on the dissociation of $H_2$ on metal surfaces

In chapter 6, the optPBE-vdW-DF and SRP48 functionals are compared to each other with respect to the application to the dissociation of $H_2$ and $D_2$ on Cu(111), Cu(100), Pt(111) and Ru(0001). The PESs for the different systems are qualitatively similar for the optPBE-vdW-DF functional and the SRP48 functional. The potential as a function of the

molecule–surface distance $Z$ rises more quickly for the optPBE-vdW-DF functional than it does for the SRP48 functional. Both functionals give a good description of dynamical properties such as sticking probabilities, although the optPBE-vdW-DF functional gives a better overall description. Reaction probabilities for $D_2$ dissociation on Ru(0001) and Pt(111) computed with the optPBE-vdW-DF functional rise less quickly with increasing incidence energy than those computed with the SRP48 functional, causing the better agreement with experiment. The vibrational efficacy for $H_2$ dissociating on Cu(111) is slightly larger for the optPBE-vdW-DF functional. The dependence of reaction on the initial rotational quantum number $J$ is different for the two functionals: the optPBE-vdW-DF functional predicts reaction to not or only slightly depend on $J$ for small $J$, but the SRP48 functional shows a larger dependence on $J$ (increasing with $J$ also for small $J$, which is in disagreement with experiment). The computed rotational quadrupole alignment parameters are lower for SRP48, consistent with the higher reaction probabilities for this functional. Overall, the optPBE-vdW-DF functional gives results in better agreement with experiments than the SRP48 functional does.

### Chapter 7: *Ab initio* molecular dynamics study of $D_2$ dissociation on CO-precovered Ru(0001)

In chapter 7, the dissociation of $D_2$ on a CO-covered Ru(0001) surface is considered. For this system, the AIMD method is used with the PBE-vdW-DF2 functional in order to incorporate the motion of the CO molecules and the ruthenium surface atoms. Two simulation cell sizes are considered: a $3 \times 3$ cell and a smaller $\sqrt{3} \times \sqrt{3}$ cell. The reaction probability at $E_{\text{trans}} = 0.466\,\text{eV}$ is about 0.05 higher for the $3 \times 3$ simulation cell than for the smaller cell. The reaction probabilities obtained with the PBE-vdW-DF2 functional are in good agreement with previously computed reaction probabilities with the RPBE functional, where no surface motion was taken into account. No large differences for the reaction probability are found between an ideal CO/Ru(0001) surface and a 180 K surface. A large amount of energy transfer to the CO molecules is found regardless, and the amount depends on the size of the simu-

lation cell chosen. At $E_{\text{trans}} = 0.466\,\text{eV}$, $0.105 \pm 0.002\,\text{eV}$ is transferred to the surface for a $\sqrt{3} \times \sqrt{3}$ simulation cell, while $0.263 \pm 0.007\,\text{eV}$ is transferred to the CO molecules and the surface for a $3 \times 3$ simulation cell. Energy transfer occurs mostly to the lateral degrees of freedom of the CO molecule. Energy transfer involving motion perpendicular to the surface occurs mostly when a molecule collides head-on with the CO molecule, which is not dependent on the simulation cell size. As the $D_2$ molecule can move into the CO layer, the difference in energy exchange for the lateral degrees of freedom is caused by the molecule pushing against mirror images in such a way that the forces working on the CO molecules partially cancel each other for smaller simulation cells. This results in a decreased amount of energy which is exchanged with the surface and CO molecules. The energy that is exchanged with the CO molecules causes the molecules to move apart, locally "opening" the surface, making it more favourable for reaction of $D_2$ to occur.

## 1.5 Outlook

Although many questions are answered by this thesis, also many new questions and ideas arose as a result of the research carried out in this thesis. In this section these questions and ideas are described and discussed.

First of all, there are several questions related to the performance of XC functionals for molecule–surface reactions. The performance of higher level DFT calculations, based on for example meta-GGA or hybrid XC functionals, is still unclear. In particular meta-GGA calculations are interesting, because functionals are available that give both a good description of the molecule–surface interaction as well as the surface itself.[60] It is, however, not yet clear how adding a van der Waals correction by combining vdW-DF or vdW-DF2 correlation with a meta-GGA exchange functional would affect the PES and dynamics of molecule–surface systems. Furthermore, it is in general not yet fully clear how large the error of GGA functionals is for barrier heights of molecule–surface systems, nor is it fully clear how this translates into errors in dynamical properties. Only for reaction probabilities this is immediately apparent: a too high barrier height generally results in too

low reaction probabilities, and *vice versa*. More complicated dynamical properties, such as vibrational efficacies or inelastic scattering probabilities may be more sensitive to more detailed properties of the PES. In order to get an idea of the sensitivity of these detailed properties, these properties should be investigated for one or more $H_2$–surface systems for several functionals, including those which give similar reaction probabilities, so that the effect of a wrong barrier height can be mostly eliminated. Also interesting is to check the performance of the optPBE-vdW-DF functional used in chapter 6 for other molecule–surface systems, and to check whether better functionals can be found.

Second, the discrepancies found between experiment and theory for both $H_2$ dissociation on Ru(0001) (chapter 4) and Pd(111) (chapter 5) suggest that either the theoretical description is incomplete or that the experimental results are not rightly interpreted. For $H_2$ on Ru(0001), the reported experimental diffraction probabilities could not be reproduced by theory, while the reaction probability could be. This may be related to the Debye–Waller extrapolation used by experimentalists to extrapolate their diffraction probabilities at elevated surface temperatures to $T_s = 0\,\mathrm{K}$ in order to compare to theoretical results. For $H_2$ dissociation on Pd(111), rather different experimental values are reported in the literature for the reaction probability. Although one can assume the latest experiments to be the most accurate, this is not a given and new experiments, preferably with a good characterisation of the molecular beam, should be performed on this system to validate the previous experiments. On the side of theory, it might also be useful to perform quantum dynamics for more XC functionals in order to validate whether the upturn observed for reaction at low collision energies can be reproduced. Additionally, one could explore whether allowing energy transfer to the surface alters the results, as energy transfer to the surface may affect non-activated dissociation quite differently than activated dissociation, for instance by promoting trapping mediated dissociation.[7,14,59]

Third, a better understanding is needed for the dissociation of $D_2$ on CO-covered Ru(0001) (chapter 7). Although energy exchange with the surface plays an important role in the dissociation dynamics, the effect it has on the reaction probability is not large enough to explain the

full difference between the present theory and the experiments. Using a larger simulation cell causes more energy to be exchanged with the surface and the reaction probability to increase somewhat. There are several possible reasons for the discrepancies between theory and experiment: (i) it is not yet fully clear whether the larger unit cell currently used is large enough to capture all possible effects; (ii) the experimental structure and coverage of CO on the surface may not precisely match to the theoretical structure and coverage; (iii) the effect of electron–hole pair excitations may be bigger than expected for this system; or (iv) the XC functional is not quite right for this system, even though it worked well for $D_2$ dissociation on bare Ru(0001). Of particular interest to theory are reasons (i) and (iv): calculations can be performed in a rather straightforward way to see whether they apply. For (i), AIMD calculations could be done on a larger simulation cell and compared to the present results. For (iv), calculations could be done using a different XC functional. It is noted however that changing the XC functional can fix most discrepancies, regardless of the origin of those discrepancies, possibly masking the relevant physics. It is therefore still needed to test whether the other reasons might apply.

Finally, it is noted that it is relatively easy to extend the static corrugation model of chapter 3 to other metal surfaces. Such an extension would allow surface temperature effects to be studied in other $H_2$–surface systems. Additionally, it may be of interest to perform quantum dynamical calculations for $H_2$/Cu(111) or other systems using a vibrational sudden approximation, in which various random geometries and thus perturbations in the PES are introduced, after which the reaction or scattering probabilities are averaged over all selected geometries. Another interesting question is how large the role of energy exchange is for systems like $H_2$ dissociation on Cu(111) and what effect this has on dynamics, if any at all. Extending a static corrugation model such as detailed in chapter 3 to also include surface motion is an interesting possibility for such a study, as the effect of energy exchange can then be studied by displacing the surface atoms but fixing them in space and comparing this to the case where the surface atoms are displaced and allowed to move. The only modification that needs to be made to such a model is the addition of a strain term, which describes how the PES

of the surface in absence of the $H_2$ molecule depends on the surface degrees of freedom.

## References

[1] V. Smil. Detonator of the population explosion. *Nature* **400**(6743), p. 415, 1999.

[2] G. Jones, J. G. Jakobsen, S. S. Shim, J. Kleis, M. P. Andersson, J. Rossmeisl, F. Abild-Pedersen, T. Bligaard, S. Helveg, B. Hinnemann, J. R. Rostrup-Nielsen, I. Chorkendorff, J. Sehested, and J. K. Nørskov. First principles calculations and experimental insight into methane steam reforming over transition metal catalysts. *Journal of Catalysis* **259**(1), pp. 147–160, 2008.

[3] G. Ertl. Studies on the mechanism of ammonia synthesis: the P. H. Emmett award address. *Catalysis Reviews: Science and Engineering* **21**(2), pp. 201–223, 1980.

[4] G. J. Kroes. Six-dimensional quantum dynamics of dissociative chemisorption of $H_2$ on metal surfaces. *Progress in Surface Science* **60**(1–4), pp. 1–85, 1999.

[5] A. Gross. Reactions at surfaces studied by *ab initio* dynamics calculations. *Surface Science Reports* **32**(8), pp. 291–340, 1998.

[6] G. J. Kroes and M. F. Somers. Six-dimensional dynamics of dissociative chemisorption of $H_2$ on metal surfaces. *Journal of Theoretical and Computational Chemistry* **04**(02), pp. 493–581, 2005.

[7] G. J. Kroes and C. Díaz. Quantum and classical dynamics of reactive scattering of $H_2$ from metal surfaces. Accepted to *Chemical Society Reviews*. doi: 10.1039/C5CS00336A. 2016.

[8] P. Nieto, E. Pijper, D. Barredo, G. Laurent, R. A. Olsen, E. J. Baerends, G. J. Kroes, and D. Farías. Reactive and nonreactive scattering of $H_2$ from a metal surface is electronically adiabatic. *Science* **312**(5770), pp. 86–89, 2006.

[9] A. C. Luntz and M. Persson. How adiabatic is activated adsorption/associative desorption? *Journal of Chemical Physics* **123**(7), 074704, 2005.

[10] A. S. Muzas, J. I. Juaristi, M. Alducin, R. Díez Muiño, G. J. Kroes, and C. Díaz. Vibrational deexcitation and rotational excitation of $H_2$ and $D_2$ scattered from Cu(111): adiabatic versus non-adiabatic dynamics. *Journal of Chemical Physics* **137**(6), 064707, 2012.

[11] J. I. Juaristi, M. Alducin, R. Díez Muiño, H. F. Busnengo, and A. Salin. Role of electron–hole pair excitations in the dissociative adsorption of diatomic molecules on metal surfaces. *Physical Review Letters* **100**(11), 116102, 2008.

[12] G. Füchsel, S. Schimka, and P. Saalfrank. On the role of electronic friction for dissociative adsorption and scattering of hydrogen molecules at a Ru(0001) surface. *Journal of Physical Chemistry A* **117**(36), pp. 8761–8769, 2013.

[13] H. F. Busnengo, W. Dong, P. Sautet, and A. Salin. Surface temperature dependence of rotational excitation of $H_2$ scattered from Pd(111). *Physical Review Letters* **87**(12), 127601, 2001.

[14] H. F. Busnengo, M. A. Di Césare, W. Dong, and A. Salin. Surface temperature effects in dynamic trapping mediated adsorption of light molecules on metal surfaces: $H_2$ on Pd(111) and Pd(110). *Physical Review B* **72**(12), 125411, 2005.

[15] B. Baule. Theoretische Behandlung der Erscheinungen in verdünnten Gasen. *Annalen der Physik* **349**(9), pp. 145–176, 1914.

[16] A. Gross. *Theoretical Surface Science*. Berlin: Springer, 2003.

[17] M. Luppi, R. A. Olsen, and E. J. Baerends. Six-dimensional potential energy surface for $H_2$ at Ru(0001). *Physical Chemistry Chemical Physics* **8**(6), pp. 688–696, 2006.

[18] I. M. N. Groot, H. Ueta, M. J. T. C. van der Niet, A. W. Kleyn, and L. B. F. Juurlink. Supersonic molecular beam studies of dissociative adsorption of $H_2$ on Ru(0001). *Journal of Chemical Physics* **127**(24), 244701, 2007.

[19] A. C. Luntz, J. K. Brown, and M. D. Williams. Molecular beam studies of $H_2$ and $D_2$ dissociative chemisorption on Pt(111). *Journal of Chemical Physics* **93**(7), pp. 5240–5246, 1990.

[20] H. A. Michelsen and D. J. Auerbach. A critical examination of data on the dissociative adsorption and associative desorption of hydrogen at copper surfaces. *Journal of Chemical Physics* **94**(11), pp. 7502–7520, 1991.

[21] B. Hammer and J. K. Nørskov. Why gold is the noblest of all the metals. *Nature* **376**(6537), pp. 238–240, 1995.

[22] C. Díaz, R. A. Olsen, D. J. Auerbach, and G. J. Kroes. Six-dimensional dynamics study of reactive and non reactive scattering of $H_2$ from Cu(111) using a chemically accurate potential energy surface. *Physical Chemistry Chemical Physics* **12**(24), pp. 6499–6519, 2010.

[23] L. Sementa, M. Wijzenbroek, B. J. van Kolck, M. F. Somers, A. Al-Halabi, H. F. Busnengo, R. A. Olsen, G. J. Kroes, M. Rutkowski, C. Thewes, N. F. Kleimeier, and H. Zacharias. Reactive scattering of $H_2$ from Cu(100): comparison of dynamics calculations based on the specific reaction parameter approach to density functional theory with experiment. *Journal of Chemical Physics* **138**(4), 044708, 2013.

[24] X. Hu, B. Jiang, D. Xie, and H. Guo. Site-specific dissociation dynamics of $H_2/D_2$ on Ag(111) and Co(0001) and the validity of the site-averaging model. *Journal of Chemical Physics* **143**(11), 114706, 2015.

[25] J. Lesnik. Untersuchungen über Vorläuferadsorption an Übergangsmetallen und Übergangsmetallegierungen. PhD thesis. Technischen Universität Graz, 2001.

[26] M. Beutl, J. Lesnik, K. D. Rendulic, R. Hirschl, A. Eichler, G. Kresse, and J. Hafner. There is a true precursor for hydrogen adsorption after all: the system $H_2$/Pd(111) + subsurface V. *Chemical Physics Letters* **342**(5–6), pp. 473–478, 2001.

[27] K. D. Rendulic, G. Anger, and A. Winkler. Wide range nozzle beam adsorption data for the systems $H_2$/nickel and $H_2$/Pd(100). *Surface Science* **208**(3), pp. 404–424, 1989.

[28] M. Beutl, J. Lesnik, E. Lundgren, C. Konvicka, P. Varga, and K. D. Rendulic. Interaction of $H_2$, CO and $O_2$ with a vanadium (111) surface. *Surface Science* **447**(1–3), pp. 245–258, 2000.

[29] H. F. Busnengo, C. Crespos, W. Dong, J. C. Rayez, and A. Salin. Classical dynamics of dissociative adsorption for a nonactivated system: the role of zero point energy. *Journal of Chemical Physics* **116**(20), pp. 9005–9013, 2002.

[30] H. F. Busnengo, E. Pijper, M. F. Somers, G. J. Kroes, A. Salin, R. A. Olsen, D. Lemoine, and W. Dong. Six-dimensional quantum and classical dynamics study of $H_2$(v=0,J=0) scattering from Pd(111). *Chemical Physics Letters* **356**(5–6), pp. 515–522, 2002.

[31] M. Beutl, J. Lesnik, and K. D. Rendulic. Adsorption dynamics for CO, CO-clusters and $H_2$ ($D_2$) on rhodium (111). *Surface Science* **429**(1–3), pp. 71–83, 1999.

[32] A. Dianat, S. Sakong, and A. Gross. Quantum dynamics of the dissociation of $H_2$ on Rh(111). *European Physical Journal B* **45**(3), pp. 425–432, 2005.

[33] E. Pijper, G. J. Kroes, R. A. Olsen, and E. J. Baerends. Reactive and diffractive scattering of $H_2$ from Pt(111) studied using a six-dimensional wave packet method. *Journal of Chemical Physics* **117**(12), pp. 5885–5898, 2002.

[34] G. Kresse. Dissociation and sticking of $H_2$ on the Ni(111), (100), and (110) substrate. *Physical Review B* **62**(12), pp. 8295–8305, 2000.

[35] A. Mondal, M. Wijzenbroek, M. Bonfanti, C. Díaz, and G. J. Kroes. Thermal lattice expansion effect on reactive scattering of $H_2$ from Cu(111) at $T_s$ = 925 K. *Journal of Physical Chemistry A* **117**(36), pp. 8770–8781, 2013.

[36] H. A. Michelsen, C. T. Rettner, and D. J. Auerbach. On the influence of surface temperature on adsorption and desorption in the $D_2$/Cu(111) system. *Surface Science* **272**(1–3), pp. 65–72, 1992.

[37] C. T. Rettner, H. A. Michelsen, and D. J. Auerbach. Quantum-state-specific dynamics of the dissociative adsorption and associative desorption of $H_2$ at a Cu(111) surface. *Journal of Chemical Physics* **102**(11), pp. 4625–4641, 1995.

[38] M. Born and R. Oppenheimer. Zur Quantentheorie der Molekeln. *Annalen der Physik* **389**(20), pp. 457–484, 1927.

[39] D. C. Langreth and M. J. Mehl. Beyond the local-density approximation in calculations of ground-state electronic properties. *Physical Review B* **28**(4), pp. 1809–1834, 1983.

[40] A. D. Becke. Density-functional exchange-energy approximation with correct asymptotic behavior. *Physical Review A* **38**(6), pp. 3098–3100, 1988.

[41] W. Kohn and L. J. Sham. Self-consistent equations including exchange and correlation effects. *Physical Review* **140**(4A), A1133–A1138, 1965.

[42] B. Hammer, K. W. Jacobsen, and J. K. Nørskov. Role of nonlocal exchange correlation in activated adsorption. *Physical Review Letters* **70**(25), pp. 3971–3974, 1993.

[43] B. Hammer, M. Scheffler, K. W. Jacobsen, and J. K. Nørskov. Multidimensional potential energy surface for $H_2$ dissociation over Cu(111). *Physical Review Letters* **73**(10), pp. 1400–1403, 1994.

[44] J. A. White, D. M. Bird, M. C. Payne, and I. Stich. Surface corrugation in the dissociative adsorption of $H_2$ on Cu(100). *Physical Review Letters* **73**(10), pp. 1404–1407, 1994.

[45] G. J. Kroes. Towards chemically accurate simulation of molecule-surface reactions. *Physical Chemistry Chemical Physics* **14**(43), pp. 14966–14981, 2012.

[46] G. J. Kroes. Toward a database of chemically accurate barrier heights for reactions of molecules with metal surfaces. *Journal of Physical Chemistry Letters* **6**(20), pp. 4106–4114, 2015.

[47] F. Nattino, H. Ueta, H. Chadwick, M. E. van Reijzen, R. D. Beck, B. Jackson, M. C. van Hemert, and G. J. Kroes. *Ab initio* molecular dynamics calculations versus quantum-state-resolved experiments on $CHD_3$ + Pt(111): new insights into a prototypical gas–surface reaction. *Journal of Physical Chemistry Letters* **5**(8), pp. 1294–1299, 2014.

[48] F. Nattino, F. Costanzo, and G. J. Kroes. $N_2$ dissociation on W(110): an *ab initio* molecular dynamics study on the effect of phonons. *Journal of Chemical Physics* **142**(10), 104702, 2015.

[49] A. C. Luntz, I. Makkonen, M. Persson, S. Holloway, D. M. Bird, and M. S. Mizielinski. Comment on "Role of electron-hole pair excitations in the dissociative adsorption of diatomic molecules on metal surfaces". *Physical Review Letters* **102**(10), 109601, 2009.

[50] A. Gross. *Ab initio* molecular dynamics study of $H_2$ adsorption on sulfur- and chlorine-covered Pd(100). *Surface Science* **608**, pp. 249–254, 2013.

[51] M. Dohle and P. Saalfrank. Surface oscillator models for dissociative sticking of molecular hydrogen at non-rigid surfaces. *Surface Science* **373**(1), pp. 95–108, 1997.

[52] M. Dohle, P. Saalfrank, and T. Uzer. Dissociative sticking of diatomic molecules on cold, non-rigid surfaces: comparison of quantal and semiclassical surface oscillator model. *Surface Science* **409**(1), pp. 37–45, 1998.

[53] M. Dohle, P. Saalfrank, and T. Uzer. The dissociation of diatomic molecules on vibrating surfaces: a semiclassical generalized Langevin approach. *Journal of Chemical Physics* **108**(10), pp. 4226–4236, 1998.

[54] M. Hand and J. Harris. Recoil effects in surface dissociation. *Journal of Chemical Physics* **92**(12), pp. 7610–7617, 1990.

[55] A. C. Luntz and J. Harris. $CH_4$ dissociation on metals: a quantum dynamics model. *Surface Science* **258**(1–3), pp. 397–426, 1991.

[56] P. Saalfrank and W. H. Miller. Quantum-mechanical rates for gas-surface processes. *Surface Science* **303**(1–2), pp. 206–230, 1994.

[57] M. Dion, H. Rydberg, E. Schröder, D. C. Langreth, and B. I. Lundqvist. Van der Waals density functional for general geometries. *Physical Review Letters* **92**(24), 246401, 2004.

[58] K. Lee, E. D. Murray, L. Kong, B. I. Lundqvist, and D. C. Langreth. Higher-accuracy van der Waals density functional. *Physical Review B* **82**(8), 081101, 2010.

[59] H. F. Busnengo, W. Dong, and A. Salin. Trapping, molecular adsorption, and precursors for nonactivated chemisorption. *Physical Review Letters* **93**(23), 236103, 2004.

[60] J. P. Perdew, A. Ruzsinszky, G. I. Csonka, L. A. Constantin, and J. Sun. Workhorse semilocal density functional for condensed matter physics and quantum chemistry. *Physical Review Letters* **103**(2), 026403, 2009.

CHAPTER 1

# CHAPTER 2

# Theory



In this chapter the theory of molecule–surface scattering is described for a diatomic molecule interacting with an ideal static surface, including methods for constructing potential energy surfaces, performing dynamics calculations on such systems as well as computing properties from the results of dynamics calculations.

## 2.1 Potential energy surfaces

In the treatment of the dynamics of a molecule–surface reaction, the ground state potential energy surface (PES) arises from the solution of the electronic Schrödinger equation for the problem, as is done in the framework of the Born–Oppenheimer approximation,[1] which is used throughout this thesis. The PES for a molecule interacting with a surface can be written as[2]

$$V(\vec{r},\vec{q}) = V^{6D}(\vec{r};\vec{q}_{id}) + V_{coup}(\vec{r},\vec{q}) + V_{strain}(\vec{q}), \tag{2.1}$$



where $\vec{r}$ are the molecular degrees of freedom, $\vec{q}$ the surface degrees of freedom, $V^{6D}(\vec{r};\vec{q}_{id})$ is the six-dimensional (6D) PES for the system where the surface atoms are in their ideal positions, $V_{strain}(\vec{q})$ a correction term for displacement of surface atoms in absence of the molecule and $V_{coup}(\vec{r},\vec{q})$ a further correction term for the displacement of surface atoms when the molecule is present. This "coupling" potential couples the motion of the surface atoms and the impinging molecule.

For the case of a molecule interacting with a frozen ideal surface, only $V^{6D}(\vec{r};\vec{q}_{id})$ is required. As this approximation is at the basis of most theoretical surface science studies, also in chapters 4 to 6 of this thesis, in the remainder of this section the interpolation of $V^{6D}(\vec{r};\vec{q}_{id})$ is described. The static corrugation model (SCM) is described in chapter 3.

### 2.1.1 Corrugation reducing procedure

For the PES of a diatomic molecule interacting with a frozen ideal surface a rather efficient interpolation procedure is available, which is called the corrugation reducing procedure (CRP).[3,4] In the CRP, the molecule–surface PES is written as

$$V^{6D}(\vec{r}) = I^{6D}(\vec{r}) + \sum_{i}^{2} V_i^{3D}(\vec{\rho}_i), \tag{2.2}$$

where $\vec{r}$ are the coordinates of the molecule, $V_i^{3D}$ is the atom–surface potential evaluated for the coordinates $\vec{\rho}_i$ of each atom $i$ of the molecule and $I^{6D}$ is the so-called interpolation function, which is defined by this equation. The inclusion of $V_i^{3D}$ serves to reduce the corrugation of the

function $I^{6D}$ compared to $V^{6D}$, and $I^{6D}$ needs to be interpolated in some way over the molecular coordinates $\vec{r}$. The atom–surface potential can further be written as

$$V_i^{3D}(\vec{\rho}_i) = I_i^{3D}(\vec{\rho}_i) + \sum_j^N V^{1D}(R_{ij}), \tag{2.3}$$

where $R_{ij}$ is the distance between atom $i$ of the molecule and atom $j$ of the surface, $V^{1D}$ a one-dimensional (1D) function which reduces the corrugation of $V_i^{3D}$, and $I_i^{3D}$ another interpolation function which is defined by this equation and needs to be interpolated over the atomic coordinates $\vec{\rho}_i$. A common choice for $V^{1D}$ is the interaction of a hydrogen atom above a top layer atom.

By performing these two steps, the corrugation of $I^{6D}$ is reduced in the $X$, $Y$, $\vartheta$ and $\varphi$ degrees of freedom with respect to $V^{6D}$, allowing for an easier interpolation.[3] Often in CRP potentials an interpolation scheme is used for $I_i^{3D}$ and $I^{6D}$ which takes into account the symmetry of the surface. An example of such a scheme, based on the method given for $H_2$/Cu(100) in reference 4, is described below. It is important to note that it is, in principle, possible to use other interpolation schemes than this, and that the interpolation scheme given in section 2.1.2 is clearly not the only possible scheme.

### 2.1.2 Symmetry-adapted interpolation

To interpolate $I^{3D}$ and $I^{6D}$ (or, if the CRP is not applied, $V^{3D}$ and $V^{6D}$) often symmetry can be used to lower the number of points needed in the interpolation. This is because usually a periodic lattice is considered, with all the surface atoms fixed in their ideal lattice positions. Additionally, for the interpolation in the plane of the surface, additional symmetry may be present in the form of, *e.g.*, mirror planes and rotation axes. Furthermore, for the interpolation over the angular degrees of freedom even more symmetry may be present, when for example a homonuclear diatomic is considered or when the molecule is above a high-symmetry site of the surface, where an $n$-fold rotation axis is present. These possibilities are considered in this section and from this an interpolation scheme is derived which has been reported only for spe-

cific symmetries in the literature[3,4] and is similar to the scheme used to construct the PES for references 5 and 6.

#### 2.1.2.1 The atom–surface potential

The atom–surface potential only depends on three degrees of freedom: the lateral coordinates $u$ and $v$, and the atom–surface distance $z$. The $z$ coordinate does not exhibit any symmetry due to the presence of the surface, and as such can be eliminated from the discussion of symmetry. As the $u$ and $v$ coordinates provide two dimensions and the PES is periodic in these degrees of freedom, the symmetry in these coordinates can be described by a wallpaper group, of which 17 exist.[7,8] For the atom–surface potential, the determination of the wallpaper group which needs to be used is simple and can be found by considering the symmetry inherent in the positions of the surface atoms. Periodic basis functions that satisfy the wallpaper group symmetry and are based on Fourier expansions have been worked out in the literature for all of the wallpaper groups.[7] In the Fourier expansion, the $\vec{r}_{\text{lat}} = (u, v)$ dependence of the PES is written as

$$V^{2D}(\vec{r}_{\text{lat}}) = \sum_{k_1,k_2} q_{k_1,k_2} \exp(i\vec{k}\vec{r}_{\text{lat}}), \tag{2.4}$$

with $\vec{k} = k_1\vec{b}_1 + k_2\vec{b}_2$, $\vec{b}_1$ and $\vec{b}_2$ the reciprocal lattice vectors, $k_1$ and $k_2$ the indices of the basis function and $q_{k_1,k_2}$ the (complex) coefficient belonging to that basis function. Because $V^{2D}$ represents a PES, $V^{2D} \in \mathbb{R}$, and it is therefore convenient to rewrite equation (2.4) to use real coefficients. This is done by

$$V^{2D}(\vec{r}_{\text{lat}}) = a_{0,0} + \sum_{k_1,k_2\neq(0,0)} a_{k_1,k_2} \cos(\vec{k}\vec{r}_{\text{lat}}) + b_{k_1,k_2} \sin(\vec{k}\vec{r}_{\text{lat}}). \tag{2.5}$$

Symmetry adapted basis functions $W_j(u, v)$ can then be obtained by considering for which $(k_1, k_2)$ terms of equation (2.5) the coefficients are related by symmetry, and can contain up to twelve terms for the most symmetric wallpaper group (p6mm).[7] The first basis function is always $W_0(u, v) = 1$, and the remainder is dependent on the symmetry of the

surface. It is noted that some sine terms will cancel out due to symmetry, as $\sin(x) + \sin(-x) = 0$, and as such, these are discarded.

A simple way to satisfy the constraints on the atom–surface potential is to first obtain at $N$ sites $V_i^{\text{atom}}(z)$, where $i$ is a particular site. This can easily be achieved by spline interpolation over $z$ of a number of points computed with density functional theory (DFT). When this is known, a set of $N$ basis functions $W_j(u, v)$ needs to be chosen which are used to perform the interpolation over $u$ and $v$. This yields a series of equations (one for each site at which the potential is known) of the form

$$\sum_j^N W_j(u_i, v_i) c_j(z) = V_i^{\text{atom}}(z), \tag{2.6}$$

with $u_i$ and $v_i$ the coordinates for site $i$. The above equation can be rewritten as a matrix-vector multiplication

$$\begin{pmatrix} W_1(u_1,v_1) & W_2(u_1,v_1) & \dots & W_N(u_1,v_1) \\ W_1(u_2,v_2) & W_2(u_2,v_2) & \dots & W_N(u_2,v_2) \\ \vdots & \vdots & \ddots & \vdots \\ W_1(u_N,v_N) & W_2(u_N,v_N) & \dots & W_N(u_N,v_N) \end{pmatrix} \begin{pmatrix} c_1 \\ c_2 \\ \vdots \\ c_N \end{pmatrix} = \begin{pmatrix} V_1^{\text{atom}} \\ V_2^{\text{atom}} \\ \vdots \\ V_N^{\text{atom}} \end{pmatrix} \tag{2.7}$$

or $\boldsymbol{W}\vec{c} = \vec{V}$. The coefficients can then be obtained by $\boldsymbol{W}^{-1}\vec{V} = \vec{c}$. Note that $\vec{c}$ depends on $z$ due to $\vec{V}$, but $\boldsymbol{W}$ does not depend on $z$. The resulting potential can then be obtained by

$$V^{\text{3D}}(u, v, z) = \sum_j^N W_j(u, v) c_j(z). \tag{2.8}$$

The question which remains is which symmetry adapted basis functions should be used. Once the symmetry of the surface unit cell is known, and thus the symmetry of the PES is known, the basis functions can be chosen. This procedure is not entirely straightforward, and care must be taken that the matrix $\boldsymbol{W}$ remains invertible, *i.e.*, no linearly dependent rows may be present. No two basis functions should therefore give the same value for all of the geometries at which the potential is known (aliasing). One particularly important thing to note is that sometimes a lower order term needs to be discarded because the basis

function is zero at all $(u, v)$ positions for which the potential is known. The choice of the basis set does not only depend on the symmetry of the surface, but may also depend on the sites at which the potential is known.

#### 2.1.2.2 The molecule–surface potential

The molecule–surface potential is more difficult to interpolate as more degrees of freedom are taken into account. Not only does an interpolation need to be performed over $U$, $V$ and $Z$, but also over $r$, $\vartheta$ and $\varphi$. Similar to the case for the atom–surface potential, no symmetry can be present in the $Z$ direction, nor can there be symmetry in the internal coordinate $r$. The angular degrees of freedom $\vartheta$ and $\varphi$ do show symmetry. Using the usual spherical coordinate system with the polar angle $\vartheta$ between 0° and 180°, and the azimuthal angle $\varphi$ between 0° and 360°, $V^{6D}(\vartheta, \varphi) = V^{6D}(180° - \vartheta, \varphi + 180°)$ for homonuclear diatomic molecules like $H_2$. The symmetry in $\varphi$ depends on whether a homonuclear diatomic is considered, but also on the presence of mirror planes and rotation axes. For a homonuclear diatomic with $\vartheta = 90°$, $V^{6D}(\vartheta = 90°, \varphi) = V^{6D}(\vartheta = 90°, \varphi + 180°)$. If the center of mass of the molecule is above a mirror plane, for some value of $\varphi_0$, $V^{6D}(\varphi - \varphi_0) = V^{6D}(\varphi_0 - \varphi)$ and $V^{6D}$ is even around $\varphi = \varphi_0$. If the center of mass of a molecule is above a $n$-fold rotation axis, $V^{6D}(\varphi) = V^{6D}(\varphi + 360°/n)$.

As a first step, the interpolation over $Z$ and $r$ is performed for each two-dimensional (2D) cut using a 2D cubic spline interpolation. Then, at each site, the interpolation over $\varphi$ is performed for each individual value of $\vartheta$. For this interpolation the first $N$ terms of the Fourier expansion are used, with $N$ the number of values of $\varphi$ for which the potential is known. The first few terms of this expansion, if a mirror plane passes through the point $(U, V)$, are

$$1,\ \cos(n\varphi - \varphi_0),\ \cos(2n\varphi - \varphi_0),\ \ldots, \tag{2.9}$$

with $n$ the order of the rotational axis present at this site and $\varphi_0$ the $\varphi$ orientation at which the molecule is aligned with the mirror plane. If

no mirror plane passes through this point, the first terms are

$$1,\ \cos(n\varphi),\ \sin(n\varphi),\ \cos(2n\varphi),\ \sin(2n\varphi),\ \ldots. \tag{2.10}$$

Note that in case of a homonuclear molecule that is parallel to the surface ($\vartheta = 90°$), an additional twofold rotational symmetry is present in $\varphi$ and this should be taken into account in $n$. The interpolation over $\vartheta$ is then performed, in which again an interpolation over the first $N$ terms of the Fourier expansion is done. In this case, the basis is given by

$$1,\ \cos(n\vartheta),\ \sin(n\vartheta),\ \cos(2n\vartheta),\ \sin(2n\vartheta),\ \ldots, \tag{2.11}$$

with $n$ equal to 2 for a homonuclear molecule and $n$ equal to 1 for a heteronuclear molecule.

Finally, the interpolation over $U$ and $V$ needs to be performed. In the interpolation over $U$ and $V$ the symmetry of $\varphi$ also needs to be taken into account. In a formal derivation from group theory this would result in a basis set of direct products of functions in $\varphi$ and functions in $U$ and $V$. This can, however, also be taken into account by mapping $V^{4D}(Z, r, \vartheta, \varphi)$ to all positions in the surface unit cell and then interpolating over $U$ and $V$ with a Fourier expansion similar to the one given in equation (2.5).[3,4] In this case the symmetry is imposed by applying the symmetry operators on the data rather than the basis functions. The interpolation over $U$ and $V$ is then based on p1 symmetry (only translation), because if the interpolation is done for a fixed $\varphi$, only for $\vartheta = 0°$ a higher symmetry than p1 is present. In order for the final PES to have the correct symmetry, all terms belonging to a particular "order" (*i.e.*, a symmetry-adapted basis function for the symmetry group of the atom–surface PES) need to be taken into account separately in the p1 interpolation. If this is not possible due to the number of points on which the potential is known, some of these terms may need to be combined.

## 2.2 Density functional theory

In order to obtain the potential energy for a particular geometry, which needs to be done for many geometries to compute a PES, an electronic structure method is needed. An efficient method to compute single

points for the PES is DFT.[9,10] In DFT, in contrast to other electronic structure methods, the potential energy is written as a functional of the electron density $n(\vec{r})$ of the system, instead of computing it from a wave function. As a result, the potential energy can be computed rather efficiently, as the electron density in a system with $N$ electrons only depends on three degrees of freedom, and the method scales as $N^3$ instead of the $N^m$ scaling with $m \geq 4$ for wave function based methods.

Hohenberg and Kohn[9] showed that for a system of electrons in an external potential the ground state wave function is a unique functional of $n(\vec{r})$. It was also shown that DFT is in principle variational, *i.e.*, the application of the Hamiltonian to an electron density which is not equivalent to the ground state electron density will result in a higher energy than the ground state energy.



In the DFT method proposed by Kohn and Sham,[10] a fictitious system consisting of non-interacting electrons in an effective external potential is considered. By comparing this fictitious system to the interacting system, the Schrödinger equation for the interacting system can be formulated as a set of $N$ single-electron equations, often referred to as the Kohn–Sham equations,

$$\left[-\frac{\nabla^2}{2} + V_{\mathrm{KS}}(\vec{r})\right]\phi_i(\vec{r}) = \epsilon_i\phi_i(\vec{r}), \tag{2.12}$$

in which the first term represents the kinetic energy of the electron, and the second term the interactions between the electron and the other particles, called the Kohn–Sham potential $V_{\mathrm{KS}}$. The electron density of the system can be computed by

$$n(\vec{r}) = \sum_{i=1}^{N} \left|\phi_i(\vec{r})\right|^2 \tag{2.13}$$

and the Kohn–Sham potential is given by

$$V_{\mathrm{KS}}(\vec{r}) = V_{\mathrm{ext}}(\vec{r}) + V_{\mathrm{H}}(\vec{r}) + V_{\mathrm{XC}}(\vec{r}), \tag{2.14}$$

in which $V_{\mathrm{ext}}(\vec{r})$ is the external potential, $V_{\mathrm{H}}$ is the Hartree (Coulomb)

potential, given by

$$V_{\mathrm{H}}(\vec{r}) = \int \frac{n(\vec{r}')}{|\vec{r} - \vec{r}'|} \mathrm{d}\vec{r}', \tag{2.15}$$

and $V_{\mathrm{XC}}$ the exchange–correlation (XC) potential, given by

$$V_{\mathrm{XC}}(\vec{r}) = \frac{\delta E_{\mathrm{XC}}[n]}{\delta n(\vec{r})}, \tag{2.16}$$

which represents the error made by the use of the classical Coulomb potential and the kinetic energy of the system of non-interacting electrons. The XC functional $E_{\mathrm{XC}}$ is not known exactly and is therefore approximated in practical calculations. These approximations are discussed in the next section.



### 2.2.1 The exchange–correlation functional

The unknown part of the complete density functional is called the XC functional, and it is clear that, because this part of the functional is not known exactly, the quality of practical applications of DFT depends strongly on the form of the XC functional that is chosen for a calculation. The simplest reasonable approximation is called the local density approximation (LDA), where the XC functional is written as[10]

$$E_{\mathrm{XC}}^{\mathrm{LDA}}[n] = \int n(\vec{r}) \epsilon_{\mathrm{XC}}^{\mathrm{LDA}}(n(\vec{r})) \mathrm{d}\vec{r}, \tag{2.17}$$

in which $n(\vec{r})$ is the electron density, and $\epsilon_{\mathrm{XC}}^{\mathrm{LDA}}$ is a function which depends only locally on the density. In the LDA, the assumption is therefore made that the XC energy of a system only depends locally on the electron density. For the LDA, conventionally the result from the homogeneous electron gas (HEG) is taken, which has an exact solution for the exchange energy, but needs to be approximated for the correlation energy:

$$\epsilon_{\mathrm{XC}}^{\mathrm{LDA}}(n(\vec{r})) = \epsilon_{\mathrm{X}}^{\mathrm{HEG}}(n(\vec{r})) + \epsilon_{\mathrm{C}}^{\mathrm{LDA}}(n(\vec{r})), \tag{2.18}$$

in which $\epsilon_{\mathrm{X}}^{\mathrm{HEG}}$ is given by

$$\epsilon_{\mathrm{X}}^{\mathrm{HEG}}(n(\vec{r})) = -\frac{3}{4}\left(\frac{3n(\vec{r})}{\pi}\right)^{1/3}. \tag{2.19}$$

Approximations for the HEG correlation energy are mostly based on Quantum Monte Carlo data by Ceperley and Alder.[11] Several popular approximations for the LDA correlation functional are given in references 12–14. Although LDA functionals work rather well for solids and in particular metals, a less good performance is to be expected for systems which have an electron density far away from the HEG, such as molecules.[15] The interaction of molecules with a surface is similarly not well described: for various strongly activated $H_2$–metal surface systems no or only a very small barrier to dissociation is found.[16–18]



The next level of approximations is the generalized gradient approximation (GGA).[19,20] In the GGA, the XC energy is still evaluated pointwise as in the LDA, but instead of the functional depending pointwise on the electron density ($n$) only, the gradient of the electron density ($\nabla n$) is added into the functional,

$$E_{\mathrm{XC}}^{\mathrm{GGA}}[n] = \int n(\vec{r}) \epsilon_{\mathrm{XC}}^{\mathrm{GGA}}(n(\vec{r}), \nabla n(\vec{r})) \mathrm{d}\vec{r}. \tag{2.20}$$

Such a functional is often called a semi-local functional due to the added density gradient dependence. Many semi-local functionals are written using so-called exchange or exchange–correlation enhancement factors:

$$\epsilon_{X(C)}^{\mathrm{GGA}}(n(\vec{r}), \nabla n(\vec{r})) = F_{X(C)}(n(\vec{r}), \nabla n(\vec{r})) \epsilon_{X}^{\mathrm{LDA}}(n(\vec{r})), \tag{2.21}$$

where $F_{X(C)}$ is the exchange(–correlation) enhancement factor. The exchange enhancement factor $F_X$ is commonly written as a function of the reduced density gradient $s$:

$$s = \frac{\left|\nabla n(\vec{r})\right|}{2k_F(\vec{r}) n(\vec{r})} = \frac{\left|\nabla n(\vec{r})\right|}{2(3\pi^2)^{1/3} n^{4/3}(\vec{r})}. \tag{2.22}$$

Equation (2.21) provides a large amount of freedom, even if known constraints[21,22] on the XC energy are taken into account.[23,24] The number of GGA functionals that exist in the literature are therefore considerable, and libraries have been created to easily evaluate such functionals.[25] In figure 2.1 the exchange enhancement factor is shown for several popular exchange functionals.

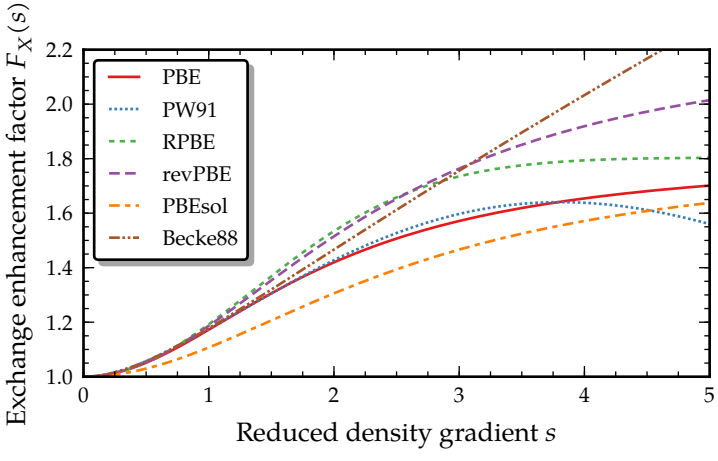


**Figure 2.1** Exchange enhancement factor for several popular GGA exchange functionals.



In surface science, the PW91[21] (or the similar PBE[22]) and RPBE[23] XC functionals are rather popular. The PBE and RPBE XC functionals only differ in the exchange functional, which for PBE is determined by

$$F_X(s) = 1 + \kappa - \frac{\kappa}{1 + \mu s^2/\kappa} \tag{2.23}$$

and for RPBE by

$$F_X(s) = 1 + \kappa \left(1 - \mathrm{e}^{-\mu s^2/\kappa}\right). \tag{2.24}$$

In PBE and RPBE, the parameter $\kappa$ is chosen in such a way that the Lieb–Oxford bound[26] is locally (and therefore also globally) satisfied.[22,27] $\mu$ is chosen to reproduce the LDA linear response by cancelling with correlation.[22]

For molecule–metal surface interactions, the GGA works considerably better[16–18] than the LDA, as also indicated by the wide variety of PESs computed with such methods that are described in the literature (*e.g.*, references 5, 28–32). Unfortunately, however, for solids the GGA does not always yield improvements. Only if GGA functionals specifically constructed to describe solids are used a good description of solids is obtained.[33]

Improving beyond the GGA can be done in many ways, but not all methods are feasible at present for computing a PES for a molecule interacting with a metal surface. The next step on the "Jacob's ladder" proposed by Perdew and Schmidt[34] is the meta-generalized gradient approximation (meta-GGA). In the meta-GGA, apart from the gradient of the density, also the kinetic energy density and/or the Laplacian of the density is added. One advantage for surface science is that a meta-GGA can, using the added variables, better distinguish between molecules and solids, as illustrated by the revTPSS functional.[35] It is possible to go even further, although it is not immediately apparent whether in all cases the application of such functionals to molecule–surface reactions is feasible. For example, the next step on the ladder is the "hyper-GGA", of which hybrid functionals such as B3LYP are an example.[34] In these functionals, Hartree-Fock exchange is added into the functional, which makes the computational cost for molecule–surface reactions considerable and unfeasible at present for a whole PES.

It is important to note that long range interactions such as van der Waals effects are not (properly) described when local or semi-local (*i.e.*, up to meta-GGA level) functionals are used. Various methods[36] have been used to overcome this problem, some more and some less applicable to problems involving metal surfaces. A popular method is the DFT-D3 method by Grimme *et al.*,[37] in which a pairwise potential based on $C_6$ coefficients computed from time-dependent density functional theory (TD-DFT) is added, in contrast to earlier methods,[38,39] where (semi)empirical values were used. Tkatchenko and Scheffler[40] have reported a method where $C_6$ coefficients are obtained from the mean-field ground state electron density. Other approaches are also possible. Dion *et al.*[41] have reported a "seamless" non-local XC functional (vdW-DF) that can describe van der Waals systems. Since then, other functionals have been reported[42–49] that attempt to improve over the original vdW-DF functional, by either changing the exchange functional, the correlation functional or both. The computational method of Román-Pérez and Soler[50] has allowed the vdW-DF[41] and vdW-DF2[45] correlation functionals to be evaluated self-consistently.

### 2.2.2 Periodic DFT using a plane wave basis set

When performing calculations of molecules on a periodic metal surface, the periodicity of the surface needs to be taken into account in order to avoid "edge" effects. One way of avoiding this is to use a sufficiently large cluster of surface atoms. Such calculations however quickly become expensive with the increased number of electrons. Another approach is to build the periodicity into the DFT calculation, by using a periodic basis set. For this basis set, plane waves are used and this method is then commonly referred to as plane wave DFT.

Although using plane waves as a basis has many upsides, there are also some downsides. First of all, generally a large number of plane waves are needed. Second, the entire simulation cell (including the adsorbate) is repeated, and not only the surface itself. This effect can be made arbitrarily small by enlarging the simulation cell so that the coverage of the surface can be decreased systematically. Finally, increasing the vacuum size in between two mirror images of a slab is penalized because more plane waves are needed. A plane wave expansion is however in other ways advantageous. For example, the basis set can be systematically improved with a single parameter and converting the wave functions between real space and momentum space can be done efficiently using fast Fourier transforms (FFTs).

## 2.3 Quasi-classical dynamics

In order to understand and compare to experimental measurements, dynamical properties need to be computed. In this thesis primarily the quasi-classical trajectory (QCT) method[51] is used for this purpose. In the QCT method, dynamical properties are obtained by computing trajectories for an ensemble of initial conditions. Each trajectory is propagated for a particular time until an outcome has been determined for this trajectory, such as dissociative chemisorption or scattering. When all the trajectories have been computed, reaction and scattering probabilities are obtained by counting how many trajectories show a particular outcome.

### 2.3.1 Initial conditions

In order to perform (quasi-)classical dynamics calculations initial positions and velocities are needed, as well as the mass of the particles. For $H_2$ dissociation on a metal surface the initial positions and velocities can be determined rather easily. The $H_2$ molecule is initially placed far away from the surface, where the potential does not depend on $Z$, with a particular velocity towards the surface that corresponds to the perpendicular incidence energy $E_\perp$. A random impact site is chosen and, if off-normal incidence is considered, a velocity vector is set up matching constraints from the parallel incidence energy $E_\parallel$ or the polar incidence angle $\vartheta_i$ and the azimuthal incidence angle $\varphi_i$. The orientation of the molecule $\vartheta$ and $\varphi$ is randomly chosen based on the selected rotational state, with the initial angular momentum $L$ of the molecule fixed by $L = \sqrt{J(J+1)}\hbar$ and the orientation of the angular momentum vector chosen randomly with the constraint $\cos\vartheta_L = m_J/\sqrt{J(J+1)}$, where $\vartheta_L$ is the angle between the angular momentum vector and the surface normal, and $m_J$ is the magnetic rotational quantum number. To take into account the zero-point energy (ZPE) of the $H_2$ molecule, the vibrational states of the molecule are calculated using the Fourier grid Hamiltonian method.[52] The $H_2$ molecule is initially given the amount of energy associated with a particular vibrational state by randomly sampling positions and momenta from a 1D classical dynamics calculation of the vibrating molecule, in which the total energy is equivalent to the energy of the selected vibrational state.

### 2.3.2 Propagation

To integrate the equations of motion, two different propagators are used. For the *ab initio* molecular dynamics (AIMD) calculations using the VASP code,[53–56] the leapfrog algorithm implemented in VASP was used. In the leapfrog algorithm, the representation of the velocities is staggered by half a time step compared to the representation of the positions. The positions are updated by

$$\vec{x}\,(t+\Delta t) = \vec{x}\,(t) + \vec{v}\,(t+\Delta t/2)\,\Delta t, \tag{2.25}$$

and the velocities by

$$\vec{v}\,(t + \Delta t/2) = \vec{v}\,(t - \Delta t/2) + \vec{a}(t)\Delta t, \tag{2.26}$$

where the accelerations are computed from the forces $F$ at time $t$. It is noted that this particular propagator is closely related to the Velocity Verlet propagator, where the velocities and positions are taken at the same time and can be evaluated by

$$\vec{v}\,(t + \Delta t/2) = \vec{v}(t) + \vec{a}(t)\Delta t/2 \tag{2.27}$$

$$\vec{x}\,(t + \Delta t) = \vec{x}(t) + \vec{v}\,(t + \Delta t/2)\,\Delta t \tag{2.28}$$

$$\vec{v}\,(t + \Delta t) = \vec{v}\,(t + \Delta t/2) + \vec{a}(t + \Delta t)\Delta t/2. \tag{2.29}$$

It is noted here that equations (2.25) and (2.28) are equivalent, while substituting equation (2.29), with the substitution $t \rightarrow t - \Delta t$, into equation (2.27) gives equation (2.26). The Velocity Verlet and leapfrog algorithms are therefore the same.[57] The advantage of the leapfrog algorithm is that with $n$ force evaluations $n$ time steps can be made, whereas with the Velocity Verlet algorithm the $n$th time step cannot be completed as equation (2.29) cannot be evaluated for the $n$th step without performing one extra force evaluation.

In the classical dynamics based on the CRP interpolated PESs, the extrapolation method by Stoer and Bulirsch[58] was used. In this method successively smaller time steps are used. This information is then used to extrapolate to an infinitely small time step.

### 2.3.3 Analysis

In a trajectory the molecule is considered to have reacted when the H–H distance $r$ first reaches a particular value. A molecule is considered to have scattered when the molecule is far away from the surface, where no interaction is present, and also has a momentum away from the surface. After a certain amount of time $t_{\text{cut}}$, if neither event has occurred, the molecule is considered to be trapped.

The reaction probability $P_r$ can then be obtained from

$$P_r = N_r/N_{\text{total}}, \tag{2.30}$$

where $N_r$ is the number of reacted trajectories and $N_{\text{total}}$ the total number of trajectories. Additional observables can be computed with the methods described in section 2.5. It should be noted that in quasi-classical dynamics certain observables, such as molecular beam sticking probabilities or degeneracy-averaged reaction probabilities, can also be computed by imposing specific initial conditions. In these cases $P_r$ represents that particular observable, rather than the fully state-resolved reaction probability.



## 2.4 Quantum dynamics

A full description of the theory of quantum dynamics for a molecule–surface reaction is beyond the scope of this thesis. The interested reader is referred to reference 59.

For the quantum dynamics calculations a time-dependent wave packet (TDWP)[60,61] method was used. To represent the wave packet in $Z$, $r$, $X$ and $Y$, a discrete variable representation (DVR)[62] was used, and to represent the wave packet in the angular degrees of freedom, a finite base representation (FBR)[63,64] was used. To transform the wave function from the FBR space to the DVR space, and *vice versa*, FFTs[65] and discrete associated Gauss–Legendre transforms[63,64] were used. To propagate the wave packet according to the time dependent Schrödinger equation, the split operator method[66] is used. The initial wave packet is placed far away from the surface, where only a negligibly small interaction is present, and is written as a product of a Gaussian wave packet for motion perpendicular to the surface, plane waves for motion parallel to the surface and a rovibrational wave function describing the initial state of the molecule.[61] The reflected wave packet is analysed using the scattering amplitude formalism[67–69] at $Z = Z_\infty$, yielding S-matrix elements for state-to-state scattering. For large $r$ or $Z$, optical potentials[70] are used to absorb the reacted ($r$) or analysed ($Z$) wave packet. Scattering probabilities were obtained from S-matrix elements over the entire range of energies present in the wave packet.

The fully initial state-resolved reaction probability is defined as

$$P_r(\nu, J, m_J) = 1 - \sum_{\substack{\nu', J', m'_J, \\ n, m}} P_{\text{scat}}(\nu, J, m_J \to \nu', J', m'_J, n, m), \tag{2.31}$$

where $P_{\text{scat}}(\nu, J, m_J \to \nu', J', m'_J, n, m)$ are the state to state scattering probabilities, $\nu$ ($\nu'$), $J$ ($J'$), $m_J$ ($m'_J$) the initial (final) vibrational, rotational and magnetic rotational quantum numbers, respectively, and $n$ and $m$ the quantum numbers for diffraction.



## 2.5 Computation of observables

### 2.5.1 Initial state-resolved reaction probability

Degeneracy averaged reaction probabilities $P_{\text{deg}}$ can be computed by

$$P_{\text{deg}}(\nu, J) = \sum_{m_J=0}^{J} \left(2 - \delta_{m_J 0}\right) P_r(\nu, J, m_J)/(2J+1), \tag{2.32}$$

in which $P_r$ is the fully initial state-resolved reaction probability and $\delta$ the Kronecker delta.

### 2.5.2 Rotational quadrupole alignment

The rotational quadrupole alignment parameter is a measure of the dependence of the reaction on the orientation of the molecule with respect to the surface. It can be written as

$$A_0^{(2)} = \left\langle 3\cos^2 \vartheta_L - 1 \right\rangle, \tag{2.33}$$

in which $\vartheta_L$ is the angle between the angular momentum vector and the surface normal. It can also be computed as[71]

$$A_0^{(2)}(\nu, J) = \frac{\sum_{m_J} P_r(\nu, J, m_J) \left(\frac{3{m_J}^2}{J(J+1)} - 1\right)}{\sum_{m_J} P_r(\nu, J, m_J)}. \tag{2.34}$$

### 2.5.3 Molecular beam sticking probabilities

The molecular beams used in experiments to measure sticking probabilities do generally not consist of molecules in a single state with one specific amount of energy. The experimental distributions should therefore be taken into account when comparing theoretical results to experimental data. The experimental conditions are taken into account in two steps. First, the initial state-resolved reaction probabilities are Boltzmann averaged over the rovibrational states populated in the molecular beam. Second, the experimental spread of incidence energies is taken into account. The first point is addressed by



$$R_{\text{mono}}(E_{\text{trans}}; T_{\text{n}}) = \sum_{\nu,J} F_B(\nu, J; T_{\text{n}}) P_{\text{deg}}(E_{\text{trans}}, \nu, J). \tag{2.35}$$

$R_{\text{mono}}$ is the mono-energetic reaction probability averaged over all states present in the molecular beam obtained with a nozzle temperature $T_{\text{n}}$. The reaction probability of each state is weighed with the Boltzmann factor

$$F_B(\nu, J; T_{\text{n}}) = \frac{w(J) F(\nu, J; T_{\text{n}})}{\sum_{\nu', J' \equiv J \pmod 2} F(\nu', J'; T_{\text{n}})}, \tag{2.36}$$

in which

$$\begin{aligned} F(\nu, J; T_{\text{n}}) = (2J+1) \exp\left(-E_{\text{vib}}(\nu, J)/(k_B T_{\text{n}})\right) \\ \cdot \exp\left(-E_{\text{rot}}(\nu, J)/(0.8 \cdot k_B T_{\text{n}})\right). \end{aligned} \tag{2.37}$$

In equation (2.36) the summation runs only over the values of $J'$ that have the same parity as $J$. $E_{\text{vib}}$ and $E_{\text{rot}}$ are the vibrational and rotational energy, respectively, of the ($\nu$, $J$) state and $k_B$ is the Boltzmann constant. In these equations, it is assumed that the rotational temperature of the molecules in the beam is lower than the nozzle temperature ($T_{\text{rot}} = 0.8 \cdot T_{\text{n}}$).[72] It is also assumed that the fractions of ortho- and para-$H_2$ and $D_2$ are equivalent to the high temperature limit, given by $w(J)$. This is usually the case in experiments, as the gas cylinder is stored at

room temperature and conversion of ortho- and para-hydrogen does not happen on the time scale of the experiment. For $H_2$, $w(J)$ is equal to $1/4$ for even $J$ and $3/4$ for odd $J$. For $D_2$, $w(J)$ is equal to $2/3$ for even $J$ and $1/3$ for odd $J$.

The mono-energetic reaction probability is then averaged over the translational energy distribution by[6]

$$R_{\text{beam}} = \frac{\int_0^\infty f(v_i; T_n) R_{\text{mono}}(E_{\text{trans}}; T_n) \mathrm{d}v_i}{\int_0^\infty f(v_i; T_n) \mathrm{d}v_i}. \tag{2.38}$$

In this equation $f$ is the flux weighted velocity distribution, which is given by[73,74]

$$f(v_i; T_n)\mathrm{d}v_i = C{v_i}^3 \exp\left[-(v_i - v_0)^2/\alpha^2\right] \mathrm{d}v_i. \tag{2.39}$$

In equation (2.39) $C$ is a constant, $v_i$ the velocity of the molecule, $v_0$ is the stream velocity and $\alpha$ is a parameter describing the width of the velocity distribution.

### 2.5.4 Vibrational efficacy

The vibrational efficacy is a measure of how "efficiently" vibrational energy can be used to promote reaction relative to (normal) translational energy.[75,76] It can be computed by

$$\chi_\nu(J) = \frac{E_0(\nu = 0, J) - E_0(\nu = 1, J)}{E_{\text{vib}}(\nu = 1, J) - E_{\text{vib}}(\nu = 0, J)} = \frac{\Delta E_0}{\Delta E_{\text{vib}}}, \tag{2.40}$$

in which $E_{\text{vib}}(\nu, J)$ is the vibrational energy corresponding to a particular state of the gas-phase molecule and $E_0(\nu, J)$ is the energy for which $P_r(E_0; \nu, J) = P_{r,0}(\nu, J)$, where $P_{r,0}(\nu, J)$ is a particular value of the reaction probability. This reaction probability is commonly taken to be half the saturation value of the reaction probability.[75] In calculations often the convention is used that $P_{r,0}(\nu = 0, J) = P_{r,0}(\nu = 1, J)$. This convention may differ from the one often used by experimentalists if the saturation values differ for $\nu = 0$ and $\nu = 1$, or if a $P_{r,0}$ is selected that does not correspond to half the saturation value for any $\nu$.

### 2.5.5 Diffraction probabilities

In chapter 4 a comparison is made between experimental and theoretical diffraction probabilities. To compare with the experimental diffraction probabilities,[77] first rovibrationally elastic diffraction probabilities were computed by

$$P_{nm}(\nu, J, m_J) = \sum_{m_J''=0}^{J} \Big( \left(2 - \delta_{m_J'' 0}\right) \cdot P_{\text{scat}}(\nu, J, m_J \to \nu' = \nu, J' = J, m_J'', n, m) \Big), \tag{2.41}$$

where $P_{nm}$ is the rovibrationally elastic probability for scattering into the diffraction state denoted by the $n$ and $m$ quantum numbers. These probabilities are then degeneracy averaged by

$$P_{nm}(\nu, J) = \sum_{m_J=-J}^{J} P_{nm}(\nu, J, m_J)/(2J+1). \tag{2.42}$$

Because in experiments mostly $J = 0$ and $J = 1$ $H_2$ were present with a narrow energy distribution,[77,78] in particular at the lowest incidence energies, a reasonable approximation should be the use of a beam of cold $n$-$H_2$ (25 % $J = 0$, 75 % $J = 1$) with a monochromatic energy. In the calculations performed in chapter 4 this approximation is made.

## References

[1] M. Born and R. Oppenheimer. Zur Quantentheorie der Molekeln. *Annalen der Physik* **389**(20), pp. 457–484, 1927.

[2] M. Bonfanti, C. Díaz, M. F. Somers, and G. J. Kroes. Hydrogen dissociation on Cu(111): the influence of lattice motion. Part I. *Physical Chemistry Chemical Physics* **13**(10), pp. 4552–4561, 2011.

[3] H. F. Busnengo, A. Salin, and W. Dong. Representation of the 6D potential energy surface for a diatomic molecule near a solid surface. *Journal of Chemical Physics* **112**(17), pp. 7641–7651, 2000.

[4] R. A. Olsen, H. F. Busnengo, A. Salin, M. F. Somers, G. J. Kroes, and E. J. Baerends. Constructing accurate potential energy surfaces for a diatomic molecule interacting with a solid surface: $H_2$+Pt(111) and $H_2$+Cu(100). *Journal of Chemical Physics* **116**(9), pp. 3841–3855, 2002.

[5] C. Díaz, E. Pijper, R. A. Olsen, H. F. Busnengo, D. J. Auerbach, and G. J. Kroes. Chemically accurate simulation of a prototypical surface reaction: $H_2$ dissociation on Cu(111). *Science* **326**(5954), pp. 832–834, 2009.

[6] C. Díaz, R. A. Olsen, D. J. Auerbach, and G. J. Kroes. Six-dimensional dynamics study of reactive and non reactive scattering of $H_2$ from Cu(111) using a chemically accurate potential energy surface. *Physical Chemistry Chemical Physics* **12**(24), pp. 6499–6519, 2010.

[7] B. Verberck. Symmetry-adapted Fourier series for the wallpaper groups. *Symmetry* **4**(3), pp. 379–426, 2012.

[8] T. J. Frankcombe, M. A. Collins, and D. H. Zhang. Modified Shepard interpolation of gas-surface potential energy surfaces with strict plane group symmetry and translational periodicity. *Journal of Chemical Physics* **137**(14), 144701, 2012.

[9] P. Hohenberg and W. Kohn. Inhomogeneous electron gas. *Physical Review* **136**(3B), B864–B871, 1964.

[10] W. Kohn and L. J. Sham. Self-consistent equations including exchange and correlation effects. *Physical Review* **140**(4A), A1133–A1138, 1965.

[11] D. M. Ceperley and B. J. Alder. Ground state of the electron gas by a stochastic method. *Physical Review Letters* **45**(7), pp. 566–569, 1980.

[12] S. H. Vosko, L. Wilk, and M. Nusair. Accurate spin-dependent electron liquid correlation energies for local spin density calculations: a critical analysis. *Canadian Journal of Physics* **58**(8), pp. 1200–1211, 1980.

[13] J. P. Perdew and Y. Wang. Accurate and simple analytic representation of the electron-gas correlation energy. *Physical Review B* **45**(23), pp. 13244–13249, 1992.

[14] J. P. Perdew and A. Zunger. Self-interaction correction to density-functional approximations for many-electron systems. *Physical Review B* **23**(10), pp. 5048–5079, 1981.

[15] S. Kurth, J. P. Perdew, and P. Blaha. Molecular and solid-state tests of density functional approximations: LSD, GGAs, and meta-GGAs. *International Journal of Quantum Chemistry* **75**(4–5), pp. 889–909, 1999.

[16] B. Hammer, K. W. Jacobsen, and J. K. Nørskov. Role of nonlocal exchange correlation in activated adsorption. *Physical Review Letters* **70**(25), pp. 3971–3974, 1993.

[17] B. Hammer, M. Scheffler, K. W. Jacobsen, and J. K. Nørskov. Multidimensional potential energy surface for $H_2$ dissociation over Cu(111). *Physical Review Letters* **73**(10), pp. 1400–1403, 1994.

[18] J. A. White, D. M. Bird, M. C. Payne, and I. Stich. Surface corrugation in the dissociative adsorption of $H_2$ on Cu(100). *Physical Review Letters* **73**(10), pp. 1404–1407, 1994.

[19] D. C. Langreth and M. J. Mehl. Beyond the local-density approximation in calculations of ground-state electronic properties. *Physical Review B* **28**(4), pp. 1809–1834, 1983.

[20] A. D. Becke. Density-functional exchange-energy approximation with correct asymptotic behavior. *Physical Review A* **38**(6), pp. 3098–3100, 1988.

[21] J. P. Perdew, J. A. Chevary, S. H. Vosko, K. A. Jackson, M. R. Pederson, D. J. Singh, and C. Fiolhais. Atoms, molecules, solids, and surfaces: applications of the generalized gradient approximation for exchange and correlation. *Physical Review B* **46**(11), pp. 6671–6687, 1992.

[22] J. P. Perdew, K. Burke, and M. Ernzerhof. Generalized gradient approximation made simple. *Physical Review Letters* **77**(18), pp. 3865–3868, 1996.

[23] B. Hammer, L. B. Hansen, and J. K. Nørskov. Improved adsorption energetics within density-functional theory using revised Perdew-Burke-Ernzerhof functionals. *Physical Review B* **59**(11), pp. 7413–7421, 1999.

[24] G. K. H. Madsen. Functional form of the generalized gradient approximation for exchange: the PBE$\alpha$ functional. *Physical Review B* **75**(19), 195108, 2007.

[25] M. A. L. Marques, M. J. T. Oliveira, and T. Burnus. Libxc: a library of exchange and correlation functionals for density functional theory. *Computer Physics Communications* **183**(10), pp. 2272–2281, 2012.

[26] E. H. Lieb and S. Oxford. Improved lower bound on the indirect Coulomb energy. *International Journal of Quantum Chemistry* **19**(3), pp. 427–439, 1981.

[27] A. Vela, V. Medel, and S. B. Trickey. Variable Lieb–Oxford bound satisfaction in a generalized gradient exchange-correlation functional. *Journal of Chemical Physics* **130**(24), 244103, 2009.

[28] P. Nieto, E. Pijper, D. Barredo, G. Laurent, R. A. Olsen, E. J. Baerends, G. J. Kroes, and D. Farías. Reactive and nonreactive scattering of $H_2$ from a metal surface is electronically adiabatic. *Science* **312**(5770), pp. 86–89, 2006.

[29] A. Gross and M. Scheffler. *Ab initio* quantum and molecular dynamics of the dissociative adsorption of hydrogen on Pd(100). *Physical Review B* **57**(4), pp. 2493–2506, 1998.

[30] J. Behler, B. Delley, S. Lorenz, K. Reuter, and M. Scheffler. Dissociation of $O_2$ at Al(111): the role of spin selection rules. *Physical Review Letters* **94**(3), 036104, 2005.

[31] G. A. Bocan, R. Díez Mui no, M. Alducin, H. F. Busnengo, and A. Salin. The role of exchange-correlation functionals in the potential energy surface and dynamics of $N_2$ dissociation on W surfaces. *Journal of Chemical Physics* **128**(15), 154704, 2008.

[32] A. Salin. Theoretical study of hydrogen dissociative adsorption on the Cu(110) surface. *Journal of Chemical Physics* **124**(10), 104704, 2006.

[33] J. P. Perdew, A. Ruzsinszky, G. I. Csonka, O. A. Vydrov, G. E. Scuseria, L. A. Constantin, X. Zhou, and K. Burke. Restoring the density-gradient expansion for exchange in solids and surfaces. *Physical Review Letters* **100**(13), 136406, 2008.

[34] J. P. Perdew and K. Schmidt. Jacob's ladder of density functional approximations for the exchange-correlation energy. *AIP Conference Proceedings* **577**(1), pp. 1–20, 2001.

[35] J. P. Perdew, A. Ruzsinszky, G. I. Csonka, L. A. Constantin, and J. Sun. Workhorse semilocal density functional for condensed matter physics and quantum chemistry. *Physical Review Letters* **103**(2), 026403, 2009.

[36] J. Klimeš and A. Michaelides. Perspective: Advances and challenges in treating van der Waals dispersion forces in density functional theory. *Journal of Chemical Physics* **137**(12), 120901, 2012.

[37] S. Grimme, J. Antony, S. Ehrlich, and H. Krieg. A consistent and accurate *ab initio* parameterization of density functional dispersion correction (DFT-D) for the 94 elements H-Pu. *Journal of Chemical Physics* **132**(15), 154104, 2010.

[38] S. Grimme. Accurate description of van der Waals complexes by density functional theory including empirical corrections. *Journal of Computational Chemistry* **25**(12), pp. 1463–1473, 2004.

[39] S. Grimme. Semiempirical GGA-type density functional constructed with a long-range dispersion correction. *Journal of Computational Chemistry* **27**(15), pp. 1787–1799, 2006.

[40] A. Tkatchenko and M. Scheffler. Accurate molecular van der Waals interactions from ground-state electron density and free-atom reference data. *Physical Review Letters* **102**(7), 073005, 2009.

[41] M. Dion, H. Rydberg, E. Schröder, D. C. Langreth, and B. I. Lundqvist. Van der Waals density functional for general geometries. *Physical Review Letters* **92**(24), 246401, 2004.

[42] V. R. Cooper. Van der Waals density functional: An appropriate exchange functional. *Physical Review B* **81**(16), 161104(R), 2010.

[43] J. Klimeš, D. R. Bowler, and A. Michaelides. Chemical accuracy for the van der Waals density functional. *Journal of Physics: Condensed Matter* **22**(2), 022201, 2010.

[44] J. Klimeš, D. R. Bowler, and A. Michaelides. Van der Waals density functionals applied to solids. *Physical Review B* **83**(19), 195131, 2011.

[45] K. Lee, E. D. Murray, L. Kong, B. I. Lundqvist, and D. C. Langreth. Higher-accuracy van der Waals density functional. *Physical Review B* **82**(8), 081101, 2010.

[46] O. A. Vydrov and T. Van Voorhis. Improving the accuracy of the nonlocal van der Waals density functional with minimal empiricism. *Journal of Chemical Physics* **130**(10), 104105, 2009.

[47] O. A. Vydrov and T. Van Voorhis. Nonlocal van der Waals density functional made simple. *Physical Review Letters* **103**(6), 063004, 2009.

[48] O. A. Vydrov and T. Van Voorhis. Implementation and assessment of a simple nonlocal van der Waals density functional. *Journal of Chemical Physics* **132**(16), 164113, 2010.

[49] O. A. Vydrov and T. Van Voorhis. Nonlocal van der Waals density functional: The simpler the better. *Journal of Chemical Physics* **133**(24), 244103, 2010.

[50] G. Román-Pérez and J. M. Soler. Efficient implementation of a van der Waals density functional: application to double-wall carbon nanotubes. *Physical Review Letters* **103**(9), 096102, 2009.

[51] M. Karplus, R. N. Porter, and R. D. Sharma. Exchange reactions with activation energy. I. Simple barrier potential for (H, $H_2$). *Journal of Chemical Physics* **43**(9), pp. 3259–3287, 1965.

[52] C. C. Marston and G. G. Balint-Kurti. The Fourier grid Hamiltonian method for bound state eigenvalues and eigenfunctions. *Journal of Chemical Physics* **91**(6), pp. 3571–3576, 1989.

[53] G. Kresse and J. Hafner. *Ab initio* molecular dynamics for liquid metals. *Physical Review B* **47**(1), pp. 558–561, 1993.

[54] G. Kresse and J. Furthmüller. Efficiency of *ab initio* total energy calculations for metals and semiconductors using a plane-wave basis set. *Computational Materials Science* **6**(1), pp. 15–50, 1996.

[55] G. Kresse and J. Furthmüller. Efficient iterative schemes for *ab initio* total-energy calculations using a plane-wave basis set. *Physical Review B* **54**(16), pp. 11169–11186, 1996.

[56] G. Kresse and D. Joubert. From ultrasoft pseudopotentials to the projector augmented-wave method. *Physical Review B* **59**(3), pp. 1758–1775, 1999.

[57] W. F. van Gunsteren and H. J. C. Berendsen. A leap-frog algorithm for stochastic dynamics. *Molecular Simulation* **1**(3), pp. 173–185, 1988.

[58] J. Stoer and R. Bulirsch. *Introduction to numerical analysis*. New York: Springer, 1980.

[59] G. J. Kroes and M. F. Somers. Six-dimensional dynamics of dissociative chemisorption of $H_2$ on metal surfaces. *Journal of Theoretical and Computational Chemistry* **04**(02), pp. 493–581, 2005.

[60] R. Kosloff. Time-dependent quantum-mechanical methods for molecular dynamics. *Journal of Physical Chemistry* **92**(8), pp. 2087–2100, 1988.

[61] E. Pijper, G. J. Kroes, R. A. Olsen, and E. J. Baerends. Reactive and diffractive scattering of $H_2$ from Pt(111) studied using a six-dimensional wave packet method. *Journal of Chemical Physics* **117**(12), pp. 5885–5898, 2002.

[62] J. C. Light, I. P. Hamilton, and J. V. Lill. Generalized discrete variable approximation in quantum mechanics. *Journal of Chemical Physics* **82**(3), pp. 1400–1409, 1985.

[63] G. C. Corey and D. Lemoine. Pseudospectral method for solving the time-dependent Schrödinger equation in spherical coordinates. *Journal of Chemical Physics* **97**(6), pp. 4115–4126, 1992.

[64] D. Lemoine. The finite basis representation as the primary space in multidimensional pseudospectral schemes. *Journal of Chemical Physics* **101**(12), pp. 10526–10532, 1994.

[65] D. Kosloff and R. Kosloff. A Fourier method solution for the time dependent Schrödinger equation as a tool in molecular dynamics. *Journal of Computational Physics* **52**(1), pp. 35–53, 1983.

[66] M. D. Feit, J. A. Fleck Jr., and A. Steiger. Solution of the Schrödinger equation by a spectral method. *Journal of Computational Physics* **47**(3), pp. 412–433, 1982.

[67] G. G. Balint-Kurti, R. N. Dixon, and C. C. Marston. Time-dependent quantum dynamics of molecular photofragmentation processes. *Journal of the Chemical Society, Faraday Transactions* **86**(10), pp. 1741–1749, 1990.

[68] G. G. Balint-Kurti, R. N. Dixon, and C. C. Marston. Grid methods for solving the Schrödinger equation and time dependent quantum dynamics of molecular photofragmentation and reactive scattering processes. *International Reviews in Physical Chemistry* **11**(2), pp. 317–344, 1992.

[69] R. C. Mowrey and G. J. Kroes. Application of an efficient asymptotic analysis method to molecule–surface scattering. *Journal of Chemical Physics* **103**(3), pp. 1216–1225, 1995.

[70] Á. Vibók and G. G. Balint-Kurti. Parametrization of complex absorbing potentials for time-dependent quantum dynamics. *Journal of Physical Chemistry* **96**(22), pp. 8712–8719, 1992.

[71] R. N. Zare. *Angular Momentum*. New York: Wiley, 1988.

[72] C. T. Rettner, H. A. Michelsen, and D. J. Auerbach. Quantum-state-specific dynamics of the dissociative adsorption and associative desorption of $H_2$ at a Cu(111) surface. *Journal of Chemical Physics* **102**(11), pp. 4625–4641, 1995.

[73] H. A. Michelsen and D. J. Auerbach. A critical examination of data on the dissociative adsorption and associative desorption of hydrogen at copper surfaces. *Journal of Chemical Physics* **94**(11), pp. 7502–7520, 1991.

[74] D. J. Auerbach. Velocity measurements by time-of-flight methods. In: *Atomic and molecular beam methods*. Ed. by G. Scoles. Vol. 1. Oxford: Oxford University Press, 1988. Chap. 14.

[75] H. A. Michelsen, C. T. Rettner, D. J. Auerbach, and R. N. Zare. Effect of rotation on the translational and vibrational energy dependence of the dissociative adsorption of $D_2$ on Cu(111). *Journal of Chemical Physics* **98**(10), pp. 8294–8307, 1993.

[76] C. Díaz and R. A. Olsen. A note on the vibrational efficacy in molecule–surface reactions. *Journal of Chemical Physics* **130**(9), 094706, 2009.

[77] P. Nieto, D. Farías, R. Miranda, M. Luppi, E. J. Baerends, M. F. Somers, M. J. T. C. van der Niet, R. A. Olsen, and G. J. Kroes. Diffractive and reactive scattering of $H_2$ from Ru(0001): experimental and theoretical study. *Physical Chemistry Chemical Physics* **13**(18), pp. 8583–8597, 2011.

[78] P. Nieto, D. Barredo, D. Farías, and R. Miranda. In-plane and out-of-plane diffraction of $H_2$ from Ru(001). *Journal of Physical Chemistry A* **115**(25), pp. 7283–7290, 2011.

CHAPTER 3

# Static surface temperature effects on the dissociation of $H_2$ and $D_2$ on Cu(111)

This chapter is based on:

M. Wijzenbroek and M. F. Somers. Static surface temperature effects on the dissociation of $H_2$ and $D_2$ on Cu(111). *Journal of Chemical Physics* **137**(5), 054703, 2012.

## Abstract

A model for taking into account surface temperature effects in molecule–surface reactions is reported and applied to the dissociation of $H_2$ and $D_2$ on Cu(111). In contrast to many models developed before, the model constructed here takes into account the effects of static corrugation of the PES rather than energy exchange between the impinging hydrogen molecule and the surface. Such an approximation is a vibrational sudden approximation. The quality of the model is assessed by comparison to a recent DFT study. It is shown that the model gives a reasonable agreement with recently performed *ab initio* molecular dynamics calculations, in which the surface atoms were allowed to move. The observed broadening of the reaction probability curve with increasing surface temperature is attributed to the displacement of surface atoms, whereas the effect of thermal expansion is found to be primarily a shift of the curve to lower energies. It is also found that the rotational quadrupole alignment parameter is generally decreased at low energies, whereas it remains approximately constant at high energies. Finally it is shown that the approximation of an ideal static surface works well for low surface temperatures, in particular for the molecular beams for this system ($T_s = 120\,\mathrm{K}$). Nonetheless, for the state-resolved reaction probability at this surface temperature, some broadening is found.




## 3.1 Introduction

One of the most studied systems in surface chemistry is the dissociation of hydrogen on a copper surface. In this work the Cu(111) face is considered; a large number of theoretical[1–21] and experimental[22–34] studies have been done for this particular surface. Theoretical studies have mostly considered motion only in the degrees of freedom of the hydrogen molecule, due to the complexity of taking into account surface degrees of freedom. In experiments, however, often high surface temperatures are applied. Instead of treating the full system, in most previous theoretical work the atoms in the surface have been assumed to be fixed to their ideal lattice positions. This approximation is expected to hold as long as the surface temperature is relatively low, but may be suspect at

high temperatures for specific observables because significant surface temperature effects were found in experiments.[27,30]

Calculations with the Born–Oppenheimer static surface (BOSS) model have provided a very good description of the experiments.[1,2] A number of approximations are made within this model. First, the surface atoms are frozen at their ideal lattice positions. Second, electron–hole pair excitations are neglected. Finally, density functional theory (DFT) is used to compute the potential energy surface (PES). Electron–hole pair excitations should not be important for hydrogen dissociating on a metal surface.[35] Recently an accurate specific reaction parameter (SRP) DFT functional was found for this system by taking a linear combination of two functionals often used for the description of molecule–surface reactions.[1,2] In this study, a number of the remaining discrepancies between theory and experiment were attributed to the neglect of phonons. For example, the rotational quadrupole alignment parameter can be expected to be dependent on the surface temperature, because a corrugated surface may allow tilted molecules that do not react on an ideal surface to react due to the surface being locally tilted. The dependence of the rotational quadrupole alignment parameter on the surface temperature has however not been measured experimentally.

The remaining discrepancies between theory and experiment therefore make it interesting to take into account the surface degrees of freedom. Although it is now possible to take into account surface temperature effects with *ab initio* molecular dynamics (AIMD),[20,21,36] these calculations are still computationally expensive, restricting the scope of these studies. It is therefore desirable to have a model which is computationally less expensive. Additionally, using a model allows a more thorough assignment of observed effects in the dynamics to structural changes caused by the surface temperature, as individual parts of a model can be switched off more easily.

In order to construct such a model efficiently, it is important to first consider precisely how surface temperature influences the atomic structure of the system. One of the most well known effects is thermal expansion, *i.e.*, the crystal expands as the surface temperature is increased.[37,38] Additionally, at the surface the interlayer spacings may be different from interlayer spacings in the bulk, and they may be temper-

ature dependent.[39] These two effects combined can be referred to as systematic (static) effects, as they involve systematic displacements of atoms in the crystal. The surface atoms will additionally vibrate around their ideal lattice positions, giving the surface atoms an instantaneous displacement.[40,41] This is a statistical effect, due to the (apparent) random displacement of atoms in the crystal. Additionally there will be dynamical effects involving the motion of surface atoms, such as energy exchange between the impinging hydrogen molecule and the surface and dissipation of heat through the crystal.

Work on surface temperature effects has mostly focused on energy exchange with surface oscillator (SO)[42–48] models, of which the most advanced study so far for hydrogen dissociating on Cu(111) has been the application[1,2] of a three-dimensional (3D) SO model.[48] It was however found that this does not account sufficiently for the effects observed experimentally.[1,2] Attempts have been made to improve the SO model. The modified surface oscillator (MSO)[42,44] model contains a microscopically motivated coupling term. Nave and Jackson[49,50] recently showed that the harmonic approximation used in the SO model is reasonable. Another model which has been applied is the surface mass (SM)[46,47] model, in which the surface does not oscillate but instead is given a certain velocity and mass, which does not allow energy exchange, but does allow recoil effects to be taken into account. Also, for $H_2$ dissociation on Pd(111), an extension of the corrugation reducing procedure (CRP) has been applied.[51] Finally, Bonfanti *et al.*[52] performed seven-dimensional (7D) quantum dynamics (QD) calculations for $H_2$ dissociation on Cu(111), in which a second layer atom was allowed to move perpendicular to the surface. In this study, calculations were additionally performed using a vibrational sudden approximation (6+1D), and reaction probabilities computed using this model were found to be in good agreement with the full 7D results.

In this chapter a model is developed to take into account the thermal displacement of surface atoms and the expansion of the crystal within a vibrational sudden approximation, in which the surface atoms are assumed to be fixed but not in their ideal positions. The model is then tested by comparison with a DFT study[53] for this system in which the influence of surface atom displacements is considered. Additionally,

three observables are computed and the results are compared, where possible, to experiments. The initial state-resolved reaction probability is considered, because for this observable strong surface temperature effects are known from experiments. These effects are manifested in the broadening of the reaction probability curves with increasing surface temperature.[27,30] Also the rotational quadrupole alignment parameter is considered, because surface temperature effects are expected for this observable. Finally, to verify the approximation previously made of an ideal static crystal being representative of a crystal at low temperatures, molecular beams are simulated to compute sticking probabilities.

The structure of this chapter is as follows. In section 3.2.1 an overview and motivation of the model that was constructed is provided, and the individual parts of the model are discussed in section 3.2.2. In section 3.2.3 the computational details of the calculations that were performed are given. Then in section 3.3 the results that were obtained by application of the model are discussed. This section is split in several parts for the different observables that are considered in the present work. First, in section 3.3.1, the quality of the model is assessed by comparison to the DFT study[53] mentioned above. In section 3.3.2 the initial state-resolved reaction probability is considered, then in section 3.3.3 the rotational quadrupole alignment parameter, and finally sticking probabilities are discussed in section 3.3.4. In section 3.4 the conclusions are given.

## 3.2 Static corrugation model

In this section the newly developed static corrugation model is described and arguments are made to support the assumptions made in the construction of the model. First a general overview of the model is given, after which a more detailed description is given. Finally the computational details and scope of the present study, the application to $H_2$ dissociation on Cu(111), are given.

### 3.2.1 Model overview

Previous work on the surface temperature effects of $H_2$ dissociation on Cu(111) has focused on the effects of energy exchange through SO models.[42–48] In SO models the entire surface is attached to a spring. As the impinging hydrogen molecule approaches the surface it can interact with the surface by exchanging energy with the oscillating surface. It has been shown that a SO model alone cannot quantitatively describe the broadening of the sticking curves as observed in experiment.[1,2]

In previous other work, mostly ideal static lattices were considered and these were assumed to be representative of a real crystal at 0 K. Results based on this model were compared with experiments done at higher temperatures ($120 - 925$ K). Such a treatment of an ideal lattice is however somewhat misleading as the surface atoms in a real 0 K crystal will not necessarily be in their ideal positions,[40,41] due to the presence of zero-point energy (ZPE) in the surface. In order to model a real 0 K crystal, the static surface approximation has to be dropped, so that the surface atoms can move due to their ZPE and energy exchange between the hydrogen molecule and the copper surface can take place. At a higher temperature, the atoms will vibrate even more and, additionally, thermal expansion may have to be taken into account.

A number of approximations are argued here to be reasonable. First of all, due to the large mass mismatch between the hydrogen molecule and the surface atoms, motion of the hydrogen molecule and the surface atoms should only be weakly coupled, *e.g.*, the effect of energy exchange should be small. Second, surface atoms move relatively slowly compared to the hydrogen molecule. This indicates that a sudden approximation, in which the surface atoms are assumed fixed but not in their ideal positions, should work well. Finally, in typical experiments the time between scattering events is long compared to a scattering event. The time between scattering events is long, as shown by the adsorption and desorption rates, which are on the order of monolayers per second.[29,32] This indicates that there is no clear correlation between the surfaces different hydrogen molecules "see".

Further motivation for these approximations can be derived from recent studies of $CH_4$ dissociation on Ni and Pt surfaces.[49,50,54,55] It was

found that only very little energy exchange occurs (20 meV at an incidence energy of 1 eV at a surface temperature of 475 K for dissociation on Ni(111)), even though $CH_4$ is significantly closer in mass to Ni than $H_2$ is to Cu ($m_{Ni}/m_{CH_4} = 3.7$, $m_{Cu}/m_{H_2} = 31.5$).

For the system considered here, hydrogen dissociation on Cu(111), a model is therefore constructed for a non-ideal but still fixed surface, in which different surface configurations are taken into account for different scattering events. It is noted that the model discussed in this chapter can in principle be combined with the SM model[46,47] so that also recoil effects can be taken into account.

### 3.2.2 Method

#### 3.2.2.1 Potential energy surface

The PES for a diatomic molecule in the vicinity of a surface can be written as[53]

$$V(\vec{r},\vec{q}) = V^{6D}(\vec{r};\vec{q}_{id}) + V_{coup}(\vec{r},\vec{q}) + V_{strain}(\vec{q}), \tag{3.1}$$

in which $V^{6D}$ is the 6D PES of the diatomic molecule in the presence of an ideal surface, $V_{coup}$ the so-called coupling potential, which is defined by this equation, and $V_{strain}$ the strain in the surface defined by $V_{strain}(\vec{q}) = V_{slab}(\vec{q}) - V_{slab}(\vec{q}_{id})$. Here, $V_{slab}$ is the potential energy of the slab in absence of the diatomic molecule (or with the diatomic molecule far away from the surface). The coordinates $\vec{r}$ are those of the diatomic molecule, and $\vec{q}$ are the coordinates of all surface atoms, with $\vec{q}_{id}$ the coordinates of the surface atoms in their ideal lattice positions. The representation of the 6D potential is now well understood; a variety of methods, such as the CRP,[56] have been developed for representing or interpolating this part of the potential. The coupling potential contains by far the most information, relating the $\vec{r}$ and $\vec{q}$ degrees of freedom. Bonfanti *et al.*[53] computed the coupling potential for $H_2$ dissociation on Cu(111) using DFT for a number of configurations, in which the $H_2$ molecule was fixed at barrier locations above the high symmetry sites while a single surface atom was moved in a particular direction. It was noted in this study that the dependence of the coupling poten-

tial on different surface degrees of freedom is, to within a reasonable approximation, additive.

From equation (3.1) a correction term can be determined for displacement of surface atoms:

$$\begin{aligned} V_{\text{corr}}(\vec{r},\vec{q}) &= V(\vec{r},\vec{q}) - V(\vec{r},\vec{q}_{\text{id}}) \\ &= V_{\text{int}}(\vec{r},\vec{q}) - V_{\text{int}}(\vec{r},\vec{q}_{\text{id}}) + V_{\text{strain}}(\vec{q}), \end{aligned} \tag{3.2}$$

as $V_{\text{coup}}(\vec{r},\vec{q}_{\text{id}}) = 0$, $V_{\text{strain}}(\vec{q}_{\text{id}}) = 0$ and $V^{6\text{D}}$ does not depend on surface degrees of freedom. Here the substitution

$$V_{\text{coup}}(\vec{r},\vec{q}) = V_{\text{int}}(\vec{r},\vec{q}) - V_{\text{int}}(\vec{r},\vec{q}_{\text{id}}) \tag{3.3}$$

has been made, in which $V_{\text{int}}$ is a term describing the interaction between the hydrogen molecule and the copper atoms. The correction term has to be added to $V^{6\text{D}}$. For static slab simulations $V_{\text{strain}}$ does not have to be taken into account in equation (3.2). It is however needed to get $V_{\text{coup}}$ in equation (3.2) and thus implicitly $V_{\text{int}}$ through equation (3.3).

Due to the large number of degrees of freedom, it is difficult to treat any of the correction terms $V_{\text{int}}(\vec{r},\vec{q})$ exactly. It may, however, be possible to use some kind of approximate analytical form. A logical choice for this form would be a small number of terms from the many-body expansion[57] of the full PES of equation (3.1).

Consider a general PES $E_M(\vec{R}_1,\vec{R}_2,\ldots,\vec{R}_M)$ for a system of $M$ atoms. In the many-body expansion this PES is written as a sum of $N$-body potential terms with $N$ up to the number of atoms considered in the full PES:[57]

$$E_M(\vec{R}_1,\vec{R}_2,\ldots,\vec{R}_M) = \sum_{N=0}^{M} E^{(N)}(\vec{R}_1,\vec{R}_2,\ldots,\vec{R}_M), \tag{3.4}$$

and each individual energy term, $E^{(N)}$, can be written as

$$E^{(N)}(\vec{R}_1,\vec{R}_2,\ldots,\vec{R}_M) = \frac{1}{N!}\sum_{m_1}^{M}\sum_{m_2}^{M}\ldots\sum_{m_N}^{M} V^{(N)}(\vec{R}_{m_1},\vec{R}_{m_2},\ldots,\vec{R}_{m_N}). \tag{3.5}$$

This expression is exact and does not provide a simplification. One could however expect that the lowest order terms are the most important ones. Expressions like this are commonly used in force fields and recently reactive force fields have been applied to molecule–surface reactions with reasonable success, as long as the force field is specifically parametrized for the description of a molecule–surface reaction.[58–61] Applying the many-body expansion to an $H_2$ molecule near a Cu surface with $n$ surface atoms, if only two-body terms are included in the expansion the full potential can be written as

$$V(\vec{r},\vec{q}) = V^{(2)}_{\mathrm{H-H}}\left(\left|\vec{R}_{\mathrm{H_1}} - \vec{R}_{\mathrm{H_2}}\right|\right) + \sum_{I}^{2}\sum_{i}^{n} V^{(2)}_{\mathrm{H-Cu}}\left(\left|\vec{R}_{\mathrm{H_I}} - \vec{R}_{\mathrm{Cu_i}}\right|\right) + \sum_{i}^{n}\sum_{j>i}^{n} V^{(2)}_{\mathrm{Cu-Cu}}\left(\left|\vec{R}_{\mathrm{Cu_i}} - \vec{R}_{\mathrm{Cu_j}}\right|\right), \tag{3.6}$$

in which $V^{(2)}_{\mathrm{H-H}}$ is the interaction between the two hydrogen atoms, $V^{(2)}_{\mathrm{H-Cu}}$ the interaction between a hydrogen atom and a copper atom, and $V^{(2)}_{\mathrm{Cu-Cu}}$ the interaction between two copper atoms. Therefore, within the two-body approximation, using equation (3.6) in equations (3.2) and (3.3),

$$V_{\mathrm{int}}(\vec{r},\vec{q}) = \sum_{I}^{2}\sum_{i}^{n} V^{(2)}_{\mathrm{H-Cu}}\left(\left|\vec{r}_I - \vec{q}_i\right|\right), \tag{3.7}$$

$$V_{\mathrm{slab}}(\vec{q}) = \sum_{i}^{n}\sum_{j>i}^{n} V^{(2)}_{\mathrm{Cu-Cu}}\left(\left|\vec{q}_i - \vec{q}_j\right|\right). \tag{3.8}$$

It is again emphasized that this last term $V_{\mathrm{slab}}$ is not needed for a static surface simulation.

#### 3.2.2.2 Fitting procedure

The form chosen for $V^{(2)}_{\mathrm{H-Cu}}$ is

$$V^{(2)}_{\mathrm{H-Cu}}(r) = (1-\rho(r))V(r) + \rho(r)V(b_2), \tag{3.9}$$

where

$$V(r) = -e^{-l(r-z)} \cdot \sum_{k=0}^{3} \left(c_k (r-z)^k\right) \tag{3.10}$$

and

$$\rho(x) = \begin{cases} 0 & \text{if } x < b_1 \\ \frac{1}{2}\cos\left(\frac{\pi(x-b_2)}{b_2-b_1}\right) + \frac{1}{2} & \text{if } b_1 \leq x \leq b_2 \\ 1 & \text{if } x > b_2. \end{cases} \tag{3.11}$$

The form of the 1D potential $V^{(2)}_{\mathrm{H-Cu}}(r)$ is therefore Rydberg-like with an added switch function. Correct parameters for equations (3.10) and (3.11) were found by fitting $V_{\mathrm{coup}}(\vec{r}, \vec{q})$ (equation (3.3)) directly to DFT data of Bonfanti *et al.*[53] The resulting fit is discussed in section 3.3.1.



#### 3.2.2.3 Surface configurations

As the strain term in equation (3.2) is at present not included, the surface atoms cannot move and surface configurations cannot be generated trivially. Therefore an alternative method is used, based on the Debye–Waller (DW) $B$ factor. To randomly displace surface atoms, surface atom position vectors are defined by

$$\vec{q}_i = \vec{q}_{\mathrm{id},i} + q_i \hat{u}_i, \tag{3.12}$$

where $\vec{q}_{\mathrm{id},i}$ is the surface atom position vector for an ideal surface associated with atom $i$, $\hat{u}_i$ is a 3D unit vector with a random orientation and $q_i$ a randomly chosen scalar displacement sampled from a Gaussian distribution with width

$$\sigma = \sqrt{\frac{3B}{8\pi^2}}. \tag{3.13}$$

In this formula $B$ is the DW factor for a particular surface temperature. The used DW factors are obtained from fits[40] to experimental neutron inelastic scattering data.[41] The approximations made here are that the displacement is assumed to be isotropic and bulk-like, so any surface

effects are neglected. Displacements obtained from the DW factor are in agreement with displacements obtained from harmonic fits to the strain potential;[53] with the DW factor $\sigma = 0.2547$ Å at $T_s = 925$ K, while for the harmonic fits $\sigma = 0.25$ Å for first layer perpendicular motion ($\omega = 16$ meV) and $\sigma = 0.21$ Å for second layer perpendicular motion ($\omega = 19$ meV) at the same surface temperature.

Only surface atoms within a radius of $16\,a_0$ of the projection of the center of mass of the initial configuration of the $H_2$ molecule on the surface are displaced from their ideal positions using this method. In table 3.1 the parameter $\sigma$ is shown for the surface temperatures that are considered.

#### 3.2.2.4 Thermal expansion and contraction/expansion of the first layer

Taking into account systematic displacements like thermal expansion is less straightforward. If a correction is made by adjusting the displaced surface atom position vectors using equation (3.2), the proper symmetry of the system is not kept. This is because the surface also expands in the surface plane and the two-body approximation is not exact, which means that the potential energy not accounted for by the two-body approximation on sites which should be equal could be different.

A possible way of taking thermal expansion into account is by removing the part of the potential energy that can be accounted for by the two-body approximation from the full $V^{6D}$, "stretching" the residual function in $X$ and $Y$ by the same factor as the expansion that occurs, and finally re-adding the part that can be accounted for by the two-body approximation:

$$V(\vec{r}_{exp}, \vec{q}_{exp}) = V^{6D}(\vec{r'}; \vec{q}_{id}) - V_{int}(\vec{r'}, \vec{q}_{id}) + V_{int}(\vec{r}_{exp}, \vec{q}_{exp}). \qquad (3.14)$$

It is pointed out here that $\vec{r'}$ and $\vec{r}_{exp}$ depend on each other. $\vec{r'}$ is related to $\vec{r}_{exp}$ so that $X' = X_{exp}/\alpha$ and $Y' = Y_{exp}/\alpha$. Here $\alpha$ is $L_{exp}/L_{id}$. $Z'$, $r'$, $\vartheta'$ and $\varphi'$ are equal to $Z_{exp}$, $r_{exp}$, $\vartheta_{exp}$ and $\varphi_{exp}$.

As there is no periodicity perpendicular to the surface, changing interlayer distances can simply be done by changing $\vec{q}$. To correct for

**Table 3.1** Model parameters $\sigma$, $\alpha$ and $d_{1-2}$ as used for the surface temperatures considered in this work. These parameters were derived from experimental results.[37–41]

| $T_s$ (K) | $\sigma$ (Å) | $\alpha$ | $d_{1-2}$ (Å) |
|---|---|---|---|
| 0 | 0.0746 | 1.0000 | 2.1200 |
| 120 | 0.0993 | 1.0001 | 2.1212 |
| 300 | 0.1470 | 1.0034 | 2.1270 |
| 600 | 0.2056 | 1.0087 | 2.1297 |
| 925 | 0.2547 | 1.0152 | 2.1739 |

**Table 3.2** Rovibrational states for which calculations have been performed. In the molecular beam simulations of section 3.3.4, all these states are included in the calculations.

| Vibration | Rotation $D_2$ | Rotation $H_2$ |
|---|---|---|
| $v = 0$ | $J = 0 \ldots 15$ | $J = 0 \ldots 11$ |
| $v = 1$ | $J = 0 \ldots 12$ | $J = 0 \ldots 7$ |
| $v = 2$ | $J = 0 \ldots 10$ | No calculations |



changes in the first interlayer spacing, all atoms below the first layer were translated up or down so that the first interlayer distance has a particular value $d_{1-2}$. Because in the present model the 1D interaction $V^{(2)}_{H-Cu}$ is switched off beyond about $7.5\,a_0$, effectively only the change in interlayer distance between the first two layers can be taken into account. In table 3.1 the parameters $\alpha$ and $d_{1-2}$ are shown for the surface temperatures that are considered. These parameters were computed based on experimental data.[37–39]

### 3.2.3 Computational details

The reaction probability was sampled for each initial rovibrational state at 20 incidence energies, spread equidistantly from 0 eV up to 1 eV. Only normal incidence is considered. The considered surface temperatures are 0 K, 120 K, 300 K, 600 K and 925 K. Additionally, calculations were also performed for an ideal lattice. Calculations were performed both with and without the model for thermal expansion. For each incidence

energy, rovibrational state and surface temperature at least $2 \times 10^4$ trajectories were computed, spread equally over the different $m_J$ states. Rovibrational states for which calculations have been performed are listed in table 3.2.

The SRP PES used by Díaz *et al.*[1,2] was used. This PES is a linear combination of two PESs interpolated with the CRP,[56] one based on calculations with the PW91 exchange–correlation (XC) functional,[62] the other based on calculations with the RPBE XC functional.[63] This PES has p6mm symmetry rather than p3m1 symmetry.[64]

The applied quasi-classical trajectory (QCT) method is mostly the same as used in a previous study.[1,2] The initial rovibrational energies of the $H_2$ molecule were computed with the Fourier grid Hamiltonian method.[65] The Hamilton equations of motion were solved by using the extrapolation method of Stoer and Bulirsch.[66] The initial angular momentum of the $H_2$ molecule is fixed by $L = \sqrt{J(J+1)}\hbar$. For $J > 0$, the orientation is chosen randomly by $\cos\vartheta_L = m_J/\sqrt{J(J+1)}$, where $\vartheta_L$ is the angle between $L$ and the axis perpendicular to the surface. The center of mass of the hydrogen molecule was initially placed 9 Å away from the surface. Reaction is considered to have occurred when the H–H distance $r$ is larger than 2.25 Å. Scattering is considered to have occurred when the hydrogen molecule has a momentum away from the surface and is further than 9 Å away from the surface. Trajectories were stopped after 20 ps. Trajectories that have not shown reaction or scattering after this time are also considered non-reactive. This choice has been made because of the static surface approximation. Although the molecule can be considered to be "trapped" in this case, motion of the surface likely leads to desorption of the trapped molecule in most cases.

## 3.3 Results and discussion

In this section, first the quality of the model is assessed by comparison to a recent DFT study.[53] After this assessment, a comparison is made between calculations performed on an ideal static surface, calculations performed on a non-ideal static surface with the static corrugation model (section 3.2; both with and without thermal expansion), recent AIMD results[20] and experiments. To do this, three observables are

considered: the initial state- and energy-resolved reaction probability; the energy resolved rotational quadrupole alignment parameter; and the reaction probability averaged over the velocity distribution and the rovibrational states present in molecular beams.

### 3.3.1 1D correction function

The 1D correction function ($V^{(2)}_{\mathrm{H-Cu}}(r)$ in equation (3.9)) used in the model is related to the coupling potential as shown in equation (3.3). As the 1D correction function to be used is fitted to reproduce the coupling potential, comparing the coupling potential computed with DFT with the coupling potential computed with the model provides a way to check the quality of the fit. In total 153 points of the coupling potential were used in the fit. Some of these points are published[53] while others are not.[67] 43 points are related to perpendicular motion of the first layer atom, 50 to perpendicular motion of the second layer atom, 44 to perpendicular motion of the third layer atom and 16 to parallel motion of the first layer atom.

In figure 3.1 the coupling potential as predicted by the model is compared with the coupling potential computed by Bonfanti *et al.*[53,67] For the first and second layer perpendicular motion the agreement is quite good, in particular for small displacements, with perhaps the exception of second layer perpendicular motion with the hydrogen molecule fixed on the TtB site. For the parallel configurations[67] the agreement is less good. The reason for this is not clear. It could be that these data points sample a different regime of $r$ which cannot be well represented due to restrictions of the form chosen for the 1D correction function. It is noted here that only a small number of points corresponding to parallel displacement (16) are included in the fit, and as such not enough weight may be put on parallel displacement in the fit. The model can clearly not reproduce parallel motion A, and for parallel motions B, C and H the agreement is also not so good. For parallel motions D to G however, the agreement between the model and the DFT calculations is quite good. Bonfanti *et al.*[53] argued that perpendicular motion of second layer atoms has the most effect on the lowest barrier for reaction.

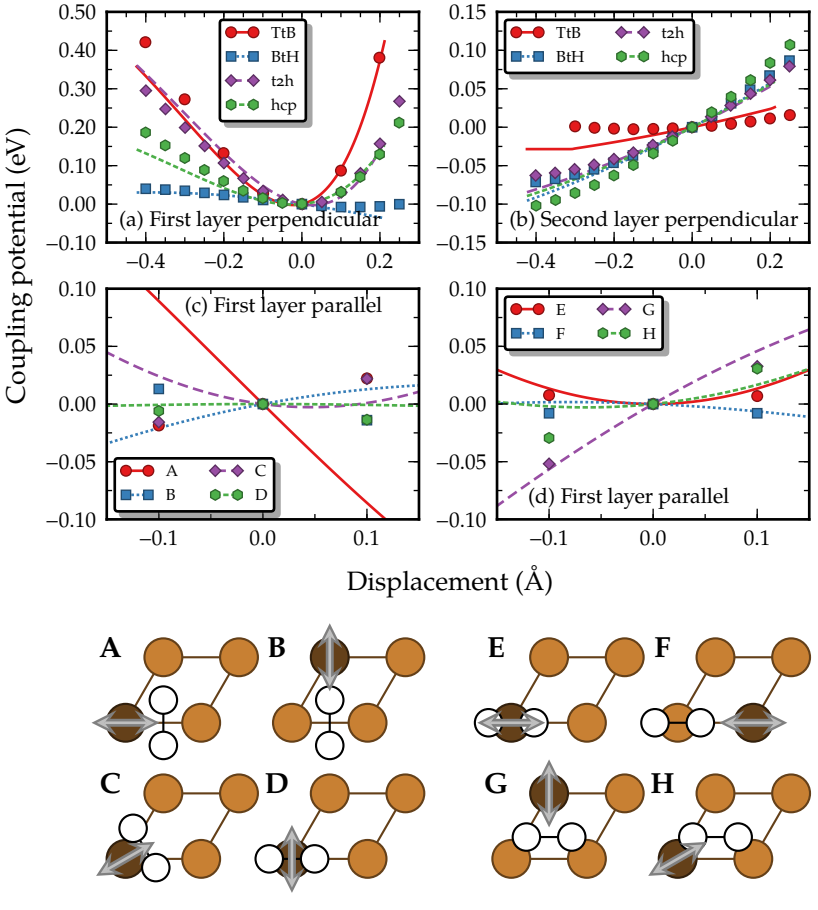


**Figure 3.1** Coupling potential computed with the model (lines) compared with the coupling potential computed by Bonfanti *et al.*[53] (points) for a number of motions. For the perpendicular displacement, the hydrogen molecule is fixed at a barrier position as indicated in the graph, while a surface atom is moved in a perpendicular direction. Data for the third layer motion is not plotted as it is zero due to the added switch function. The bottom graphs represent unpublished data[67] for 8 configurations in which a first layer atom is moved in a parallel direction. These configurations are described in the bottom figure.

**Table 3.3** Parameters used for the 1D correction function as defined in equations (3.9) to (3.11).

| Parameter | Value |
|---|---|
| $z$ | $2.301\,a_0$ |
| $l$ | $1.274/a_0$ |
| $c_0$ | $-0.030\,30\,E_\mathrm{h}$ |
| $c_1$ | $0.1035\,E_\mathrm{h}/a_0$ |
| $c_2$ | $-0.069\,25\,E_\mathrm{h}/{a_0}^2$ |
| $c_3$ | $-4.135\times10^{-9}\,E_\mathrm{h}/{a_0}^3$ |
| $b_1$ | $7.444\,a_0$ |
| $b_2$ | $7.464\,a_0$ |



The conclusion is therefore that a pair potential can represent quite well the behaviour of the coupling potential for perpendicular motion, and that for parallel motion the agreement is perhaps less good, but it is possible that the agreement can be improved if more configurations are added into the fit. It is even possible to extend the model to include three-body terms in $V_\mathrm{int}$ although this does increase the computational cost of using such a model. The agreement could also be improved by using a layer-dependent 1D correction function. This would allow a better description of the various ranges of $r$ spanned by different motions and might also improve the agreement for first layer parallel motion. Both of these extensions require more DFT points than are used at present.

The fitted parameters are given in table 3.3. The function is also plotted in figure 3.2. It should be clear the interaction is relatively long range, up to approximately $7.5\,a_0$, which suggests it is important to take into account many surface atoms in equation (3.2).

### 3.3.2 Initial state-resolved reaction probability

Experimentally, Michelsen *et al.*,[28,29] Murphy and Hodgson,[30] and Rettner *et al.*[32] have measured desorption probabilities for $H_2$ and $D_2$ desorbing into a specific rovibrational state and, by invoking detailed balance, fitted the corresponding reaction probabilities to expressions

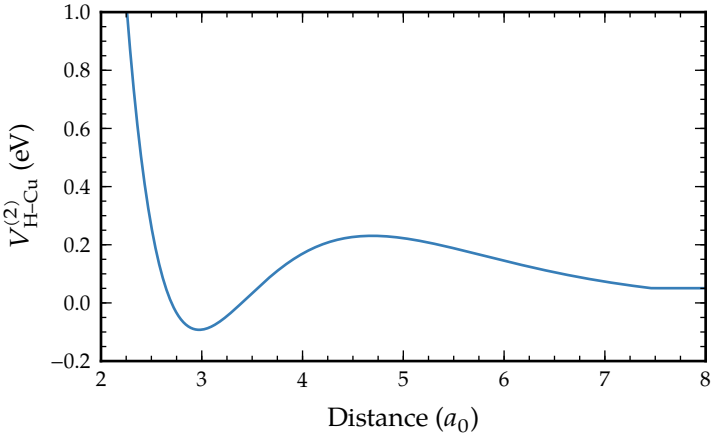


**Figure 3.2** The 1D correction function $V^{(2)}_{\mathrm{H-Cu}}(r)$ based on the parameters of table 3.3.

of the form

$$R(E_{\mathrm{trans}};\nu,J) = \frac{A(\nu,J)}{2}\left(1+\mathrm{erf}\left(\frac{E_{\mathrm{trans}}-E_0(\nu,J)}{W(\nu,J)}\right)\right), \qquad (3.15)$$

in which $E_{\mathrm{trans}}$ is the translational energy of the $H_2$ molecule, $A(\nu,J)$ the saturation value of the reaction probability, $E_0(\nu,J)$ the translational energy for which the reaction probability is half the saturation value (the "dynamical barrier height") and $W(\nu,J)$ a width parameter that describes the steepness of the curve. The experimentalists found $E_0$ to be approximately independent of $T_s$, while they found $W$ to increase with increasing $T_s$.

Reaction probabilities for adsorption from an initial state were computed for all states and surface temperatures listed in section 3.2.3 and these are compared to the available experimental data.

#### 3.3.2.1 Thermal displacement

In figure 3.3 the reaction probability for a number of initial rovibrational states is shown, with only thermal displacement taken into account. If the surface temperature is increased, at low energies the reaction prob-

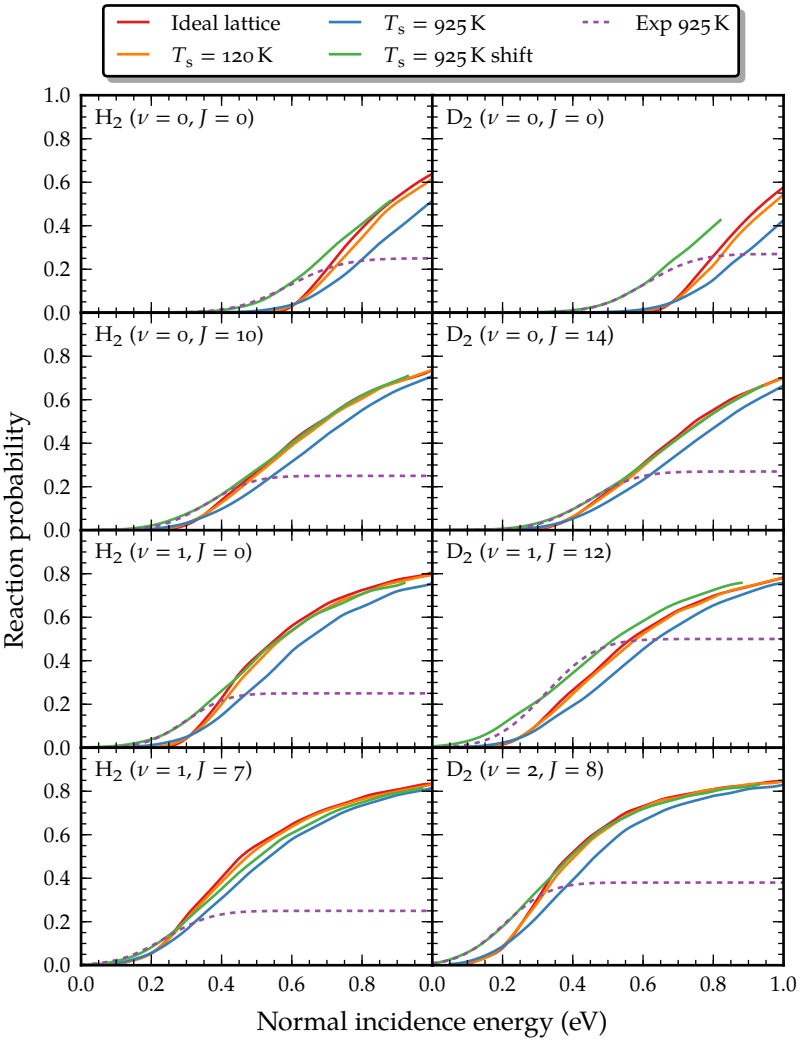


**Figure 3.3** Broadening of the sticking curves as the surface temperature is increased, for a selection of initial rovibrational states, only taking into account the effects of thermal displacement. Also plotted are the experimental sticking curves obtained by Michelsen *et al.*[28,29] and Rettner *et al.*[32]

ability in general is slightly increased, whereas at high energies the reaction probability is decreased. In other words, a broadening occurs. As argued in a previous study,[1,2] there should not be a large difference between the ideal lattice and a real crystal at a low temperature. The findings here are consistent with that, although some broadening is observed for $T_s = 120\,\mathrm{K}$. The available experimental data[28,29,32] was obtained for a surface temperature $T_s = 925\,\mathrm{K}$. The agreement with the experiments generally is improved for the width (shape) of the curve, but not for the dynamical barrier height ($E_0$). Generally the curve is shifted too much to higher energies, *i.e.*, the system is found to not be reactive enough. To compare the width and shape of the computed $T_s = 925\,\mathrm{K}$ reaction probability curves with the experimentally measured sticking curves, the computed $T_s = 925\,\mathrm{K}$ reaction probability curves are also plotted shifted to lower energies in such a way that agreement is obtained at the experimental $E_0$. The agreement for the shape at low energies is excellent, except for ($\nu = 1$, $J = 12$) $D_2$, where the computed reaction probability curve seems to be slightly too broad.

The trends found in figure 3.3 are general for all initial states and surface temperatures considered. To emphasize this point, in figure 3.4 the reaction probability of $D_2$ initially in the ($\nu = 0$, $J = 11$) and ($\nu = 1$, $J = 6$) states for all surface temperatures considered is shown. As the surface temperature is increased, the sticking curve gradually broadens, increasing the reaction probability at low incidence energies, while decreasing the reaction probability at high incidence energies. All curves seem to intersect at one point close to the experimental $E_0$ value, and at this point the reaction probability for ($\nu = 0$, $J = 11$) is approximately 0.04 and for ($\nu = 1$, $J = 6$) is approximately 0.1. This finding is qualitatively consistent with the experiments, where it is known that the $E_0$ parameter of the sticking curve does not depend significantly on the surface temperature.[30,32] The experimentally obtained reaction probability for the intersection point is, however, higher. The calculations also indicate that the reaction probability does not saturate, in contrast to what is found in experiments. This discrepancy could possibly be explained by the low population of hydrogen molecules desorbing from the surface with high energies. As equation (3.15) has a saturation inherent to the form, and there is only a small weight attached to the high energy

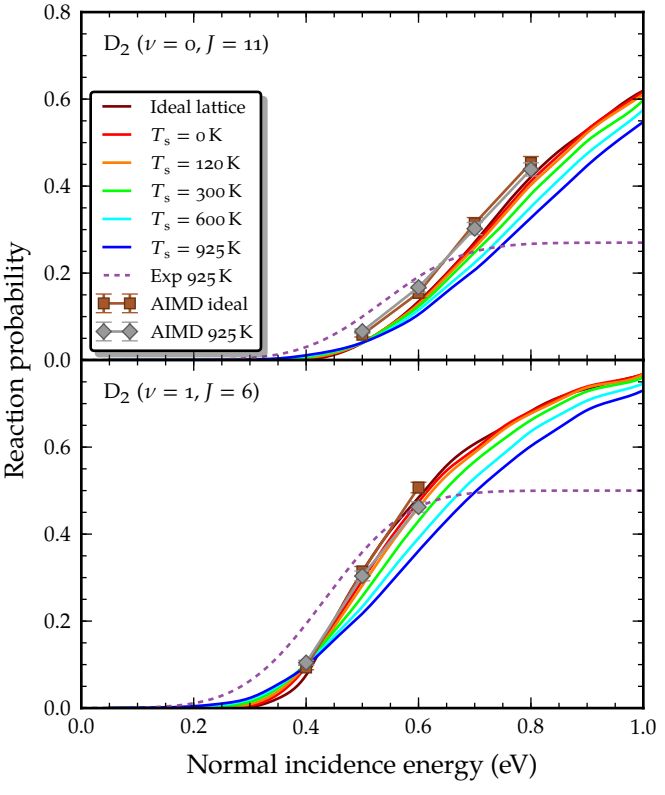


**Figure 3.4** Broadening of the sticking curve for $D_2$ initially in the ($\nu = 0$, $J = 11$) and ($\nu = 1$, $J = 6$) states, for all considered surface temperatures, only taking into account the effects of thermal displacement. The experimental sticking curve[29] is also plotted, as well as the AIMD results by Nattino *et al.*[20]

data, the predicted fit parameters could be wrong.

The trends found for ($\nu = 0$, $J = 11$) and ($\nu = 1$, $J = 6$) $D_2$ are also generally valid for all states. The intersection point is found to be at a reaction probability of approximately 0.04 to 0.1 for $D_2$, while for $H_2$ it is found at reaction probabilities of up to 0.15. It seems clear that the displacement of surface atoms alone does not yield a good enough description of the process, although it does seem to account for (most of) the broadening. This can be understood as follows. Displacement of surface atoms will modulate the barrier height and position.[53] Therefore,

under the influence of thermal displacement, for each configuration of the surface atoms, some barrier heights will be decreased, while others will be increased. At low incidence energies, when only very few molecules react, an increase of the barrier will not change the results considerably, however a decrease of the barrier will make more trajectories reactive. At higher energies, when almost all molecules react, a decrease of the barrier will not change the results considerably, but an increase of the barrier will make fewer trajectories reactive. The net effect of averaging over surface configurations is therefore an increase of reactivity at low incidence energies and a decrease of reactivity at high incidence energies, in other words, a broadening. The amount of broadening is determined by the magnitude of the change in barrier height, while the point with respect to which broadening occurs (the intersection point) is determined by the precise distribution of barriers for all possible surface configurations.

The effects found for ($\nu = 0, J = 11$) and ($\nu = 1, J = 6$) $D_2$ are larger than those found in the AIMD study by Nattino *et al.*[20] The reaction probability curves found in the present study seem to be broader than those found by AIMD. The reason for this is not fully clear. As argued in section 3.2.1, due to the relatively slow desorption speed from the metal surface, there is a long time between different scattering events, and different hydrogen molecules therefore meet surface configurations which are not clearly related to each other. Nattino *et al.*[20] used snapshots from 1 ps dynamics simulations of eight different slabs as initial configuration of the surface, from which one is selected at random. In this study, a new surface configuration is generated for every trajectory from a distribution based on experiments. It is possible that snapshots from a 1 ps dynamics simulation are not different enough from each other, or that not enough slabs have been used, but this is not fully clear. Additionally, in the AIMD calculation a unit cell of finite size is used and periodic boundary conditions are applied while this is not assumed in the calculations on the static corrugation model. The size of the unit cell could be important due to the relatively long range interaction of $V^{(2)}_{\mathrm{H-Cu}}(r)$ (see figure 3.2).

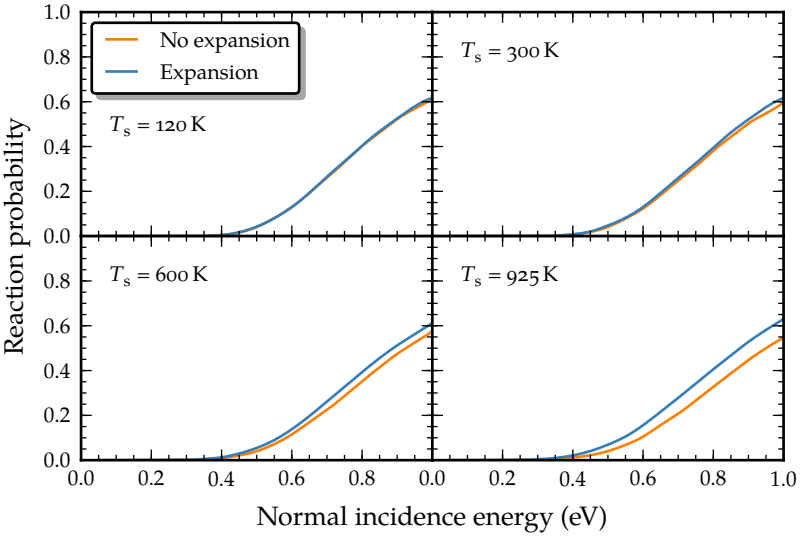




**Figure 3.5** Thermal expansion effects for all surface temperatures considered for $D_2$ initially in the ($\nu = 0, J = 11$) state.

#### 3.3.2.2 Thermal expansion and change in first interlayer distance

In figure 3.5 an overview is provided for thermal expansion effects for $D_2$ initially in the ($\nu = 0, J = 11$) state for all four surface temperatures that are considered. The results show that the most important effect is a shift of the reaction probability curve to lower energies. The size of this shift increases as the surface temperature is increased, being almost non-existent at $T_s = 120\,\mathrm{K}$, but significant at $T_s = 925\,\mathrm{K}$. Additionally, the shape of the curve is also somewhat altered: the curve is slightly narrower when thermal expansion effects are taken into account. This can be explained as follows. As the effect of the inclusion of non-ideal surface configurations is an increase of the corrugation of the PES, causing the broadening of the reaction probability curve, expansion of the crystal tends to locally flatten the surface a bit due to the larger distances between surface atoms. The shift of the reaction probability curve to lower energies can be understood as well. Nattino *et al.*[20] found a decrease of the barrier height as the crystal was expanded. For $T_s = 925\,\mathrm{K}$, a decrease of the lowest barrier to dissociation, the bridge to hollow bar-

rier, of about 3.5 kJ/mol was found. The decrease found here is somewhat larger (up to approximately 5 kJ/mol) and $J$-dependent, as will become clear later.

In figure 3.6 the reaction probability for a number of initial rovibrational states is shown, with both thermal displacement and thermal expansion taken into account. The agreement with experiment here is in general significantly better than in figure 3.3, where only thermal displacement was taken into account. The effects seem to be in particular large for ($\nu = 1, J = 0$) $H_2$, where most of the broadening caused by the thermal displacement has vanished. In general, however, in particular for higher $J$ the agreement is quite good, and the computed $T_s = 925$ K curves mostly line up with the experiments at low incidence energies.

In figure 3.7 the reaction probability is shown for the same two states as in figure 3.4. The curves for $T_s = 925$ K seem to be somewhat too broad, but not by much. The broadening found here is still bigger than the broadening found in the AIMD calculations by Nattino *et al.*[20] The point where the $T_s = 925$ K curve intersects the ideal lattice curve is however in reasonable agreement with the AIMD calculations. It is however noted that the agreement with experiment seems to be better than the AIMD calculations, especially for low energies for ($\nu = 1, J = 6$) $D_2$.

#### 3.3.2.3 Comparison to desorption experiments

To make a full comparison with the desorption experiments by Rettner *et al.*,[32] Michelsen *et al.*,[28,29] and Murphy and Hodgson,[30] first the similarities and differences in the experimental results are discussed. All of the experimental sticking curves were originally fitted to the form of equation (3.15). Nattino *et al.*[21] re-analysed the experimental sticking curves of Michelsen *et al.*[29] for $D_2$ on Cu(111) by fitting to a different functional form, which resulted in a higher saturation value for $\nu = 0$. The analysis below is based on the original sticking curves which were fitted to equation (3.15). Michelsen *et al.*[28,29] and Rettner *et al.*[32] measured the desorption probability for a large number of final states, allowing them to determine the $A$ parameter by fitting to adsorption experiments (which yield, in contrast to desorption experiments, absolute reaction probabilities). Murphy and Hodgson[30] only measured the de-

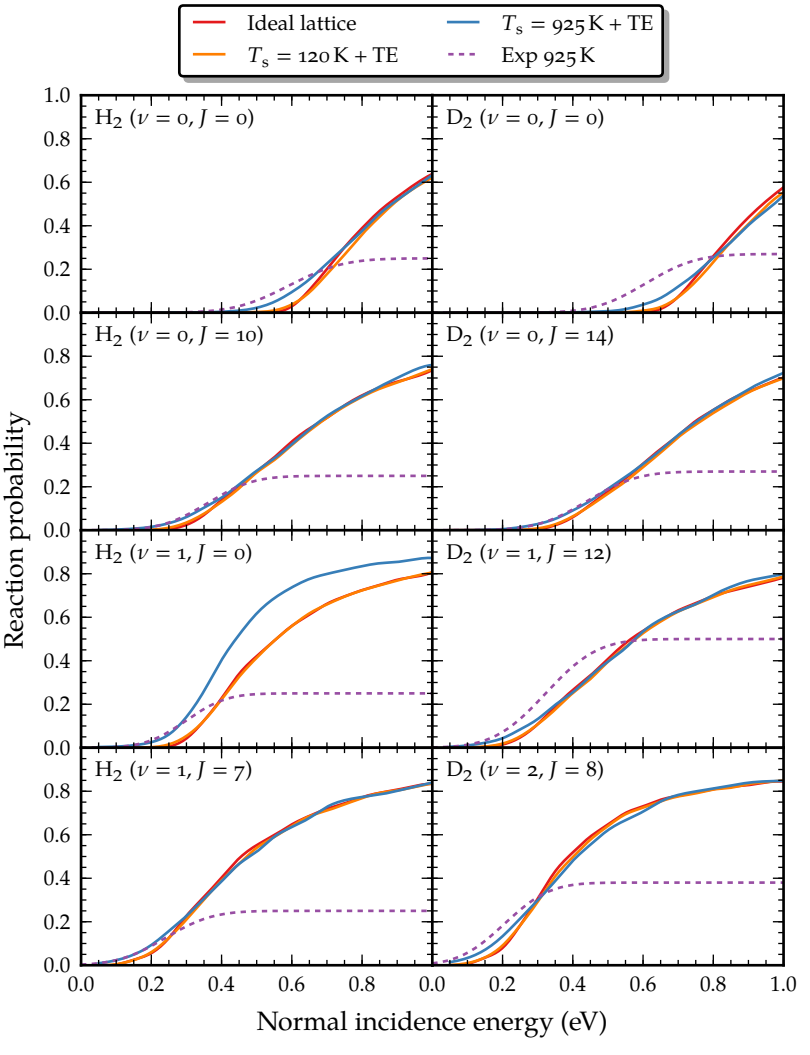


**Figure 3.6** Broadening of the sticking curves as the surface temperature is increased, for a selection of initial rovibrational states, taking into account the effects of thermal displacement and thermal expansion (TE) effects. Also plotted are the experimental sticking curves obtained by Michelsen *et al.*[28,29] and Rettner *et al.*[32]

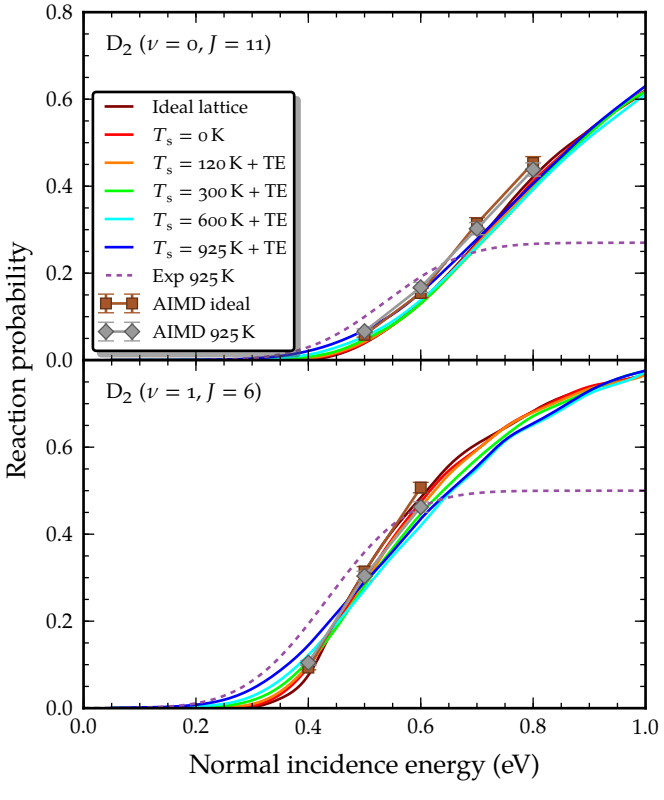


**Figure 3.7** Broadening of the sticking curve for $D_2$ initially in the ($\nu = 0$, $J = 11$) and ($\nu = 1$, $J = 6$) states, for all considered surface temperatures, taking into account the effects of thermal displacement and thermal expansion (TE). The experimental sticking curve[29] is also plotted, as well as the AIMD results by Nattino *et al.*[20]

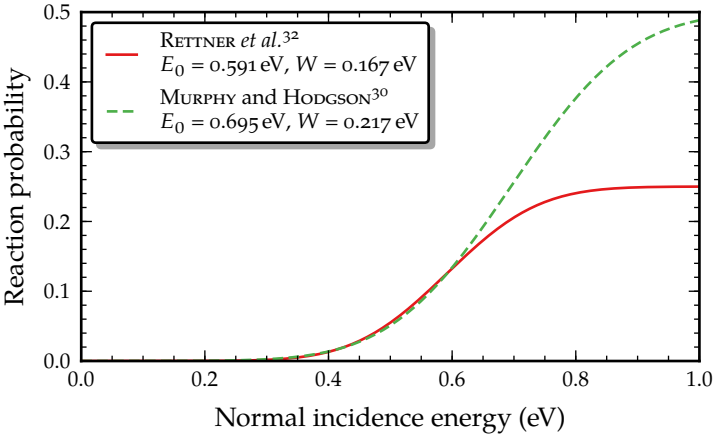


**Figure 3.8** Comparison of the sticking curves for ($\nu = 0, J = 5$) $H_2$ by Murphy and Hodgson[30] and Rettner *et al.*[32] The saturation value for the experiment by Murphy and Hodgson[30] is unknown, and if this would be approximately 0.5 the two experiments are in agreement with each other.



sorption probability for a few final states, which means only $E_0$ and $W$ were determined. Murphy and Hodgson[30] found significantly larger $E_0$ and $W$ parameters than Michelsen *et al.*[28,29] and Rettner *et al.*,[32] but no explanation was offered for this.

A possible explanation could be that the sticking curves by Murphy and Hodgson[30] have a higher saturation value. In figure 3.8 the sticking curves of Murphy and Hodgson[30] and Rettner *et al.*[32] for ($\nu = 0$, $J = 5$) $H_2$ are compared, taking for $A$ the value which gives best agreement between the two different experiments. At low energies, the two curves are essentially the same up to experimental precision. This can be argued to be the most important region for the comparison due to the population of low energies being highest. This shows therefore that the two experiments *could* be in agreement with each other, but it cannot be rigorously proven.

In figure 3.9 the reaction probability for ($\nu = 0, J = 5$) $H_2$ computed with the model at $T_s = 925\,\mathrm{K}$ is plotted both on a linear scale and on a logarithmic scale. Fits are also shown if $A$ is kept fixed during the fitting procedure for two $A$ parameters. It is shown that the reaction

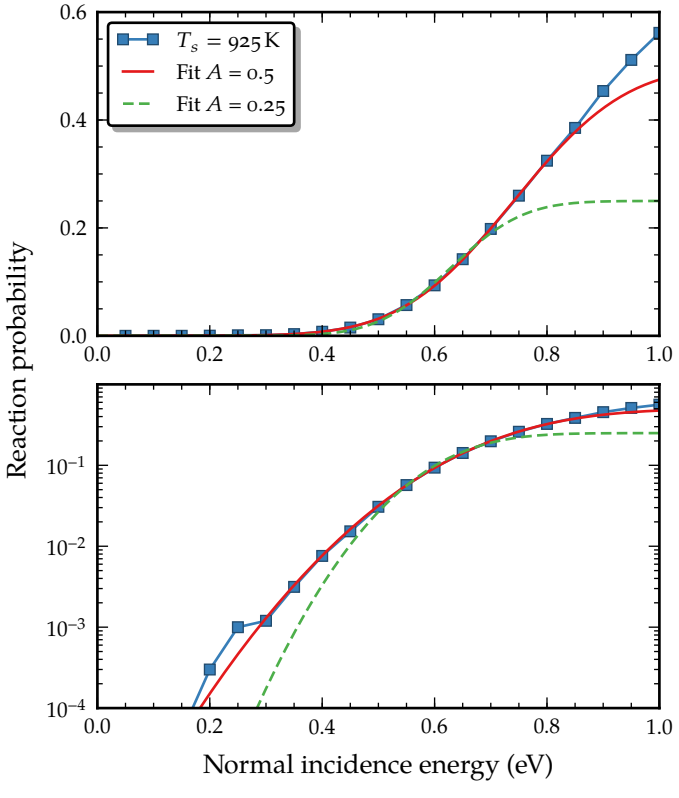


**Figure 3.9** Fits for the computed sticking curve at $T_s = 925\,K$ for ($v = 0$, $J = 5$) $H_2$ with $A = 0.25$, the experimental value reported by Rettner *et al.*,[32] and $A = 0.5$, which yields a much better description of the computed sticking curve.

probability can be well described by the form of equation (3.15), however, if the $A$ parameter determined by Michelsen *et al.* is used the low energy regime is not described well, but also the high energy regime is not described well. Although a low energy "tail" is known,[30] the calculations show a larger difference between the fit to equation (3.15) and the computed values. In fact, it is found that increasing $A$ in the fitting procedure provides a significantly better description of the sticking curve. The similarity between the $A$ value used here (0.5) and the $A$ value used to reconcile the fits of Michelsen *et al.* and those of Murphy and Hodgson[30] is pointed out (see figure 3.8).

As shown in figure 3.9, the calculated sticking curve can be well represented by equation (3.15). If $E_0$ is fixed to a particular value, $W$ determines the shape of the sticking curve and $E_0$ its position on the energy axis. Therefore, if $W$ and $E_0$ are obtained from accurate fits with an $A$ equal to the experimentally found saturation value, a reasonable comparison can be made with experiment. As noted earlier, a higher $A$ value generally provides a better description of the curve at low energies, however in that case no comparison can be made with the experimental data, as $E_0$ and $W$ will in this case be too high. In the fits below $A$ will be assumed to be equal to the values reported by Michelsen *et al.* and Rettner *et al.* In the fits, data points with a reaction probability smaller than 1% are not taken into account for accuracy reasons; data points with a reaction probability larger than $0.6 \cdot A$ are also not taken into account as they decrease the quality of the description at lower energies, where the population is highest in desorption experiments. Díaz *et al.*[1,2] found that, for the ideal lattice, the fits start to deviate from the computed reaction probabilities above a reaction probability of about $0.75 \cdot A$.



In figure 3.10 the fit parameters are shown for $D_2$ with $A = 0.27$ ($v = 0$), $A = 0.5$ ($v = 1$) and $A = 0.38$ ($v = 2$). The behaviour of the model with thermal expansion and expansion or contraction of the first interlayer distance is somewhat suspicious for low $J$ ($J < 4$). Although the dynamical barrier height $E_0$ at $J = 0$ is considerably more decreased than $E_0$ at high $J$ when the surface temperature is increased, this seems to not be the case for $J = 1$, where it is unchanged or even increased. The curves for $E_0$ versus rotational state are therefore not as smooth as one might expect. This could be due to the use of a PES for the 6D system with p6mm symmetry, while the symmetry in reality is p3m1. p3m1 symmetry has to be assumed for the surface atom position vectors in the model. Because this could change the anisotropy of the PES, thermal expansion could introduce an error in the PES for the $J$ dependency. Additionally, the pair potential as used in the present model might be too restrictive for correcting for thermal expansion. The effects of thermal expansion are again underlined here: the dynamical barrier height is decreased (system becomes more reactive), while at the same time the width decreases. Overall, the $W$ parameter determining

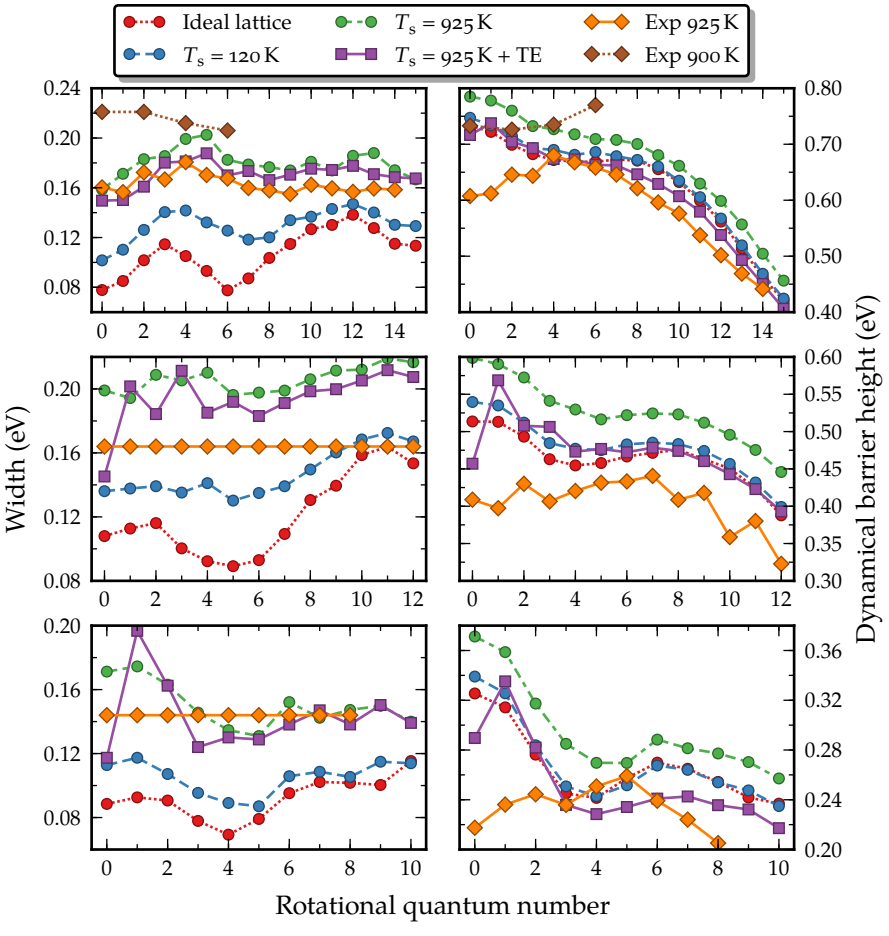


**Figure 3.10** Fitted parameters to equation (3.15) for all considered initial states of $D_2$. Results including thermal expansion are listed as TE. Top panels: ($v = 0$). Middle panels: ($v = 1$). Bottom panels: ($v = 2$). Experimental data with $T_s = 925\,K$ by Michelsen *et al.*[28,29] Experimental data with $T_s = 900\,K$ by Murphy and Hodgson.[30]

the shape of the reaction probability curve is in good agreement with the experiments by Michelsen *et al.*,[28,29] except for ($\nu = 1$), where it is somewhat too large. It is however noted that significant errors in the ratios of $A$ from the experiments ($A(\nu = 0) : A(\nu = 1) : A(\nu = 2) = (0.54 \pm 0.16) : 1.00 : (0.77 \pm 0.18)$)[29] manifest itself here in terms of the $W$ parameters as $A$ was assumed to be fixed to the experimentally reported value. For example, if $A(\nu = 1)$ is assumed to be slightly smaller (0.4 instead of 0.5) the agreement for the width is as good as for other states and the decrease of $A$ is (almost) within the reported errors of the ratios. Overall, the agreement for the $E_0$ parameter determining the position of the reaction probability curve on the energy axis is improved if also thermal expansion and expansion or contraction of the first interlayer distance is taken into account, but not if only thermal displacement is taken into account. Although the high $J$ behaviour seems good, the low $J$ behaviour is suspicious. Again here for ($\nu = 1$) $D_2$ the agreement is not so good, but if $A$ is adjusted to 0.4 the agreement is again very good.



In figure 3.11 the fit parameters are shown for $H_2$ with $A = 0.25$. The agreement with the experiments by Rettner *et al.*[32] is less good than for $D_2$. It is possible that this could be caused by the use of quasi-classical rather than quantum dynamics. Because $H_2$ has a lower mass than $D_2$, quantum effects are more important for $H_2$ due to this mass difference. Previously with the BOSS model[1,2] significant differences were found between results obtained with quasi-classical and quantum dynamics for $H_2$ dissociating on Cu(111). Similar effects as found in the results for $D_2$ above are also found for $H_2$. Overall the agreement with experiment is good, but for ($\nu = 1$) $H_2$ the agreement is less good than for ($\nu = 0$) $H_2$.

Compared to results reported in the literature[1,8,27,30,32,45] for SM[46,47] and (M)SO[42–48] models, significantly better width values are obtained. If the SM model were to be applied on top of the model applied here, only a small amount of extra broadening would be expected, due to the unfavourable $H_2$/Cu mass ratio. Darling and Holloway[8] already reported in 1994 that the static corrugation which is introduced by thermal displacement of surface atoms could be very important.

Clearly the presented results are sensitive to the accuracy of the experimentally obtained $A$ value. A better comparison would be to

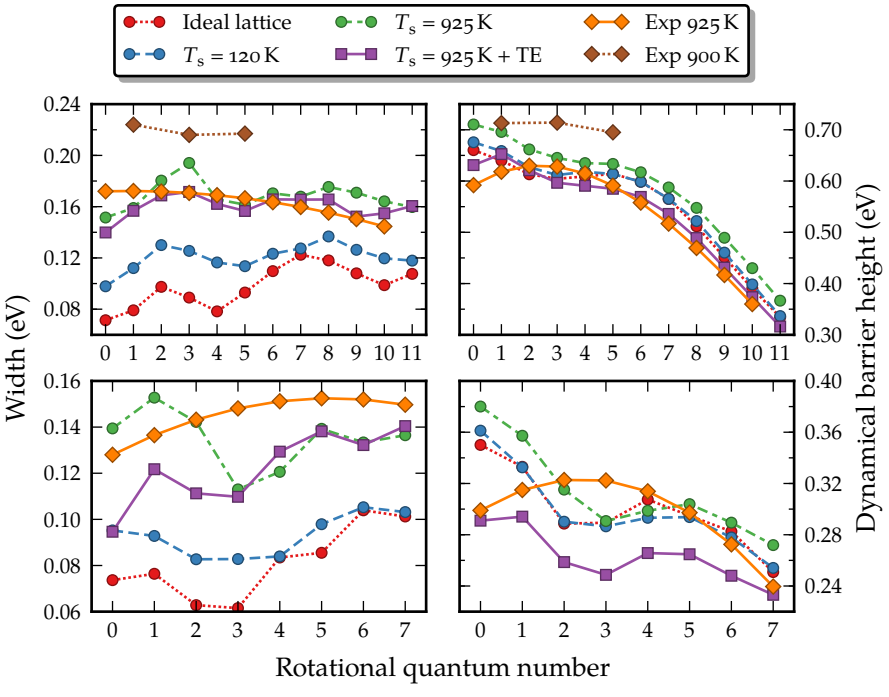


**Figure 3.11** Fitted parameters to equation (3.15) for all considered initial states of $H_2$. Results including thermal expansion are listed as TE. Top panels: ($v = 0$). Bottom panels: ($v = 1$). Experimental data with $T_s = 925$ K by Rettner *et al.*[32] Experimental data with $T_s = 900$ K by Murphy and Hodgson.[30]

compare the theoretical results directly to the raw experimental time-of-flight (TOF) data from which the $A$, $W$ and $E_0$ parameters were indirectly extracted. Such a direct comparison has for example been done in 2014 for AIMD calculations on $H_2$/Cu(111).[21]

### 3.3.3 Rotational quadrupole alignment parameter

The rotational quadrupole alignment parameter for $D_2$ desorbing from a Cu(111) surface was measured by Gulding *et al.*,[24] Hou *et al.*,[25] and Wetzig *et al.*[34] The rotational quadrupole alignment parameter is a measurement of preference of desorption in a particular $m_J$ state and the definition of this parameter is given by equation (2.33). Equa-

tion (2.34) shows how it can be computed from the initial state-resolved reaction probability.

Hou *et al.*[25] measured the energy-resolved rotational quadrupole alignment parameter for desorption into two states, while Gulding *et al.*[24] and Wetzig *et al.*[34] measured the rotational quadrupole alignment parameter for desorption into a larger number of states, but these measurements were not energy-resolved. In this study only the energy-resolved rotational quadrupole alignment parameter is considered due to sampling-related inaccuracies of (quasi-)classical methods at low energies.

In figure 3.12 the rotational quadrupole alignment parameter is plotted for a variety of models, comparing the ideal lattice results with the results of the static corrugation model, the experimental data and recent AIMD calculations. The effect of thermal displacement is also a broadening of the rotational quadrupole alignment parameter curve; at low energies the rotational quadrupole alignment parameter is considerably decreased, while at high energies the rotational quadrupole alignment parameter is slightly increased. Including thermal expansion effects in the calculations tends to lead to a further decrease of the rotational quadrupole alignment parameter. Comparing the static corrugation model results with the experimental results, the agreement at low energies is considerably improved, although the observed effect is slightly too large for ($\nu = 1, J = 6$) $D_2$. At high energies however, the agreement is not improved. It is not clear why this is the case. It is however noted that the experimentalists have calculated the rotational quadrupole alignment parameter from fits to TOF spectra, and these fits may be, like the fits for the desorption probability considered in section 3.3.2, relatively insensitive to the high energy regime, although this does not seem to be reflected in the size of the experimental error bars.

The dependence of the rotational quadrupole alignment parameter on the surface temperature can be explained. It is likely that the arguments (see section 3.3.2) for the broadening and shifting of the $J$-resolved reaction probability curve also hold for the $m_J$-resolved reaction probability curves. The calculations done here are in agreement with this. At low energies, the overall reaction probability is increased with increasing surface temperature. This leads to a larger denomin-

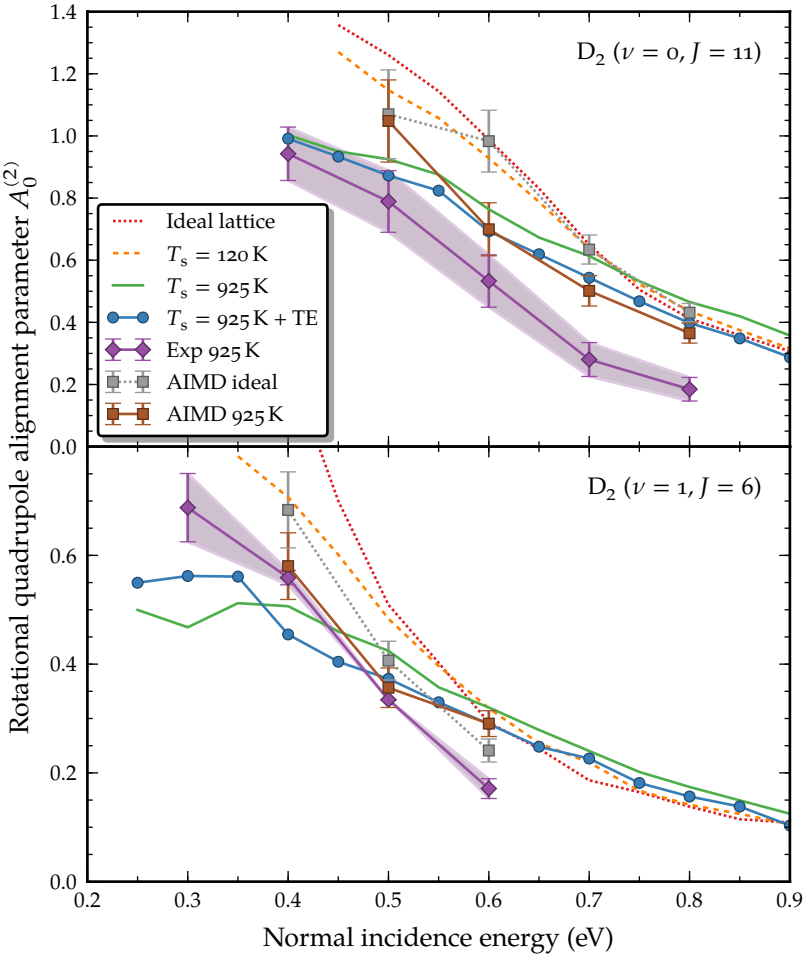


**Figure 3.12** Comparison of the rotational quadrupole alignment parameter computed with different models. Plotted are the rotational quadrupole alignment parameter for an ideal crystal, for a crystal with $T_s = 120\,K$, $T_s = 925\,K$, $T_s = 925\,K$ with thermal expansion effects (TE), the experimental data by Hou *et al.*[25] and the AIMD results by Nattino *et al.*,[20] for a rigid ideal surface and moving surface at $T_s = 925\,K$.

ator in equation (2.34). The numerator will decrease because tilted molecules will react more due to the locally tilted surface. This results in a lower alignment parameter. At high energies, the overall reaction probability is only slightly decreased, resulting in a slightly lower denominator. In the limit of saturation (reaction probability equal to unity), the first molecules to react less are the unfavourably tilted ones, resulting in a slightly higher numerator. Overall this leads to a slight increase of the alignment parameter.

### 3.3.4 Molecular beams

To make a comparison with molecular beam experiments possible, two things have to be taken into account. First, the state-resolved reaction probabilities should be averaged over all states with significant population in the beam. Second, the experimental spread in incidence energies has to be taken into account. The way in which this has been done has been described in section 2.5.3 of this thesis.



Experiments were performed for $D_2$ by Michelsen *et al.*[29] and for $H_2$ by Rettner *et al.*[32] The parameters for the velocity distribution, equation (2.39), for these experiments were obtained by Díaz *et al.*[1,2] In the calculations all rovibrational states listed in table 3.2 are included.

In figure 3.13 the molecular beam simulations are shown for the ideal lattice and for $T_s = 120\,\mathrm{K}$. For $T_s = 120\,\mathrm{K}$ the results are not changed much if thermal expansion effects are taken into account: only a slight increase in reaction is found due to the small shift of the reaction probability curve to lower energies. For low average collision energies, reaction is generally found to be slightly increased for $T_s = 120\,\mathrm{K}$ with respect to the ideal lattice, while for higher average collision energies reaction is generally found to be slightly decreased. Comparing the results found here with the AIMD results for this trend is difficult, as no calculations were performed for the ideal lattice and the surface temperature effects are very small. It is noted that the differences found for the initial state-resolved reaction probability of $D_2$ in the $(v = 0, J = 11)$ state between the SRP potential[1,2] as used here and the AIMD calculations[20] (figure 3.4), might have a consequence for the molecular beam results. The AIMD results for this state were found to be more reactive

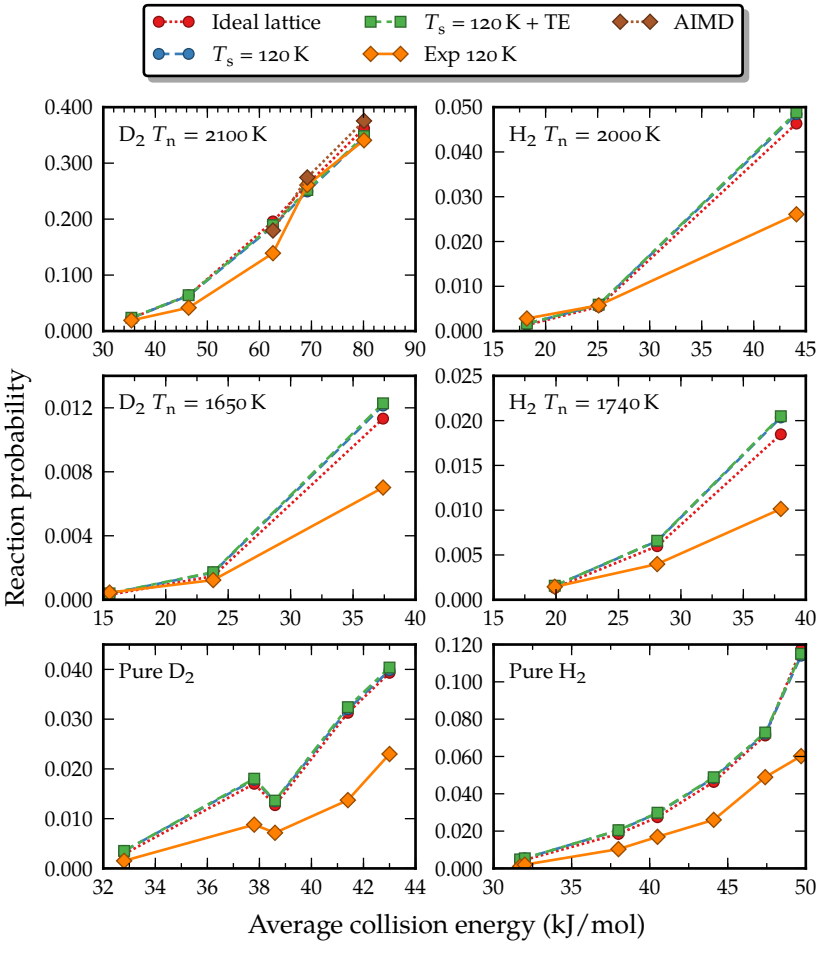


**Figure 3.13** Effect of surface temperature on molecular beams, with (TE) and without thermal expansion effects, for a variety of $H_2$ and $D_2$ beams. Experiments for $D_2$ by Michelsen *et al.*[29] and for $H_2$ by Rettner *et al.*[32] Parameters for the velocity distribution of the molecular beams were extracted by Díaz *et al.*[1,2] *Ab initio* molecular dynamics results by Nattino *et al.*[20]

than the results with the SRP potential used here. If this effect is general for $D_2$ in the ($\nu = 0$) state, a significant shift should be observed in the molecular beam results. Combined with the significant error in the AIMD results due to a limited number of trajectories being sampled in AIMD, the conclusion here is that the AIMD results are consistent with the results for the static corrugation model.

## 3.4 Conclusions

A model has been constructed to take into account surface temperature effects for $H_2$ or $D_2$ dissociating on a Cu(111) surface. The model is general and does not require a special form for the PES. It is based on the assumption that in different scattering events the hydrogen molecule experiences different non-ideal but (almost) static surfaces. This approximation is reasoned to work well, based on the physics of the event taking place and is corroborated by previous calculations on $CH_4$ dissociation on metal surfaces. The model introduces a correction term for displacement of surface atoms based on the coupling potential.



The quality of the model has been assessed based on a comparison with a recent DFT study and the comparison of three computed observables with experiments and recent AIMD calculations. The observables that were considered are the initial state-resolved reaction probability, the rotational quadrupole alignment parameter and the reaction probability averaged over the distribution in molecular beams. Overall, the agreement with experiments and the AIMD calculations is found to be good. Apparently bigger overall effects are found here than were found in AIMD calculations, however. The agreement with experiment seems however to be better in some cases for the calculations performed in this work. It is not fully clear why this happens. A possible explanation could be differences in the sampling of surface configurations. For the AIMD calculations a limited number of surface configurations are sampled whereas here surface atoms are displaced individually per trajectory according to a model based on DW factors. The model also differs from AIMD in a different way: whereas in AIMD a $2 \times 2$ unit cell is used, here no periodic boundary conditions are applied to the surface atoms. The 1D correction function is relatively long range ($7.5\,a_0$),

which might indicate a larger unit cell might be needed.

For the comparison with the DFT study it is concluded that the chosen form for the 1D correction potential can reproduce well the behaviour of the coupling potential at high-symmetry barrier positions in an ideal surface for perpendicular displacements.

For the initial state-resolved reaction probability, it is found that both thermal displacement and thermal expansion are of importance. Thermal displacement causes the broadening that has been experimentally observed as the surface temperature increases, whereas thermal expansion primarily makes the system more reactive by shifting the reaction probability curves. The discrepancy between two sets of experimental data has been attributed to the fact that experimentalists are not able to measure absolute desorption probabilities. Therefore the experimentalists had to obtain one parameter from a fit to adsorption experiments, which was not done for one of the experiments. The agreement with the AIMD calculations is reasonable, but somewhat broader reaction probability curves are found here. The width of these curves is however generally found to be in agreement with the experiments.

For the rotational quadrupole alignment parameter, it is found that, analogous to the reaction probability, thermal displacement tends to broaden the rotational quadrupole alignment parameter curve, whereas thermal expansion tends to shift the curve. At low energies, the rotational quadrupole alignment parameter is decreased with increasing surface temperature, whereas at high energies, the rotational quadrupole alignment parameter is slightly increased with increasing surface temperature. The agreement with experiment is good at low energies, but less good at high energies. In recent AIMD calculations a decrease with increasing surface temperature was also found at low energies, and one state considered also showed an increase at high energies. A larger broadening of the rotational quadrupole alignment parameter curve is found in the calculations performed here, which provides a better agreement with experiments at low energies.

For the comparison to molecular beam sticking experiments, it is found that the approximation of an ideal surface being representative of a low temperature surface, as previously used, is good. This was also found in recent AIMD calculations. Only very weak surface temperat-

ure effects are found in the molecular beam simulations, in which the surface temperature is 120 K.

The model constructed here is therefore able to reproduce most of the surface temperature effects observed experimentally, without energy exchange between the molecule and the surface being possible. It has been previously suspected, based on model calculations by Darling and Holloway,[8] that the effect of static corrugation could be important, and the calculations performed confirm that idea.

## References


[1] C. Díaz, R. A. Olsen, D. J. Auerbach, and G. J. Kroes. Six-dimensional dynamics study of reactive and non reactive scattering of $H_2$ from Cu(111) using a chemically accurate potential energy surface. *Physical Chemistry Chemical Physics* **12**(24), pp. 6499–6519, 2010.

[2] C. Díaz, E. Pijper, R. A. Olsen, H. F. Busnengo, D. J. Auerbach, and G. J. Kroes. Chemically accurate simulation of a prototypical surface reaction: $H_2$ dissociation on Cu(111). *Science* **326**(5954), pp. 832–834, 2009.

[3] J. Dai and J. C. Light. The steric effect in a full dimensional quantum dynamics simulation for the dissociative adsorption of $H_2$ on Cu(111). *Journal of Chemical Physics* **108**(18), pp. 7816–7820, 1998.

[4] J. Dai and J. C. Light. Six dimensional quantum dynamics study for dissociative adsorption of $H_2$ on Cu(111) surface. *Journal of Chemical Physics* **107**(5), pp. 1676–1679, 1997.

[5] J. Dai, J. Sheng, and J. Z. H. Zhang. Symmetry and rotational orientation effects in dissociative adsorption of diatomic molecules on metals: $H_2$ and HD on Cu(111). *Journal of Chemical Physics* **101**(2), pp. 1555–1563, 1994.

[6] J. Dai and J. Z. H. Zhang. Quantum adsorption dynamics of a diatomic molecule on surface: Four-dimensional fixed-site model for $H_2$ on Cu(111). *Journal of Chemical Physics* **102**(15), pp. 6280–6289, 1995.

[7] J. Dai and J. Z. H. Zhang. Steric effect in dissociative chemisorption of hydrogen on Cu. *Surface Science* **319**(1–2), pp. 193–198, 1994.

[8] G. R. Darling and S. Holloway. Surface temperature effects in the dissociative adsorption of $D_2$/Cu(111) revisited. *Surface Science* **321**(3), pp. L189–L194, 1994.

[9] G. R. Darling and S. Holloway. Rotational motion and the dissociation of $H_2$ on Cu(111). *Journal of Chemical Physics* **101**(4), pp. 3268–3281, 1994.

[10] G. R. Darling and S. Holloway. Dissociation thresholds and the vibrational excitation process in the scattering of $H_2$. *Surface Science* **307–309**(A), pp. 153–158, 1994.

[11] G. R. Darling and S. Holloway. Translation-to-vibrational excitation in the dissociative adsorption of $D_2$. *Journal of Chemical Physics* **97**(1), pp. 734–736, 1992.

[12] A. Forni, G. Wiesenekker, E. J. Baerends, and G. F. Tantardini. A dynamical study of the chemisorption of molecular hydrogen on the Cu(111) surface. *Journal of Physics: Condensed Matter* **7**(36), pp. 7195–7207, 1995.

[13] A. Forni, G. Wiesenekker, E. J. Baerends, and G. F. Tantardini. The chemisorption of hydrogen on Cu(111): a dynamical study. *International Journal of Quantum Chemistry* **52**(4), pp. 1067–1080, 1994.

[14] A. Gross, B. Hammer, M. Scheffler, and W. Brenig. High-dimensional quantum dynamics of adsorption and desorption of $H_2$ at Cu(111). *Physical Review Letters* **73**(23), pp. 3121–3124, 1994.

[15] B. Hammer, M. Scheffler, K. W. Jacobsen, and J. K. Nørskov. Multidimensional potential energy surface for $H_2$ dissociation over Cu(111). *Physical Review Letters* **73**(10), pp. 1400–1403, 1994.

[16] S. Nave, D. Lemoine, M. F. Somers, S. M. Kingma, and G. J. Kroes. Six-dimensional quantum dynamics of ($v$ = 0, $j$ = 0) $D_2$ and of ($v$ = 1, $j$ = 0) $H_2$ scattering from Cu(111). *Journal of Chemical Physics* **122**(21), 214709, 2005.

[17] U. Nielsen, D. Halstead, S. Holloway, and J. K. Nørskov. The dissociative adsorption of hydrogen: two-, three-, and four-dimensional quantum simulations. *Journal of Chemical Physics* **93**(4), pp. 2879–2884, 1990.

[18] J. Sheng and J. Z. H. Zhang. Quantum dynamics studies of adsorption and desorption of hydrogen at a Cu(111) surface. *Journal of Chemical Physics* **99**(2), pp. 1373–1381, 1993.

[19] M. F. Somers, S. M. Kingma, E. Pijper, G. J. Kroes, and D. Lemoine. Six-dimensional quantum dynamics of scattering of ($v$ = 0, $j$=0) $H_2$ and $D_2$ from Cu(111): test of two LEPS potential energy surfaces. *Chemical Physics Letters* **360**(3–4), pp. 390–399, 2002.

[20] F. Nattino, C. Díaz, B. Jackson, and G. J. Kroes. Effect of surface motion on the rotational quadrupole alignment parameter of $D_2$ reacting on Cu(111). *Physical Review Letters* **108**(23), 236104, 2012.

[21] F. Nattino, A. Genova, M. Guijt, A. S. Muzas, C. Díaz, D. J. Auerbach, and G. J. Kroes. Dissociation and recombination of $D_2$ on Cu(111): *ab initio* molecular dynamics calculations and improved analysis of desorption experiments. *Journal of Chemical Physics* **141**(12), 124705, 2014.

[22] G. Anger, A. Winkler, and K. D. Rendulic. Adsorption and desorption kinetics in the systems $H_2$/Cu(111), $H_2$/Cu(110) and $H_2$/Cu(100). *Surface Science* **220**(1), pp. 1–17, 1989.

[23] H. F. Berger, M. Leisch, A. Winkler, and K. D. Rendulic. A search for vibrational contributions to the activated adsorption of $H_2$ on copper. *Chemical Physics Letters* **175**(5), pp. 425–428, 1990.

[24] S. J. Gulding, A. M. Wodtke, H. Hou, C. T. Rettner, H. A. Michelsen, and D. J. Auerbach. Alignment of $D_2$(v, J) desorbed from Cu(111): low sensitivity of activated dissociative chemisorption to approach geometry. *Journal of Chemical Physics* **105**(21), pp. 9702–9705, 1996.

[25] H. Hou, S. J. Gulding, C. T. Rettner, A. M. Wodtke, and D. J. Auerbach. The stereodynamics of a gas-surface reaction. *Science* **277**(5322), pp. 80–82, 1997.

[26] H. A. Michelsen and D. J. Auerbach. A critical examination of data on the dissociative adsorption and associative desorption of hydrogen at copper surfaces. *Journal of Chemical Physics* **94**(11), pp. 7502–7520, 1991.

[27] H. A. Michelsen, C. T. Rettner, and D. J. Auerbach. State-specific dynamics of $D_2$ desorption from Cu(111): the role of molecular rotational motion in activated adsorption-desorption dynamics. *Physical Review Letters* **69**(18), pp. 2678–2681, 1992.

[28] H. A. Michelsen, C. T. Rettner, and D. J. Auerbach. On the influence of surface temperature on adsorption and desorption in the $D_2$/Cu(111) system. *Surface Science* **272**(1–3), pp. 65–72, 1992.

[29] H. A. Michelsen, C. T. Rettner, D. J. Auerbach, and R. N. Zare. Effect of rotation on the translational and vibrational energy dependence of the dissociative adsorption of $D_2$ on Cu(111). *Journal of Chemical Physics* **98**(10), pp. 8294–8307, 1993.

[30] M. J. Murphy and A. Hodgson. Adsorption and desorption dynamics of $H_2$ and $D_2$ on Cu(111): the role of surface temperature and evidence for corrugation of the dissociation barrier. *Journal of Chemical Physics* **108**(10), pp. 4199–4211, 1998.

[31] C. T. Rettner, D. J. Auerbach, and H. A. Michelsen. Role of vibrational and translational energy in the activated dissociative adsorption of $D_2$ on Cu(111). *Physical Review Letters* **68**(8), pp. 1164–1167, 1992.

[32] C. T. Rettner, H. A. Michelsen, and D. J. Auerbach. Quantum-state-specific dynamics of the dissociative adsorption and associative desorption of $H_2$ at a Cu(111) surface. *Journal of Chemical Physics* **102**(11), pp. 4625–4641, 1995.

[33] C. T. Rettner, H. A. Michelsen, and D. J. Auerbach. Determination of quantum-state-specific gas-surface energy transfer and adsorption probabilities as a function of kinetic energy. *Chemical Physics* **175**(1), pp. 157–169, 1993.

[34] D. Wetzig, M. Rutkowski, R. David, and H. Zacharias. Rotational corrugation in associative desorption of $D_2$ from Cu(111). *Europhysics Letters* **36**(1), pp. 31–36, 1996.

[35] P. Nieto, E. Pijper, D. Barredo, G. Laurent, R. A. Olsen, E. J. Baerends, G. J. Kroes, and D. Farías. Reactive and nonreactive scattering of $H_2$ from a metal surface is electronically adiabatic. *Science* **312**(5770), pp. 86–89, 2006.

[36] A. Gross and A. Dianat. Hydrogen dissociation dynamics on precovered Pd surfaces: Langmuir is still right. *Physical Review Letters* **98**(20), 206107, 2007.

[37] F. R. Kroeger and C. A. Swenson. Absolute linear thermal-expansion measurements on copper and aluminum from 5 to 320 K. *Journal of Applied Physics* **48**(3), pp. 853–864, 1977.

[38] I. E. Leksina and S. I. Novikova. Thermal expansion of copper, silver, and gold within a wide range of temperatures. *Soviet Physics - Solid State* **5**(4), pp. 798–801, 1963.

[39] K. H. Chae, H. C. Lu, and T. Gustafsson. Medium-energy ion-scattering study of the temperature dependence of the structure of Cu(111). *Physical Review B* **54**(19), pp. 14082–14086, 1996.

[40] V. F. Sears and S. A. Shelley. Debye-Waller factor for elemental crystals. *Acta Crystallographica* **A47**(4), pp. 441–446, 1991.

[41] E. C. Svensson, B. N. Brockhouse, and J. M. Rowe. Crystal dynamics of copper. *Physical Review* **155**(3), pp. 619–632, 1967.

[42] M. Dohle and P. Saalfrank. Surface oscillator models for dissociative sticking of molecular hydrogen at non-rigid surfaces. *Surface Science* **373**(1), pp. 95–108, 1997.

[43] M. Dohle, P. Saalfrank, and T. Uzer. Dissociative sticking of diatomic molecules on cold, non-rigid surfaces: comparison of quantal and semiclassical surface oscillator model. *Surface Science* **409**(1), pp. 37–45, 1998.

[44] M. Dohle, P. Saalfrank, and T. Uzer. The dissociation of diatomic molecules on vibrating surfaces: a semiclassical generalized Langevin approach. *Journal of Chemical Physics* **108**(10), pp. 4226–4236, 1998.

[45] M. Hand and J. Harris. Recoil effects in surface dissociation. *Journal of Chemical Physics* **92**(12), pp. 7610–7617, 1990.

[46] A. C. Luntz and J. Harris. $CH_4$ dissociation on metals: a quantum dynamics model. *Surface Science* **258**(1–3), pp. 397–426, 1991.

[47] P. Saalfrank and W. H. Miller. Quantum-mechanical rates for gas-surface processes. *Surface Science* **303**(1–2), pp. 206–230, 1994.

[48] H. F. Busnengo, W. Dong, P. Sautet, and A. Salin. Surface temperature dependence of rotational excitation of $H_2$ scattered from Pd(111). *Physical Review Letters* **87**(12), 127601, 2001.

[49] S. Nave and B. Jackson. Methane dissociation on Ni(111): the effects of lattice motion and relaxation on reactivity. *Journal of Chemical Physics* **127**(22), 224702, 2007.

[50] S. Nave and B. Jackson. Methane dissociation on Ni(111): the role of lattice reconstruction. *Physical Review Letters* **98**(17), 173003, 2007.

[51] N. Pineau, H. F. Busnengo, J. C. Rayez, and A. Salin. Relaxation of hot atoms following $H_2$ dissociation on a Pd(111) surface. *Journal of Chemical Physics* **122**(21), 214705, 2005.



[52] M. Bonfanti, M. F. Somers, C. Díaz, H. F. Busnengo, and G. J. Kroes. 7D quantum dynamics of $H_2$ scattering from Cu(111): the accuracy of the phonon sudden approximation. *Zeitschrift für Physikalische Chemie* **227**(11), pp. 1397–1420, 2013.

[53] M. Bonfanti, C. Díaz, M. F. Somers, and G. J. Kroes. Hydrogen dissociation on Cu(111): the influence of lattice motion. Part I. *Physical Chemistry Chemical Physics* **13**(10), pp. 4552–4561, 2011.

[54] A. K. Tiwari, S. Nave, and B. Jackson. The temperature dependence of methane dissociation on Ni(111) and Pt(111): mixed quantum-classical studies of the lattice response. *Journal of Chemical Physics* **132**(13), 134702, 2010.

[55] A. K. Tiwari, S. Nave, and B. Jackson. Methane dissociation on Ni(111): a new understanding of the lattice effect. *Physical Review Letters* **103**(25), 253201, 2009.

[56] H. F. Busnengo, A. Salin, and W. Dong. Representation of the 6D potential energy surface for a diatomic molecule near a solid surface. *Journal of Chemical Physics* **112**(17), pp. 7641–7651, 2000.

[57] R. Drautz, M. Fähnle, and J. M. Sanchez. General relations between many-body potentials and cluster expansions in multicomponent systems. *Journal of Physics: Condensed Matter* **16**(23), pp. 3843–3852, 2004.

[58] J. Ludwig, D. G. Vlachos, A. C. T. van Duin, and W. A. Goddard. Dynamics of the dissociation of hydrogen on stepped platinum surfaces using the ReaxFF reactive force field. *Journal of Physical Chemistry B* **110**(9), pp. 4274–4282, 2006.

[59] P. Valentini, T. E. Schwartzentruber, and I. Cozmuta. Molecular dynamics simulation of $O_2$ sticking on Pt(111) using the *ab initio* based ReaxFF reactive force field. *Journal of Chemical Physics* **133**(8), 084703, 2010.

[60] Y. Xiao, W. Dong, and H. F. Busnengo. Reactive force fields for surface chemical reactions: A case study with hydrogen dissociation on Pd surfaces. *Journal of Chemical Physics* **132**(1), 014704, 2010.

[61] X. J. Shen, A. Lozano, W. Dong, H. F. Busnengo, and X. H. Yan. Towards bond selective chemistry from first principles: methane on metal surfaces. *Physical Review Letters* **112**(4), 046101, 2014.

[62] J. P. Perdew, J. A. Chevary, S. H. Vosko, K. A. Jackson, M. R. Pederson, D. J. Singh, and C. Fiolhais. Atoms, molecules, solids, and surfaces: applications of the generalized gradient approximation for exchange and correlation. *Physical Review B* **46**(11), pp. 6671–6687, 1992.

[63] B. Hammer, L. B. Hansen, and J. K. Nørskov. Improved adsorption energetics within density-functional theory using revised Perdew-Burke-Ernzerhof functionals. *Physical Review B* **59**(11), pp. 7413–7421, 1999.

[64] B. Verberck. Symmetry-adapted Fourier series for the wallpaper groups. *Symmetry* **4**(3), pp. 379–426, 2012.

[65] C. C. Marston and G. G. Balint-Kurti. The Fourier grid Hamiltonian method for bound state eigenvalues and eigenfunctions. *Journal of Chemical Physics* **91**(6), pp. 3571–3576, 1989.

[66] J. Stoer and R. Bulirsch. *Introduction to numerical analysis*. New York: Springer, 1980.

[67] M. Bonfanti. Personal communication. 2011.

CHAPTER

3

CHAPTER 4

# The effect of the exchange–correlation functional on $H_2$ dissociation on Ru(0001)

This chapter is based on:

M. Wijzenbroek and G. J. Kroes. The effect of the exchange-correlation functional on $H_2$ dissociation on Ru(0001). *Journal of Chemical Physics* **140**(8), 084702, 2014.

## Abstract

The specific reaction parameter (SRP) approach to density functional theory (DFT) has enabled a chemically accurate description of reactive scattering experiments for activated $H_2$–metal surface systems ($H_2$/Cu(111) and Cu(100)), but its application has not yet resulted in a similarly accurate description of non-activated or weakly activated $H_2$–metal surface systems. In this study, the effect of the choice of the exchange-correlation functional in DFT on the potential energy surface and dynamics of $H_2$ dissociation on Ru(0001), a weakly activated system, is investigated. In total, full potential energy surfaces were calculated for over 20 different functionals. The functionals investigated include functionals incorporating an approximate description of the van der Waals dispersion in the correlation functional (vdW-DF and vdW-DF2 functionals), as well as the revTPSS meta-GGA. With two of the functionals investigated here, which include vdW-DF and vdW-DF2 correlation, it has been possible to accurately reproduce molecular beam experiments on sticking of $H_2$ and $D_2$, as these functionals yield a reaction probability curve with an appropriate energy width. Diffraction probabilities computed with these two functionals are however too high compared to experimental diffraction probabilities, which are extrapolated from surface temperatures ($T_s$) $\geq$ 500 K to 0 K using a Debye–Waller model. Further research is needed to establish whether this constitutes a failure of the two candidate SRP functionals or a failure of the Debye–Waller model, the use of which can perhaps in future be avoided by performing calculations that include the effect of surface atom displacement or motion, and thereby of the experimental $T_s$.




## 4.1 Introduction

To perform accurate dynamics calculations on molecule–surface reactions, such as the dissociation of small molecules on metal surfaces, accurate potential energy surfaces (PESs) are needed. Due to the large, delocalized nature of these systems, electronic structure calculations on such systems are computationally expensive. Efficient electronic structure methods are therefore needed if one wishes to study such a system

in detail.

For molecule–surface reactions, one is limited to an electronic structure method with a favourable computational scaling, which in practice means density functional theory (DFT)[1,2] using an approximate exchange–correlation (XC) functional at the generalized gradient approximation (GGA) level. As of yet, it is not quantitatively known how large the error of using such an approximate XC functional is for barrier heights of molecule–surface reactions. Such studies have been performed for gas-phase reactions,[3,4] but remain challenging for molecule–surface reactions because of the lack of benchmark databases available for these systems. For chemisorption energies a database of experimental values is available,[5] but for barrier heights only a very small database may be said to exist, with only two entries in it.[6] Another database of molecule–surface barrier heights exists,[7,8] but this database is based on DFT calculations using the RPBE[9] functional, and can as such not be used to estimate the error made by the use of DFT in general.

For molecule–surface interactions, additional complications arise because also the surface introduces many additional degrees of freedom: energy exchange is possible with surface phonons and electron–hole pair excitations are possible.[10–12] For $H_2$ dissociation on metal surfaces, these effects can however be mostly avoided. Energy exchange with surface phonons may be expected to be a small effect[13] due to the large mass mismatch between the $H_2$ molecule and a surface atom. It has furthermore been argued that electron–hole pair excitation should only have a small effect on $H_2$–surface reactions.[14] These effects are discussed further in section 4.2.1.

For dissociation of $H_2$ on Cu(111), which is an activated late barrier molecule–surface reaction, it has been shown that neither of two popular XC functionals in the surface science community, the PW91[15] and the RPBE[9] functionals, could give a good agreement with experiment.[16,17] By employing a specific reaction parameter (SRP)[18] approach adapted to molecule–surface reactions,[16,17] good agreement could be obtained with a broad range of reaction and scattering experiments. The functional that was obtained as a result of the SRP procedure for $H_2$ on Cu(111) was also found to work well for $H_2$ on Cu(100).[19] In the SRP

procedure previously used for $H_2$ on Cu(111), a parameter ($\alpha$) mixing two functionals by

$$E_{XC}^{SRP} = \alpha E_{XC}^{1} + (1 - \alpha) E_{XC}^{2}. \tag{4.1}$$

where $E_{XC}^{1}$ and $E_{XC}^{2}$ are the XC energies obtained from the two functionals, was fitted in such a way that the reaction probability obtained from the SRP (mixed) functional matched the values measured in molecular beam experiments. As a result of this fitting procedure, the functional provides a reasonable description of the barrier height for reaction.[16] The test of an SRP functional is that it should also yield a good description of other observables than the one it was fitted to for the system investigated. It should be pointed out however that it is possible that one particular functional can already yield a good description of the ongoing processes, and as such the mixing procedure may not be needed.

It is currently not clear to what extent such a procedure is valid for weakly activated early barrier molecule–surface reactions. $H_2$ dissociation on Ru(0001) is an example of such an early barrier molecule–surface reaction. This reaction is also of catalytic importance, as ruthenium-based catalysts can be used to catalyse the production of ammonia from $H_2$ and $N_2$,[20–24] and the dissociation of $H_2$ on ruthenium is one of the elementary steps in this process. Although the dissociation of $N_2$ on ruthenium is thought to be the rate determining step in this process,[25,26] it is nonetheless important to have a detailed understanding of the other steps.

Previously, PESs were constructed for $H_2$ dissociation on Ru(0001),[27] and quantum dynamics calculations have been performed[28,29] to compare the performance of two DFT XC functionals, PW91[15] and RPBE,[9] with each other. Comparisons have also been made to experimental molecular beam studies on dissociative adsorption[30] as well as diffractive scattering.[29] The results of the comparison with experiments showed that neither functional could properly describe reaction over the entire interval of incidence energy, in the sense that the calculated reaction probability curve as a function of incidence energy was too narrow compared to the experimental curve, suggesting that the energetic corrugation of the used PESs is too small.[29,30] The same semi-empirical mixture of these two functionals as the one which worked well for $H_2$

dissociation on Cu(111),[16,17] was also not able to describe the reaction probability of $H_2$ on Ru(0001) over the entire range of incidence energies. Additionally, calculated diffraction probabilities were generally (somewhat) higher than the experimental diffraction probabilities. This discrepancy was attributed to the used XC functionals.[29] It was argued that the van der Waals interaction, which is not taken into account in the usual (semi-)local XC functionals,[31,32] could be important for an early barrier system such as $H_2$ dissociation on Ru(0001). Furthermore, in calculations on $H_2$ on Ru(0001) in which electron–hole pair excitations were incorporated by the use of electronic friction coefficients, the width of the reaction probability curve was found to be influenced only weakly by electronic friction.[33]

In the present work, an extensive study of XC functionals for $H_2$ dissociation on Ru(0001) is reported. The goal of the present work is twofold: first, to determine whether improved XC functionals, such as van der Waals-corrected functionals or meta-generalized gradient approximation (meta-GGA) functionals, can lead to an improved description of this system, and second, to obtain a SRP functional which is able to describe this system. To achieve this, PESs were constructed for $H_2$ on Ru(0001) using more than 20 different XC functionals. Barrier heights for reaction are analysed and from this analysis, and based on reaction probabilities obtained from quasi-classical trajectory (QCT) calculations, interesting functionals are identified. Quantum dynamics (QD) calculations are performed for the functionals giving the best description of reaction to compare with diffraction experiments.

In section 4.2 the methods used are explained, starting with the dynamical model and dynamics methods in section 4.2.1. The construction of PESs is discussed in section 4.2.2. Section 4.2.3 focuses on the calculation of observables. In section 4.2.4 the computational details are given. In section 4.3 the results of the calculations are shown and discussed, starting with an overview of the constructed PESs in section 4.3.1. Initial state-resolved reaction probabilities and rotational quadrupole alignment parameters are discussed in section 4.3.2 and simulations of molecular beam sticking experiments are discussed in section 4.3.3. Diffractive scattering and reaction at off-normal incidence are discussed in section 4.3.4. Finally, in section 4.4, the conclusions

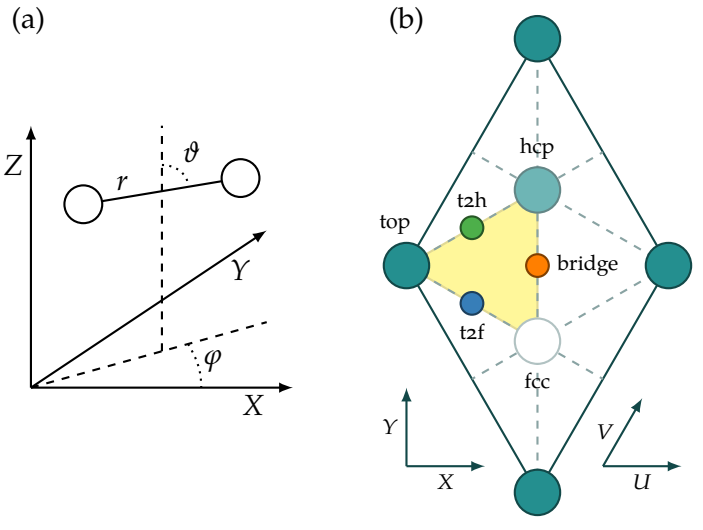


FIGURE 4.1 (a) The center of mass coordinate system used for the description of the $H_2$ molecule. (b) The surface unit cell and the sites considered. The origin of the coordinate system ($X$=$U$=0, $Y$=$V$=0, $Z$=0) is at a top layer atom (top site).



are given.

## 4.2 Theory

### 4.2.1 Dynamical model

Both quantum dynamics and quasi-classical dynamics calculations have been performed. For all calculations, the Born–Oppenheimer static surface (BOSS) model is used. In the BOSS model, two approximations are made. First of all, the Born–Oppenheimer approximation[34] is made. Second, a static surface approximation is made, in which the surface atoms are assumed to be fixed at their ideal lattice positions, and therefore, only the six degrees of freedom of the $H_2$ molecule are taken into account in the dynamics. The coordinate system used is shown in figure 4.1(a).

The use of these approximations for $H_2$/metal surface scattering is supported by previous work. For $H_2$ dissociation on Pt(111) it has pre-

viously been argued that non-adiabatic effects should not play an important role, for reasons that are generic to $H_2$/metal systems.[14] Non-adiabatic effects have been incorporated in calculations on $H_2$ dissociation on Cu(111),[35,36] Cu(110)[37] and Ru(0001),[33] using electronic friction. No large non-adiabatic effects were found in these dynamics calculations, suggesting that the Born–Oppenheimer approximation works well for these systems.

The validity of the static surface approximation has been tested recently for $H_2$ dissociation on Cu(111) using *ab initio* molecular dynamics (AIMD) calculations,[38] in which surface atoms in three layers of a $2 \times 2$ unit cell were allowed to move, and static corrugation model (SCM) calculations (chapter 3), which excluded energy exchange with the surface but included the displacement of surface atoms and surface expansion effects. In these studies, good agreement was found between static surface calculations and calculations at the experimental surface temperature ($T_s = 120\,K$). These calculations suggested thermal expansion of the surface to be important, which has been tested recently.[39]

For $H_2$ dissociation on Ru(0001), the neglect of surface temperature is not expected to have a big effect. The importance of energy exchange is not expected to be large. Due to the large mass mismatch between a $H_2$ molecule and a surface atom, motion of the $H_2$ molecule and the surface atoms should only be weakly coupled, *i.e.*, the effect of energy exchange should be small. The effect of the static displacement of surface atoms is also expected to be small. This is because $H_2$ dissociation on Ru(0001) is an early barrier system: the barriers are located far from the surface, therefore the coupling between the $H_2$ molecule located at the barrier and the closest surface atoms should be small. Finally, also thermal expansion is expected to be a rather small effect. Bulk ruthenium expands by about 0.24% in $a$ and 0.36% in $c$ from 0 K to 500 K.[40] The first interlayer spacing $d_{12}$ contracts slightly with increasing surface temperature.[41] It should be noted that the surface temperature used in the diffraction experiments ($T_s = 500\,K$[29]) is somewhat higher than the surface temperature used in the molecular beam experiments ($T_s = 180\,K$[30]), which suggests that if surface temperature does play a role it would do so predominantly in the diffraction experiments.

#### 4.2.1.1 Quantum and quasi-classical dynamics

For the quantum dynamics calculations a time-dependent wave packet (TDWP)[42,43] method was used. This method is described in section 2.4.

The QCT[44] method was also used, as described in section 2.3. At each computed point on a reaction probability curve, to get accurate results, at least $10^4$ trajectories were computed. The $H_2$ molecule was initially placed at $Z = 9$ Å. The molecule was considered to have dissociated when $r > 2.25$ Å.

### 4.2.2 Construction of potential energy surfaces

Full 6D PESs were constructed from self-consistent DFT calculations with various XC functionals. To construct a PES, a number of DFT calculations are performed. First, to obtain the lattice constants $a$ and $c$ to use for ruthenium, a bulk hexagonal close packed (HCP) unit cell containing two atoms was set up. This unit cell was relaxed, during which the size and shape of the unit cell was allowed to change. Second, to obtain the structure of the slab to use, a slab was set up with a structure resembling the bulk structure obtained in the first step, after which the positions of the atoms were allowed to relax in the direction perpendicular to the slab. Finally, to map out the molecule–surface interaction on various sites in the Ru(0001) surface unit cell, a $H_2$ molecule was added to the unit cell obtained in the second step, and a large number of single point calculations were carried out with the $H_2$ molecule in various geometries.



To interpolate the results from the single point calculations, the corrugation reducing procedure (CRP) was used,[45,46] as described in section 2.1.1. In the interpolation a 60° skewed coordinate system ($U$, $V$) is used (see also figure 4.1(b)). In the discussion below this ($U$, $V$) coordinate system is assumed to be scaled such that the closest surface atom–surface atom distance within a layer is unity.

For the interpolation of $I^{6D}$ a total of 29 configurations ($U$, $V$, $\vartheta$, $\varphi$) are used, spread over 6 different sites ($U$, $V$) (see also figure 4.1(b)). The used configurations have been listed in table 4.1. The interpolation is done in several steps, similar to the method used for $H_2$/Cu(100) by Olsen *et al.*[46] First, for every configuration, the interpolation over the $r$

**Table 4.1** Configurations used in the interpolation of $H_2$/Ru(0001) PES. The sites listed here correspond to the sites listed in table 4.2, and are also shown graphically in figure 4.1.

| Site | $\vartheta$ (°) | $\varphi$ (°) |
|---|---|---|
| Top | 0 | |
| Top | 90 | 0, 30 |
| t2h | 0 | |
| t2h | 45 | 30, 120, 210 |
| t2h | 90 | 30, 120 |
| HCP | 0 | |
| HCP | 45 | 30, 210 |
| HCP | 90 | 0, 30 |
| Bridge | 0 | |
| Bridge | 90 | 0, 60, 90 |
| FCC | 0 | |
| FCC | 45 | 150, 330 |
| FCC | 90 | 0, 330 |
| t2f | 0 | |
| t2f | 45 | 150, 240, 330 |
| t2f | 90 | 240, 330 |



and $Z$ degrees of freedom is performed. This interpolation is performed over a 14×15 ($r \times Z$) grid using a 2D cubic spline interpolation. Then, on every site, the interpolation is performed over the $\vartheta$ and $\varphi$ degrees of freedom using symmetry adapted sine and cosine functions. Finally, the interpolation over $U$ and $V$ is performed, again using symmetry adapted sine and cosine functions.

For the interpolation of $I^{3D}$ a total of 10 sites in ($u$, $v$) are used. The used configurations have been listed in table 4.2. The interpolation is performed in two steps. First, for every site, a 1D cubic spline interpolation over 57 points in $z$ is performed. Then the interpolation over the $u$ and $v$ degrees of freedom is performed, using symmetry adapted sine and cosine functions. For $V^{1D}$ the spline interpolation of the interaction of the H atom above the top site is used, similar to previous studies.[45]

**TABLE 4.2** Sites used in the interpolation of the H/Ru(0001) PES.

| Site | $u$ | $v$ |
|---|---|---|
| Top | 0 | 0 |
| Bridge | 1/2 | 0 |
| HCP | 1/3 | 1/3 |
| t2h | 1/6 | 1/6 |
| $\epsilon$ | 1/3 | 1/6 |
| $\tau$ | 1/6 | 0 |
| $\eta$ | 1/3 | 0 |
| t2f | 1/3 | -1/6 |
| $\epsilon'$ | 1/2 | -1/6 |
| FCC | 2/3 | -1/3 |

From $Z = 3.4$ Å to $Z = 4.0$ Å the PES is switched from the full $V^{6D}$ to a 2D gas phase interaction $V^{2D}$, as the dependence on the other degrees of freedom far away from the surface is small. This gas phase potential is given by

$$V^{2D}(r, Z) = V^{ext}(Z) + V^{gas}(r), \tag{4.2}$$

where $V^{ext}$ is a function describing the dependence of the PES on $Z$ beyond $Z = 4.0$ Å and $V^{gas}$ is the interaction at $Z = Z_{max}$. For the work described in this chapter these functions are represented by 1D cubic splines, with $Z_{max}$ taken to be 6 Å.

### 4.2.3 Calculation of observables

Initial state-resolved reaction probabilities, rotational quadrupole alignment parameters, molecular beam sticking probabilities and diffraction probabilities were computed as described in section 2.5. The parameters for the $H_2$ and $D_2$ beams of GROOT *et al.*[30] are shown in table 4.3. These parameters were obtained by fitting

$$G(t; T_n) = c_1 + c_2 {v_i}^4 \exp\left[-(v_i - v_0)^2/\alpha^2\right] \tag{4.3}$$

to the experimental time-of-flight (TOF) spectra.[47] It is noted here that the parameters describing the $H_2$ molecular beam differ somewhat from

**Table 4.3** Parameters used for the molecular beam simulations of $H_2$ and $D_2$ on Ru(0001). The parameters were obtained from fits of equation (4.3) to the experimental TOF spectra.[47]

| | $\langle E_i \rangle$ (eV) | $v_0$ (m/s) | $\alpha$ (m/s) | $T_{\text{nozzle}}$ (K) |
|---|---|---|---|---|
| $H_2$ | 0.061 | 2375.3 | 167.3 | 300 |
| | 0.075 | 2641.8 | 329.2 | 300 |
| | 0.129 | 3334.2 | 607.5 | 500 |
| | 0.182 | 3862.9 | 852.0 | 700 |
| | 0.232 | 4264.6 | 1088.9 | 900 |
| | 0.274 | 4564.2 | 1266.7 | 1100 |
| | 0.328 | 4907.6 | 1473.7 | 1300 |
| | 0.377 | 5154.2 | 1687.5 | 1500 |
| | 0.430 | 5391.6 | 1901.9 | 1700 |
| $D_2$ | 0.078 | 1932.3 | 193.6 | 300 |
| | 0.124 | 2372.5 | 295.1 | 500 |
| | 0.219 | 3090.8 | 527.4 | 900 |
| | 0.316 | 3625.4 | 765.6 | 1300 |
| | 0.363 | 3818.9 | 908.9 | 1700 |
| | 0.455 | 4051.2 | 1261.8 | 1700 |
| | 0.466 | 4268.9 | 1097.1 | 1700 |

the parameters presented earlier,[29] as an error was made in the analysis of the TOF measurements.[47]

### 4.2.4 Computational details

For the electronic structure calculations VASP[61–63] (version 5.2.12) was used. To allow the use of XC functionals not present in VASP, the LibXC[64] library (version 1.2.0) has been used.

Potential energy surfaces have been constructed for a wide range of XC functionals. The functionals used are listed in table 4.4. For the GGA functionals, except for the PBELDA and PBE$\alpha$LDA functionals, the standard[65] VASP ultrasoft pseudopotentials (USPPs)[66] were used. For all other functionals, projector augmented wave (PAW)[67] potentials[68] were used. The vdW-DF functionals were evaluated within the scheme of Román-Pérez and Soler.[69]

**Table 4.4** The XC functionals used in this work. Also shown are the lattice constants obtained for ruthenium (best matches shown in bold typeface).

| Name | Type | Exchange | Correlation | a (Å) | c (Å) |
|---|---|---|---|---|---|
| BLYP | GGA | Becke88[48] | LYP[49] | 2.775 | 4.363 |
| BP | GGA | Becke88[48] | Perdew86[50] | 2.735 | 4.308 |
| HTBS | GGA | HTBS[51] | PBE[52] | **2.706** | **4.268** |
| PBE$\alpha$ | GGA | PBE$\alpha$=0.5[53] | PBE[52] | 2.720 | 4.288 |
| PBE$\alpha$LDA | GGA | PBE$\alpha$=0.5[53] | LDA (PW[54]) | 2.778 | 4.369 |
| PBE$\alpha$LYP | GGA | PBE$\alpha$=0.5[53] | LYP[49] | 2.763 | 4.348 |
| PBE$\alpha$:RPBE(85:15)LYP | GGA | 0.85 PBE$\alpha$=0.5[53] + 0.15 RPBE[9] | LYP[49] | 2.767 | 4.353 |
| PBE | GGA | PBE[52] | PBE[52] | 2.730 | 4.304 |
| PBELDA | GGA | PBE[52] | LDA (PW[54]) | 2.790 | 4.387 |
| PBELYP | GGA | PBE[52] | LYP[49] | 2.775 | 4.365 |
| PBEP | GGA | PBE[52] | Perdew86[50] | 2.735 | 4.310 |
| PBE-vdW-DF | vdW-DF | PBE[52] | vdW-DF[55] | 2.751 | 4.336 |
| PBE-vdW-DF2 | vdW-DF | PBE[52] | vdW-DF2[56] | 2.754 | 4.341 |
| PBE:RPBE(50:50)-vdW-DF | vdW-DF | 0.5 PBE[52] + 0.5 RPBE[9] | vdW-DF[55] | 2.758 | 4.347 |
| PW91 | GGA | PW91[15] | PW91[15] | 2.732 | 4.305 |
| (revPBE-)vdW-DF | vdW-DF | revPBE[57] | vdW-DF[55] | 2.761 | 4.351 |
| revTPSS | meta-GGA | revTPSS[58] | revTPSS[58] | **2.690** | **4.246** |
| RPBE | GGA | RPBE[9] | PBE[52] | 2.744 | 4.325 |
| RPBELYP | GGA | RPBE[9] | LYP[49] | 2.790 | 4.388 |
| RPBE-vdW-DF | vdW-DF | RPBE[9] | vdW-DF[55] | 2.765 | 4.357 |
| RPBE-vdW-DF2 | vdW-DF | RPBE[9] | vdW-DF2[56] | 2.768 | 4.362 |
| (rPW86-)vdW-DF2 | vdW-DF | rPW86[56] | vdW-DF2[56] | 2.799 | 4.412 |
| WC | GGA | WC[59] | PBE[52] | **2.706** | **4.267** |
| Experiment (295 K)[60] | | | | 2.706 | 4.281 |
| Extrapolation (0 K)[40] | | | | 2.703 | 4.274 |

Tests were performed on the bulk system and the molecule–surface system to find a $k$-point sampling and plane wave cut-off yielding converged results. The convergence was found to be nearly independent of the XC functional, although for vdW-DF functionals the convergence was somewhat less good, but still good enough. For this reason, as well as consistency, the $k$-point sampling and plane wave cut-off were chosen to be equal for all functionals. For the bulk calculations, a $20 \times 20 \times 20$ Γ-centered Monkhorst–Pack[70] grid was used with a plane wave cut-off of 450 eV. For the slab calculations, a $20 \times 20 \times 1$ Γ-centered Monkhorst–Pack grid was used with the same plane wave cut-off. For the single point calculations to determine the molecule–surface interaction, a $8 \times 8 \times 1$ Γ-centered Monkhorst–Pack grid was used with a plane wave cut-off of 350 eV. A $2 \times 2$ supercell with a vacuum of 13 Å between images of the slab was used. For all calculations, to speed up convergence, Fermi smearing was used with a width of 0.1 eV. Finally, in all calculations a five-layer slab was considered. Convergence tests with respect to the number of layers for two geometries close to the transition state for the top($\vartheta = 90°$, $\varphi = 0°$) and hcp($\vartheta = 90°$, $\varphi = 30°$) configurations, showed that for a range of GGA functionals the difference between using a five- and seven-layer slab was on average about 5 meV for the top to bridge case and about 10 meV for the hcp case. This error was found to not depend much on the chosen XC functional.

For the quantum dynamics calculations on reaction at normal incidence, two wave packets with different energy ranges were propagated. The lower energy range was taken from 40 meV to 200 meV, the high energy range from 150 meV to 600 meV. For calculations on diffraction at off-normal incidence however, only the lower energy range was calculated. Convergence tests indicated that the same parameters could be used for all calculations. The parameters used are shown in table 4.5.

## 4.3 Results and discussion

### 4.3.1 Potential energy surfaces

It should be clear that with the large number of PESs considered here, a full analysis is beyond the scope of this chapter. It is nonetheless import-

**Table 4.5** Parameters for quantum dynamics calculations on $H_2$ dissociation and scattering from Ru(0001). Values for odd values of $J$, where different, are listed in parentheses. All values are in atomic units.

| Parameter | Description | Value |
|---|---|---|
| $N_X = N_Y$ | Number of grid points in $X$ and $Y$ | 18 |
| $J_{\max}$ | Maximum $J$ in basis set | 16(17) |
| $m_{J,\max}$ | Maximum $m_J$ in basis set | 16(17) |
| $r_{\min}$ | Start of grid in $r$ | 0.4 |
| $\Delta r$ | Spacing of grid in $r$ | 0.25 |
| $N_r$ | Number of grid points in $r$ | 32 |
| $Z_{\min}$ | Start of grid in $Z$ | -1.0 |
| $\Delta Z$ | Spacing of grid in $Z$ | 0.135 |
| $N_Z$ | Number of grid points in $Z$ | 128 |
| $N_{Z,\mathrm{sp}}$ | Number of grid points in specular $Z$ | 256 |
| $\Delta t$ | Propagation time step | 5.0 |
| $\Delta t_{\mathrm{ana}}$ | Analysis time step | 40.0 |
| $Z_0$ | Center of initial wave packet | 16.955 |
| $Z_\infty$ | Location of analysis line | 12.5 |
| $A_2^Z$ | Optical potential strength in $Z$ | 0.002 |
| $Z_{\min}^{\mathrm{opt}}$ | Start optical potential in $Z$ | 12.5 |
| $Z_{\max}^{\mathrm{opt}}$ | End optical potential in $Z$ | 16.145 |
| $A_2^{Z,\mathrm{sp}}$ | Optical potential strength in $Z_{\mathrm{sp}}$ | 0.0035 |
| $Z_{\mathrm{sp,min}}^{\mathrm{opt}}$ | Start optical potential in $Z_{\mathrm{sp}}$ | 22.355 |
| $Z_{\mathrm{sp,max}}^{\mathrm{opt}}$ | End optical potential in $Z_{\mathrm{sp}}$ | 33.425 |
| $A_2^r$ | Optical potential strength in $r$ | 0.008 |
| $r_{\min}^{\mathrm{opt}}$ | Start optical potential in $r$ | 4.15 |
| $r_{\max}^{\mathrm{opt}}$ | End optical potential in $r$ | 8.15 |

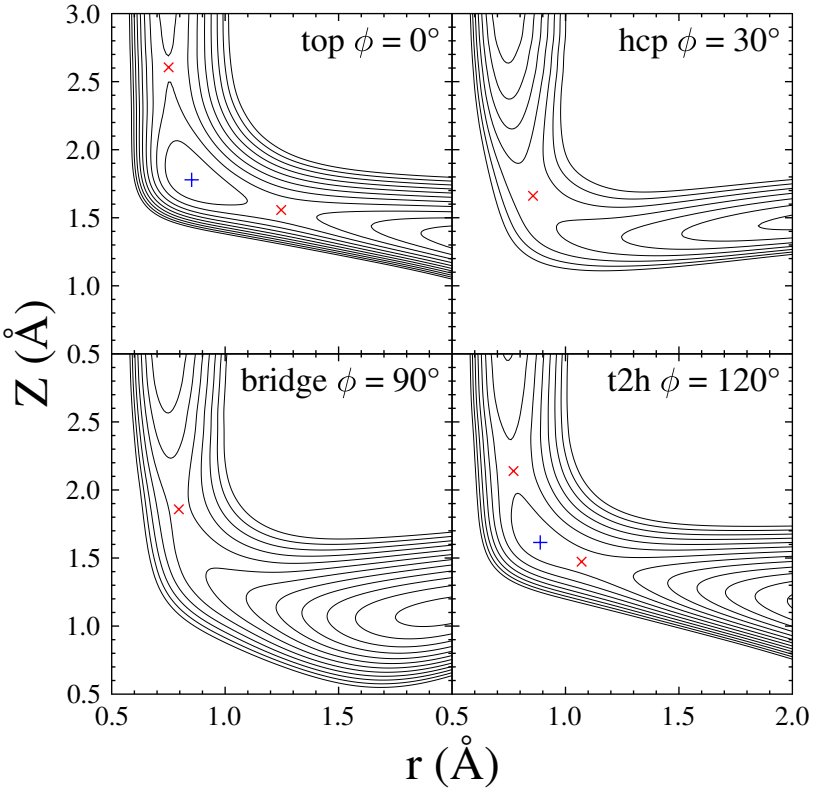


**Figure 4.2** Contour plots of the $H_2$ on Ru(0001) PES for four high symmetry configurations with $\vartheta = 90°$, for the PBE-vdW-DF2 functional. Transition states are indicated by (red) crosses while local minima in the potential are indicated by (blue) plus symbols. The spacing between contour lines is 0.1 eV.

ant, however, to highlight several features of the created PESs, thereby extending the previous analysis by Luppi *et al.*[27]

Contour plots of all 2D cuts that were used for the construction of the PES were made and the transition states on these contour plots were identified. In figure 4.2, contour plots of several high symmetry configurations are shown, from one of the PESs which was found to give the best description of the molecular beam experiments (see also section 4.3.3). Consistent with previous calculations,[27] the barrier height increases in the order top < t2h/t2f < bridge < hcp/fcc. In most cases,

**Table 4.6** Barrier geometries and barrier heights, relative to the gas phase minimum, for the four geometries depicted in figure 4.2. Where available, both barriers have been indicated. With MIX-vdW-DF the PBE:RPBE(50:50)-vdW-DF functional is meant.

| Parameter | top 1 | top 2 | t2h 1 | t2h 2 | bri | hcp |
|---|---|---|---|---|---|---|
| $\varphi$ | 0° | 0° | 120° | 120° | 90° | 30° |
| $Z_b^{\text{PBE-vdW-DF2}}$ (Å) | 2.605 | 1.557 | 2.139 | 1.473 | 1.858 | 1.661 |
| $Z_b^{\text{MIX-vdW-DF}}$ (Å) | 2.605 | 1.559 | 2.122 | 1.474 | 1.830 | 1.646 |
| $Z_b^{\text{PBE}}$ (Å) | 2.736 | 1.544 | 2.350 | - | 2.069 | 1.926 |
| $r_b^{\text{PBE-vdW-DF2}}$ (Å) | 0.751 | 1.247 | 0.771 | 1.071 | 0.796 | 0.857 |
| $r_b^{\text{MIX-vdW-DF}}$ (Å) | 0.751 | 1.249 | 0.771 | 1.072 | 0.799 | 0.861 |
| $r_b^{\text{PBE}}$ (Å) | 0.757 | 1.251 | 0.767 | - | 0.785 | 0.805 |
| $E_b^{\text{PBE-vdW-DF2}}$ (eV) | 0.004 | -0.073 | 0.115 | 0.061 | 0.276 | 0.432 |
| $E_b^{\text{MIX-vdW-DF}}$ (eV) | 0.004 | -0.044 | 0.125 | 0.096 | 0.295 | 0.459 |
| $E_b^{\text{PBE}}$ (eV) | 0.022 | -0.366 | 0.092 | - | 0.198 | 0.304 |



except for the rPW86-vdW-DF2 functional, the hcp barrier was found to be slightly higher (by up to 46 meV for the revTPSS functional) than the fcc barrier. It should be emphasized that most of the trends seen in figure 4.2 are qualitatively reproduced by most functionals, but quantitatively (large) differences can be found.

A notable feature of the $H_2$ on Ru(0001) PES is the presence of two barriers on several 2D cuts. On the top site two barriers are found with a well in between. This feature is general for all functionals. This is also, for several functionals, found to be the case for the t2h($\vartheta = 90°$, $\varphi = 120°$) and t2f($\vartheta = 90°$, $\varphi = 240°$) configurations. Differences were found with respect to the relative energy of the early and late barriers present in 2D cuts above the top site. For most XC functionals, the early barrier was found to be highest, but for several others the late barrier was found to be highest. The difference between the two barrier heights ($E_b^{\text{top,late}} - E_b^{\text{top,early}}$) was found to vary between −0.64 eV for the WC functional to 0.14 eV for the rPW86-vdW-DF2 functional. These results suggest that care should be taken with the choice of an XC functional, as this could have a drastic influence on the dynamics. Barrier geometries and

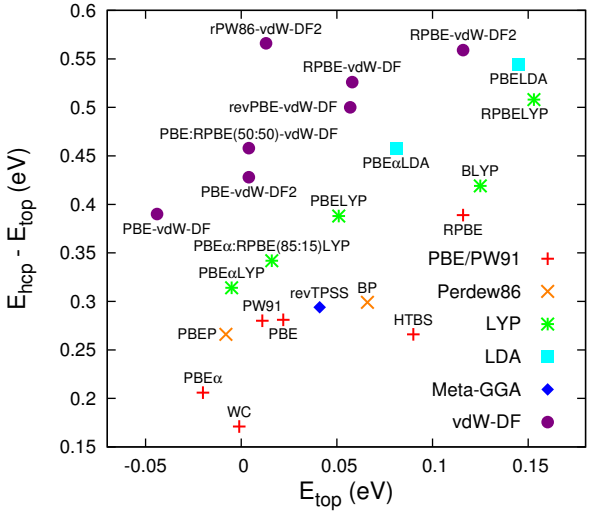


**Figure 4.3** Energetic corrugation of the potential versus lowest barrier height for the constructed PESs. The functionals are grouped (symbols) by correlation functional.

heights for the geometries depicted in figure 4.2 are given in table 4.6, for the PBE-vdW-DF2, PBE:RPBE(50:50)-vdW-DF and PBE functionals. These two vdW-DF functionals, included because they yield the best description of the molecular beam experiments (see section 4.3.3), yield similar barrier geometries and heights, and in all cases barriers are obtained which are closer to the surface than obtained with the reference PBE functional.

The energetic corrugation has also been considered. The energetic corrugation is defined here as the difference between the hcp($\vartheta = 90°$, $\varphi = 30°$) barrier height and the top($\vartheta = 90°$, $\varphi = 0°$) barrier height. The energetic corrugation of a PES is a useful quantity as it is typically found to correspond to the "width" of the reaction probability curve for activated dissociation systems.[71] By the width, one usually means the range of energies over which the reaction probability increases more or less linearly from an onset energy that is close to the reaction threshold to an energy at which the reaction probability starts to plateau. As such, the width of the reaction probability curve is inversely related to the slope of the reaction probability over this energy region, and the slope

of the curve is therefore also related to the energetic corrugation of the PES. In this chapter, the width of the reaction probability curve is rather loosely defined in this way. In some cases reaction probability curves may be fitted rather well with sigmoidal functions like

$$S(E_{\text{trans}}) = \frac{A}{2}\left[1 + \text{erf}\left(\frac{E_{\text{trans}} - E_0}{W}\right)\right], \tag{4.4}$$

as used for instance in references 72 and 73, and in such cases the width has a well-defined meaning and is given by the value of a specific parameter of the fit function ($W$ in the example given, furthermore $A$ is the maximum value of the reaction probability, and $E_0$ the energy at which the reaction probability becomes half its maximum value).

For facilitating a comparison of the energetic corrugation among various functionals, in all cases the height of the early barrier on the top site was used, even if the late barrier was higher in energy than the early barrier. LUPPI *et al.* previously noted that the PW91 and RPBE functionals showed a large difference in the energetic corrugation.[27] Figure 4.3, in which the energetic corrugation is plotted against the top to bridge barrier height, shows that the results obtained here support this. A number of features should be pointed out. No very clear overall correlation is found between the lowest barrier height and energetic corrugation of the potential. Functionals with LYP or LDA correlation however show a higher energetic corrugation than the functionals with PBE or Perdew86 correlation, while functionals using vdW-DF or vdW-DF2 correlation show an even higher energetic corrugation. For the functionals considered here, it seems that the energetic corrugation is higher for the functionals which yield a higher top($\vartheta = 90°$, $\varphi = 0°$) barrier height. The functionals within a correlation group (*i.e.*, a group of functionals with the same correlation, as indicated in figure 4.3 by the use of one specific symbol), show a somewhat stronger correlation between the top($\vartheta = 90°$, $\varphi = 0°$) barrier height and the energetic corrugation, in the sense that functionals with a higher top to bridge barrier height mostly give a larger energetic corrugation. Such a trend is especially apparent for functionals incorporating a "PBE-like" exchange functional, namely the exchange functional sequence PBE$\alpha$ → PBE → RPBE, but less so for other exchange functionals such as rPW86 or HTBS.

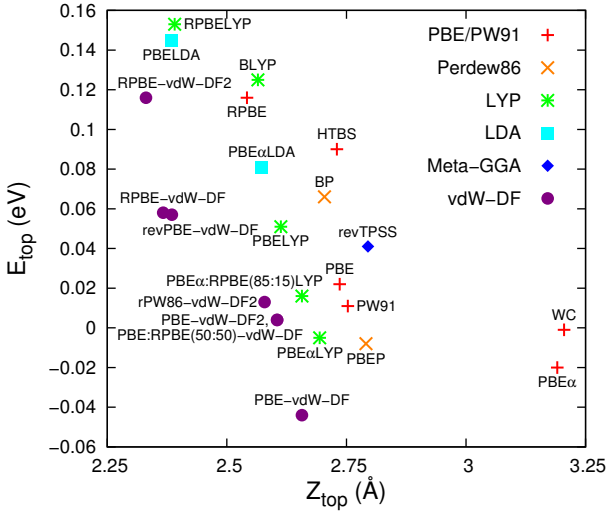


**Figure 4.4** Height of the top to bridge barrier versus position of the top to bridge barrier for the constructed PESs. The functionals are grouped (symbols) by correlation functional.

It is not fully understood at present why there is an almost linear correlation between the energetic corrugation and the minimum barrier height for functionals with PBE-like exchange within correlation groups. It is also not completely clear why for $H_2$ on Ru(0001) the energetic corrugation varies so strongly with the minimum barrier height. It should, however, be pointed out that this could be related to the rather large difference in distance to the surface ($Z$) of the top($\vartheta = 90°$, $\varphi = 0°$) and hcp($\vartheta = 90°$, $\varphi = 30°$) barrier (also referred to as geometric corrugation[27]): the top($\vartheta = 90°$, $\varphi = 0°$) barrier is much further away from the surface than the hcp($\vartheta = 90°$, $\varphi = 30°$) barrier (see table 4.6). For the $H_2$ on Cu(111) system, the geometric corrugation is smaller (all barriers are late and their positions fall between $Z = 2.2 - 2.6\,a_0$), and for this system no large differences in energetic corrugation between PW91 and RPBE were found, while larger differences were found between PW91 and RPBE barrier heights.[16,17]

In figure 4.4 the height of the top to bridge barrier has been plotted against the distance of the same barrier to the surface. There is no

clear correlation between the position and height of the barrier. Similar correlations as in figure 4.3 can however be found within a correlation group, although these correlations are less clear here. Barriers obtained with vdW-DF functionals are usually closest to the surface, while functionals with PBE or Perdew86 correlation are usually furthest from the surface. The top to bridge barrier can therefore shift by about 0.4 Å with the choice of the XC functional in $Z$ for a particular top to bridge barrier height. This rather large shift can have dramatic effects on the anisotropy or corrugation of the potential barrier which is experienced by the $H_2$ molecule. For the functionals considered here, it seems that the barriers are higher the closer they are to the surface, but it should be noted that this correlation is rather weak.

The lattice constants for ruthenium obtained with various functionals were compared to experiment.[60] Because no experimental data is available for low temperatures, also a comparison is made to an extrapolation of experimental data to 0 K.[40] The computed values for the lattice constants are shown in table 4.4. It is clear that most functionals overestimate the lattice constant. Of all the functionals which were tested only the revTPSS, WC and HTBS functionals yield a lattice constant in reasonable agreement with experiment. This is not surprising because the WC functional is a functional created for describing solids,[59] and the HTBS and revTPSS functionals are functionals created to yield a good description of both solids and molecules[51,58] at the GGA and meta-GGA level, respectively.

Finally, in figure 4.5 the height of the top to bridge barrier and the energetic corrugation have been plotted against the lattice constant $a$. There is, as shown in the bottom panel, a rather clear overall correlation between the energetic corrugation and the lattice constant, in the sense that functionals giving a higher energetic corrugation also predict a larger lattice constant. In spite of this clear trend, there is still some variation. In particular the LYP and LDA functionals considered here, as well as the rPW86-vdW-DF2 functional, yield a relatively low energetic corrugation for the obtained lattice constant. The HTBS and revTPSS functionals yield a relatively high energetic corrugation (similar to the PBE value) for the lattice constants obtained with these functionals. As shown in the top panel of figure 4.5, there seems to be no clear

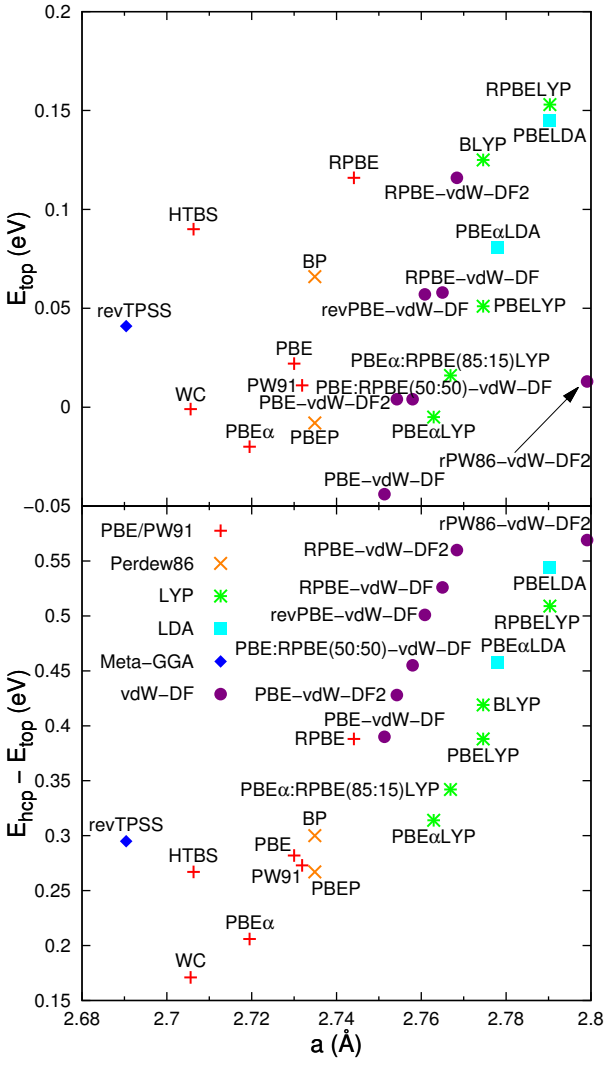


**Figure 4.5** Height of the top to bridge barrier (top panel) and energetic corrugation (bottom panel) versus lattice constant for the constructed potential energy surfaces. The functionals are grouped (symbols) by correlation functional.

overall correlation between the minimum (top to bridge) barrier height and the lattice constant, although a clearer and near-linear correlation is present for functionals containing PBE-like exchange and belonging to the same correlation group, as in figures 4.3 and 4.4. In fact, this is not so surprising, as a similar correlation has been observed before between the CO adsorption energy on specific metal surfaces and the metal surface energy computed with GGAs[74,75] (interestingly, similar to what is found here, the revTPSS meta-GGA result fell away from the line correlating the CO adsorption energy and the surface energy[75]). A correlation would then be expected also between barrier heights and lattice constants because adsorption energies and reaction barrier heights are correlated (as described by the so-called Brønsted–Evans–Polanyi relations[76,77]), while the metal surface energy and the lattice constant of the metal are both functions of the cohesive strength of the metal.

### 4.3.2 Initial state-resolved reaction and rotational quadrupole alignment



In figure 4.6 the initial state-resolved (degeneracy averaged) reaction probability $P_{\mathrm{deg}}(E_{\mathrm{trans}}; \nu, J)$ for $H_2$ dissociating on Ru(0001) obtained from QCT calculations is compared to QD calculations for the PBE-vdW-DF2 and PBE:RPBE(50:50)-vdW-DF functionals. At the lowest energies some small oscillations are present in the QD results. In spite of this, the agreement between QCT and QD is found to be excellent, in particular for the higher rotational states. This good agreement makes it possible to use QCT instead of QD results for the simulation of molecular beam sticking.

In figure 4.7 the degeneracy averaged reaction probability for $H_2$ dissociating on Ru(0001) obtained from QCT is compared for various initial rovibrational states for the PBE and PBE-vdW-DF2 functionals. It is clear that the PBE-vdW-DF2 functional gives rise to less steep reaction probability curves than the PBE functional. This can be understood from the increased energetic corrugation (see figure 4.3) of the PES. Furthermore, the ordering of the curves is different. With the PBE-vdW-DF2 functional first reaction decreases with increasing $J$ up to about $J = 5$, after which reaction increases again with increasing $J$. With the

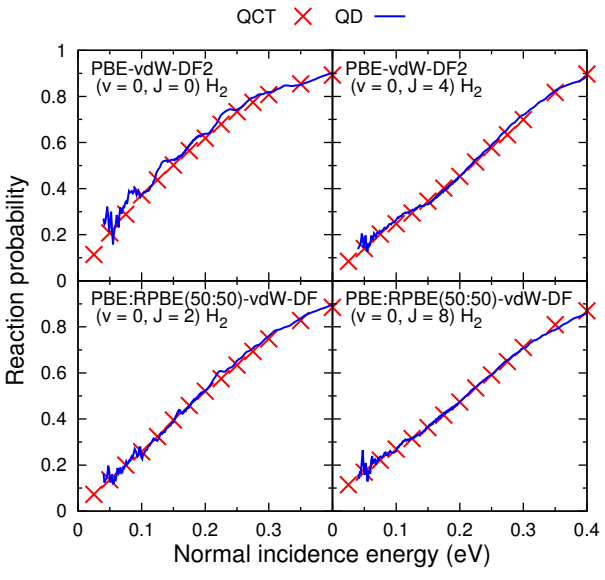


**Figure 4.6** Comparison between the initial state-resolved reaction probability calculated with quantum dynamics and quasi-classical trajectory calculations.

PBE functional, reaction first slightly increases with $J$ up to $J = 2$, then slightly decreases with $J$ up to $J = 5$, and then increases further with increasing $J$. This shows that the PBE and PBE-vdW-DF2 functional clearly have a different anisotropy, as the anisotropy of the potential determines the rotational dependence of reaction. The precise feature of the PES responsible for this difference is however not clear and is considered beyond the scope of this chapter. Because the PBE-vdW-DF2 functional gives barriers which are closer to the surface than the PBE functional however, a larger anisotropy is expected for the PBE-vdW-DF2 functional, which is also found in the PESs (see table 4.6). The PBE functional gives smaller rotational effects than the PBE-vdW-DF2 functional, consistent with the differences in anisotropy.

It should be noted that for $H_2$ and $D_2$ dissociation on Cu(111) experimental studies[72,78,79] showed a behaviour similar to the one here observed with the PBE-vdW-DF2 functional, in the sense that reaction at first decreases with $J$, after which it increases with $J$. This trend could not be reproduced in recent calculations[16,17] in which the PW91 and

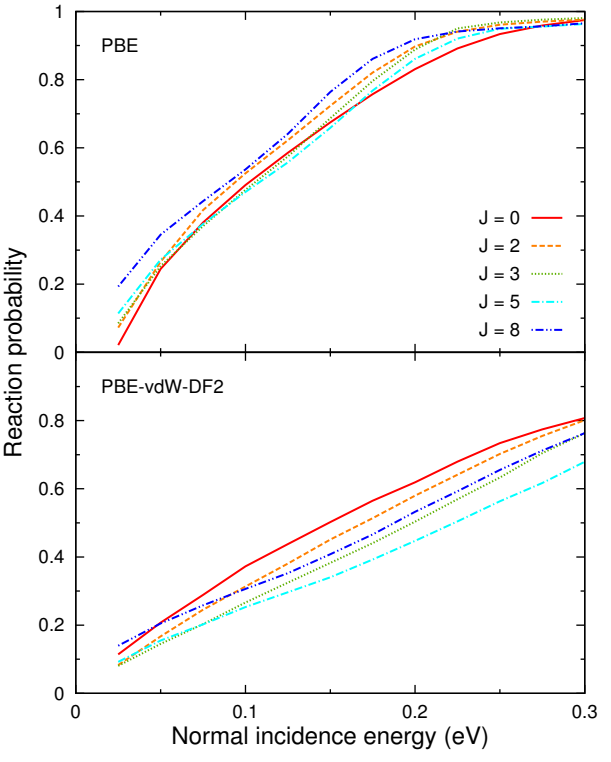




**Figure 4.7** The degeneracy averaged reaction probability for the PBE and PBE-vdW-DF2 functionals for several rotational states in the vibrational ground state. The probabilities were computed with the quasi-classical trajectory method.

RPBE functionals were used. In these calculations, a behaviour similar to the one here observed with the PBE functional was found. This therefore suggests that the use of vdW-DF functionals on $H_2$ or $D_2$ dissociation on Cu(111) could lead to an improved description of that system, as will be discussed further in chapter 6.

The differences in anisotropy between the PBE and PBE-vdW-DF2 functionals are emphasized even more when the orientational dependence of reaction is considered. In figure 4.8 the rotational quadrupole alignment parameter computed with QCT is shown for the same two functionals. Several differences are found between the two functionals. For a specific $J$ state, the rotational quadrupole alignment parameter for

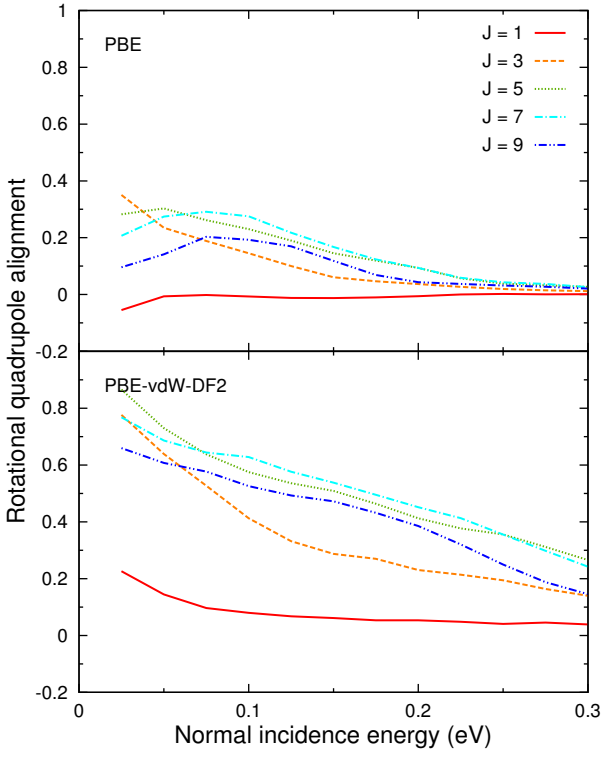


**Figure 4.8** The rotational quadrupole alignment parameter, computed with the quasi-classical trajectory method, for the PBE and PBE-vdW-DF2 functionals for several rotational states in the vibrational ground state.

the PBE functional is generally lower than for the PBE-vdW-DF2 functional. On the investigated interval, the rotational quadrupole alignment parameter reaches a maximum value of about 0.4 for the PBE functional, while the PBE-vdW-DF2 functional reaches a maximum value of about 0.9. This rather large difference can be understood if the positions of the barriers are considered. For example, on the hcp site, the barrier computed with the PBE functional is at $Z_b = 1.93$ Å, while the barrier computed with the PBE-vdW-DF2 functional is at $Z_b = 1.66$ Å (see also table 4.6). This leads to a higher anisotropy on the barrier for the PBE-vdW-DF2 functional, which in turn leads to a higher rotational quadrupole alignment parameter, because the higher anisotropy leads to an increased preference for reaction of helicoptering molecules.

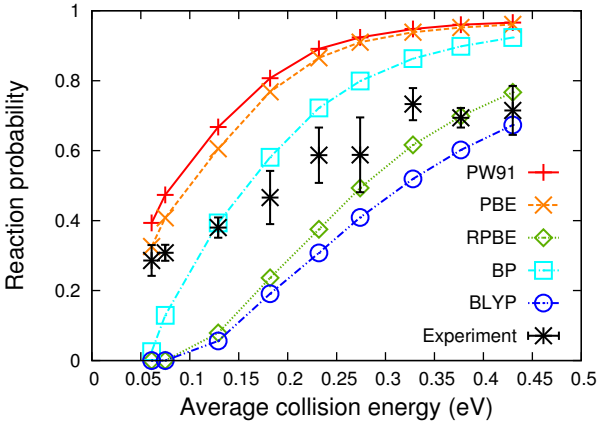


FIGURE 4.9 Reaction probability for molecular beams of $H_2$ dissociating on Ru(0001) computed with various standard functionals, compared to experiment.[30]

### 4.3.3 Molecular beam sticking

In figure 4.9 the molecular beam simulations for $H_2$ dissociating on Ru(0001) are shown for several commonly used XC functionals. It is clear that, similar to previous results by NIETO *et al.*,[29] the computed reaction probability curves are narrower than the experimental curve. For the width, the best agreement with experiment is found for the RPBE and BLYP functionals, but both of these underestimate the reaction probability for the lowest collision energies considerably. The PESs obtained from these functionals therefore have too high minimum barriers. The PW91 and PBE reaction probability curves are quite similar, which is not surprising as the PBE functional is overall quite similar[52] to PW91. It should be clear that the reaction probability follows the trends shown in figure 4.3 for the energetic corrugation and lowest barrier height at least qualitatively.

In figure 4.10 the molecular beam simulations for $H_2$ dissociating on Ru(0001) are shown for the revTPSS and HTBS functionals, with a comparison to results obtained with related functionals. The HTBS functional yields a reaction probability curve which is in between the reaction probability curves obtained with the WC and RPBE functionals. The reaction probability obtained with the HTBS PES at low energies is

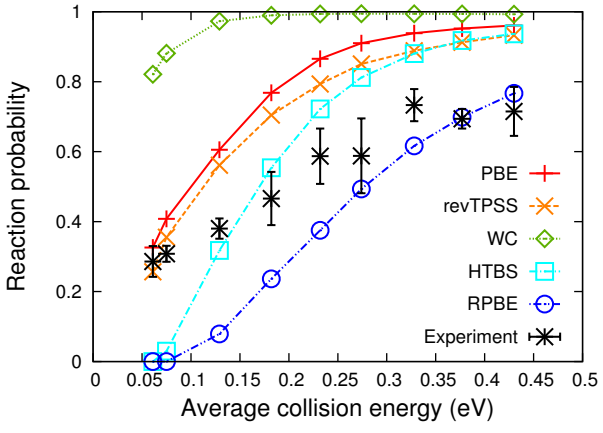


**Figure 4.10** Reaction probability for molecular beams of $H_2$ dissociating on Ru(0001) computed with the revTPSS and HTBS functionals. For comparison, the PBE, WC and RPBE molecular beam reaction probabilities are plotted, as well as experimental results.[30]

underestimated, while it is overestimated at high energies. The width of the HTBS reaction probability curve seems to be equal to or even slightly smaller than the width of the PBE reaction probability curve. The revTPSS functional yields reaction probabilities which are slightly lower than PBE and are therefore in better overall agreement with the experiments. The width of the reaction probability curve is however not much changed and can in this sense not explain the experimental dependence of the reaction probability on the incidence energy. It is difficult to say much of general validity about the importance of the meta-GGA approximation for molecule–surface reactions, as only a single meta-GGA functional is tested here for a single system. For the system considered here, however, the strength of the meta-GGA approximation seems to lie in the better simultaneous description of the surface, as evidenced by a better lattice constant (see table 4.4), and the molecule–surface interaction, as evidenced by the reaction probabilities computed with the PBE and revTPSS functionals being similar. The better simultaneous description of the molecule and the surface is in agreement with previous results obtained with the revTPSS functional,[75] and is consistent with construction principles used in the development of this functional

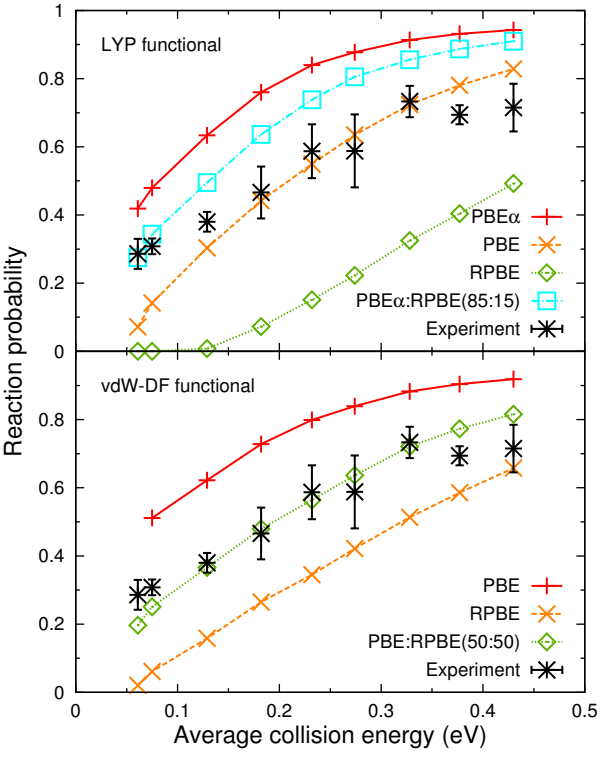


**FIGURE 4.11** Reaction probability for moleculars beams of $H_2$ and $D_2$ dissociating on Ru(0001) computed with various functionals containing LYP and vdW-DF correlation, compared with experimental results.[30] In the legend, only the name of the exchange functional is given.

(better simultaneous description of molecules and solids).[58] The finding that the revTPSS functional yields similar values of the minimum barrier height and the energetic corrugation for $H_2$ on Ru(0001) but yield a different and somewhat better value of the Ru lattice constant suggests that meta-GGA functionals could be devised that give a systematically better simultaneous description of surface reactivity and the metal lattice. This could be relevant to being able to simulate reactive scattering processes in a specific system over a large range of surface temperatures.[80]

The relatively high energetic corrugation of the LYP- and vdW-DF-based functionals suggests that if suitable exchange functionals are

chosen, they could be used for a mixing procedure similar to the one previously applied for $H_2$ on Cu(111).[16,17] The results of such a mixing procedure, in which only the exchange functional is mixed and the correlation functional kept fixed, are shown in figure 4.11. For the LYP functionals, it is found that PBE$\alpha$LYP (with $\alpha = 0.5$) and RPBELYP could form a pair for the mixing procedure, in the sense that one functional consistently overestimates the reaction probability and the other consistently underestimates. The PBELYP functional already provides a reasonable description at higher energies, but underestimates the reaction probability at the lowest energies. A 85:15 mixture of the PBE$\alpha$ and RPBE functionals gives a good agreement for the lowest energies. For the vdW-DF functionals, the PBE-vdW-DF and RPBE-vdW-DF functionals could also form such a pair (see bottom panel of figure 4.11). A 50:50 mixture of the PBE and RPBE functionals gives a good agreement over the whole energy range. For the vdW-DF2 functional, it was found that no mixing procedure was needed, as is shown in figure 4.12.

In figure 4.12 the molecular beam simulations for $H_2$ and $D_2$ dissociating on Ru(0001) are shown for the PBE-vdW-DF2, PBE:RPBE(50:50)-vdW-DF and PBE$\alpha$:RPBE(85:15)LYP functionals. The PBE-vdW-DF2 reaction probability is at all points slightly higher than the PBE:RPBE-(50:50)-vdW-DF reaction probability, even though the minimum barrier heights are almost the same for these functionals. The PBE$\alpha$:RPBE-(85:15)LYP functional gives a reaction probability curve which is slightly more reactive and narrower. The agreement with experiment is good for both vdW-DF functionals, except perhaps at the highest two energies. It should however be pointed out that a somewhat oscillatory behaviour is present in the experimental data at the highest points, which is not reproduced by theory. Overall, the agreement with experiment is quite good for the two vdW-DF functionals. This suggests that these functionals can be considered candidate SRP functionals.

### 4.3.4 Scattering and reaction at off-normal incidence

In figure 4.13 the reaction probability of cold $n$-$H_2$ ($25\%\, J = 0, 75\%\, J = 1$) computed with quantum dynamics is plotted against normal incidence energy for normal and off-normal incidence, for the PBE-vdW-DF2 func-

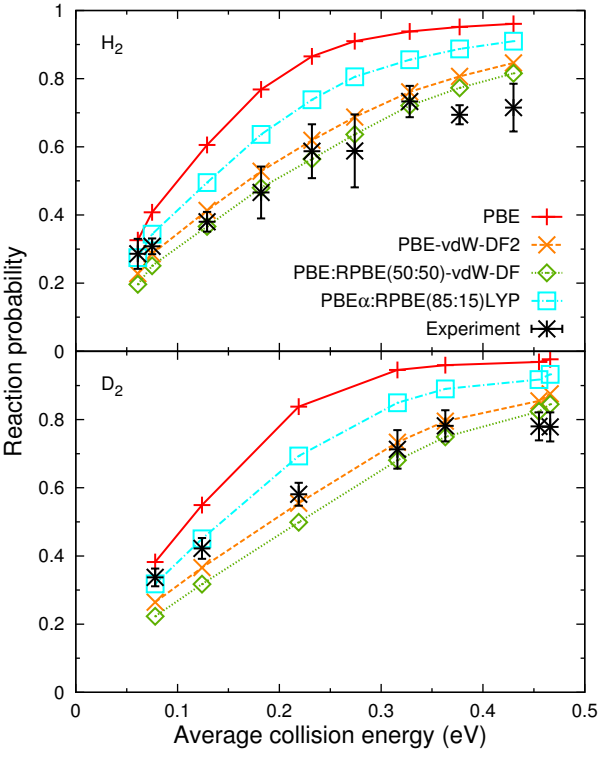


**FIGURE 4.12** Reaction probability for molecular beams for $H_2$ and $D_2$ dissociating on Ru(0001) computed with the PBE-vdW-DF2 functional and the two mixed functionals of figure 4.11, compared with experimental results.[30] For comparison, the PBE molecular beam reaction probability has been plotted.

tional. It should be noted that normal energy scaling does not seem to be completely obeyed. Molecular beam experiments however suggested that normal energy scaling is obeyed.[30] The effect of parallel incidence energy is, at the energies considered, a decrease of the reaction probability, consistent with previous calculations on $H_2$ dissociation on Pt(111)[43] and model potentials.[81] It should furthermore be noted that small oscillations occur in the curve at low energies, suggesting that the hydrogen molecule can be temporarily trapped in one of the wells present in the PES. These oscillations were not present in previous PW91 results.[29]

In figure 4.14 probabilities for various scattering processes computed with quantum dynamics are shown for cold $n$-$H_2$ scattering

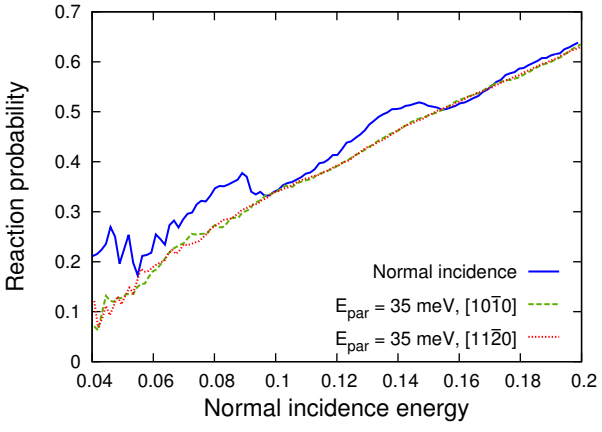


**Figure 4.13** Reaction probability for $n$-$H_2$ reacting on Ru(0001), shown as a function of normal incidence energy, computed with the PBE-vdW-DF2 functional for various incidence conditions.

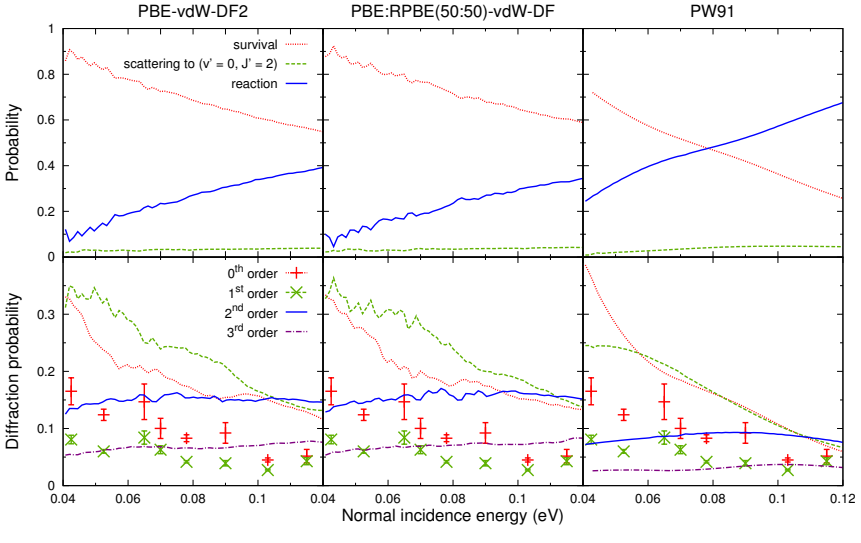


**Figure 4.14** Various scattering probabilities for $n$-$H_2$ scattering from Ru(0001) with an initial parallel energy of 35 meV in the [11$\bar{2}$0] incidence direction computed with the PBE-vdW-DF2 and PBE:RPBE(50:50)-vdW-DF XC functionals. Theoretical results: lines, experimental results:[29] symbols. Top panels: rovibrationally elastic scattering (survival), rotational excitation ($v' = 0$, $J' = 2$) and reaction. Bottom panels: per-order diffraction probabilities for rovibrationally elastic scattering. For comparison, previous PW91 results[29] are also shown.

from Ru(0001) with an initial parallel energy of 35 meV in the $[11\bar{2}0]$ incidence direction. The reaction probability computed with the PBE-vdW-DF2 and PBE:RPBE(50:50)-vdW-DF functionals is lower than the reaction probability previously obtained with the PW91 functional over the entire range of incidence energies considered. Rotational excitation into ($\nu' = 0$, $J' = 2$) for the vdW-DF functionals has a probability similar to the one previously obtained with the PW91 functional, and is the dominant rovibrational excitation channel. Vibrational excitation is not an open channel at the energies considered here. The probability for survival in ($\nu' = 0$, $J' = 0$) or ($\nu' = 0$, $J' = 1$) is higher with the PBE-vdW-DF2 and PBE:RPBE(50:50)-vdW-DF functionals than those previously obtained with the PW91 functional.

The total per-order diffraction probabilities obtained with the PBE-vdW-DF2 and PBE:RPBE(50:50)-vdW-DF functionals are generally higher than those obtained with PW91. The shape of the per-order diffraction probability curves is however almost the same for the different functionals considered. The second and third order diffraction probabilities do not change much over the considered energy range, while the zeroth and first order diffraction probability curves in all cases decrease with increasing incidence energy. For the vdW-DF based functionals, the total first order diffraction probability is higher than the zeroth order diffraction probability, whereas they are almost the same for the PW91 functional, except at the lowest energies. The PW91 functional is the only functional reproducing the experimental trend that zeroth order diffraction is more probable than first order diffraction, but only at the lowest energies. All functionals predict a reasonable amount of second and third order diffraction, in disagreement with experiments (in experiments, second order diffraction channels were found to be an order of magnitude lower in intensity than first order diffraction channels[29]). For the $[10\bar{1}0]$ incidence direction similar results were obtained.

In figure 4.15 diffraction probabilities for rovibrationally elastic scattering of cold $n$-$H_2$ computed with quantum dynamics are shown for the PBE:RPBE(50:50)-vdW-DF and PBE-vdW-DF2 functionals, and compared to experiments and previous results[29] obtained with the PW91 functional. The two vdW-DF functionals considered here, PBE-vdW-

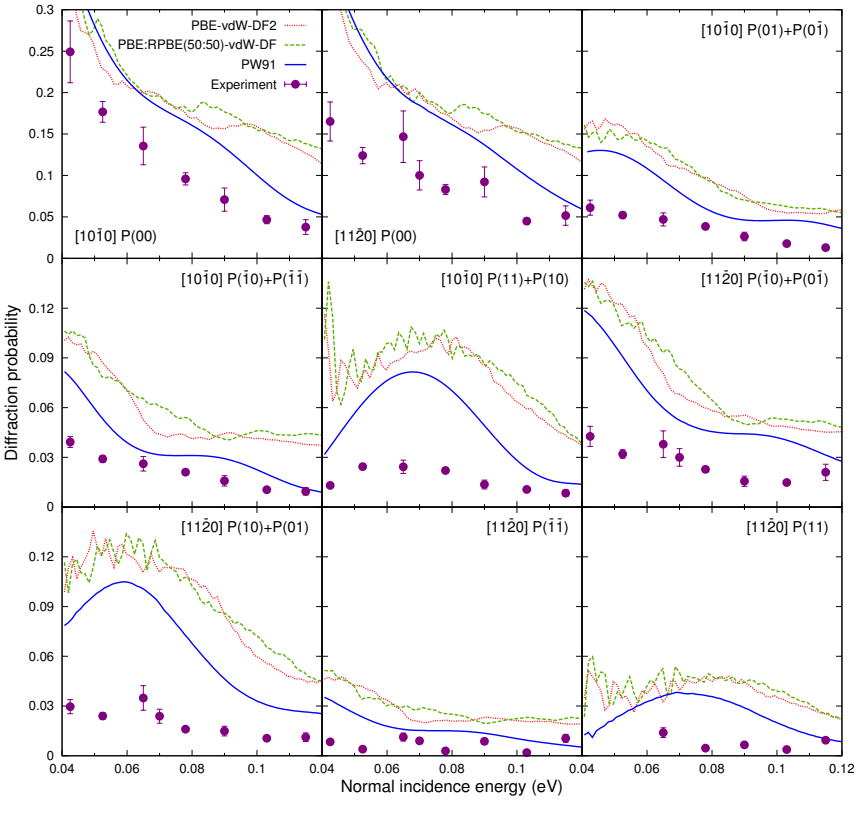


**Figure 4.15** Diffraction probabilities for $n$-$H_2$ scattering from Ru(0001) with an initial parallel energy of 35 eV in the [10$\bar{1}$0] or [11$\bar{2}$0] incidence directions computed with the PBE-vdW-DF2 and PBE:RPBE(50:50)-vdW-DF XC functionals. For comparison, experimental results[29] and previous PW91 results[29] are also shown.

DF2 and PBE:RPBE(50:50)-vdW-DF, give results in good agreement with each other. Furthermore, the order of the curves is mostly in agreement with the previous PW91 calculations. The diffraction probability at higher energies is however somewhat higher than obtained with the PW91 calculations, especially at higher incidence energies. The results from the vdW-DF functionals overestimate the experimental diffraction probability by at most about a factor 2 for zeroth order diffraction and by around a factor 3 for first order diffraction.

The agreement with the diffraction experiments is clearly not as good as the agreement obtained for the reaction probability in section 4.3.3. The computed diffraction probabilities are too high compared to the experiments, in particular for first order diffraction. There are several possible explanations for this and these will be discussed below.

First, the effects of surface temperature should be considered. For the reaction probability, no large surface temperature effects are expected. This has several reasons. The surface temperature used in the experiments, $T_s = 180\,K$,[30] is rather low. In AIMD calculations[38] and SCM calculations (chapter 3), almost no effects were found for $H_2$ dissociating on Cu(111) at a surface temperature $T_s = 120\,K$. While the surface temperature for the molecular beam experiments on $H_2$ dissociation on Ru(0001) was slightly higher, the experimentalists did not find surface temperature effects down to $T_s = 140\,K$.[30] Furthermore, the lowest barriers in the $H_2$ on Ru(0001) system are further away from the surface than was the case for $H_2$ on Cu(111), suggesting a weaker coupling between $H_2$ and surface degrees of freedom. Finally, energy exchange is not expected to be important for this system due to the large mass mismatch between a $H_2$ molecule and a ruthenium atom, and due to reaction being activated for this system. For $H_2$ dissociation on Pd(111) it was found that a considerable amount of trapping can occur through energy exchange, and that this can promote reaction, but on Pd(111) $H_2$ dissociation is non-activated.[82,83]

The importance of surface temperature effects could however be different for the case of diffraction. In the diffraction experiments, a higher surface temperature of $T_s = 500\,K$[29,84] was used. It is known that surface temperature can lead to a dramatic decrease of the meas-

ured diffraction probability due to Debye–Waller (DW) attenuation.[85] To correct for this, the experimental data was extrapolated to $T_s = 0\,K$ using a DW model.[29] Experiments in the range $T_s = 500 - 1000\,K$ were found to obey such a DW model.[29] It is, however, not clear to what extent such a model holds below $T_s = 500\,K$, as no measurements were possible below this temperature due to a build-up of a hydrogen layer on the surface.[29] The quality of such a DW extrapolation can be tested theoretically by performing calculations at a higher surface temperature. Recently quantum dynamics calculations have been performed for $H_2$ dissociation on Cu(111) where one surface degree has been taken into account either completely (7D) or using a phonon sudden approximation (6+1D).[86] Such calculations, or calculations taking into account even more degrees of freedom, could help clarify to what extent such a DW model holds.

Second, it should be noted that it is not possible to rule out that the XC functionals used are still not quite correct, in the sense that they could predict a too weak anisotropy in the PES and therefore a too low rotational excitation probability, and therefore too high rotationally elastic diffraction probabilities. With respect to this possibility, it should be noted that previous calculations using PW91 and RPBE showed a similar rotational excitation probability (at the highest incidence energy considered, approximately 5%[29]), and as such it is not clear whether this could explain the observed discrepancies.

Third, it should be noted that in the theoretical calculations only the ($\nu = 0$, $J = 0$) and ($\nu = 0$, $J = 1$) states were considered, while in the experiments also other states than these could be present. It was estimated previously that 73% of the molecules were in the $J = 1$ state at the lowest energy considered in experiments in contrast to 60% at the highest energy considered. As discussed in section 4.3.2, the reaction probability decreases slightly with increasing $J$ up to $J = 5$. Assuming normal energy scaling to hold to a reasonable extent, this could lead to an increase of the scattering probabilities of, in the most extreme case ($J = 5$), less than 20% compared to $J = 1$. If all the ortho-$H_2$ not present in the $J = 1$ state would be in the $J = 5$ state (most would actually be in the $J = 3$ state), this would lead to a change in scattering probability of at most about $20\% \cdot 15\% = 3\%$ at the highest energy considered. A

smaller contribution is expected from the para-$H_2$ molecules. At low energies, the number of rotationally excited molecules is simply too low to come even remotely close to explaining the observed discrepancies. As such, the incorporation of additional rotational states in the calculation is therefore not expected to improve the results considerably.

In summary, it is not yet clear whether the disagreement with the experimental diffraction probabilities reflects a failure of the two candidate SRP density functionals or a failure of the DW model to extrapolate the measured diffraction probabilities from $T_s \geq 500\,\mathrm{K}$ to 0 K. Hopefully, future calculations incorporating the effect of surface temperature can resolve this issue. In addition, new and detailed reactive scattering experiments on $H_2$/Ru(0001) would be useful, as such experiments could yield observables which can be used to validate the candidate SRP XC functionals, without the incoherent scattering problems that affect diffraction experiments. Examples of such experiments include associative desorption experiments, which by application of detailed balance may yield initial state-resolved reaction probabilities (measured for, for instance, $H_2$[72] and $D_2$[79,87] dissociation on Cu(111)). Alternatively, such experiments may also yield rotational state populations (as measured for $H_2$ + Pd(100)[88]), average translational energies for $H_2$ desorbing from the surface in particular $(v, J)$ states (as measured for $H_2$/Cu(100)[19]) and initial rotational quadrupole alignment parameters describing the orientational dependence of reaction (measured for, for instance, $H_2$/Cu(111),[89–91] $H_2$/Cu(100)[19] and $H_2$/Pd(100)[92]). Additional valuable information can perhaps be obtained from experiments that use laser excitation and detection using resonance enhanced multi-photon ionization (REMPI) to determine probabilities for rotationally inelastic scattering, like the experiments performed earlier for $H_2$/Cu(111),[93] $H_2$,[94] HD[95] and $D_2$[96]/Cu(100) and $H_2$,[97] HD[95] and $D_2$[96]/Pd(111).



## 4.4 Conclusions

Potential energy surfaces have been constructed for the dissociation of $H_2$ on Ru(0001) from DFT calculations, using over 20 different XC functionals. To compare with experimentally measured sticking probabilit-

ies and diffraction probabilities, quasi-classical and quantum dynamics calculations have been performed.

The functionals investigated yield a wide range of lattice constants, barrier heights and barrier positions. In particular the energetic corrugation, defined as the difference in barrier height between the hcp and top sites, shows a wide variation. The energetic corrugation is one of the factors determining the width of the reaction probability curve, which was in a previous study found to be too narrow for this system. Functionals containing LYP or LDA correlation yield a higher energetic corrugation than functionals containing PBE or Perdew86 correlation, and functionals containing vdW-DF correlation yield an even higher energetic corrugation. A similar trend was found for the barrier positions, where the vdW-DF functionals yield barriers closest to the surface, and functionals with PBE or Perdew86 correlation yield barriers furthest away from the surface.

From a comparison of the initial state-resolved reaction probability and rotational quadrupole alignment parameter between the PBE functional and the PBE-vdW-DF2 functional, it is concluded that the vdW-DF functional has a higher anisotropy of the potential at the barrier because the barriers obtained with this functional are closer to the surface.

From the comparison to molecular beam sticking experiments, it is concluded that, out of the functionals tested, only functionals which incorporate the van der Waals interaction in an approximate way can reasonably well describe the width of the reaction probability curve, as already expected from the energetic corrugation of these functionals. The PBE-vdW-DF2 and PBE:RPBE(50:50)-vdW-DF functionals describe the sticking experiments reasonably well, with the largest discrepancies occurring at the highest incidence energies, suggesting that these functionals can be considered candidate specific reaction parameter functionals.

For the comparison to diffraction experiments for the PBE-vdW-DF2 and PBE:RPBE(50:50)-vdW-DF functionals, it is found that the computed diffraction probabilities are higher than the DW-extrapolated experimental results. Two possible explanations are offered: either the DW model cannot be used to extrapolate from the lowest surface temperature probed in experiments ($T_s = 500\,\mathrm{K}$) to $0\,\mathrm{K}$, or the candidate

specific reaction parameter XC functionals considerably underestimate the amount of rotational excitation occurring in the scattering process. The first point can be addressed by performing calculations at a higher surface temperature, in which the instantaneous displacements and possibly also motion of surface atoms are taken into account, to test the quality of the DW model. Only such calculations can determine whether or not the PBE-vdW-DF2 and PBE:RPBE(50:50)-vdW-DF functionals can also give a good description of diffractive scattering.

## References


[1] W. Kohn and L. J. Sham. Self-consistent equations including exchange and correlation effects. *Physical Review* **140**(4A), A1133–A1138, 1965.

[2] P. Hohenberg and W. Kohn. Inhomogeneous electron gas. *Physical Review* **136**(3B), B864–B871, 1964.

[3] K. Yang, J. Zheng, Y. Zhao, and D. G. Truhlar. Tests of the RPBE, revPBE, $\tau$-HCTHhyb, $\omega$B97X-D, and MOHLYP density functional approximations and 29 others against representative databases for diverse bond energies and barrier heights in catalysis. *Journal of Chemical Physics* **132**(16), 164117, 2010.

[4] J. Zheng, Y. Zhao, and D. G. Truhlar. The DBH24/08 database and its use to assess electronic structure model chemistries for chemical reaction barrier heights. *Journal of Chemical Theory and Computation* **5**(4), pp. 808–821, 2009.

[5] J. Wellendorff, K. T. Lundgaard, A. Møgelhøj, V. Petzold, D. D. Landis, J. K. Nørskov, T. Bligaard, and K. W. Jacobsen. Density functionals for surface science: exchange-correlation model development with Bayesian error estimation. *Physical Review B* **85**(23), 235149, 2012.

[6] G. J. Kroes. Toward a database of chemically accurate barrier heights for reactions of molecules with metal surfaces. *Journal of Physical Chemistry Letters* **6**(20), pp. 4106–4114, 2015.

[7] J. S. Hummelshøj, F. Abild-Pedersen, F. Studt, T. Bligaard, and J. K. Nørskov. CatApp: a web application for surface chemistry and heterogeneous catalysis. *Angewandte Chemie International Edition* **51**(1), pp. 272–274, 2012.

[8] S. Wang, V. Petzold, V. Tripkovic, J. Kleis, J. G. Howalt, E. Skúlason, E. M. Fernández, B. Hvolbæk, G. Jones, A. Toftelund, H. Falsig, M. Björketun, F. Studt, F. Abild-Pedersen, J. Rossmeisl, J. K. Nørskov, and T. Bligaard. Universal transition state scaling relations for (de)hydrogenation over transition metals. *Physical Chemistry Chemical Physics* **13**(46), pp. 20760–20765, 2011.

[9] B. Hammer, L. B. Hansen, and J. K. Nørskov. Improved adsorption energetics within density-functional theory using revised Perdew-Burke-Ernzerhof functionals. *Physical Review B* **59**(11), pp. 7413–7421, 1999.

[10] G. J. Kroes. Frontiers in surface scattering simulations. *Science* **321**(5890), pp. 794–797, 2008.

[11] G. J. Kroes. Towards chemically accurate simulation of molecule-surface reactions. *Physical Chemistry Chemical Physics* **14**(43), pp. 14966–14981, 2012.

[12] A. Gross. Reactions at surfaces studied by *ab initio* dynamics calculations. *Surface Science Reports* **32**(8), pp. 291–340, 1998.

[13] H. F. Busnengo, W. Dong, P. Sautet, and A. Salin. Surface temperature dependence of rotational excitation of $H_2$ scattered from Pd(111). *Physical Review Letters* **87**(12), 127601, 2001.

[14] P. Nieto, E. Pijper, D. Barredo, G. Laurent, R. A. Olsen, E. J. Baerends, G. J. Kroes, and D. Farías. Reactive and nonreactive scattering of $H_2$ from a metal surface is electronically adiabatic. *Science* **312**(5770), pp. 86–89, 2006.

[15] J. P. Perdew, J. A. Chevary, S. H. Vosko, K. A. Jackson, M. R. Pederson, D. J. Singh, and C. Fiolhais. Atoms, molecules, solids, and surfaces: applications of the generalized gradient approximation for exchange and correlation. *Physical Review B* **46**(11), pp. 6671–6687, 1992.

[16] C. Díaz, E. Pijper, R. A. Olsen, H. F. Busnengo, D. J. Auerbach, and G. J. Kroes. Chemically accurate simulation of a prototypical surface reaction: $H_2$ dissociation on Cu(111). *Science* **326**(5954), pp. 832–834, 2009.

[17] C. Díaz, R. A. Olsen, D. J. Auerbach, and G. J. Kroes. Six-dimensional dynamics study of reactive and non reactive scattering of $H_2$ from Cu(111) using a chemically accurate potential energy surface. *Physical Chemistry Chemical Physics* **12**(24), pp. 6499–6519, 2010.

[18] Y. Y. Chuang, M. L. Radhakrishnan, P. L. Fast, C. J. Cramer, and D. G. Truhlar. Direct dynamics for free radical kinetics in solution: solvent effect on the rate constant for the reaction of methanol with atomic hydrogen. *Journal of Physical Chemistry A* **103**(25), pp. 4893–4909, 1999.

[19] L. Sementa, M. Wijzenbroek, B. J. van Kolck, M. F. Somers, A. Al-Halabi, H. F. Busnengo, R. A. Olsen, G. J. Kroes, M. Rutkowski, C. Thewes, N. F. Kleimeier, and H. Zacharias. Reactive scattering of $H_2$ from Cu(100): comparison of dynamics calculations based on the specific reaction parameter approach to density functional theory with experiment. *Journal of Chemical Physics* **138**(4), 044708, 2013.

[20] S. Dahl, J. Sehested, C. J. H. Jacobsen, E. Törnqvist, and I. Chorkendorff. Surface science based microkinetic analysis of ammonia synthesis over ruthenium catalysts. *Journal of Catalysis* **192**(2), pp. 391–399, 2000.

[21] S. Dahl, P. A. Taylor, E. Törnqvist, and I. Chorkendorff. The synthesis of ammonia over a ruthenium single crystal. *Journal of Catalysis* **178**(2), pp. 679–686, 1998.

[22] C. J. H. Jacobsen, S. Dahl, P. L. Hansen, E. Törnqvist, L. Jensen, H. Topsøe, D. V. Prip, P. B. Møenshaug, and I. Chorkendorff. Structure sensitivity of supported ruthenium catalysts for ammonia synthesis. *Journal of Molecular Catalysis A: Chemical* **163**(1–2), pp. 19–26, 2000.

[23] S. Uchiyama, Y. Hattori, K. Aika, and A. Ozaki. Ammonia synthesis from carbon monoxide, water, and dinitrogen over Ru-MgO-$Cs_2O$. *Chemistry Letters* **10**(10), pp. 1463–1464, 1981.

[24] K. Honkala, A. Hellman, I. N. Remediakis, A. Logadottir, A. Carlsson, S. Dahl, C. H. Christensen, and J. K. Nørskov. Ammonia synthesis from first-principles calculations. *Science* **307**(5709), pp. 555–558, 2005.

[25] L. R. Danielson, M. J. Dresser, E. E. Donaldson, and J. T. Dickinson. Adsorption and desorption of ammonia, hydrogen, and nitrogen on ruthenium (0001). *Surface Science* **71**(3), pp. 599–614, 1978.

[26] T. Matsushima. Angular distribution of the combinative desorption of nitrogen atoms on Ru(001) surfaces. *Surface Science* **197**(3), pp. L287–L291, 1988.

[27] M. Luppi, R. A. Olsen, and E. J. Baerends. Six-dimensional potential energy surface for $H_2$ at Ru(0001). *Physical Chemistry Chemical Physics* **8**(6), pp. 688–696, 2006.

[28] J. K. Vincent, R. A. Olsen, G. J. Kroes, M. Luppi, and E. J. Baerends. Six-dimensional quantum dynamics of dissociative chemisorption of $H_2$ on Ru(0001). *Journal of Chemical Physics* **122**(4), 044701, 2005.

[29] P. Nieto, D. Farías, R. Miranda, M. Luppi, E. J. Baerends, M. F. Somers, M. J. T. C. van der Niet, R. A. Olsen, and G. J. Kroes. Diffractive and reactive scattering of $H_2$ from Ru(0001): experimental and theoretical study. *Physical Chemistry Chemical Physics* **13**(18), pp. 8583–8597, 2011.

[30] I. M. N. Groot, H. Ueta, M. J. T. C. van der Niet, A. W. Kleyn, and L. B. F. Juurlink. Supersonic molecular beam studies of dissociative adsorption of $H_2$ on Ru(0001). *Journal of Chemical Physics* **127**(24), 244701, 2007.

[31] F. O. Kannemann and A. D. Becke. Van der Waals interactions in density-functional theory: rare-gas diatomics. *Journal of Chemical Theory and Computation* **5**(4), pp. 719–727, 2009.

[32] J. Klimeš and A. Michaelides. Perspective: Advances and challenges in treating van der Waals dispersion forces in density functional theory. *Journal of Chemical Physics* **137**(12), 120901, 2012.

[33] G. Füchsel, S. Schimka, and P. Saalfrank. On the role of electronic friction for dissociative adsorption and scattering of hydrogen molecules at a Ru(0001) surface. *Journal of Physical Chemistry A* **117**(36), pp. 8761–8769, 2013.

[34] M. Born and R. Oppenheimer. Zur Quantentheorie der Molekeln. *Annalen der Physik* **389**(20), pp. 457–484, 1927.

[35] A. C. Luntz and M. Persson. How adiabatic is activated adsorption/associative desorption? *Journal of Chemical Physics* **123**(7), 074704, 2005.

[36] A. S. Muzas, J. I. Juaristi, M. Alducin, R. Díez Muiño, G. J. Kroes, and C. Díaz. Vibrational deexcitation and rotational excitation of $H_2$ and $D_2$ scattered from Cu(111): adiabatic versus non-adiabatic dynamics. *Journal of Chemical Physics* **137**(6), 064707, 2012.

[37] J. I. Juaristi, M. Alducin, R. Díez Muiño, H. F. Busnengo, and A. Salin. Role of electron–hole pair excitations in the dissociative adsorption of diatomic molecules on metal surfaces. *Physical Review Letters* **100**(11), 116102, 2008.

[38] F. Nattino, C. Díaz, B. Jackson, and G. J. Kroes. Effect of surface motion on the rotational quadrupole alignment parameter of $D_2$ reacting on Cu(111). *Physical Review Letters* **108**(23), 236104, 2012.

[39] A. Mondal, M. Wijzenbroek, M. Bonfanti, C. Díaz, and G. J. Kroes. Thermal lattice expansion effect on reactive scattering of $H_2$ from Cu(111) at $T_s = 925$ K. *Journal of Physical Chemistry A* **117**(36), pp. 8770–8781, 2013.

[40] J. W. Arblaster. Crystallographic properties of ruthenium. *Platinum Metals Review* **56**(3), pp. 181–189, 2013.

[41] A. P. Baddorf, V. Jahns, D. M. Zehner, H. Zajonz, and D. Gibbs. Relaxation and thermal expansion of Ru(0001) between 300 and 1870 K and the influence of hydrogen. *Surface Science* **498**(1–2), pp. 74–82, 2002.

[42] R. Kosloff. Time-dependent quantum-mechanical methods for molecular dynamics. *Journal of Physical Chemistry* **92**(8), pp. 2087–2100, 1988.

[43] E. Pijper, G. J. Kroes, R. A. Olsen, and E. J. Baerends. Reactive and diffractive scattering of $H_2$ from Pt(111) studied using a six-dimensional wave packet method. *Journal of Chemical Physics* **117**(12), pp. 5885–5898, 2002.

[44] M. Karplus, R. N. Porter, and R. D. Sharma. Exchange reactions with activation energy. I. Simple barrier potential for (H, $H_2$). *Journal of Chemical Physics* **43**(9), pp. 3259–3287, 1965.

[45] H. F. Busnengo, A. Salin, and W. Dong. Representation of the 6D potential energy surface for a diatomic molecule near a solid surface. *Journal of Chemical Physics* **112**(17), pp. 7641–7651, 2000.

[46] R. A. Olsen, H. F. Busnengo, A. Salin, M. F. Somers, G. J. Kroes, and E. J. Baerends. Constructing accurate potential energy surfaces for a diatomic molecule interacting with a solid surface: $H_2$+Pt(111) and $H_2$+Cu(100). *Journal of Chemical Physics* **116**(9), pp. 3841–3855, 2002.

[47] I. M. N. Groot. Personal communication. 2013.

[48] A. D. Becke. Density-functional exchange-energy approximation with correct asymptotic behavior. *Physical Review A* **38**(6), pp. 3098–3100, 1988.

[49] C. Lee, W. Yang, and R. G. Parr. Development of the Colle-Salvetti correlation-energy formula into a functional of the electron density. *Physical Review B* **37**(2), pp. 785–789, 1988.

[50] J. P. Perdew. Density-functional approximation for the correlation energy of the inhomogeneous electron gas. *Physical Review B* **33**(12), pp. 8822–8824, 1986.

[51] P. Haas, F. Tran, P. Blaha, and K. Schwarz. Construction of an optimal GGA functional for molecules and solids. *Physical Review B* **83**(20), 205117, 2011.

[52] J. P. Perdew, K. Burke, and M. Ernzerhof. Generalized gradient approximation made simple. *Physical Review Letters* **77**(18), pp. 3865–3868, 1996.

[53] G. K. H. Madsen. Functional form of the generalized gradient approximation for exchange: the PBE$\alpha$ functional. *Physical Review B* **75**(19), 195108, 2007.

[54] J. P. Perdew and Y. Wang. Accurate and simple analytic representation of the electron-gas correlation energy. *Physical Review B* **45**(23), pp. 13244–13249, 1992.

[55] M. Dion, H. Rydberg, E. Schröder, D. C. Langreth, and B. I. Lundqvist. Van der Waals density functional for general geometries. *Physical Review Letters* **92**(24), 246401, 2004.

[56] K. Lee, E. D. Murray, L. Kong, B. I. Lundqvist, and D. C. Langreth. Higher-accuracy van der Waals density functional. *Physical Review B* **82**(8), 081101, 2010.

[57] Y. Zhang and W. Yang. Comment on "Generalized gradient approximation made simple". *Physical Review Letters* **80**(4), p. 890, 1998.

[58] J. P. Perdew, A. Ruzsinszky, G. I. Csonka, L. A. Constantin, and J. Sun. Workhorse semilocal density functional for condensed matter physics and quantum chemistry. *Physical Review Letters* **103**(2), 026403, 2009.

[59] Z. Wu and R. E. Cohen. More accurate generalized gradient approximation for solids. *Physical Review B* **73**(23), 235116, 2006.

[60] M. Černohorský. The ratio method for absolute measurements of lattice parameters with cylindrical cameras. *Acta Crystallographica* **13**(10), pp. 823–826, 1960.

[61] G. Kresse and J. Hafner. *Ab initio* molecular dynamics for liquid metals. *Physical Review B* **47**(1), pp. 558–561, 1993.

[62] G. Kresse and J. Furthmüller. Efficiency of *ab initio* total energy calculations for metals and semiconductors using a plane-wave basis set. *Computational Materials Science* **6**(1), pp. 15–50, 1996.

[63] G. Kresse and J. Furthmüller. Efficient iterative schemes for *ab initio* total-energy calculations using a plane-wave basis set. *Physical Review B* **54**(16), pp. 11169–11186, 1996.

[64] M. A. L. Marques, M. J. T. Oliveira, and T. Burnus. Libxc: a library of exchange and correlation functionals for density functional theory. *Computer Physics Communications* **183**(10), pp. 2272–2281, 2012.

[65] G. Kresse and J. Hafner. Norm-conserving and ultrasoft pseudopotentials for first-row and transition elements. *Journal of Physics: Condensed Matter* **6**(40), pp. 8245–8257, 1994.

[66] D. Vanderbilt. Soft self-consistent pseudopotentials in a generalized eigenvalue formalism. *Physical Review B* **41**(11), pp. 7892–7895, 1990.

[67] P. E. Blöchl. Projector augmented-wave method. *Physical Review B* **50**(24), pp. 17953–17979, 1994.

[68] G. Kresse and D. Joubert. From ultrasoft pseudopotentials to the projector augmented-wave method. *Physical Review B* **59**(3), pp. 1758–1775, 1999.

[69] G. Román-Pérez and J. M. Soler. Efficient implementation of a van der Waals density functional: application to double-wall carbon nanotubes. *Physical Review Letters* **103**(9), 096102, 2009.

[70] H. J. Monkhorst and J. D. Pack. Special points for Brillouin-zone integrations. *Physical Review B* **13**(12), pp. 5188–5192, 1976.

[71] A. Gross, B. Hammer, M. Scheffler, and W. Brenig. High-dimensional quantum dynamics of adsorption and desorption of $H_2$ at Cu(111). *Physical Review Letters* **73**(23), pp. 3121–3124, 1994.

[72] C. T. Rettner, H. A. Michelsen, and D. J. Auerbach. Quantum-state-specific dynamics of the dissociative adsorption and associative desorption of $H_2$ at a Cu(111) surface. *Journal of Chemical Physics* **102**(11), pp. 4625–4641, 1995.

[73] H. A. Michelsen, C. T. Rettner, and D. J. Auerbach. On the influence of surface temperature on adsorption and desorption in the $D_2$/Cu(111) system. *Surface Science* **272**(1–3), pp. 65–72, 1992.

[74] L. Schimka, J. Harl, A. Stroppa, A. Grüneis, M. Marsman, F. Mittendorfer, and G. Kresse. Accurate surface and adsorption energies from many-body perturbation theory. *Nature Materials* **9**(9), pp. 741–744, 2010.

[75] J. Sun, M. Marsman, A. Ruzsinszky, G. Kresse, and J. P. Perdew. Improved lattice constants, surface energies, and CO desorption energies from a semilocal density functional. *Physical Review B* **83**(12), 121410(R), 2011.

[76] J. K. Nørskov, T. Bligaard, A. Logadottir, S. Bahn, L. B. Hansen, M. Bollinger, H. Bengaard, B. Hammer, Z. Sljivancanin, M. Mavrikakis, Y. Xu, S. Dahl, and C. J. H. Jacobsen. Universality in heterogeneous catalysis. *Journal of Catalysis* **209**(2), pp. 275–278, 2002.

[77] J. K. Nørskov, F. Abild-Pedersen, F. Studt, and T. Bligaard. Density functional theory in surface chemistry and catalysis. *Proceedings of the National Academy of Sciences* **108**(3), pp. 937–943, 2011.

[78] H. A. Michelsen, C. T. Rettner, and D. J. Auerbach. State-specific dynamics of $D_2$ desorption from Cu(111): the role of molecular rotational motion in activated adsorption-desorption dynamics. *Physical Review Letters* **69**(18), pp. 2678–2681, 1992.

[79] H. A. Michelsen, C. T. Rettner, D. J. Auerbach, and R. N. Zare. Effect of rotation on the translational and vibrational energy dependence of the dissociative adsorption of $D_2$ on Cu(111). *Journal of Chemical Physics* **98**(10), pp. 8294–8307, 1993.

[80] A. A. Marashdeh, S. Casolo, L. Sementa, H. Zacharias, and G. J. Kroes. Surface temperature effects on dissociative chemisorption of $H_2$ on Cu(100). *Journal of Physical Chemistry C* **117**(17), pp. 8851–8863, 2013.

[81] G. R. Darling and S. Holloway. The role of parallel momentum in the dissociative adsorption of $H_2$ at highly corrugated surfaces. *Surface Science* **304**(3), pp. L461–L467, 1994.

[82] H. F. Busnengo, W. Dong, and A. Salin. Trapping, molecular adsorption, and precursors for nonactivated chemisorption. *Physical Review Letters* **93**(23), 236103, 2004.

[83] H. F. Busnengo, M. A. Di Césare, W. Dong, and A. Salin. Surface temperature effects in dynamic trapping mediated adsorption of light molecules on metal surfaces: $H_2$ on Pd(111) and Pd(110). *Physical Review B* **72**(12), 125411, 2005.

[84] P. Nieto, D. Barredo, D. Farías, and R. Miranda. In-plane and out-of-plane diffraction of $H_2$ from Ru(001). *Journal of Physical Chemistry A* **115**(25), pp. 7283–7290, 2011.

[85] D. Farías and R. Miranda. Diffraction of molecular hydrogen from metal surfaces. *Progress in Surface Science* **86**(9–10), pp. 222–254, 2011.

[86] M. Bonfanti, M. F. Somers, C. Díaz, H. F. Busnengo, and G. J. Kroes. 7D quantum dynamics of $H_2$ scattering from Cu(111): the accuracy of the phonon sudden approximation. *Zeitschrift für Physikalische Chemie* **227**(11), pp. 1397–1420, 2013.

[87] C. T. Rettner, D. J. Auerbach, and H. A. Michelsen. Role of vibrational and translational energy in the activated dissociative adsorption of $D_2$ on Cu(111). *Physical Review Letters* **68**(8), pp. 1164–1167, 1992.

[88] D. Wetzig, M. Rutkowski, H. Zacharias, and A. Gross. Vibrational and rotational population distribution of $D_2$ associatively desorbing from Pd(100). *Physical Review B* **63**(20), 205412, 2001.

[89] H. Hou, S. J. Gulding, C. T. Rettner, A. M. Wodtke, and D. J. Auerbach. The stereodynamics of a gas-surface reaction. *Science* **277**(5322), pp. 80–82, 1997.

[90] D. Wetzig, M. Rutkowski, R. David, and H. Zacharias. Rotational corrugation in associative desorption of $D_2$ from Cu(111). *Europhysics Letters* **36**(1), pp. 31–36, 1996.

[91] S. J. Gulding, A. M. Wodtke, H. Hou, C. T. Rettner, H. A. Michelsen, and D. J. Auerbach. Alignment of $D_2$(v, J) desorbed from Cu(111): low sensitivity of activated dissociative chemisorption to approach geometry. *Journal of Chemical Physics* **105**(21), pp. 9702–9705, 1996.

[92] D. Wetzig, R. Dopheide, M. Rutkowski, R. David, and H. Zacharias. Rotational alignment in associative desorption of $D_2(v'' = 0$ and 1) from Pd(100). *Physical Review Letters* **76**(3), pp. 463–466, 1996.

[93] A. Hodgson, P. Samson, A. Wight, and C. Cottrell. Rotational excitation and vibrational relaxation of $H_2$ ($v$=1,J=0) scattered from Cu(111). *Physical Review Letters* **78**(5), pp. 963–966, 1997.

[94] E. Watts and G. O. Sitz. State-to-state scattering in a reactive system: $H_2$($v$=1, $J$=1) from Cu(100). *Journal of Chemical Physics* **114**(9), pp. 4171–4179, 2001.

[95] L. C. Shackman and G. O. Sitz. Rotationally inelastic scattering of HD from Cu(100) and Pd(111). *Journal of Chemical Physics* **122**(11), 114702, 2005.

[96] L. C. Shackman and G. O. Sitz. State-to-state scattering of $D_2$ from Cu(100) and Pd(111). *Journal of Chemical Physics* **123**(6), 064712, 2005.

[97] M. Gostein, E. Watts, and G. O. Sitz. Vibrational relaxation of $H_2$ ($v$=1,$J$=1) on Pd(111). *Physical Review Letters* **79**(15), pp. 2891–2894, 1997.

CHAPTER 4

CHAPTER 5

# Towards a specific reaction parameter density functional for reactive scattering of $H_2$ from Pd(111)

This chapter is based on:

J. M. Boereboom, M. Wijzenbroek, M. F. Somers, and G. J. Kroes. Towards a specific reaction parameter density functional for reactive scattering of $H_2$ from Pd(111). *Journal of Chemical Physics* **139**(24), 244707, 2013.

## Abstract

Recently, an implementation of the specific reaction parameter (SRP) approach to density functional theory (DFT) was used to study several reactive scattering experiments of $H_2$ on Cu(111). It was possible to obtain chemical accuracy (1 kcal/mol $\approx$ 4.2 kJ/mol), and therefore, accurately model the dissociation of hydrogen on an activated metal surface. In this work, the SRP-DFT methodology is applied to the dissociation of hydrogen on a Pd(111) surface, in order to test whether the SRP-DFT approach is also applicable to non-activated systems. In the calculations, the Born–Oppenheimer and static surface (BOSS) approximations are used. A comparison to molecular beam sticking experiments on $H_2$/Pd(111) suggested the PBE-vdW-DF functional as a candidate exchange–correlation functional describing the reactive scattering of $H_2$ on Pd(111), because at high incidence energies simulated molecular beam reaction probabilities obtained with the quasi-classical trajectory (QCT) method and using a PBE-vdW-DF potential energy surface are in good agreement with experimental sticking probabilities. Unfortunately, quantum dynamics calculations are not able to reproduce the molecular beam sticking results for low incidence energies. From a comparison to initial state-resolved (degeneracy averaged) sticking probabilities it seems clear that for $H_2$/Pd(111) dynamic trapping and steering effects are important, which are not yet well modelled with the potential energy surfaces (PESs) considered here. Applying the SRP-DFT method to systems where $H_2$ dissociation is non-activated remains difficult. It is suggested that a density functional that yields a broader barrier distribution than PBE-vdW-DF (*i.e.*, non-activated dissociation at some sites but similarly high barriers at the high energy end of the spectrum) could allow a more accurate description of the available experiments.




## 5.1 Introduction

A large number of chemical reactions involve gas–surface interactions. These interactions are of great importance to the chemical industry, where heterogeneous catalysis lies at the heart of the synthesis of many

important compounds.[1] One famous example is the Haber–Bosch process, which is arguably the most important invention of the twentieth century.[2] This process is the main industrial route to produce ammonia, which is used in fertilizers. The dissociative chemisorption of hydrogen on metal surfaces is one of the most fundamental gas–surface reactions. Heterogeneously catalysed processes typically involve several of such elementary surface reaction steps.[3,4]

Unfortunately, it is difficult to accurately model the dissociation of hydrogen on metal surfaces.[5] In order to correctly calculate the reaction probability of hydrogen dissociation on a metal surface, one needs to obtain reaction barriers with chemical accuracy (1 kcal/mol ≈ 4.2 kJ/mol).[6] Currently, the electronic structure method of choice to study the dissociation of $H_2$ on a metal surface is density functional theory (DFT),[7] with functionals based on the generalized gradient approximation (GGA). Even these calculations, however, have mean absolute errors of at best 4 kcal/mol, for gas-phase reaction barrier heights[8,9] (unfortunately, for molecule–surface reactions such systematic investigations are currently not available).[10] In contrast, high accuracy for gas-phase reactions is available from high-level *ab initio* theory, and to a lesser extent from DFT with hybrid functionals.[8,9] The scaling of such methods, however, is rather unfavourable, so that in practice these methods cannot yet be applied to the computation of global potential energy surfaces (PESs) for molecule–surface reactions. Therefore, recently an implementation[6] of the specific reaction parameter (SRP) approach to DFT,[11,12] adapted to molecule–surface reactions, was proposed. This allowed a quantitative description of several reactive scattering experiments of $H_2$ on Cu(111), which is a benchmark system for activated hydrogen–metal surface reactions.[6] It was shown that this SRP exchange–correlation (XC) functional was also transferable to the $H_2$/Cu(100) reaction.[13]

In calculations on $H_2$ dissociation on Cu(111),[6] a SRP XC functional was constructed in the following way,

$$E_{XC}^{SRP} = \alpha E_{XC}^{1} + (1 - \alpha) E_{XC}^{2}. \tag{5.1}$$

Here, the energy of the SRP XC functional can be written as a linear combination of $E_{XC}^{1}$ and $E_{XC}^{2}$, the energy expression of any two arbitrary

XC functionals. The essence of the SRP approach to DFT is that an XC functional is found (possibly through an empirical fit) that yields an excellent agreement with the sticking probability measured in molecular beam experiments, with the desired result that also other, more detailed observables (like diffraction probabilities) are described well. Therefore, the SRP XC functional need not be a mix of two XC functionals. The question remains, however, if the approach first tested and found to work well for activated hydrogen–metal systems (*i.e.*, fitting an XC functional by demanding that dynamics calculations performed with the Born–Oppenheimer static surface (BOSS) model on a PES obtained from DFT calculations reproduce molecular beam sticking probability measurements) is also appropriate to model $H_2$ dissociation in non-activated systems. In this work, the specific reaction parameter methodology will be applied to the dissociation of hydrogen on a Pd(111) surface, in order to test whether the SRP approach is applicable to non-activated systems as well.

Several molecular beam experiments have been performed by the Rendulic group on the sticking of $H_2$ on Pd(111).[14–17] Furthermore, molecular beam experiments have been performed for this system by Gostein and Sitz,[18] who analysed their results to extract initial state-resolved reaction probabilities.

Unfortunately, there are large discrepancies between the sticking probabilities obtained from the different molecular beam studies. In figure 5.1, the molecular beam sticking probabilities for all the available experiments are plotted. It can be seen that there is a large spread in the experimental data of the molecular beam experiments by the group of Rendulic. From private correspondence,[19] it becomes clear that the latest experiment (exp. Rendulic 2001[16,17]) is probably the most reliable. This experiment is also in reasonably good agreement with the rotationally averaged sticking coefficients obtained by Gostein and Sitz.[18]

Apart from experimental work on the dissociation of hydrogen on Pd(111), this system has also been studied theoretically.[20–28] The theoretical work mainly focused on rotational effects on the dissociation of hydrogen on Pd(111), and on the role zero-point energy (ZPE) plays in the classical dynamics of $H_2$ dissociation. Surface temperature effects

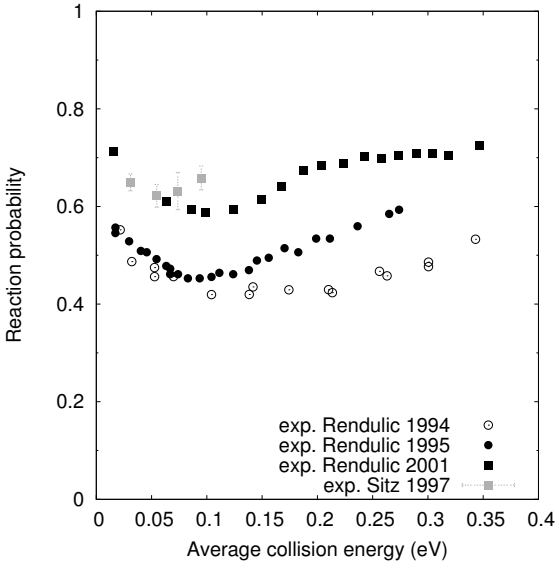


**Figure 5.1** Molecular beam sticking probabilities for all the available experiments. The experiment by Resch *et al.*[14] is labelled exp. Rendulic 1994, the experiment by Beutl *et al.*[15] is labelled exp. Rendulic 1995, and the experiment performed by Lesnik[16] and Beutl *et al.*[17] is labelled exp. Rendulic 2001. The experiment by Gostein and Sitz[18] is labelled exp. Sitz 1997.

have also been considered.[27,28] In these studies it was found that energy exchange can promote trapping of the $H_2$ near the surface, and thereby reaction (trapping mediated reaction). There have also been a few studies which focused on the scattering of $H_2$ from Pd(111),[29,30] but in this work scattering processes will not be discussed. Also other low index surfaces have been studied intensively. Experimental data is available for Pd(100)[31–34] and Pd(110),[35] and theoretical studies have also been performed on Pd(100)[36–40] and Pd(110).[35,41–43]

This chapter is organized as follows: in section 5.2, the methods used to obtain the PES and to carry out the dynamics calculations in this work are presented. The computational details are also discussed there. The results and discussion can be found in section 5.3, where first the PESs is discussed in section 5.3.1, after which a candidate for the specific reaction parameter XC functional is discussed in section 5.3.2. For this candidate functional, quantum dynamics (QD) calculations

have been performed, and are compared with results obtained with the quasi-classical trajectory (QCT) method and experiment. This comparison is done for both molecular beams (section 5.3.2) and initial state-specific reaction probabilities (section 5.3.3). The main conclusions will be summarized and presented in section 5.4.

## 5.2 Methods

### 5.2.1 Born–Oppenheimer static surface model

In this work the BOSS model has been used. Within this model the $H_2$–surface system is treated using six molecular degrees of freedom, by freezing the positions of the surface atoms in their ideal lattice positions. The coordinate system used to describe the position and orientation of the molecule with respect to the surface can be found in figure 5.2(a). Here, $X$, $Y$, and $Z$ are the center of mass coordinates of $H_2$, $r$ is the H–H distance, $\vartheta$ is the polar angle of the molecular axis with the $Z$-axis, and $\varphi$ is the azimuthal angle. In the BOSS model electron–hole (e–h) pair excitation and phonons are neglected. Reactive scattering calculations on $H_2$/Pt(111) using a single PES and neglecting e–h pair excitation were able to describe the dissociation and diffractive scattering of hydrogen on Pt(111) accurately.[44] Moreover, calculations on $H_2$/Cu(111),[45] Cu(110),[46] and Ru(0001)[47] modelling e–h pair excitation with friction coefficients showed very small non-adiabatic energy losses. These results suggest that non-adiabatic effects are not important when modelling $H_2$–metal surface systems, supporting the validity of the Born–Oppenheimer approximation for these systems.

The validity of the static surface approximation has been tested by static surface QCT calculations on the reactive scattering of $D_2$ from Cu(111) at low surface temperature ($T_s = 120$ K).[6,48] These calculations were in good agreement with *ab initio* molecular dynamics (AIMD) results,[49] which modelled phonon motion. Also results obtained with the static corrugation model (SCM) in chapter 3, which excluded energy exchange with the surface but included the displacement of surface atoms, were in good agreement with the results above for low surface temperatures. These studies suggested that, for high surface temper-

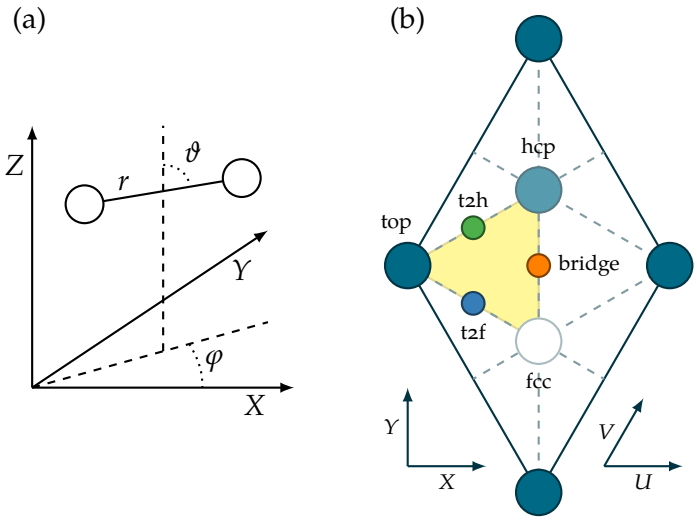


**Figure 5.2** (a) Coordinate system for dissociation of $H_2$ on a surface. In the plot, $X$, $Y$, and $Z$ are the center of mass coordinates of $H_2$, $r$ is the H–H distance, $\vartheta$ is the polar angle of the molecular axis with the $Z$-axis, and $\varphi$ is the azimuthal angle. (b) Schematic representation of the unit cell with the high symmetry sites on the Pd(111) surface, and of considered $H_2$–surface geometries.

atures, thermal expansion of the surface can be important, which has been tested recently.[50]

### 5.2.2 Electronic structure method

To construct 6D PESs, plane wave DFT calculations were performed for H/Pd(111) and $H_2$/Pd(111) with version 5.2.12 of the VASP[51–54] software package. The surface is modelled by a five layer slab representation[55,56] using a 2 × 2 supercell.[57] Each PES has p3m1 symmetry.[58] As a consequence, a distinction can be made between second and third layer hollow sites, called HCP and FCC respectively, which are shown in figure 5.2(b). PESs have been calculated for four different XC functionals: PBE,[59] RPBE,[60] PBE-vdW-DF,[59,61] and PBE$\alpha$-vdW-DF.[61,62] In the PBE$\alpha$-vdW-DF functional, $\alpha = 0.5$ is chosen. In the PBE$\alpha$ method $\alpha$ is defined in such a way that $\alpha = 1$ corresponds to PBE, and $\alpha = \infty$ corresponds to RPBE.[62] For PBE-vdW-DF and PBE$\alpha$-vdW-DF, the

PBE correlation is replaced by vdW-DF correlation[61] resulting in PBE and PBE$\alpha$ exchange and vdW-DF correlation. In VASP the vdW-DF method uses[63] the method of Román-Pérez and Soler.[64] The lattice constants have been calculated using a plane wave energy cutoff of 450 eV, sampling the Brillouin zone by a $20 \times 20 \times 20$ $\Gamma$-centered $k$-point mesh. Subsequently, a five layer slab was optimized, with the same energy cutoff, and with a $20 \times 20 \times 1$ $\Gamma$-centered $k$-point mesh to sample the Brillouin zone. Each PES is based on more than 6000 single DFT points. These single points are calculated using a plane wave cut-off of 400 eV, and using a $9 \times 9 \times 1$ $\Gamma$-centered $k$-point mesh to sample the Brillouin zone. Convergence tests suggested that the error made in the single DFT points, due to the basis set size and numerical integration, is around 5 meV. The PBE and RPBE functionals from LibXC[65] version 1.2.0 were used. To describe the core electrons, the projector augmented wave (PAW) method[66,67] has been used for PBE-vdW-DF and PBE$\alpha$-vdW-DF. For PBE and RPBE ultrasoft pseudopotentials (USPPs) have been used.[68,69]

### 5.2.3 PES interpolation

The 6D PESs were constructed in a way analogous to that described in section 4.2.2. In total, 29 2D PESs were used in the interpolation procedure for the molecule–surface PES. The 2D PESs are a function of $Z$ and $r$, and represent the most important configurations of the $H_2$ molecule interacting with Pd(111). Each 2D PES is based on a cubic spline interpolation of 196 points (14 in $r$ and 14 in $Z$) which are calculated with DFT. The positions ($X$, $Y$) and orientation ($\vartheta$, $\varphi$) of $H_2$ in the 2D cuts can be found in table 4.1. A very important task is to interpolate the 2D PESs to obtain an accurate 6D PES. Due to the strong corrugation of the potential near the surface, a direct interpolation can lead to large errors in the interpolated PES.[70] The corrugation reducing procedure (CRP) method,[21,71] as discussed in section 2.1.1 has therefore been used.The required 1D PESs representing the H–surface interaction were calculated for 10 different sites (table 4.2).

### 5.2.4 Dynamics methods

QCT calculations for each initial $(v, J)$ state were performed for 14 normal incidence energies, spread equidistantly over a normal incidence energy interval of $25 - 350$ meV. The used QCT method has been described in section 2.3 of this thesis. Initially, the center of mass of the hydrogen molecule is placed at a distance of 7 Å from the surface. It is assumed that dissociation occurs when $r$ (the H–H distance) exceeds 2.25 Å. Scattering is assumed to have occurred when the hydrogen molecule has a momentum away from the surface, and a hydrogen–surface distance larger than 7 Å is reached. To obtain statistically accurate results for each point at least $10^4$ trajectories were computed, which are sampled equally over the possible $m_J$ states.

The QD calculations have been carried out using a time-dependent wave packet (TDWP) method[72,73] as described in section 2.4. In order to cover a large range of normal incidence energies ($40-600$ meV) two calculations are performed with separate energy ranges: $40-200$ meV and $150 - 600$ meV. This is done to avoid problems which may arise from the interaction of the optical potential with the low energy components in the wave packet, if only one broad Gaussian initial wave packet is used to cover the entire range from $40 - 600$ meV.[73]

### 5.2.5 Computation of observables

Initial state-resolved reaction probabilities and molecular beam sticking probabilities were computed as discussed in section 2.5. In order to compare the computed sticking probabilities with molecular beam experiments from the Rendulic group, the parameters $v_0$ and $\alpha$ (see also equation (2.39)), characterizing the molecular beam, are needed. Unfortunately, for the molecular beam experiments on Pd(111)[14–17] no time-of-flight (TOF) spectra were published. Therefore, the parameters are obtained from experiments with pure beams on $H_2$ scattering from Cu(111), which were performed by Berger *et al.* in the group of Rendulic. The TOF intensities $G(t; T_n)$ characterizing the $H_2$ beams are presented in figure 4.4 from the thesis by Berger[74] for $T_n$ = 100, 300, 500, 800, 1100, 1400, and 1700 K. This figure was digitized and fitted[75] according

**Table 5.1** Parameters used to simulate the molecular beam experiments. The parameters were obtained by digitizing and fitting figure 4.4 from the thesis by Berger[74] according to equation (5.2). In order to simulate the molecular beam sticking probabilities (equation (2.38)) these parameters enter the flux weighted velocity distribution (equation (2.39)).

| $T_n$ (K) | $\langle E_i \rangle$ (eV) | $v_0$ (m/s) | $\alpha$ (m/s) |
|---|---|---|---|
| 100 | 0.035 | 1820.7 | 78.7 |
| 300 | 0.068 | 2503.9 | 237.6 |
| 500 | 0.126 | 3162.2 | 781.7 |
| 800 | 0.150 | 3300.1 | 1007.3 |
| 1100 | 0.240 | 3691.5 | 1694.6 |
| 1400 | 0.391 | 3510.8 | 2897.2 |
| 1700 | 0.445 | 3096.6 | 3411.0 |

to,

$$G(t; T_n) = c_1 + c_2 \cdot {v_i}^4 \exp\left[-\left(\frac{v_i - v_0}{\alpha}\right)^2\right], \tag{5.2}$$

where $c_1$ and $c_2$ are constants. The parameters obtained from the fits are presented in table 5.1. Note that reference 6 only presented parameters for $T_n \geq 1100$ K.



### 5.2.6 Computational details

The relevant input parameters for the QD calculations are listed in table 5.2. For both energy ranges ($40 - 200$ meV and $150 - 600$ meV) the same input parameters could be used. For the low energy range the convergence errors are lower than for the high energy range (errors of the order of 1% for low incidence energies, and not more than 2% for the high energy range). A long propagation time is needed, due to a chemisorption well in front of the barrier. The wave function is propagated long enough to ensure that the norm of the wave function which is still on the grid at the end of the calculation is no more than 0.01. The total propagation time ranges from $60 \times 10^3$ to $360 \times 10^3$ a.u.

**Table 5.2** Input parameters for the quantum dynamical calculations of $H_2$ dissociating on Pd(111). For a detailed description of the parameters, see reference 73. For both energy ranges the same input parameters could be used. The values are listed for the calculations with $J$ even, when the calculations with $J$ odd have different parameters they are listed in parentheses. All values are given in atomic units.

| Parameter | Description | Value |
|---|---|---|
| $N_X = N_Y$ | no. of grid points in $X$ and $Y$ | 24 |
| $N_Z$ | no. of grid points in $Z$ | 128 |
| $N_{Z(\mathrm{sp})}$ | no. of specular grid points | 240 |
| $\Delta Z$ | spacing of $Z$ grid points | 0.135 |
| $Z_{\mathrm{min}}$ | minimum value of $Z$ | -1.0 |
| $N_r$ | no. of grid points in $r$ | 32 |
| $\Delta r$ | spacing of $r$ grid points | 0.25 |
| $r_{\mathrm{min}}$ | minimum value of $r$ | 0.4 |
| $\mathrm{j}_{\mathrm{max}}$ | maximum $J$ value in basis set | 18(19) |
| $m_{\mathrm{j}_{\mathrm{max}}}$ | maximum $m_J$ value in basis set | 18(19) |
| $\Delta t$ | time step | 2.5 |
| $Z_0$ | center of initial wave packet | 16.64 |
| $Z_\infty$ | location of analysis line | 12.5 |
| $Z^{\mathrm{opt}}_{\mathrm{start}}$ | start of optical potential in $Z$ | 12.5 |
| $Z^{\mathrm{opt}}_{\mathrm{end}}$ | end of optical potential in $Z$ | 16.145 |
| $\mathrm{A}_Z$ | strength optical potential in $Z$ | 0.0041 |
| $r^{\mathrm{opt}}_{\mathrm{start}}$ | start of optical potential in $r$ | 4.4 |
| $r^{\mathrm{opt}}_{\mathrm{end}}$ | end of optical potential in $r$ | 8.15 |
| $\mathrm{A}_r$ | strength optical potential in $r$ | 0.005 |
| $Z(\mathrm{sp})^{\mathrm{opt}}_{\mathrm{start}}$ | start of optical potential in $Z(\mathrm{sp})$ | 22.22 |
| $Z(\mathrm{sp})^{\mathrm{opt}}_{\mathrm{end}}$ | end of optical potential in $Z(\mathrm{sp})$ | 31.265 |
| $\mathrm{A}_{Z(\mathrm{sp})}$ | strength optical potential in $Z(\mathrm{sp})$ | 0.0041 |

**Table 5.3** The lattice constants (in angstrom), and the first and second interlayer spacings (in Å) for all four computed PESs. Note that the experimental value for the lattice constant is obtained at 4.2 K, whereas the calculations assume a surface temperature of 0 K.

| | Lattice constant | $d_{1-2}$ | $d_{2-3}$ |
|---|---|---|---|
| PBE | 3.966 | 2.289 | 2.281 |
| PBE-vdW-DF | 3.996 | 2.313 | 2.304 |
| RPBE | 4.007 | 2.311 | 2.300 |
| PBE$\alpha$-vdW-DF | 3.968 | 2.294 | 2.284 |
| Experiment[77] | 3.872 | – | – |

## 5.3 Results and discussion

### 5.3.1 Potential energy surface

In table 5.3, the lattice constants and interlayer spacings, computed through energy minimization with DFT, can be found for the four different XC functionals investigated. All the computed lattice constants were converged within 0.003 Å. From the table, it becomes apparent that the calculations overestimate the lattice constant of palladium. In general, GGA functionals cannot give both correct accurate atomic exchange energies, and accurate bond lengths.[76] Since for gas-phase molecules (where GGA functionals are most applied) accurate atomic exchange energies are more important than the precise bond length, GGA functionals typically overestimate the lattice constant. Because the slab relaxations are performed with five layers, the 1$^{st}$ and 4$^{th}$, and the 2$^{nd}$ and 3$^{rd}$ interlayer spacings are almost identical to one another. Note that justifications of the use of symmetrized slabs are given in reference 50. Test calculations with slabs consisting of up to ten layers confirmed that the interlayer spacings were well converged (discrepancy at most 0.004 Å).

In figure 5.3, four relevant 2D cuts of the PES are shown for the PBE-vdW-DF functional. The top and t2f sites can have both an early and a late barrier, whereas the bridge and FCC sites are early barrier sites. In table 5.4, the corresponding barriers for dissociation of $H_2$ on Pd(111), relative to the gas-phase minimum, are given for these configurations

**Table 5.4** The energy barriers (in meV) for the dissociation of $H_2$ on Pd(111) relative to the gas-phase minimum are given for four different PESs. The configurations which are listed here are the top ($\vartheta = 90°$, $\varphi = 0°$) site, the bridge ($\vartheta = 90°$, $\varphi = 90°$) site, the FCC ($\vartheta = 90°$, $\varphi = 330°$) site, and the t2f ($\vartheta = 90°$, $\varphi = 240°$) site.

| | Top (early) | (late) | Bridge | FCC | t2f (early) | (late) |
|---|---|---|---|---|---|---|
| PBE$\alpha$-vdW-DF | – | −34 | −18 | 22 | −115 | −65 |
| PBE | −5 | 0 | 83 | 118 | 12 | −75 |
| PBE-vdW-DF | −93 | 158 | 116 | 157 | −6 | 133 |
| RPBE | 66 | 307 | 276 | 322 | 165 | 227 |

for the four PESs obtained with the different XC functionals. The first thing to note is that, as expected, the barrier heights are highly dependent on the choice of XC functional. The variation of the barrier height with impact site is also heavily dependent on the XC functional. For example for PBE the bridge site has a higher barrier than the top site, but for PBE-vdW-DF the barrier of the bridge site is actually lower than that of the top site.

The barrier heights and positions for the dissociation of $H_2$ on Pd(111) can be found in figure 5.4. Here, the top-to-bridge (top $\vartheta = 90°$, $\varphi = 0°$) cut of the potential energy is shown and the location of the barriers for the other configurations used in the construction of the PES are shown by the closed (early barriers) and open (late barriers) symbols. The colour of these symbols indicate the barrier height, with red symbols indicating energetically low barriers, and blue symbols indicating energetically high barriers. It can be seen from the figure that there is a correlation between barrier height and barrier position. The general trend is that late barriers are energetically higher than early barriers. It should be noted that, especially for PBE, this trend can be divided into two separate regimes, *i.e.*, $r < 1$ Å, and $r > 1$ Å.

The interpolation of the PESs by the CRP has been tested thoroughly. QCT calculations were used to sample configurations of the PES which are dynamically relevant. For each PES, all the intermediate points of 100 trajectories were logged for the seven different nozzle temperatures of the calculated molecular beams (see table 5.1). For 500 points

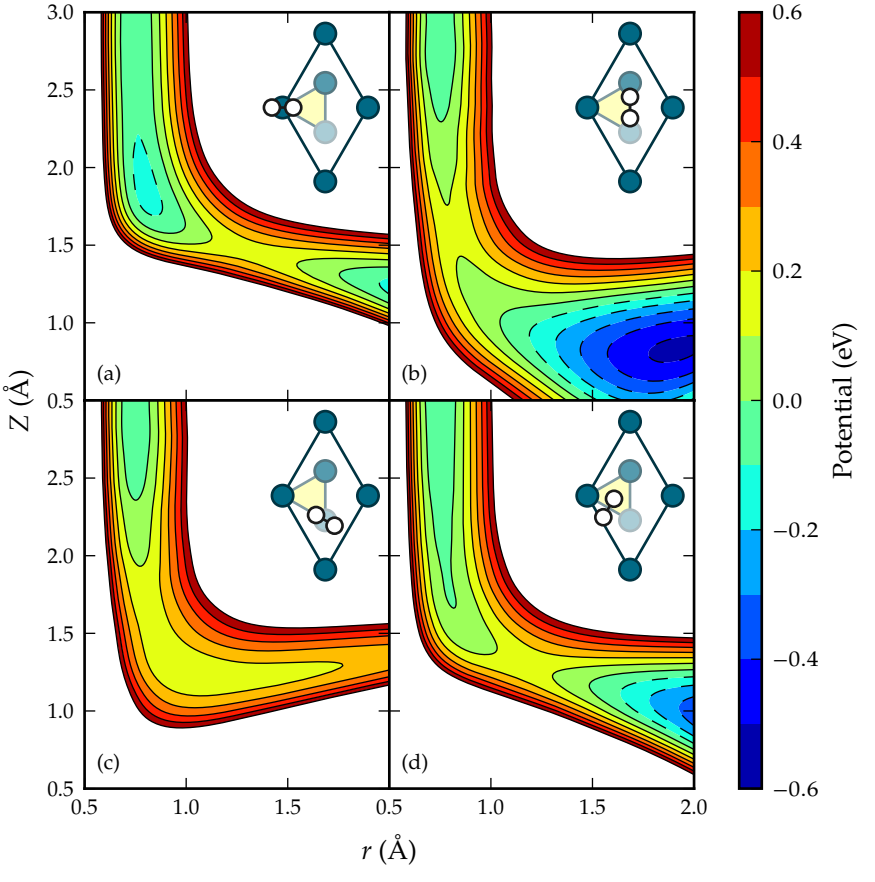


**Figure 5.3** 2D contour plots (in $Z$ and $r$) of the PBE-vdW-DF PES for four different configurations. The configurations are the (a) top ($\vartheta = 90°$, $\varphi = 0°$), (b) bridge ($\vartheta = 90°$, $\varphi = 90°$), (c) FCC ($\vartheta = 90°$, $\varphi = 330°$), and (d) t2f ($\vartheta = 90°$, $\varphi = 240°$) dissociation geometries. The zero of the potential energy is set to the gas-phase minimum energy, and the contours span the interval [−0.6, 0.6] eV, with steps of 100 meV.

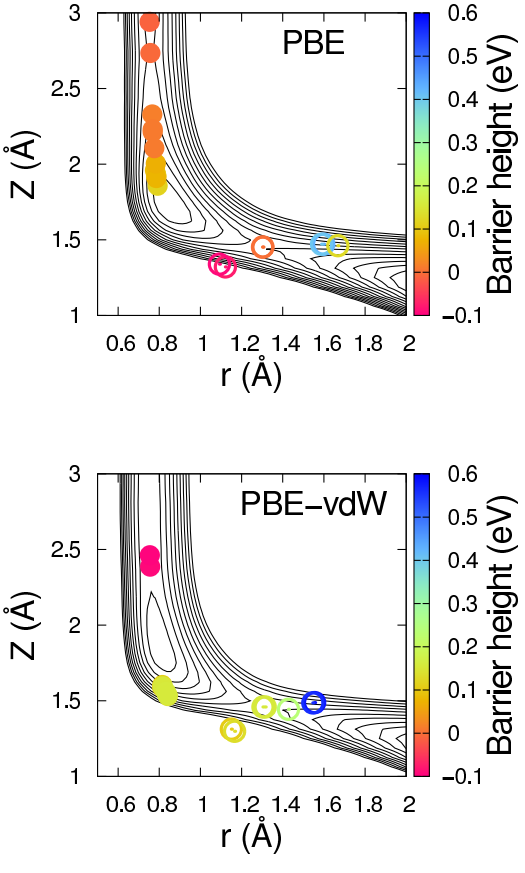


**Figure 5.4** Barrier heights and positions for $H_2$ on Pd(111) for the computed configurations used in the construction of the PES, together with the top-to-bridge (top $\vartheta = 90°$, $\varphi = 0°$) cut of the PES. Closed symbols denote early barriers, and open symbols denote late barriers. The zero of the potential energy is set equal to the gas-phase minimum energy, and the solid line contours span the interval $[-1, 0.35]$ eV, with steps of 50 meV.

(which were randomly extracted) per PES, the quality of interpolation was tested. Those points were binned on their respective $Z$ value in order to test the PES for specific regions. Bin 1 has $Z$ values of 4 to 6.5 Å, which corresponds to the gas-phase. The early barrier region has $Z$ values between 2 and 4 Å, which are binned in bin 2. All the points, which have $Z$ values of less than 2 Å, were additionally binned on their $r$ value. Bin 3 has $r$ values which are smaller than 1.5 Å, these correspond to the late barrier region. Finally, bin 4 has the points where $r > 1.5$ Å; the points in this bin correspond to trajectories which have already reacted, and these points are therefore dynamically the least important. The results, which can be found in table 5.5, show that the root mean square error (RMSE) is small for the gas-phase and early barrier region ($\sim$ 1 to 5 meV), and somewhat larger for the late barrier region (roughly $12 - 17$ meV). The largest absolute error which can be found for each PES, however, is on the order of 50 to 100 meV, and can be found in the late barrier region (bin 3). From this it can be concluded that, although overall the CRP works quite well, for specific cases the error in the interpolation of the PES can be rather large. The RMSE values reported here are somewhat larger than in previous studies,[6,71] because of the used testing procedure. Here, the sampled points were selected at random from dynamics calculations, which is more thorough than previous tests where potential cuts in only one or two dimensions were considered.



### 5.3.2 Molecular beam sticking probabilities

The accuracy of the reaction probabilities obtained with classical and QCT methods for $H_2$/Pd(111) has been studied extensively.[21,24,26] It was found that for this system the QCT method describes dynamic trapping poorly, because dynamic trapping is quenched due to an unphysical conversion of vibrational ZPE to rotational energy. The classical trajectory (CT) method describes the role of dynamic trapping much better because no initial ZPE is present. Direct dissociation, however, is not well described by the CT method. The result is that at low incidence energies both of the methods are not able to accurately calculate the reaction probability. For high incidence energies the QCT method is,

**Table 5.5** RMSE for all four different computed PESs. The test points are sampled from QCT calculations and are randomly extracted. All the test points are binned according to their $Z$ value. For $Z < 2$ Å the test points are additionally binned according to their $r$ value.

| | Bin 1 $Z = 4 - 6.5$ Å all $r$ values | | Bin 2 $Z = 2 - 4$ Å all $r$ values | | Bin 3 $Z = 0 - 2$ Å $r \leq 1.5$ Å | | Bin 4 $Z = 0 - 2$ Å $r > 1.5$ Å | |
|---|---|---|---|---|---|---|---|---|
| PES | N | RMSE (meV) | N | RMSE (meV) | N | RMSE (meV) | N | RMSE (meV) |
| PBE | 174 | 1.0 | 218 | 3.1 | 85 | 16.9 | 23 | 27.4 |
| PBE-vdW-DF | 153 | 2.9 | 307 | 5.5 | 36 | 12.2 | 4 | 22.9 |
| RPBE | 213 | 0.8 | 246 | 4.9 | 34 | 13.2 | 7 | 29.7 |
| PBE$\alpha$-vdW-DF | 143 | 3.1 | 243 | 3.9 | 86 | 13.6 | 28 | 20.4 |





CHAPTER 5

Towards a specific reaction parameter density functional for reactive scattering of $H_2$ from Pd(111)

however, in good agreement with QD, because dynamic trapping does not play a significant role for high incidence energies.[24]

Therefore, in order to check the performance of XC functionals it is best to compare reaction probabilities obtained with the QCT method with experiments for high incidence energies. If a good candidate SRP functional is found, QD calculations can then be performed for this XC functional. The results of QD calculations can then be compared with experimental sticking probabilities over the entire incidence energy region to assess the quality of the functional.

In figure 5.5, the experimental sticking probability of the latest (and presumably best) molecular beam experiment from the Rendulic group[16,17] is compared with the simulated molecular beam reaction probabilities obtained with the QCT method for four different PESs for the incidence energy region of $125 - 400$ meV, for which the QCT method should work reasonably well. It can be seen that the probability of hydrogen dissociation on Pd(111) is heavily dependent on the choice of the XC functional used in the DFT calculation of the PES. Furthermore, the reaction probability obtained with the PBE-vdW-DF functional is in reasonable agreement with experiment. Therefore, out of these functionals, the PBE-vdW-DF XC functional seems the best candidate. Hence, QD calculations will be performed for this functional only.

In order to validate if the candidate functional is indeed able to describe the molecular beam experiment also for low energies, QD calculations were performed for the PBE-vdW-DF functional. In figure 5.6, the experimental molecular beam sticking probabilities are presented from Gostein and Sitz[18] (labeled exp. Sitz), and from Lesnik[16] and Beutl *et al.*[17] (labeled exp. Rendulic 2001). The reaction probabilities obtained with the PBE-vdW-DF functional computed with the QCT method and with QD can also be found in this figure. Unfortunately, the molecular beam simulations using QD are not able to reproduce the non-monotonic behaviour of the experiment. Therefore, assuming the BOSS model gives correct results, we can disregard the PBE-vdW-DF functional as a good candidate for the specific reaction parameter functional for $H_2$/Pd(111). In fact, the QD molecular beam result is not a significant improvement over the molecular beam results obtained

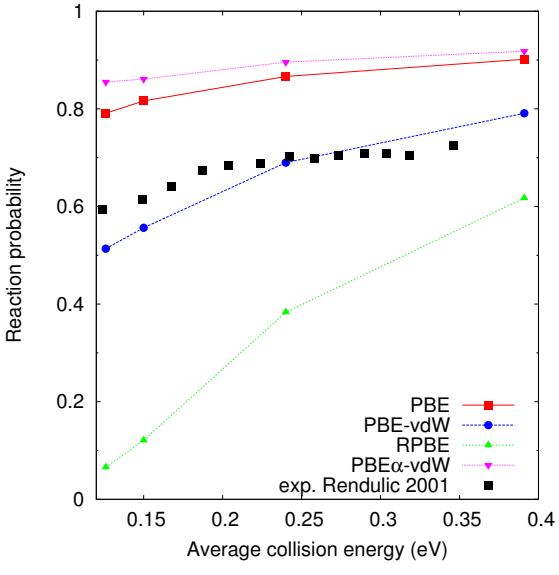


**Figure 5.5** Reaction probabilities of the simulated molecular beams computed with the QCT method alongside the experimental molecular beam sticking probabilities performed by Lesnik[16] and Beutl *et al.*[17] (labeled exp. Rendulic 2001) for an incidence energy interval of 125 − 400 meV.

with the QCT method. This suggests that (for the selected functional) quantum effects, such as ZPE and tunnelling do not play an important role, and that most of the reaction occurs classically over the energy barrier. The lack of dynamic trapping could therefore be due to the PES rather than to the use of the QCT method. It is however important to note that dynamic trapping can also be enhanced by allowing energy exchange with surface atoms,[27,28] which suggests that, apart from the functional, also surface temperature effects may need to be taken into account.

Note that the point at 35 meV (corresponding to $T_n = 100$ K) is omitted for the PBE-vdW-DF QD results. This was done because there is a large uncertainty for that point, which arises from the extrapolation of the state-resolved reaction curves towards low incidence energies. For Pd(111) it is non-trivial how to extrapolate towards low incidence energies. For activated systems the reaction curve can be extrapolated to

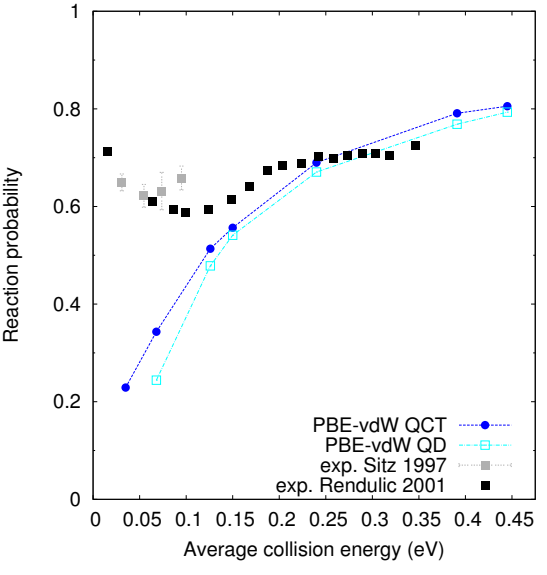


**Figure 5.6** Reaction probabilities obtained with the PBE-vdW-DF functional for the simulated molecular beams computed with the QCT method, and with QD are compared with the most experimental molecular beam sticking probabilities. The experiment by Gostein and Sitz[18] is labelled exp. Sitz 1997, and the experiment performed by Lesnik[16] and Beutl *et al.*[17] is labelled exp. Rendulic 2001.

zero, but for this non-activated system it is not clear how to extrapolate towards low incidence energies. Tests with several extrapolation schemes indicated that the resulting uncertainty in the reaction probability in the point at 35 meV can be as large as 30%. Fortunately, for all other calculated points this extrapolation towards low incidence energies does not significantly change the reaction probability (changes are in the order of 0.001).

### 5.3.3 Initial state-resolved reaction probabilities

The discrepancy between the molecular beam experiment and the simulated molecular beam with QD can have multiple causes: (i) effects of surface motion are not modelled, because of the static surface approximation in the BOSS method;[10] (ii) incorrect assumptions about the dis-

tribution of energies in the molecular beam can introduce errors; and (iii) errors in the anisotropy and corrugation of the PES. In this work, it is not studied whether surface motion plays an important role in the dissociation of $H_2$ on Pd(111), which may be important for properly describing trapping of molecules, and trapping mediated reaction.[27,28] In order to clarify the latter two points the initial state-resolved (degeneracy averaged) reaction probabilities obtained with the QCT method using four different PESs, and reaction probabilities obtained with QD for PBE-vdW-DF will be compared with the state-resolved experiment by Gostein and Sitz.[18]

In figure 5.7, initial state-resolved (degeneracy averaged) reaction probabilities can be found for the ($v = 0, J = 0$) and ($v = 0, J = 1$) states. Again, as expected, the state-resolved reaction probabilities are very dependent on the choice of XC functional. The PBE-vdW-DF functional clearly underestimates the initial state-resolved reaction probabilities for the ($v = 0, J = 0$) and ($v = 0, J = 1$) states. There is a good agreement between the state-resolved reaction probabilities obtained with the QCT method and those obtained with QD for the PBE-vdW-DF functional, especially for the ($v = 0, J = 1$) state. This confirms the previous conclusion that quantum effects do not play an important role in the reaction probability for this functional. The discrepancy observed for low incidence energies between the simulated molecular beams and the molecular beam experiments are probably not only caused by errors in the distribution of energies in the molecular beam, because also for the initial state-resolved reaction probabilities there is a discrepancy between experiment and the calculations. Furthermore, for low translational energies the width of the translational energy distribution in experiments tends to be narrow.

Surprisingly, for the ($v = 0, J = 0$) state, there is an excellent agreement between the calculated reaction probability obtained for the PBE$\alpha$-vdW-DF functional and the state-resolved experiment by Gostein and Sitz.[18] For the reaction probability of the ($v = 0, J = 1$) state, however, this good agreement is not reproduced, as can be seen on the right panel of figure 5.7. Here, PBE$\alpha$-vdW-DF clearly overestimates the reaction probability for dissociation of hydrogen on Pd(111).

In order to elucidate the origin of the discrepancy between calcu-

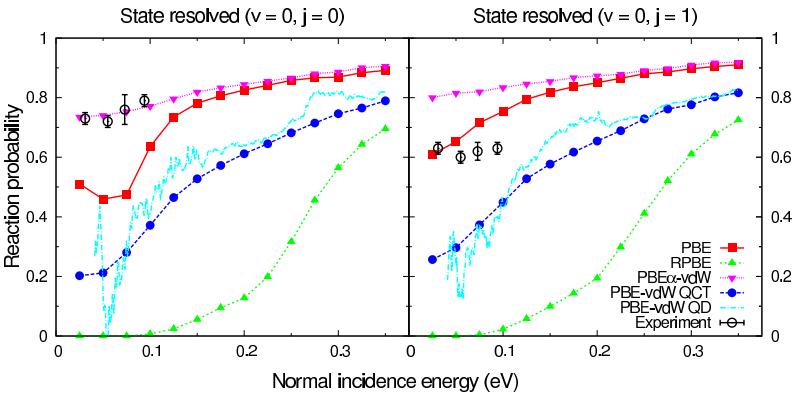


**Figure 5.7** Rotational state-resolved reaction probabilities of the dissociation of hydrogen on a Pd(111) surface. On the left ($v = 0$, $J = 0$), and on the right ($v = 0$, $J = 1$). The experiment[18] was performed with a surface temperature of 423 K. If not mentioned otherwise the calculated results are obtained with the QCT method. The quantum results have been smoothed by a weighted Gaussian with a width of 0.5 meV.

lated reaction probabilities and experiment, the reaction probability of $H_2$ dissociating on a Pd(111) surface has been plotted versus the initial rotational state ($J$) for an incidence energy of 94 meV. This is shown in figure 5.8. For all functionals the reaction probability increases with $J$ up to $J = 2$ for the calculations performed with the QCT method. Then, for all functionals except RPBE, the reaction probability decreases with increasing $J$ and stabilizes. Experimentally, however, a sharp decrease in reaction probability is observed between $J = 0$ and $J = 1$.[18] After that, the reaction probability increases a little and stabilizes. The QD calculations show a small improvement over the QCT calculations, but they are also not able to reproduce the experimental trend in the dependence of the reaction probability on $J$. The calculations cannot reproduce the decrease in reaction probability with increasing rotational quantum number ($J$), as is experimentally found.

### 5.3.4 Comparison to experiment and outlook

The discrepancies noted between the experiments and the theoretical calculations on $H_2$/Pd(111) can be due to several reasons, *i.e.*, (i) errors

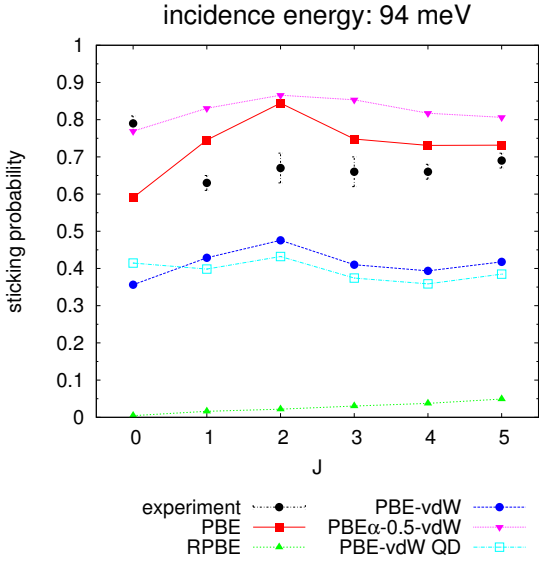


**Figure 5.8** Dissociative reaction probability as a function of initial quantum number $J$ for an incidence energy of 94 meV. If not mentioned otherwise the calculated results are obtained with the QCT method. The state-resolved experiments were performed by Gostein and Sitz.[18]

in the experiments; (ii) errors in the simulation of the experiments due to assuming wrong translational energy distributions or nozzle temperatures; (iii) errors in the PES used; and (iv) errors in the dynamical model used. These error sources will now be discussed one by one, ending with a brief outlook on how progress may be achieved with modelling the reactive scattering of $H_2$ from Pd(111) in future work.

As noted already in the introduction rather diverse sets of measurements have been published on sticking of $H_2$ on Pd(111). The latest set of measurements from the Rendulic group[16,17] and the measurements by Gostein and Sitz[18] are in reasonable agreement with one another, but they still differ from one another at the higher incidence energies probed by Gostein and Sitz (see figure 5.1). Also, for neither set of measurements the beam conditions have been published, while accurate calculations on $H_2$/Cu(111)[6] show that the knowledge of the nozzle temperature and the parameters characterising the translational energy

distribution of $H_2$ beams is essential for accurately simulating reactive scattering of $H_2$ from metal surfaces. The absence of these data (the assumption had to be made that the beam parameters for $H_2$/Pd(111) were the same as those used in other experiments of the Rendulic group on $H_2$/Cu(111)) makes it harder to describe the experiments on these systems accurately. The result that the sticking probability first decreases and then increases with incidence energy is, however, not in doubt, as it is observed in all the measurements shown in figure 5.1. We also note that knowledge of the translational energy distributions is less critical to simulating sticking measurements for low average incidence energies, as the translational energy distributions are typically rather narrow for low incidence energies (nozzle temperatures).

Errors in the PES can be due to errors in the interpolation of the DFT data and to the density functional yielding an inaccurate description of the molecule–surface interaction. Due to the accuracy of the CRP method used to interpolate the PES for $H_2$/Pd(111) (see section 5.3.1) and other $H_2$ + metal surface systems (see for instance references 6 and 44) it can be safely assumed that if errors in the PES are to blame for the discrepancy with experiment, then they are most likely due to the use of an inaccurate density functional. This point will now be discussed in more detail.

The discrepancies of the dynamics results based on the PBE-vdW-DF candidate SRP density functional with the measured sticking probabilities and initial state-resolved reaction probabilities can be summarized as follows. (i) Although the computed sticking probabilities are in reasonable agreement with the experiments of Lesnik[16] and Beutl *et al.*[17] for incidence energies $\geq 125$ meV, the computed reaction probability curve does not show the upturn occurring at low energies with decreasing incidence energy, as manifest in both the experiments of Lesnik[16] and Beutl *et al.*[17] and those by Gostein and Sitz.[18] (ii) The computed initial state-resolved reaction probabilities do not show the decrease occurring in the experimental results going from non-rotating $H_2$ ($J = 0$) to rotating $H_2$ ($J = 1 - 5$). Both experimental observations are manifestations of a reaction mechanism whereby the molecule reacts without barrier either through "steering"[36,37] or "dynamic trapping".[25,26] Molecules with a low incidence energy are more easily

trapped at the surface through energy transfer from translation to rotation,[25] and have more time to be steered to sites or orientations for which reaction is barrierless.[36] Likewise, non-rotating molecules are more easily steered to an orientation for which reaction is barrierless,[37] and they are more easily dynamically trapped.[26] Both discrepancies with experiment therefore point to one and the same defect in the theoretical treatment: the correct functional should show barrierless dissociation for at least some impact sites and orientations. The problem with the candidate PBE-vdW-DF SRP density functional is that it does not show barrierless dissociation for any of the high symmetry sites investigated. The fact that it performs well for high incidence energies suggests that a functional is needed with a broader distribution of barrier heights over the impact sites, with the distribution of barrier heights skewed more to lower energies than obtained for the PBE-vdW-DF density functional.

Finally, the discrepancies between theory and experiment can in principle also de due to the dynamical model (the BOSS model) being inadequate to describe the experiments on $H_2$/Pd(111) here discussed. For reasons discussed in section 5.2.1, it is it unlikely that the Born–Oppenheimer approximation is responsible for the large deviations between experiment and theory. The presence of phonons in the dynamical model might facilitate trapping, but for this to facilitate reaction at low incidence energies a PES which shows barrierless dissociation for at least some impact sites and orientations would still be needed. In previous calculations on this system, energy exchange was found to alter the probability for trapping.[27,28] The PES used in these studies however already showed barrierless dissociation if energy exchange was not taken into account. For these reasons, the dynamical model is not the first place to look for improvements of the theoretical description of the reactive scattering experiments on $H_2$/Pd(111) discussed here, but the possibility that phonons are needed for an accurate description of these experiments cannot be excluded.

It is therefore suggested that future theoretical calculations on $H_2$/Pd(111) first investigate the performance of candidate SRP density functionals which have a broader distribution of barrier heights for this system, so that they show barrierless dissociation for at least some impact sites and orientations, while showing similar barrier heights

at the high energy end of the spectrum. The availability of new well-characterised molecular beam sticking experiments on $H_2$/Pd(111) (or detailed information on the beam parameters used in the experiments of Lesnik *et al.* and of Gostein and Sitz) would also facilitate the development of an accurate theoretical description of this system. The availability of new and well-characterised molecular beam sticking experiments on $H_2$/Pd(100) would also be useful, as associative desorption experiments are also available for this system,[34,78] and an SRP density functional developed for $H_2$ interacting with the Pd(100) surface is likely to be accurate for $H_2$/Pd(111) as well.[13]

## 5.4 Summary and conclusions

Potential energy surfaces have been calculated for $H_2$/Pd(111) for four different XC functionals. The barrier heights are highly dependent on the choice of XC functional. Moreover, the way in which the barrier height varies with the impact site is also dependent on the choice of XC functional. It is found that there is a correlation between the barrier height and barrier position, where the general trend is that late barriers are energetically higher than early barriers. With the CRP method used to interpolate the DFT results, the RMSE of the interpolation of the PESs is small for the gas-phase and early barrier region ($\sim$ 1 to 5 meV), and somewhat larger for the late barrier region (roughly 12 to 17 meV).

A candidate SRP density functional was obtained by comparing simulated molecular beam reaction probabilities obtained with the QCT method with experimental sticking probabilities for high incidence energy (above 125 meV). The reaction probability is, as expected, heavily dependent on the choice of XC functional. The PBE-vdW-DF functional was proposed as a candidate XC functional describing the reactive scattering of $H_2$ on Pd(111), because at high incidence energies simulated molecular beam reaction probabilities obtained with the QCT method were in reasonable agreement with experimental sticking probabilities. In order to check the validity of the candidate functional, QD calculations were performed for the PBE-vdW-DF functional. The simulated molecular beam results obtained with QD, however, were not in good agreement with experimental sticking probabilities at low incidence en-

ergies. Therefore, the candidate (PBE-vdW-DF) XC functional is disregarded. The fact that the QD molecular beam simulated results are not a significant improvement over the QCT results suggest that (for the selected functional) quantum effects, such as ZPE conservation and tunnelling, do not play an important role in the reactive scattering of $H_2$ on Pd(111). In previous calculations,[24] steering effects were observed in the QD calculation of $H_2$ on Pd(111), with the PES of Dong and Hafner[20] and Busnengo *et al.*[25] based on the PW91 functional.[79]

Among the possible origins of the discrepancies between the theoretical PBE-vdW-DF results and the experimental results for $H_2$/Pd(111), the most likely cause is that the functional used does not yield barrierless dissociation for at least some impact sites and orientations, so that the upturn of the reaction probability curve at low incidence energy is not recovered. It is therefore suggested that the use of a density functional yielding a broader barrier height distribution (and barrierless dissociation for at least some impact sites and orientations) is explored first to achieve a more accurate theoretical description of $H_2$ on Pd(111). For this, the availability of new well-characterised molecular beam sticking experiments on $H_2$/Pd(111) or Pd(100) (or detailed information on the beam parameters used in the experiments of Lesnik and of Gostein and Sitz on $H_2$/Pd(111)) would also be helpful. Additionally surface temperature effects should be taken into account, as this may provide an increased probability for trapping.[27,28]



## References

[1] C. T. Rettner, D. J. Auerbach, J. C. Tully, and A. W. Kleyn. Chemical dynamics at the gas-surface interface. *Journal of Physical Chemistry* **100**(31), pp. 13021–13033, 1996.

[2] V. Smil. Detonator of the population explosion. *Nature* **400**(6743), p. 415, 1999.

[3] G. A. Somorjai and Y. Li. Impact of surface chemistry. *Proceedings of the National Academy of Sciences* **108**(3), pp. 917–924, 2011.

[4] K. Honkala, A. Hellman, I. N. Remediakis, A. Logadottir, A. Carlsson, S. Dahl, C. H. Christensen, and J. K. Nørskov. Ammonia synthesis from first-principles calculations. *Science* **307**(5709), pp. 555–558, 2005.

[5] G. J. Kroes. Frontiers in surface scattering simulations. *Science* **321**(5890), pp. 794–797, 2008.

[6] C. Díaz, E. Pijper, R. A. Olsen, H. F. Busnengo, D. J. Auerbach, and G. J. Kroes. Chemically accurate simulation of a prototypical surface reaction: $H_2$ dissociation on Cu(111). *Science* **326**(5954), pp. 832–834, 2009.

[7] B. Hammer, M. Scheffler, K. W. Jacobsen, and J. K. Nørskov. Multidimensional potential energy surface for $H_2$ dissociation over Cu(111). *Physical Review Letters* **73**(10), pp. 1400–1403, 1994.

[8] J. Zheng, Y. Zhao, and D. G. Truhlar. The DBH24/08 database and its use to assess electronic structure model chemistries for chemical reaction barrier heights. *Journal of Chemical Theory and Computation* **5**(4), pp. 808–821, 2009.

[9] K. Yang, J. Zheng, Y. Zhao, and D. G. Truhlar. Tests of the RPBE, revPBE, $\tau$-HCTHhyb, $\omega$B97X-D, and MOHLYP density functional approximations and 29 others against representative databases for diverse bond energies and barrier heights in catalysis. *Journal of Chemical Physics* **132**(16), 164117, 2010.

[10] G. J. Kroes and C. Díaz. Quantum and classical dynamics of reactive scattering of $H_2$ from metal surfaces. Accepted to *Chemical Society Reviews*. doi: 10.1039/C5CS00336A. 2016.

[11] Y. Y. Chuang, M. L. Radhakrishnan, P. L. Fast, C. J. Cramer, and D. G. Truhlar. Direct dynamics for free radical kinetics in solution: solvent effect on the rate constant for the reaction of methanol with atomic hydrogen. *Journal of Physical Chemistry A* **103**(25), pp. 4893–4909, 1999.

[12] A. Chakraborty, Y. Zhao, H. Lin, and D. G. Truhlar. Combined valence bond-molecular mechanics potential-energy surface and direct dynamics study of rate constants and kinetic isotope effects for the H + $C_2H_6$ reaction. *Journal of Chemical Physics* **124**(4), 044315, 2006.

[13] L. Sementa, M. Wijzenbroek, B. J. van Kolck, M. F. Somers, A. Al-Halabi, H. F. Busnengo, R. A. Olsen, G. J. Kroes, M. Rutkowski, C. Thewes, N. F. Kleimeier, and H. Zacharias. Reactive scattering of $H_2$ from Cu(100): comparison of dynamics calculations based on the specific reaction parameter approach to density functional theory with experiment. *Journal of Chemical Physics* **138**(4), 044708, 2013.

[14] Ch. Resch, H. F. Berger, K. D. Rendulic, and E. Bertel. Adsorption dynamics for the system hydrogen/palladium and its relation to the surface electronic structure. *Surface Science* **316**(3), pp. L1105–L1109, 1994.

[15] M. Beutl, M. Riedler, and K. D. Rendulic. Strong rotational effects in the adsorption dynamics of $H_2$/Pd(111): evidence for dynamical steering. *Chemical Physics Letters* **247**(3), pp. 249–252, 1995.

[16] J. Lesnik. Untersuchungen über Vorläuferadsorption an Übergangsmetallen und Übergangsmetallegierungen. PhD thesis. Technischen Universität Graz, 2001.

[17] M. Beutl, J. Lesnik, K. D. Rendulic, R. Hirschl, A. Eichler, G. Kresse, and J. Hafner. There is a true precursor for hydrogen adsorption after all: the system $H_2$/Pd(111) + subsurface V. *Chemical Physics Letters* **342**(5–6), pp. 473–478, 2001.

[18] M. Gostein and G. O. Sitz. Rotational state-resolved sticking coefficients for $H_2$ on Pd(111): testing dynamical steering in dissociative adsorption. *Journal of Chemical Physics* **106**(17), pp. 7378–7390, 1997.

[19] A. Winkler. Personal communication. 2012.

[20] W. Dong and J. Hafner. $H_2$ dissociative adsorption on Pd(111). *Physical Review B* **56**(23), pp. 15396–15403, 1997.

[21] H. F. Busnengo, A. Salin, and W. Dong. Representation of the 6D potential energy surface for a diatomic molecule near a solid surface. *Journal of Chemical Physics* **112**(17), pp. 7641–7651, 2000.

[22] C. Crespos, H. F. Busnengo, W. Dong, and A. Salin. Analysis of $H_2$ dissociation dynamics on the Pd(111) surface. *Journal of Chemical Physics* **114**(24), pp. 10954–10962, 2001.

[23] H. F. Busnengo, C. Crespos, W. Dong, A. Salin, and J. C. Rayez. Role of orientational forces in nonactivated molecular dissociation on a metal surface. *Physical Review B* **63**(4), 041402, 2001.

[24] H. F. Busnengo, E. Pijper, M. F. Somers, G. J. Kroes, A. Salin, R. A. Olsen, D. Lemoine, and W. Dong. Six-dimensional quantum and classical dynamics study of $H_2$(v=0,J=0) scattering from Pd(111). *Chemical Physics Letters* **356**(5–6), pp. 515–522, 2002.

[25] H. F. Busnengo, C. Crespos, W. Dong, J. C. Rayez, and A. Salin. Classical dynamics of dissociative adsorption for a nonactivated system: the role of zero point energy. *Journal of Chemical Physics* **116**(20), pp. 9005–9013, 2002.

[26] H. F. Busnengo, E. Pijper, G. J. Kroes, and A. Salin. Rotational effects in dissociation of $H_2$ on Pd(111): quantum and classical study. *Journal of Chemical Physics* **119**(23), pp. 12553–12562, 2003.

[27] H. F. Busnengo, W. Dong, and A. Salin. Trapping, molecular adsorption, and precursors for nonactivated chemisorption. *Physical Review Letters* **93**(23), 236103, 2004.

[28] H. F. Busnengo, M. A. Di Césare, W. Dong, and A. Salin. Surface temperature effects in dynamic trapping mediated adsorption of light molecules on metal surfaces: $H_2$ on Pd(111) and Pd(110). *Physical Review B* **72**(12), 125411, 2005.

[29] H. F. Busnengo, W. Dong, P. Sautet, and A. Salin. Surface temperature dependence of rotational excitation of $H_2$ scattered from Pd(111). *Physical Review Letters* **87**(12), 127601, 2001.

[30] C. Díaz, H. F. Busnengo, F. Martin, and A. Salin. Angular distribution of $H_2$ molecules scattered from the Pd(111) surface. *Journal of Chemical Physics* **118**(6), pp. 2886–2892, 2003.

[31] K. D. Rendulic, G. Anger, and A. Winkler. Wide range nozzle beam adsorption data for the systems $H_2$/nickel and $H_2$/Pd(100). *Surface Science* **208**(3), pp. 404–424, 1989.

[32] C. T. Rettner and D. J. Auerbach. Search for oscillations in the translational energy dependence of the dissociation of $H_2$ on Pd(100). *Chemical Physics Letters* **253**(3–4), pp. 236–240, 1996.

[33] D. Wetzig, R. Dopheide, M. Rutkowski, R. David, and H. Zacharias. Rotational alignment in associative desorption of $D_2(v'' = 0$ and 1) from Pd(100). *Physical Review Letters* **76**(3), pp. 463–466, 1996.

[34] D. Wetzig, M. Rutkowski, W. Etterich, R. David, and H. Zacharias. Rotational alignment in associative desorption of $H_2$ from Pd(100). *Surface Science* **402–404**, pp. 232–235, 1998.

[35] D. Barredo, G. Laurent, C. Díaz, P. Nieto, H. F. Busnengo, A. Salin, D. Farías, and F. Martín. Experimental evidence of dynamic trapping in the scattering of $H_2$ from Pd(110). *Journal of Chemical Physics* **125**(5), 051101, 2006.

[36] A. Gross, S. Wilke, and M. Scheffler. Six-dimensional quantum dynamics of adsorption and desorption of $H_2$ at Pd(100): steering and steric effects. *Physical Review Letters* **75**(14), pp. 2718–2721, 1995.

[37] A. Gross, S. Wilke, and M. Scheffler. Six-dimensional quantum dynamics of adsorption and desorption of $H_2$ at Pd(100): no need for a molecular precursor adsorption state. *Surface Science* **357–358**, pp. 614–618, 1996.

[38] A. Gross and M. Scheffler. *Ab initio* quantum and molecular dynamics of the dissociative adsorption of hydrogen on Pd(100). *Physical Review B* **57**(4), pp. 2493–2506, 1998.

[39] A. Gross. *Ab initio* molecular dynamics simulations of the adsorption of $H_2$ on palladium surfaces. *ChemPhysChem* **11**(7), pp. 1374–1381, 2010.

[40] A. Gross. Coverage effects in the adsorption of $H_2$ on Pd(100) studied by *ab initio* molecular dynamics simulations. *Journal of Chemical Physics* **135**(17), 174707, 2011.

[41] M. A. Di Césare, H. F. Busnengo, W. Dong, and A. Salin. Role of dynamic trapping in $H_2$ dissociation and reflection on Pd surfaces. *Journal of Chemical Physics* **118**(24), pp. 11226–11234, 2003.

[42] A. Dianat and A. Gross. High-dimensional quantum dynamical study of the dissociation of $H_2$ on Pd(110). *Journal of Chemical Physics* **120**(11), pp. 5339–5346, 2004.

[43] C. Díaz, F. Martín, H. F. Busnengo, and A. Salin. Theoretical analysis of the relation between $H_2$ dissociation and reflection on Pd surfaces. *Journal of Chemical Physics* **120**(1), pp. 321–328, 2004.

[44] P. Nieto, E. Pijper, D. Barredo, G. Laurent, R. A. Olsen, E. J. Baerends, G. J. Kroes, and D. Farías. Reactive and nonreactive scattering of $H_2$ from a metal surface is electronically adiabatic. *Science* **312**(5770), pp. 86–89, 2006.

[45] A. C. Luntz and M. Persson. How adiabatic is activated adsorption/associative desorption? *Journal of Chemical Physics* **123**(7), 074704, 2005.

[46] J. I. Juaristi, M. Alducin, R. Díez Muiño, H. F. Busnengo, and A. Salin. Role of electron–hole pair excitations in the dissociative adsorption of diatomic molecules on metal surfaces. *Physical Review Letters* **100**(11), 116102, 2008.

[47] G. Füchsel, S. Schimka, and P. Saalfrank. On the role of electronic friction for dissociative adsorption and scattering of hydrogen molecules at a Ru(0001) surface. *Journal of Physical Chemistry A* **117**(36), pp. 8761–8769, 2013.

[48] C. Díaz, R. A. Olsen, D. J. Auerbach, and G. J. Kroes. Six-dimensional dynamics study of reactive and non reactive scattering of $H_2$ from Cu(111) using a chemically accurate potential energy surface. *Physical Chemistry Chemical Physics* **12**(24), pp. 6499–6519, 2010.

[49] F. Nattino, C. Díaz, B. Jackson, and G. J. Kroes. Effect of surface motion on the rotational quadrupole alignment parameter of $D_2$ reacting on Cu(111). *Physical Review Letters* **108**(23), 236104, 2012.

[50] A. Mondal, M. Wijzenbroek, M. Bonfanti, C. Díaz, and G. J. Kroes. Thermal lattice expansion effect on reactive scattering of $H_2$ from Cu(111) at $T_s$ = 925 K. *Journal of Physical Chemistry A* **117**(36), pp. 8770–8781, 2013.

[51] G. Kresse and J. Hafner. *Ab initio* molecular dynamics for liquid metals. *Physical Review B* **47**(1), pp. 558–561, 1993.

[52] G. Kresse and J. Hafner. *Ab initio* molecular-dynamics simulation of the liquid-metal–amorphous-semiconductor transition in germanium. *Physical Review B* **49**(20), pp. 14251–14269, 1994.

[53] G. Kresse and J. Furthmüller. Efficiency of *ab initio* total energy calculations for metals and semiconductors using a plane-wave basis set. *Computational Materials Science* **6**(1), pp. 15–50, 1996.

[54] G. Kresse and J. Furthmüller. Efficient iterative schemes for *ab initio* total-energy calculations using a plane-wave basis set. *Physical Review B* **54**(16), pp. 11169–11186, 1996.

[55] G. te Velde and E. J. Baerends. Precise density-functional method for periodic structures. *Physical Review B* **44**(15), pp. 7888–7903, 1991.

[56] G. te Velde and E. J. Baerends. Slab versus cluster approach for chemisorption studies. CO on Cu(100). *Chemical Physics* **177**(2), pp. 399–406, 1993.

[57] R. A. Olsen, G. J. Kroes, and E. J. Baerends. Atomic and molecular hydrogen interacting with Pt(111). *Journal of Chemical Physics* **111**(24), pp. 11155–11163, 1999.

[58] T. J. Frankcombe, M. A. Collins, and D. H. Zhang. Modified Shepard interpolation of gas-surface potential energy surfaces with strict plane group symmetry and translational periodicity. *Journal of Chemical Physics* **137**(14), 144701, 2012.

[59] J. P. Perdew, K. Burke, and M. Ernzerhof. Generalized gradient approximation made simple. *Physical Review Letters* **77**(18), pp. 3865–3868, 1996.

[60] B. Hammer, L. B. Hansen, and J. K. Nørskov. Improved adsorption energetics within density-functional theory using revised Perdew-Burke-Ernzerhof functionals. *Physical Review B* **59**(11), pp. 7413–7421, 1999.

[61] M. Dion, H. Rydberg, E. Schröder, D. C. Langreth, and B. I. Lundqvist. Van der Waals density functional for general geometries. *Physical Review Letters* **92**(24), 246401, 2004.

[62] G. K. H. Madsen. Functional form of the generalized gradient approximation for exchange: the PBE$\alpha$ functional. *Physical Review B* **75**(19), 195108, 2007.

[63] J. Klimeš, D. R. Bowler, and A. Michaelides. Van der Waals density functionals applied to solids. *Physical Review B* **83**(19), 195131, 2011.

[64] G. Román-Pérez and J. M. Soler. Efficient implementation of a van der Waals density functional: application to double-wall carbon nanotubes. *Physical Review Letters* **103**(9), 096102, 2009.

[65] M. A. L. Marques, M. J. T. Oliveira, and T. Burnus. Libxc: a library of exchange and correlation functionals for density functional theory. *Computer Physics Communications* **183**(10), pp. 2272–2281, 2012.

[66] P. E. Blöchl. Projector augmented-wave method. *Physical Review B* **50**(24), pp. 17953–17979, 1994.

[67] G. Kresse and D. Joubert. From ultrasoft pseudopotentials to the projector augmented-wave method. *Physical Review B* **59**(3), pp. 1758–1775, 1999.

[68] D. Vanderbilt. Soft self-consistent pseudopotentials in a generalized eigenvalue formalism. *Physical Review B* **41**(11), pp. 7892–7895, 1990.

[69] G. Kresse and J. Hafner. Norm-conserving and ultrasoft pseudopotentials for first-row and transition elements. *Journal of Physics: Condensed Matter* **6**(40), pp. 8245–8257, 1994.

[70] E. Pijper, G. J. Kroes, R. A. Olsen, and E. J. Baerends. The effect of corrugation on the quantum dynamics of dissociative and diffractive scattering of $H_2$ from Pt(111). *Journal of Chemical Physics* **113**(18), pp. 8300–8312, 2000.

[71] R. A. Olsen, H. F. Busnengo, A. Salin, M. F. Somers, G. J. Kroes, and E. J. Baerends. Constructing accurate potential energy surfaces for a diatomic molecule interacting with a solid surface: $H_2$+Pt(111) and $H_2$+Cu(100). *Journal of Chemical Physics* **116**(9), pp. 3841–3855, 2002.

[72] R. Kosloff. Time-dependent quantum-mechanical methods for molecular dynamics. *Journal of Physical Chemistry* **92**(8), pp. 2087–2100, 1988.

[73] E. Pijper, G. J. Kroes, R. A. Olsen, and E. J. Baerends. Reactive and diffractive scattering of $H_2$ from Pt(111) studied using a six-dimensional wave packet method. *Journal of Chemical Physics* **117**(12), pp. 5885–5898, 2002.

[74] H. F. Berger. Über den Einfluß des Quantenzustands auf die dissoziative Adsorption von Wasserstoff. PhD thesis. Technischen Universität Graz, 1992.

[75] D. W. Marquardt. An algorithm for least-squares estimation of nonlinear parameters. *SIAM Journal on Applied Mathematics* **11**(2), pp. 431–441, 1963.

[76] J. P. Perdew, A. Ruzsinszky, G. I. Csonka, O. A. Vydrov, G. E. Scuseria, L. A. Constantin, X. Zhou, and K. Burke. Restoring the density-gradient expansion for exchange in solids and surfaces. *Physical Review Letters* **100**(13), 136406, 2008.

[77] J. A. Rayne. Elastic constants of palladium from 4.2–300 °K. *Physical Review* **118**(6), pp. 1545–1549, 1960.

[78] D. Wetzig, M. Rutkowski, R. David, and H. Zacharias. Rotational corrugation in associative desorption of $D_2$ from Cu(111). *Europhysics Letters* **36**(1), pp. 31–36, 1996.

[79] J. P. Perdew, J. A. Chevary, S. H. Vosko, K. A. Jackson, M. R. Pederson, D. J. Singh, and C. Fiolhais. Atoms, molecules, solids, and surfaces: applications of the generalized gradient approximation for exchange and correlation. *Physical Review B* **46**(11), pp. 6671–6687, 1992.

CHAPTER 6

# Performance of a non-local van der Waals density functional on the dissociation of $H_2$ on metal surfaces

This chapter is based on:

M. Wijzenbroek, D. M. Klein, B. Smits, M. F. Somers, and G. J. Kroes. Performance of a non-local van der Waals density functional on the dissociation of $H_2$ on metal surfaces. *Journal of Physical Chemistry A* **119**(50), pp. 12146–12158, 2015.

## Abstract

Van der Waals functionals have been applied in chapter 4 to obtain a potential energy surface to describe the dissociation of $H_2$ on Ru(0001). An improvement was found for computed reaction probabilities compared to experiment, which could not be achieved with the use of other exchange–correlation functionals. It is, however, not yet clear to what extent van der Waals functionals give a better description of other molecule–metal surface systems. In this chapter, the optPBE-vdW-DF functional is compared to the SRP48 functional, which was originally fitted to describe the dissociation of $H_2$ on Cu(111), in terms of the resulting potential energy surfaces and results of quasi-classical dynamics calculations and their agreement with experiment for different $H_2$–metal surface systems. It is found that overall the optPBE-vdW-DF functional yields potential energy surfaces which are very similar to potential energy surfaces computed with the SRP48 functional. In dynamics calculations the optPBE-vdW-DF functional gives a slightly better description of molecular beam experiments. Also a different dependence of reaction on the rotational quantum number $J$ is found, which is in better agreement with experimental data for $H_2$ dissociation on Cu(111). The vibrational efficacy is found to be relatively insensitive to which of the two functionals is chosen.


## 6.1 Introduction

To perform accurate calculations on molecule–surface reactions, it is important to have an accurate potential energy surface (PES). It is, however, not clear which precise electronic structure method should be used to compute such a PES in order to obtain a desirable accuracy. In practice, due to limitations in computational power, one is limited to density functional theory (DFT)[1,2] using approximate exchange–correlation (XC) functionals. These functionals are usually taken to be generalized gradient approximation (GGA)[3–8] level functionals due to the larger computational expense of higher level methods such as meta-generalized gradient approximation (meta-GGA)[9–11] level functionals, and hybrid functionals,[12] which introduce Hartree–Fock exchange into

the functional. Additionally, because for such systems often only dynamical properties such as reaction probabilities are known from experiments, and no or little knowledge is available from higher level electronic structure methods, it is often necessary to perform dynamics calculations[13,14] in order to benchmark electronic structure methods. This further makes such investigations computationally challenging, as either a high dimensional PES is needed, or dynamics needs to be performed based on energies and forces computed directly on the DFT level in *ab initio* molecular dynamics (AIMD) calculations.

One particular example of molecule–metal surface reactions is the dissociation of $H_2$ on metal surfaces. This particular example is a useful benchmark system for electronic structure methods, for several reasons. First of all, a large amount of experimental data is available for such systems. Additionally, these systems have also been well studied in theoretical calculations using various electronic structure and dynamics methods (see for instance references 13–23).

Second, in general molecule–surface systems are rather complex because, apart from the degrees of freedom of the molecule, in principle also degrees of freedom from the surface should be included, such as phonons and electron–hole pair excitations.[15,24,25] It is however expected for hydrogen dissociation on metal surfaces that the effects associated with these degrees of freedom are rather limited. For $H_2$ dissociation on metal surfaces the neglect of electron–hole pair excitations and surface motion seems to be a good approximation. it has been argued[16] for $H_2$ dissociation on Pt(111) that electron–hole pair excitations should not play an important role in such processes. Additionally, for $H_2$ dissociation on Cu(111),[26,27] Cu(110)[28] and Ru(0001)[22] non-adiabatic effects have been taken into account in dynamical calculations using electronic friction. In these calculations no large non-adiabatic effects were found, which suggests that for $H_2$–metal systems the Born–Oppenheimer approximation works well. Furthermore, for activated dissociation systems energy exchange with phonons is expected to be a small effect[29,30] due to the large mass mismatch between the $H_2$ molecule and a metal surface atom. The validity of the neglect of surface motion and surface temperature has been recently tested for $H_2$ dissociation on Cu(111), using AIMD calculations,[21] in which the surface atoms were allowed to

move. Additionally, calculations have been performed in chapter 3 on the same system using a static corrugation model (SCM), in which energy exchange with the surface is not possible, but the displacement of surface atoms and thermal expansion of the crystal lattice are taken into account. In particular, in both studies, a good agreement with ideal static surface calculations was found for $H_2$ dissociation on a low temperature Cu(111) surface ($T_s = 120\,K$).

Finally, because hydrogen is a small and simple molecule, if the surface degrees of freedom are neglected, the PES of the reaction is relatively simple (6-dimensional) and it becomes feasible to accurately map out the PES. Additionally, symmetry is often present in the systems of interest and thus can often be applied in the construction of the PES, as is often done in for example the corrugation reducing procedure (CRP).[31,32] The application of symmetry can often reduce the computational costs for PESs for $H_2$ dissociation on ideal low-index surfaces considerably. Hydrogen–metal surface systems thus are useful for benchmarking the performance of electronic structure methods for molecule–surface reactions.[25]

It has been shown in chapter 4 for hydrogen dissociation on Ru(0001), which is a system with low barriers to reaction, that a functional containing vdW-DF[33] or vdW-DF2[34] correlation was needed to obtain a good agreement with experimental data, and that other functionals did not give a proper 'width' of the reaction probability as a function of incidence energy. It is however not yet clear to what extent vdW-DF-like functionals improve or worsen agreement for other systems, such as systems with a high barrier to reaction like $H_2$ dissociation on Cu(111) or Cu(100), or other systems with low barriers to reaction such as $H_2$ dissociation on Pt(111).

One of the problems of DFT for molecule–surface reactions is that computed barrier heights are often not in agreement with experiments and can differ wildly for different functionals, as shown in chapter 4 and reference 18. It is known that, for barriers of gas-phase reactions, using GGA level functionals mean absolute errors are obtained which are at best 4 kcal/mol.[35–37] Recently, fitted functionals on the meta-GGA level have been proposed claiming mean absolute errors of about 2 kcal/mol.[37–40] It is however not clear how such functionals would

perform for molecule–surface reactions as such systems have not been considered for the fitting set of these functionals.

To address the problem of accuracy in DFT, Díaz *et al.*[18] proposed an implementation of the specific reaction parameter (SRP) approach[41] in which the XC functional is adapted to the system at hand by optimising $\alpha$ in

$$E_{XC}^{SRP} = \alpha E_{XC}^{1} + (1 - \alpha) E_{XC}^{2}, \tag{6.1}$$

where $E_{XC}^{1}$ and $E_{XC}^{2}$ are two 'standard' (*i.e.*, GGA level) XC functionals, of which one generally tends to provide barriers which are too low, while the other generally provides barriers which are too high. Standard XC functionals used for molecule–surface reactions are the PW91[6] (or the similar PBE[7]) and RPBE[8] functionals. The optimisation of $\alpha$ is done in such a way that an important experiment which provides information about the barrier height is well described. As a result, one hopes that the barrier heights for the system are well described and that other observables that have not been fitted are better described for the system considered. The downside of such a procedure however is that it gives only limited predictive power, as for each specific system of interest in principle at least one experiment is needed in order to construct such a functional, which then is specific to one particular system. The quality of the description thus relies on the quality of the experiment to which the functional was fitted. Note however that the functional which was fitted for $H_2$ dissociation on Cu(111)[18] could also give a reasonable description of experimental data of $H_2$ dissociation on Cu(100),[42] suggesting that an XC functional which works well for one system may also work well for a sufficiently similar system.

In the present study an SRP approach is not taken. Instead, in order to investigate to what extent current XC functionals can describe $H_2$–metal surface systems, and to what extent van der Waals effects are needed for a description of such systems, the performance of functionals for not one but several $H_2$–metal systems is considered. The $H_2$/Cu(111), $H_2$/Cu(100), $H_2$/Pt(111) and $H_2$/Ru(0001) systems are considered, because relatively well characterised experimental data is available for these systems. Two functionals are considered, one with a non-local van der Waals correction to the correlation functional and one

without. For the non-corrected functional SRP48[21] is taken, as this functional gives a good agreement with experiments for $H_2$/Cu(111).

Over the past years, the inclusion of van der Waals effects in DFT has gathered a large interest, in particular for the interaction of molecules with surfaces.[43–47] Many methods to incorporate van der Waals effects in DFT have been developed, including the vdW-DF method by Dion *et al.*,[33] the DFT-D3 method by Grimme *et al.*[48] and the PBE+vdW method by Tkatchenko and Scheffler.[49] For a full overview, the reader is referred to recent review papers, such as references 44 or 45. In the vdW-DF method non-local correlation is used in an XC functional instead of standard (semi-)local correlation. Several revisions of this method have been published, including revisions of the vdW-DF correlation functional such as vdW-DF2,[34] but also functionals in which other exchange functionals such as optB88 and optPBE,[50] optB86b,[51] C09[52] and LV-PW86r,[53] are combined with the vdW-DF correlation functional. Recently, it has been shown for adsorption of benzene on transition metal surfaces that the optB88-vdW-DF and optPBE-vdW-DF functionals yield good adsorption energies, whereas the original vdW-DF and vdW-DF2 XC functionals yield adsorption energies that are smaller than the experimental values.[54–56] For $H_2$ dissociation on Ru(0001) it was found in chapter 4 that the vdW-DF and vdW-DF2 XC functionals yield barriers for reaction that are too high. For these reasons, here the optPBE-vdW-DF functional is chosen as the vdW-corrected functional to be tested. This functional has also recently been tested for the dissociation of $N_2$ on W(110).[57]

In section 6.2 the methods used are explained, beginning with the dynamical model in section 6.2.1. The construction of the PESs needed for the calculations is explained in section 6.2.2, and the computational details are given in section 6.2.3. The results are given in section 6.3, beginning with several properties and differences of the computed PESs in section 6.3.1. Molecular beam sticking results are shown in section 6.3.2 and state-resolved reaction probabilities and rotational quadrupole alignment parameters are considered in section 6.3.3. Effects of changing the exchange functional and correlation functional separately are discussed in section 6.3.4. Finally, the conclusions are given in section 6.4.

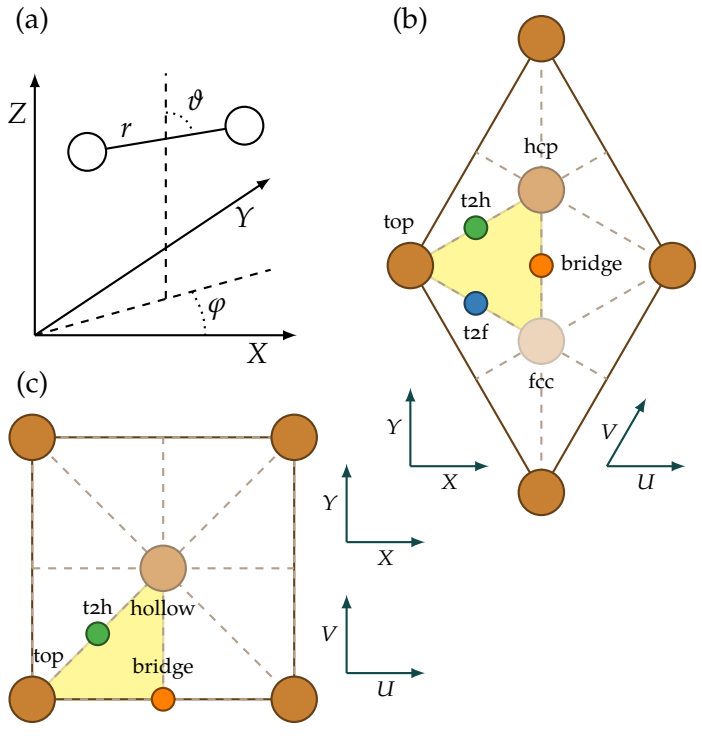


**Figure 6.1** (a) The center of mass coordinate system used for the description of the $H_2$ molecule. (b) The surface unit cell and the sites considered for the Cu(111), Pt(111) and Ru(0001) surfaces. (c) The surface unit cell and the sites considered for the Cu(100) surface. In both (b) and (c), the origin of the coordinate system ($X = U = 0$, $Y = V = 0$, $Z = 0$) is at a top layer atom (top site). In (b), the fcc site is above a third layer atom for Cu(111) and Pt(111), but for Ru(0001) no surface atom is present at this site.

## 6.2 Theory

### 6.2.1 Dynamical model

In all calculations the Born–Oppenheimer static surface (BOSS) model is used. As suggested by the name of the model, first of all, the Born–Oppenheimer approximation[58] is used. Second, the surface atoms are taken to be fixed at their ideal lattice positions. As a result, only the 6 degrees of freedom of the $H_2$ molecule are taken into account in the dynamical model. In figure 6.1(a), the coordinate system used is shown,

in figure 6.1(b) the surface unit cell for the Cu(111), Pt(111) and Ru(0001) systems, and in figure 6.1(c) the surface unit cell for the Cu(100) system.

Quasi-classical dynamics calculations are performed in favour of quantum dynamics calculations for computational simplicity. For activated $H_2$ and, in particular, $D_2$ dissociation on metal surfaces, this is in general a good approximation, as shown for $H_2$ dissociation on Cu(111),[18,59,60] Cu(100),[61] Ru(0001) (chapter 4) and Pt(111),[62] *i.e.*, for all systems considered here. In the dynamics calculations the Hamilton equations of motion are solved using the extrapolation method by Stoer and Bulirsch.[63] The initial conditions of the $H_2$ molecules are selected using standard Monte Carlo methods. In order to obtain $m_J$ resolved reaction probabilities, the initial angular momentum of the molecule is fixed by $L = \sqrt{J(J+1)}\hbar$ and the orientation is chosen with the constraint $\cos\vartheta_L = m_J/\sqrt{J(J+1)}$, where $\vartheta_L$ is the angle between the angular momentum vector and the surface normal. To obtain accurate statistics, for each set of incidence conditions at least $10^4$ trajectories were computed. The $H_2$ molecule is initially placed beyond the point where the PES no longer depends on $Z$ ($Z > 6.5$ Å). The molecule is considered to have dissociated when $r > 2.25$ Å, and the molecule is considered to have scattered when $Z > 6.5$ Å with the momentum vector pointing away from the surface.

### 6.2.2 Construction of potential energy surfaces

Full 6D PESs were constructed from self-consistent DFT calculations using the optPBE-vdW-DF[50] and SRP48[21] functionals. The SRP48 functional contains a linear combination of 48 % RPBE exchange[8] and 52 % PBE exchange[7] together with PBE correlation.[7] The optPBE-vdW-DF functional combines an optimized PBE-like exchange functional (optPBE[50]) with vdW-DF correlation.[33]

In the interpolation of the PESs the CRP,[31,32] discussed in section 2.1.1, is used. The idea behind the CRP is to interpolate $I^{6D}$ instead of $V^{6D}$, as $I^{6D}$ is much less corrugated in the $U$, $V$, $\vartheta$ and $\varphi$ degrees of freedom than $V^{6D}$ is (see section 2.1.1 for the definition of these symbols).[31] The $(U, V)$ coordinate system is a coordinate system in which the surface lattice vectors are taken as unit vectors. For $H_2$ dissociation

**Table 6.1** Configurations used in the interpolation of the $H_2$/Cu(100) PESs. The sites listed here correspond to the sites listed in table 6.2, and are also shown graphically in figure 6.1(c).

| Site | $\vartheta$ (°) | $\varphi$ (°) |
|---|---|---|
| Top | 0 | |
| Top | 90 | 0, 45 |
| t2h | 0 | |
| t2h | 45 | 45, 135, 225 |
| t2h | 90 | 45, 135 |
| Hollow | 0 | |
| Hollow | 90 | 0, 45 |
| Bridge | 0 | |
| Bridge | 90 | 0, 45, 90 |

on Cu(111), Pt(111) and Ru(0001) the skewing angle of this coordinate system thus is 60°, while for $H_2$ dissociation on Cu(100) the skewing angle is 90° as for the Cartesian coordinate system (also see figure 6.1(b) and (c)). The interpolation over $U$, $V$, $\vartheta$ and $\varphi$ is done using symmetry adapted functions, in a way similar to the method used for $H_2$/Cu(100) by Olsen *et al.*[32] The interpolation procedure used for potentials for the $H_2$/Cu(111), Pt(111) and Ru(0001) systems is the same as used in chapter 4 for $H_2$/Ru(0001) (p3m1 symmetry). The interpolation for $H_2$/Cu(100) (p4mm symmetry) is detailed below.

For the interpolation of $I^{6D}$ for potentials with p4mm symmetry, 16 configurations ($U$, $V$, $\vartheta$, $\varphi$) are used, spread over 4 different sites ($U$, $V$). These sites are also shown in figure 6.1(c). The configurations used are shown in table 6.1. The interpolation is done in several steps. First, for every configuration, the interpolation is performed over the $r$ and $Z$ degrees of freedom. For this interpolation a $14 \times 14$ ($r \times Z$) grid is used employing a 2D cubic spline interpolation, where $r_{\text{min}} = 0.4$ Å, $r_{\text{max}} = 2.3$ Å, $Z_{\text{min}} = 0.25$ Å and $Z_{\text{max}} = 4$ Å. Then, for every site ($U$, $V$) the interpolation is performed over the $\vartheta$ and $\varphi$ degrees of freedom using symmetry adapted sine and cosine functions. Finally, an interpolation over $U$ and $V$ is performed, for which again symmetry adapted sine and

**Table 6.2** Sites used in the interpolation of the H/Cu(100) PES.

| Site | $u$ | $v$ |
|---|---|---|
| Top | 0 | 0 |
| t2h | 1/4 | 1/4 |
| Hollow | 1/2 | 1/2 |
| b2h | 1/2 | 1/4 |
| Bridge | 1/2 | 0 |
| t2b | 1/4 | 0 |

cosine functions are used.

In order to represent interactions that are rather long-ranged in the potential, the potential is switched between $Z = 3.4$ Å and 4.0 Å from the full 6D potential to a 2D gas-phase potential only dependent on $r$ and $Z$, because far away from the surface the corrugation is small. This gas phase potential is represented by

$$V^{2D}(r, Z) = V^{ext}(Z) + V^{gas}(r), \tag{6.2}$$

where $V^{ext}$ is a function describing the dependence of the PES on $Z$ beyond $Z = 4$ Å and $V^{gas}$ is the interaction at $Z = Z_{asy}$, taken to be 6.5 Å.

For the interpolation of $I^{3D}$ six sites in $(u, v)$ are used for the potentials with p4mm symmetry, which are listed in table 6.2. The sites b2h and t2b correspond to the sites in between bridge and hollow, and top and bridge, respectively. For each site, 57 points are taken in $Z$, with $Z_{min} = -1.06$ Å and $Z_{max} = 5.6$ Å. The reference function $V^{1D}$ is taken to be the H atom–surface interaction for the H atom above the top site, as used in previous studies.[31]

### 6.2.3 Computational details

For the electronic structure calculations version 5.2.12 of the VASP[64–67] software package was used. For calculations with the SRP48 functional, the standard[68] VASP ultrasoft pseudopotentials[69] were used. For the optPBE-vdW-DF functional, the standard[67] projector augmented wave

(PAW)[70] potentials were used. VASP evaluates the non-local vdW-DF correlation functional within the scheme of Román-Pérez and Soler.[71]

For the computation of the PESs, a $9 \times 9 \times 1$ Γ-centered $k$-point mesh was used with a plane wave cut-off of 400 eV, except for the $H_2$/Ru(0001) PESs where a $8 \times 8 \times 1$ mesh was used with a plane wave cut-off of 350 eV. For $H_2$ dissociation on Cu(100) and Cu(111), a 4 layer slab was used, while for $H_2$ dissociation on Ru(0001) and Pt(111) a 5 layer slab was used, which is consistent with previous calculations[16,18,42] on these systems (see also chapter 4). In all cases a $2 \times 2$ supercell was considered with a 13 Å vacuum between different images of the slab. Fermi smearing with a width of 0.1 eV was used to speed up convergence of the DFT calculations. The convergence with respect to the plane wave cut-off and $k$-point sampling was tested for $H_2$/Cu(111) and $H_2$/Pt(111) at three different geometries close to or at the barrier geometry and is expected to be well within 10 meV of the fully converged value.

## 6.3 Results and discussion

### 6.3.1 Potential energy surfaces and barrier heights

In table 6.3 barrier heights are given for three high symmetry dissociation paths for the computed PESs, together with the distance of the $H_2$ molecule to the surface ($Z$) and the distance between the two H atoms ($r$) at the transition state. For the $H_2$/Cu(111) and $H_2$/Cu(100) systems, both functionals predict the lowest barrier to be for bridge-to-hollow (BtH) dissociation, consistent with previous calculations.[18,42] For these systems the energetic corrugation (denoted in table 6.3 by $\xi$, here defined as the difference between the highest and lowest investigated barrier) is smaller for the optPBE-vdW-DF functional than for the SRP48 functional. For the $H_2$/Ru(0001) and $H_2$/Pt(111) systems, both functionals predict the lowest barrier to be for top-to-bridge (TtB) dissociation, which is also consistent with previous calculations[16,20,72] (see also chapter 4). For these systems the optPBE-vdW-DF functional yields a larger energetic corrugation than the SRP48 functional. Compared to the SRP48 barrier heights, for the $H_2$/Cu(111) and $H_2$/Cu(100) systems the optPBE-vdW-DF functional generally predicts larger barrier heights,

**Table 6.3** Barrier heights ($E_b$), positions ($r_b$, $Z_b$) and energetic corrugation ($\xi$, in eV) for SRP48 and optPBE-vdW-DF PESs for $H_2$ dissociation on Cu(111), Cu(100), Ru(0001) and Pt(111) above three different sites. For all geometries, $\vartheta = 90°$. On the HCP and hollow sites, $\varphi = 0°$. Also see figure 6.1(b) and figure 6.1(c) and the definitions given in the text.

| | | SRP48 | | | optPBE-vdW-DF | | |
|---|---|---|---|---|---|---|---|
| | | $E_b$ (eV) | $r_b$ (Å) | $Z_b$ (Å) | $E_b$ (eV) | $r_b$ (Å) | $Z_b$ (Å) |
| **Cu(111)** | BtH | 0.636 | 1.030 | 1.172 | 0.712 | 1.053 | 1.165 |
| | TtB | 0.887 | 1.396 | 1.394 | 0.915 | 1.382 | 1.396 |
| | HCP | 1.047 | 1.539 | 1.269 | 1.070 | 1.427 | 1.271 |
| | $\xi$ | 0.411 | | | 0.358 | | |
| **Cu(100)** | BtH | 0.742 | 1.239 | 0.992 | 0.822 | 1.237 | 0.996 |
| | HOL | 0.836 | 1.099 | 1.031 | 0.896 | 1.112 | 1.050 |
| | TtB | 0.867 | 1.432 | 1.379 | 0.883 | 1.413 | 1.383 |
| | $\xi$ | 0.125 | | | 0.074 | | |
| **Ru(0001)** | TtB | 0.066 | 0.757 | 2.650 | −0.013 | 0.755 | 2.662 |
| | BtH | 0.281 | 0.789 | 1.997 | 0.219 | 0.793 | 1.934 |
| | HCP | 0.398 | 0.812 | 1.869 | 0.361 | 0.835 | 1.762 |
| | $\xi$ | 0.332 | | | 0.374 | | |
| **Pt(111)** | TtB | 0.102 | 0.767 | 2.292 | 0.034 | 0.774 | 2.152 |
| | HCP | 0.490 | 0.847 | 1.669 | 0.506 | 0.874 | 1.602 |
| | BtH | 0.492 | 0.837 | 1.602 | 0.530 | 0.862 | 1.506 |
| | $\xi$ | 0.390 | | | 0.496 | | |

whereas the optPBE-vdW-DF barrier heights for $H_2$/Ru(0001) are generally smaller. For $H_2$/Pt(111), the optPBE-vdW-DF barrier height is smaller for TtB dissociation, but larger for HCP and BtH dissociation.

The barrier positions for the two PESs are similar for the $H_2$/Cu(111) and $H_2$/Cu(100) systems, but are less similar for the $H_2$/Ru(0001) and $H_2$/Pt(111) systems, where the barriers for optPBE-vdW-DF are mostly closer to the surface than for SRP48. For $H_2$/Ru(0001), in chapter 4, where a large number of functionals were considered, it was found for the TtB barrier that functionals containing vdW-DF correlation predict a barrier closer to the surface than functionals containing another type of correlation, *e.g.*, PBE correlation as used in the SRP48 functional, for

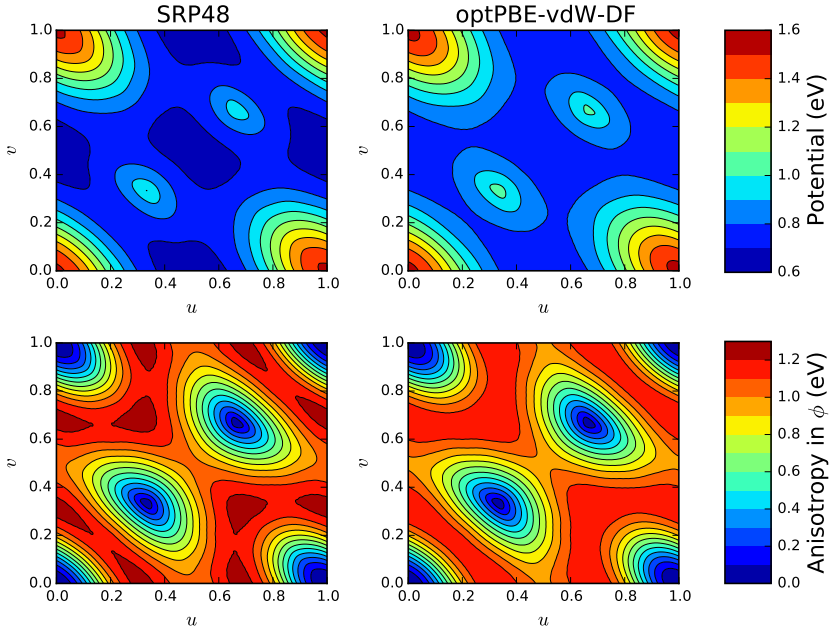


**Figure 6.2** $(U, V)$ dependence of the PESs for $H_2$ dissociation on Cu(111), for $r = 1.2$ Å, $Z = 1.2$ Å and $\vartheta = 90°$. Top panels: full potential with $\varphi$ optimized. Bottom panels: anisotropy in $\varphi$, as explained in the text.

a similar barrier height. The present results for Ru(0001), but also for Pt(111), are in agreement with this.

In figure 6.2 the $(U, V)$ dependence of the SRP48 and optPBE-vdW-DF PESs for $H_2$ dissociation on Cu(111) is shown, together with the anisotropy in $\varphi$ at the same points, for a point ($r = 1.2$ Å, $Z = 1.2$ Å) close to the barrier geometry with $\vartheta = 90°$. The anisotropy in $\varphi$ is here defined as the difference between the highest and lowest potential encountered while rotating the molecule around 360° over $\varphi$ for $\vartheta = 90°$. The potential energy shown in the top panels is the minimum potential energy encountered during this rotation over $\varphi$.

The anisotropy of the two potentials close to the barrier geometry is remarkably similar, with the anisotropy for optPBE-vdW-DF being slightly lower than the anisotropy for SRP48. The remarkable similarity

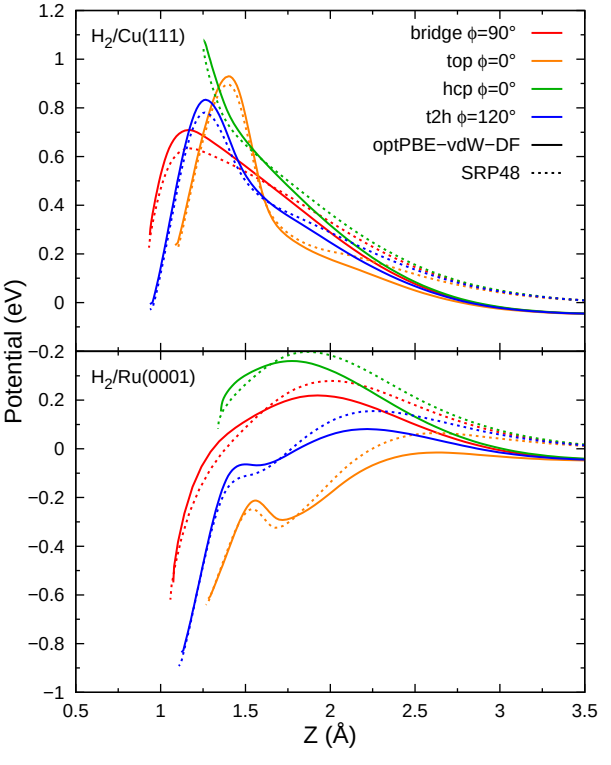


**Figure 6.3** Reaction paths based on nudged elastic band (NEB) calculations on a spline interpolation of computed 2D PES cuts for the $H_2$/Cu(111) and $H_2$/Ru(0001) systems, for four different dissociation geometries. A potential of 0 eV corresponds to the gas-phase minimum. Results for optPBE-vdW-DF are indicated by solid lines, while results for SRP48 are indicated by dotted lines.

between the SRP48 and optPBE-vdW-DF PESs for both the full potential, minimized over $\varphi$, and the anisotropy in $\varphi$, as well as the barrier positions shown in table 6.3, suggests that also dynamical observables that are dependent on more detailed properties of the PES, such as the anisotropy or the corrugation of the PES should be reasonably similar, except for a small shift or broadening due to the different barrier heights. Similar plots for the other systems considered show similar behaviour in the sense that the anisotropy of the SRP48 and optPBE-vdW-DF PESs is at least qualitatively similar.

Minimum energy paths were computed with the nudged elastic band (NEB) method applied to 2D cuts through the interpolated PES for $H_2$ dissociation on Cu(111) and Ru(0001) for four different dissociation pathways. These pathways are shown in figure 6.3. Several features of the PES are apparent in this figure. First of all, far away from the surface, near $Z = 3.5$ Å, the optPBE-vdW-DF potential is lower than the SRP48 potential. This is a result of the van der Waals attraction, which leads to a well in the PES. This well is present in the optPBE-vdW-DF PESs, but not in the SRP48 PESs, as (semi-)local functionals such as SRP48 cannot describe van der Waals effects.[45] Beyond this well, moving the molecule closer to the surface, the PES for both functionals qualitatively changes in the same way: the ordering of the potential for different reaction paths is the same for both surfaces.

There are, however, some more subtle differences which seem to be relevant. First of all, for $H_2$ dissociation on Cu(111), the optPBE-vdW-DF potential rises more quickly when the molecule is moved toward the surface than for the SRP48 potential. This causes the optPBE-vdW-DF and SRP48 potentials to cross one another at about $Z = 1.6$ Å. Second, for $H_2$ dissociation on Ru(0001), similar effects occur although the effects seem smaller for this system. In this case a similar crossing occurs as for Cu(111), but here the crossing occurs after the SRP48 transition state, at about $Z = 1.6 - 1.8$ Å, similar to the crossing for Cu(111). In the optPBE-vdW-DF PES, the $Z$ dependence of the potential for $H_2$/Ru(0001) is also somewhat stronger than in the SRP48 PES, although this effect seems to be smaller than for $H_2$ dissociation on Cu(111). The barriers for $H_2$ dissociation on Ru(0001) are generally closer to the surface for optPBE-vdW-DF than for SRP48. $H_2$/Cu(100) behaves similarly to $H_2$/Cu(111), while $H_2$/Pt(111) behaves similarly to $H_2$/Ru(0001).

It is clear that such effects should be present if a functional with a van der Waals correction is used which, additionally, gives the same or nearly the same description of the barrier height as the non-vdW functional, as is the case here. The interaction present in the regular, non-vdW corrected functional approximately starts at a value of $Z$ which corresponds to the bottom of the van der Waals well. In order to obtain the same barrier height and position with the vdW functional that the

non-vdW functional would yield (the effective barrier from this point to reaction has gone up by the well depth), this non-vdW interaction in the vdW corrected functional either has to start earlier (at a larger value of $Z$) or has to be stronger (*i.e.*, yields a stronger $Z$ dependence of the potential). As shown in figure 6.3, the non-vdW interaction does not seem to start earlier for optPBE-vdW-DF than for SRP48 (an extrapolation of the SRP48 curves to the bottom of the well in figure 6.3 suggests the interaction should then start at $Z \approx 3.5$ Å). As this is not the case, the $Z$ dependence of the potential should be stronger. A proper van der Waals corrected functional for such systems is therefore expected to yield a steeper $Z$ dependence than a non-vdW corrected functional would.

By considering these effects for early and late barriers it is possible to explain the differences between SRP48 and optPBE-vdW-DF barriers in table 6.3, as well as make more general predictions for differences between van der Waals and standard GGA functionals. Due to the steeper $Z$ dependence of the PES, for late barriers, which occur beyond the crossing point ($Z < 1.6$ Å), the barrier will in general be increased by going from SRP48 to optPBE-vdW-DF. For systems containing only late barriers, such as the highly activated $H_2$/Cu(111) and $H_2$/Cu(100) here, all barrier heights will therefore in general increase. For early barriers, which occur before the crossing point ($Z > 1.8$ Å), the barrier will in general be decreased and occur at a smaller value of $Z$ for the optPBE-vdW-DF functional. The results in table 6.3 are mostly in agreement with this. It should be noted that for $H_2$ dissociation on Ru(0001) it was previously found that there is a trend between the barrier height and position, in the sense that higher barriers generally occur closer to the surface,[72] which was also found in chapter 4. For systems containing early barriers such as $H_2$/Pt(111) and $H_2$/Ru(0001) however, in general both earlier and later barriers will be present, and for these systems the later barrier heights therefore increase slightly compared to the earlier barrier heights, yielding an increased energetic corrugation. It should be noted that, in principle, these arguments can be extended to other pairs of well performing functionals and systems as well, provided that one knows where the crossing point for the two functionals occurs, which is determined by the steepness of the potential in $Z$ and the depth of the

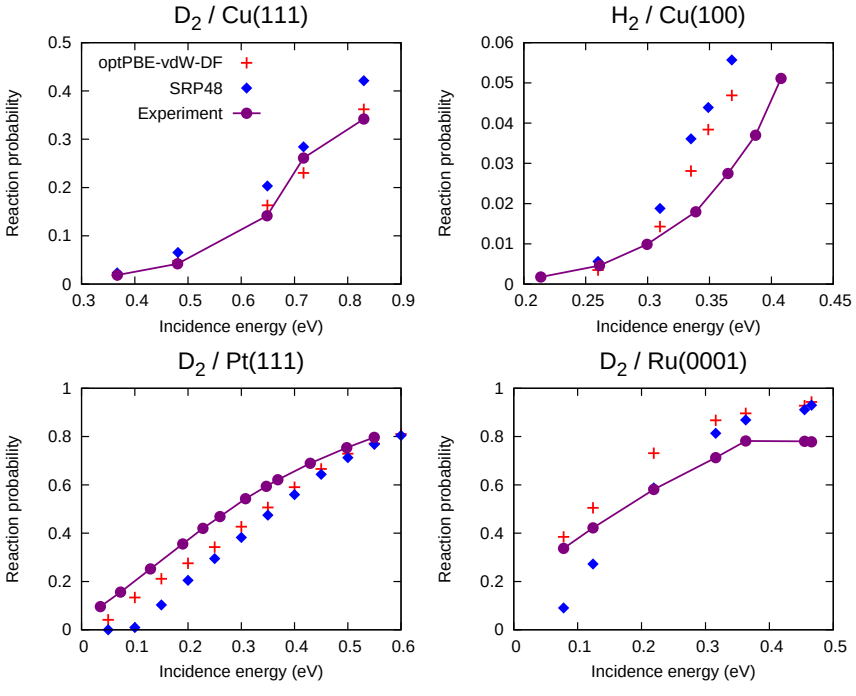


**Figure 6.4** Molecular beam simulations for the optPBE-vdW-DF and SRP48 functionals, applied to the four systems considered in this study. Beam parameters used for the Cu(111) and Cu(100) calculations were taken from Díaz *et al.*[18] Beam parameters used for the Ru(0001) calculations were taken from chapter 4. For the Pt(111) surface the ($\nu = 0$, $J = 0$) reaction probability is shown as no beam parameters are known. Experimental data for Cu(111) by Michelsen *et al.*,[73] for Cu(100) by Anger *et al.*,[74] for Pt(111) by Luntz *et al.*[75] and Ru(0001) by Groot *et al.*[76]

physisorption well.

### 6.3.2 Molecular beam sticking

In figure 6.4 sticking probabilities are shown for $D_2$ dissociation on Cu(111), $H_2$ dissociation on Cu(100) and $D_2$ dissociation on Ru(0001), and the initial state-resolved reaction probability is shown for ($\nu = 0$, $J = 0$) $D_2$ dissociation on Pt(111), for the optPBE-vdW-DF and SRP48 functionals. A comparison is made with available experimental data.[73–76] As expected, for $D_2$ dissociation on Cu(111) the SRP48 re-

action probability is in good agreement with experiment. This is not surprising because this functional was constructed[18,21] to reproduce this particular molecular beam experiment. The optPBE-vdW-DF functional also performs well, giving somewhat lower reaction probabilities in line with the higher barriers present in the PES (see table 6.3). For $H_2$ dissociation on Cu(100) the same holds. The agreement for the SRP48 functional is similar to that found in previous calculations with a similar functional,[42] and the agreement for the optPBE-vdW-DF functional is again somewhat better due to the higher barriers to dissociation given by this functional. For $D_2$ dissociation on Pt(111) and Ru(0001), however, the optPBE-vdW-DF functional gives higher reaction probabilities than the SRP48 functional. For $D_2$ dissociation on Pt(111), the agreement is better for the optPBE-vdW-DF functional than for the SRP48 functional. The optPBE-vdW-DF reaction probability rises less steeply with increasing incidence energy than the SRP48 reaction probability. Such a 'broadening' effect resulting from the use of XC functionals containing vdW-DF correlation was also found for hydrogen dissociation on Ru(0001) in chapter 4. Finally, for $D_2$ dissociation on Ru(0001), the SRP48 functional gives a reaction probability curve which is too narrow, which was also found in previous calculations with a similar functional.[20] The optPBE-vdW-DF functional gives a somewhat better width for the reaction probability curve and better agreement with experiment. Overall, for the systems considered here, the optPBE-vdW-DF functional tends to outperform the SRP48 functional.

### 6.3.3 State-resolved reaction probability and rotational quadrupole alignment



In figure 6.5 the reaction probability for ($v = 0, J = 0$) and ($v = 1, J = 0$) $D_2$ dissociating on Cu(111) is shown for the SRP48 and optPBE-vdW-DF functionals. Despite the difference in energetic corrugation (for SRP48 $\xi = 0.411\,\text{eV}$, while for optPBE-vdW-DF $\xi = 0.358\,\text{eV}$), for neither ($v = 0, J = 0$) nor ($v = 1, J = 0$) $D_2$ noticeable differences are found between the slopes of the reaction probability curves obtained with the two functionals, which contrasts with the large difference found for $H_2$

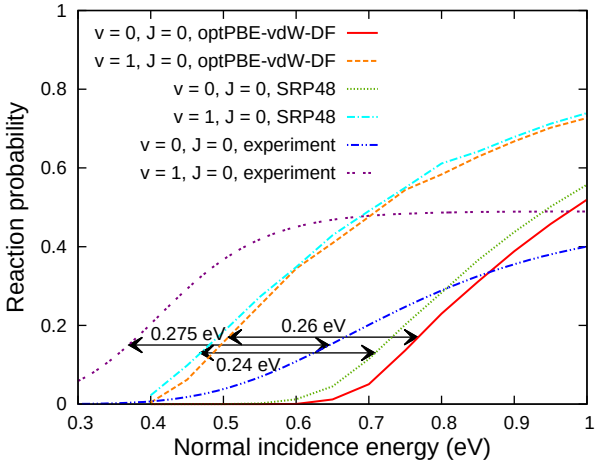


**Figure 6.5** Reaction probability as a function of normal incidence energy for ($\nu = 0$, $J = 0$) $D_2$ and ($\nu = 1$, $J = 0$) $D_2$ dissociating on Cu(111) for the SRP48 and optPBE-vdW-DF functionals. $\Delta E_0$ at a reaction probability of 15% are indicated. Experimental data for $T_s = 925$ K by Michelsen *et al.*,[73] reanalysed by Nattino *et al.*[77]

**Table 6.4** Vibrational efficacy for ($\nu = 0 \rightarrow 1$) $D_2$ dissociating on Cu(111).

| Method | Vibrational efficacy |
|---|---|
| SRP48 | 0.65 |
| optPBE-vdW-DF | 0.71 |
| Re-analysis[77] ($P_{r,0} = 0.05$) | 0.62 |
| Re-analysis[77] ($P_{r,0} = 0.15$) | 0.74 |
| Re-analysis[77] ($P_{r,0} = 0.25$) | 0.88 |

dissociation on Ru(0001) in chapter 4. The ($\nu = 0$) and ($\nu = 1$) curves have a similar shape and slope for each functional, in disagreement with the results of the analysis of experiments, which show large differences between the slopes of ($\nu = 0$) and ($\nu = 1$) curves.[73,77] Note, however, that the effect of surface temperature is not taken into account in the calculations reported here, and it is known from experiments that this should cause a broadening of the reaction probability curves, which should be prominent at the experimental $T_s$ (925 K).[78,79]

The use of the optPBE-vdW-DF functional leads to a slightly higher value of the vibrational efficacy ($\chi_\nu = 0.71$) than the use of the SRP48 functional ($\chi_\nu = 0.65$) (see table 6.4). This reflects the slightly larger shift of the ($\nu = 1$) reaction probability curve relative to the ($\nu = 0$) curve for the optPBE-vdW-DF functional (0.26 eV) than observed for the SRP48 functional (0.24 eV, see equation (2.40)). These numbers can be compared to the value of $\chi_\nu$ that can be obtained from a recent re-analysis[77] of the original experimental data.[73] This experimental value depends on the value selected for $P_{r,0}$ used to define $E_0$ in equation (2.40) (see section 2.5.4) because the shapes of the reaction probability curves for ($\nu = 1$) and ($\nu = 0$) extracted from experiment differ: for $P_{r,0} = 0.15$, $\chi_\nu = 0.74$ is obtained, and for $P_{r,0} = 0.05$, $\chi_\nu = 0.62$ (see table 6.4). To which theoretical value of $\chi_\nu$ the experimental value should be compared is not so straightforward. The experimental fits could be argued to be the most accurate where the time-of-flight (TOF) intensity is highest. For ($\nu = 0, J = 0$) this is at a reaction probability of about 0.1. On the other hand, the reaction probability at the so-called effective barrier height in the old experimental fits was 0.135 and 0.25, for $\nu = 0$ and $\nu = 1$, respectively. To a good approximation, at the corresponding collision energy the reaction probability does not vary with $T_s$.[78,79] A useful compromise therefore seems to be to evaluate the vibrational efficacy for a reaction probability of about 0.15. As it is not fully clear which reaction probability should be considered, the vibrational efficacy is shown for several values of the reaction probability in table 6.4. On the basis of these values, no preference for SRP48 or optPBE-vdW-DF can be found from the calculated $\chi_\nu$, as both functionals perform equally well. Finally, note that the experimental value for $D_2$/Cu(111) was originally reported to be $\chi_\nu = 0.54$,[73] but this was based on a different definition of the vibrational efficacy, in which different values for $P_{r,0}$ are used for $\nu = 0$ and $\nu = 1$.

In figure 6.6 the reaction probability for ($\nu = 0, J = 0, 2, 4, 6, 8$) $D_2$ dissociating on Cu(111) is shown for both tested functionals, also comparing to the reaction probability curves extracted from experiments.[77] The analysis of the experimental results showed that reaction first decreases with $J$, up to about $J = 4$, and then increases with $J$.[73,77] The behaviour of the optPBE-vdW-DF results is closest to this: for optPBE-

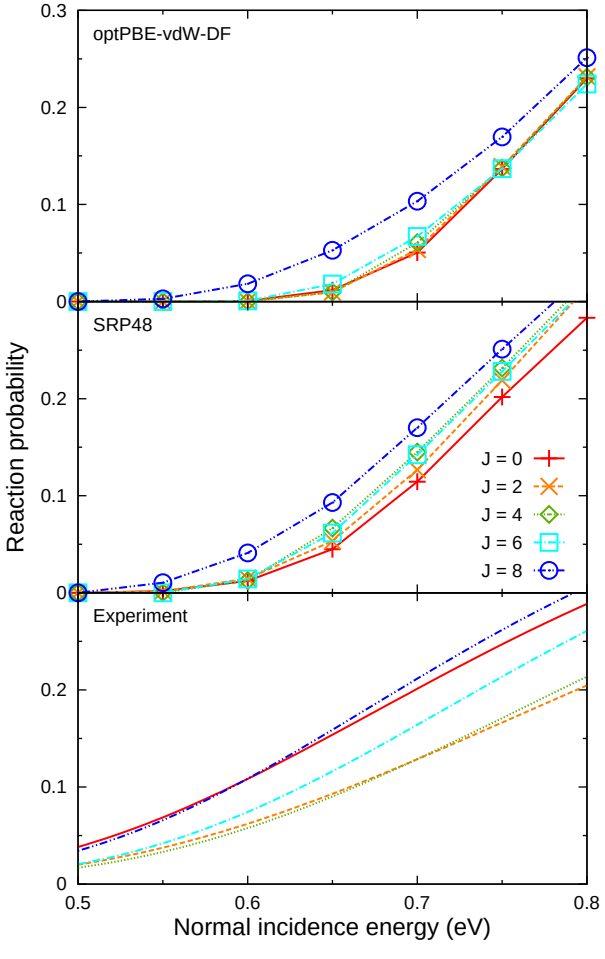


**Figure 6.6** Reaction probability as a function of normal incidence energy for several rotational states of $D_2$ dissociating on Cu(111) for the optPBE-vdW-DF and SRP48 functionals. Fits to experimental results[73] at $T_s = 925$ K by Nattino *et al.*[77]

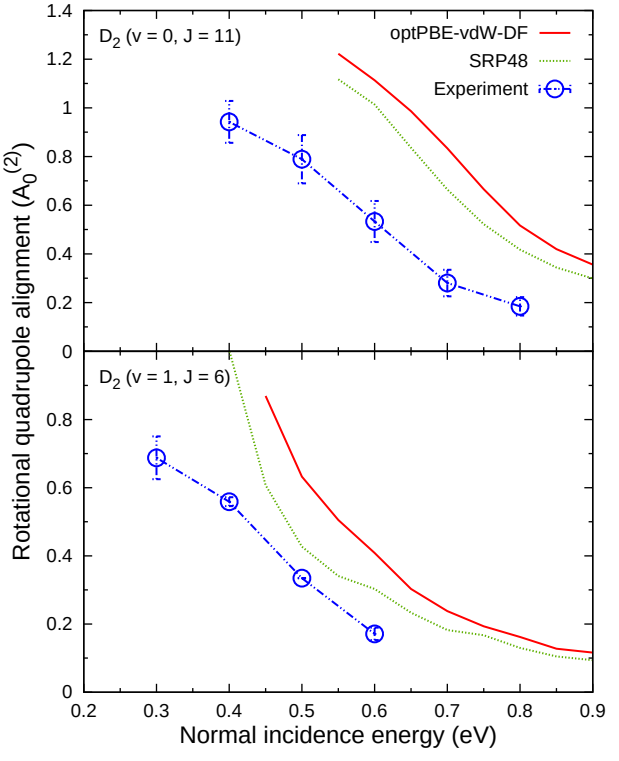


**Figure 6.7** Rotational quadrupole alignment parameter for $D_2$ dissociation on Cu(111) as a function of normal incidence energy for the optPBE-vdW-DF and SRP48 functionals. Experimental results at $T_s = 925\,K$ by Hou *et al.*[80]

vdW-DF, up to $J = 6$ no large dependence of reaction on $J$ is found, and for higher $J$ the reaction probability increases with $J$. For the SRP48 functional, however, reaction actually increases up to about $J = 4$, in direct contrast to the behaviour observed in experiment. The optPBE-vdW-DF functional therefore seems to show a somewhat better performance than the SRP48 functional.

The rotational quadrupole alignment parameter $A_0^{(2)}(v, J)$ is shown in figure 6.7 for ($v = 0$, $J = 11$) and ($v = 1$, $J = 6$) $D_2$ dissociating on Cu(111) for both functionals, also comparing to experiments.[80] The $A_0^{(2)}(v, J)$ computed with SRP48 is shifted to lower energies than the one computed with optPBE-vdW-DF for both states at all energies considered, by about 0.05 eV for ($v = 0$, $J = 11$) and 0.06 eV for ($v = 1$,

**Table 6.5** Minimum barrier height ($E_b$, in eV) and energetic corrugation ($\xi$, in eV), of $H_2$/Cu(111) obtained with the optPBE and PBE exchange functionals combined with PBE correlation.

| Exchange functional | $E_b$ (eV) | $\xi$ (eV) |
|---|---|---|
| optPBE | 0.460 | 0.416 |
| PBE | 0.484 | 0.406 |

$J = 6$). The agreement of the static ideal surface theoretical results with the experimental data is not so good for either state and for either functional. However, previous work employing the SRP48 functional[21] and a similar functional (chapter 3) showed that taking into account the effect of the surface temperature used in the experiments (925 K[80]) leads to a substantial decrease of the computed $A_0^{(2)}(\nu, J)$ and to much better agreement with experiment, although the computed $A_0^{(2)}(\nu, J)$ were still somewhat too high. Taking into account the surface temperature for the optPBE-vdW-DF functional should also lead to a decrease in the $A_0^{(2)}(\nu, J)$ computed with this functional, and to a better agreement with experiment. It is however not yet clear whether surface temperature has the same quantitative effect for the optPBE-vdW-DF functional, and it is therefore not yet fully clear which functional performs better for $A_0^{(2)}(\nu, J)$.

### 6.3.4 The effect of changing the exchange and the correlation functionals separately

In the above sections, dynamics results for two XC functionals, *i.e.*, the SRP48 and the optPBE-vdW-DF XC functionals, have been discussed. One might wonder whether some of the results that are obtained, such as the better performance of optPBE-vdW-DF for sticking of $D_2$ on Ru(0001) (figure 6.4) or the difference in performance of the two functionals for reproducing the $A_0^{(2)}$ measured for $D_2$/Cu(111) (figure 6.7), is due to changing the exchange functional, the correlation functional, or both. The following can be said about this.

Starting from the SRP48 functional, changing only the exchange functional amounts to using the optPBE exchange functional and the

PBE correlation functional ("optPBE-PBE"). Inspection of table 6.5 suggests that this would yield a functional that is similar to the PBE functional: for $H_2$/Cu(111), the minimum barrier height and the energetic corrugation are very similar for these functionals. However, it is known that the PBE functional does not yield a correct description of sticking of $H_2$ to Ru(0001) (see figure 4.10) because functionals with PBE correlation underestimate the energetic corrugation of the $H_2$/Ru(0001) PES, as shown in chapter 4. Specifically, with the PBE functional the sticking probability is considerably overestimated at large average collision energies, and the same would be expected to hold for the similar optPBE-PBE functional. In contrast, reasonable values of both the minimum barrier height and the energetic corrugation can be obtained by using vdW-DF correlation. In fact, using SRP48 exchange and vdW-DF correlation would be very similar to using one of the candidate SRP functionals that described sticking of $H_2$ and $D_2$ to Ru(0001) quite well in chapter 4 and even better than the optPBE-vdW-DF functional. Here, the only difference between the SRP48 and the candidate SRP functional is that the former employs 48% RPBE and 52% PBE exchange, whereas the latter uses 50% RPBE and 50% PBE exchange. In other words, the better performance of the optPBE-vdW-DF functional than that of SRP48 comes from changing the PBE to the vdW-DF correlation functional, and not from changing the SRP48 to the optPBE exchange functional.

Similarly, the good performance of the optPBE-vdW-DF functional for $H_2$/Cu(111) does certainly not come only from changing the SRP48 to the optPBE exchange functional. As discussed above (see again table 6.5) optPBE-PBE and PBE yield very similar values of the minimum barrier height and energetic corrugation of $H_2$/Cu(111). However, it is known that using the PW91 functional[6] leads to hugely overestimated sticking probabilities for $H_2$/Cu(111) when comparing with experimental values.[18] The same should hold for the PBE functional, as the PBE functional was designed to reproduce PW91 energies,[7] and the PBE and PW91 barrier heights for $H_2$/Cu(111) are indeed very similar.[18] Then, the use of the optPBE-PBE functional should likewise lead to hugely overestimated sticking probabilities for $H_2$/Cu(111). Quantum dynamics calculations using a PW91 PES suggest that using the optPBE-

PBE functional to compute $A_0^{(2)}$ values for $D_2$/Cu(111) should likewise lead to incorrect results: within the static and ideal surface approximation, the use of PW91 leads to computed $A_0^{(2)}$ values that underestimate the experimental values for ($\nu = 1$, $J = 6$) $D_2$ (see figure 11 of ref. 59). Also taking into account the effect of the high surface temperature in the experiments (925 K[80]) would lead to a further decrease of the computed $A_0^{(2)}$, as shown in chapter 3 and reference 21, and therefore to an even worse comparison with experiment. In other words, maintaining good agreement with experiment for $H_2$/Cu(111) depends on changing not only the exchange functional, but also the correlation functional when changing the SRP48 XC functional to the optPBE-vdW-DF XC functional.

## 6.4 Conclusions and outlook

Potential energy surfaces are constructed for the dissociation of $H_2$ on Cu(111), Cu(100), Pt(111) and Ru(0001) from DFT calculations using two different XC functionals, one with non-local vdW-DF correlation (optPBE-vdW-DF) and one with standard GGA (PBE) correlation (SRP48). To determine to what extent using the non-local vdW-DF functional improves the description of the molecule–surface interaction over the non-corrected case, the PESs for the two functionals have been compared to one another in terms of barrier heights, anisotropy in $\varphi$ and the corrugation in $U$ and $V$. A comparison is also made between reaction probabilities and rotational quadrupole alignment parameters obtained from quasi-classical dynamics calculations and experiments, where possible.

In the analysis of the PESs in terms of barrier heights, different behaviours were found for the weakly activated $H_2$/Pt(111) and $H_2$/Ru(0001) systems on the one hand and the highly activated $H_2$/Cu(111) and $H_2$/Cu(100) systems on the other hand. For $H_2$ dissociation on Ru(0001) and Pt(111), the barriers are generally found to be later for the optPBE-vdW-DF PES than for the SRP48 PES, whereas for $H_2$ dissociation on Cu(111) and Cu(100) the barriers were approximately equally late. For $H_2$ dissociation on Ru(0001) and Pt(111), the energetic corrugation (difference in barrier height of the lowest and highest investigated barrier)

is larger for optPBE-vdW-DF than for SRP48, whereas for $H_2$ dissociation on Cu(111) and Cu(100) the opposite is found. This is explained by considering the minimum energy pathways to dissociation for several geometries. For both $H_2$ dissociation on Ru(0001) and Cu(111), the minimum energy pathways cross at a value of $Z \approx 1.6 - 1.8$ Å. If the barrier occurs after this crossing (closer to the surface), as for $H_2$ dissociation on Cu(111) and Cu(100), the barrier is generally increased because optPBE-vdW-DF shows a more steeply rising potential along the reaction path. If the barrier occurs before this crossing, as found for $H_2$ dissociation on Ru(0001) and Pt(111), the barrier is decreased, because the optPBE-vdW-DF functional shows a physisorption well far away from the surface for all considered surfaces, and the barrier is usually also later.

Dynamics results show that reaction probabilities obtained with the optPBE-vdW-DF functional tend to be in better overall agreement with experiments than the SRP48 functional. For both $D_2$ dissociation on Ru(0001) and Pt(111) the optPBE-vdW-DF sticking curve is broader (less steep increase with incidence energy) than the SRP48 sticking curve. The primary difference between the sticking curves for the $D_2$/Cu(111) and $H_2$/Cu(100) systems is a shift, the optPBE-vdW-DF functional showing overall less reactivity.

For $D_2$ dissociating on Cu(111) the $J$-dependence of reaction has also been investigated, as well as the vibrational efficacy and the rotational quadrupole alignment parameter. The vibrational efficacy as computed with the optPBE-vdW-DF functional is slightly higher than for SRP48. Based on this, and uncertainties in the experimental data, no preference for one of the two tested functionals can be assigned. For the $J$-dependence of reaction of $D_2$ on Cu(111), however, the optPBE-vdW-DF functional shows that reaction for low rotational states ($J < 8$) is virtually independent of the rotational state, whereas SRP48 shows reaction to increase with increasing $J$. As experimental data for this system shows reaction to decrease with increasing $J$ state at first, the optPBE-vdW-DF results are in qualitatively better agreement with the experimental data. The rotational quadrupole alignment parameter for $D_2$ on Cu(111) is for both functionals too high compared to experiments. It should be noted however, that the temperature of the surface was not

taken into account in this study. It is known from previous studies that the temperature of the surface can greatly influence the rotational quadrupole alignment parameter. Although the known surface temperature dependence for SRP48 suggests this functional to work better, in order to determine a preference for either functional based on the rotational quadrupole alignment parameter the surface temperature dependence of both functionals should be investigated.

Overall, the optPBE-vdW-DF functional seems to yield results in better agreement with experimental data for the systems considered, especially for the molecular beam sticking probabilities and the width (steepness) of the associated reaction probability curves. It is satisfying to see that including non-local vdW-DF correlation in the XC functional not only improves the description of weakly activated dissociation (as seen for $H_2$/Ru(0001) in chapter 4), but also of highly activated dissociation.

In the future, it would be of interest to also apply the optPBE-vdW-DF functional to non-activated dissociation problems, such as $H_2$/Pd(111),[81,82] $H_2$/Pd(100),[83,84] or $H_2$/Ni(110).[84] A correct description of these systems would demonstrate the correct addition of strongly attractive chemical interactions to the van der Waals interaction in a region that is potentially even closer to the surface, which might constitute an additional challenge. We note that $H_2$/Pd(111) has already been studied with functionals containing vdW-DF correlation in chapter 5; a problem with this system is that there is considerable uncertainty regarding the experimental sticking probability, due to experimental discrepancies. The $N_2$/W(110) system, in which the dissociation is also considerably affected by the presence of molecular chemisorption wells, has also recently been studied with the use of vdW functionals.[57] However, the outcome of these calculations should be somewhat uncertain, because the effect of energy transfer to the W(110) surface was not yet taken into account, while AIMD calculations suggest a large effect on the reactivity of this energy transfer.[85]



## References

[1] W. Kohn and L. J. Sham. Self-consistent equations including exchange and correlation effects. *Physical Review* **140**(4A), A1133–A1138, 1965.

[2] P. Hohenberg and W. Kohn. Inhomogeneous electron gas. *Physical Review* **136**(3B), B864–B871, 1964.

[3] D. C. Langreth and M. J. Mehl. Beyond the local-density approximation in calculations of ground-state electronic properties. *Physical Review B* **28**(4), pp. 1809–1834, 1983.

[4] A. D. Becke. Density-functional exchange-energy approximation with correct asymptotic behavior. *Physical Review A* **38**(6), pp. 3098–3100, 1988.

[5] J. P. Perdew. Density-functional approximation for the correlation energy of the inhomogeneous electron gas. *Physical Review B* **33**(12), pp. 8822–8824, 1986.

[6] J. P. Perdew, J. A. Chevary, S. H. Vosko, K. A. Jackson, M. R. Pederson, D. J. Singh, and C. Fiolhais. Atoms, molecules, solids, and surfaces: applications of the generalized gradient approximation for exchange and correlation. *Physical Review B* **46**(11), pp. 6671–6687, 1992.

[7] J. P. Perdew, K. Burke, and M. Ernzerhof. Generalized gradient approximation made simple. *Physical Review Letters* **77**(18), pp. 3865–3868, 1996.

[8] B. Hammer, L. B. Hansen, and J. K. Nørskov. Improved adsorption energetics within density-functional theory using revised Perdew-Burke-Ernzerhof functionals. *Physical Review B* **59**(11), pp. 7413–7421, 1999.

[9] J. P. Perdew and K. Schmidt. Jacob's ladder of density functional approximations for the exchange-correlation energy. *AIP Conference Proceedings* **577**(1), pp. 1–20, 2001.

[10] J. P. Perdew, J. Tao, V. N. Staroverov, and G. E. Scuseria. Meta-generalized gradient approximation: explanation of a realistic nonempirical density functional. *Journal of Chemical Physics* **120**(15), pp. 6898–6911, 2004.

[11] J. P. Perdew, A. Ruzsinszky, G. I. Csonka, L. A. Constantin, and J. Sun. Workhorse semilocal density functional for condensed matter physics and quantum chemistry. *Physical Review Letters* **103**(2), 026403, 2009.

[12] A. D. Becke. Density-functional thermochemistry. III. The role of exact exchange. *Journal of Chemical Physics* **98**(7), pp. 5648–5652, 1993.

[13] G. J. Kroes. Six-dimensional quantum dynamics of dissociative chemisorption of $H_2$ on metal surfaces. *Progress in Surface Science* **60**(1–4), pp. 1–85, 1999.

[14] G. J. Kroes and M. F. Somers. Six-dimensional dynamics of dissociative chemisorption of $H_2$ on metal surfaces. *Journal of Theoretical and Computational Chemistry* **04**(02), pp. 493–581, 2005.

[15] A. Gross. Reactions at surfaces studied by *ab initio* dynamics calculations. *Surface Science Reports* **32**(8), pp. 291–340, 1998.

[16] P. Nieto, E. Pijper, D. Barredo, G. Laurent, R. A. Olsen, E. J. Baerends, G. J. Kroes, and D. Farías. Reactive and nonreactive scattering of $H_2$ from a metal surface is electronically adiabatic. *Science* **312**(5770), pp. 86–89, 2006.

[17] M. Pozzo and D. Alfè. Hydrogen dissociation on Mg(0001) studied via quantum Monte Carlo calculations. *Physical Review B* **78**(24), 245313, 2008.

[18] C. Díaz, E. Pijper, R. A. Olsen, H. F. Busnengo, D. J. Auerbach, and G. J. Kroes. Chemically accurate simulation of a prototypical surface reaction: $H_2$ dissociation on Cu(111). *Science* **326**(5954), pp. 832–834, 2009.

[19] A. Gross. *Ab initio* molecular dynamics simulations of the adsorption of $H_2$ on palladium surfaces. *ChemPhysChem* **11**(7), pp. 1374–1381, 2010.

[20] P. Nieto, D. Farías, R. Miranda, M. Luppi, E. J. Baerends, M. F. Somers, M. J. T. C. van der Niet, R. A. Olsen, and G. J. Kroes. Diffractive and reactive scattering of $H_2$ from Ru(0001): experimental and theoretical study. *Physical Chemistry Chemical Physics* **13**(18), pp. 8583–8597, 2011.

[21] F. Nattino, C. Díaz, B. Jackson, and G. J. Kroes. Effect of surface motion on the rotational quadrupole alignment parameter of $D_2$ reacting on Cu(111). *Physical Review Letters* **108**(23), 236104, 2012.

[22] G. Füchsel, S. Schimka, and P. Saalfrank. On the role of electronic friction for dissociative adsorption and scattering of hydrogen molecules at a Ru(0001) surface. *Journal of Physical Chemistry A* **117**(36), pp. 8761–8769, 2013.

[23] G. J. Kroes and C. Díaz. Quantum and classical dynamics of reactive scattering of $H_2$ from metal surfaces. Accepted to *Chemical Society Reviews*. doi: 10.1039/C5CS00336A. 2016.

[24] G. J. Kroes. Frontiers in surface scattering simulations. *Science* **321**(5890), pp. 794–797, 2008.

[25] G. J. Kroes. Towards chemically accurate simulation of molecule-surface reactions. *Physical Chemistry Chemical Physics* **14**(43), pp. 14966–14981, 2012.

[26] A. C. Luntz and M. Persson. How adiabatic is activated adsorption/associative desorption? *Journal of Chemical Physics* **123**(7), 074704, 2005.

[27] A. S. Muzas, J. I. Juaristi, M. Alducin, R. Díez Muiño, G. J. Kroes, and C. Díaz. Vibrational deexcitation and rotational excitation of $H_2$ and $D_2$ scattered from Cu(111): adiabatic versus non-adiabatic dynamics. *Journal of Chemical Physics* **137**(6), 064707, 2012.

[28] J. I. Juaristi, M. Alducin, R. Díez Muiño, H. F. Busnengo, and A. Salin. Role of electron–hole pair excitations in the dissociative adsorption of diatomic molecules on metal surfaces. *Physical Review Letters* **100**(11), 116102, 2008.

[29] H. F. Busnengo, W. Dong, P. Sautet, and A. Salin. Surface temperature dependence of rotational excitation of $H_2$ scattered from Pd(111). *Physical Review Letters* **87**(12), 127601, 2001.

[30] H. F. Busnengo, M. A. Di Césare, W. Dong, and A. Salin. Surface temperature effects in dynamic trapping mediated adsorption of light molecules on metal surfaces: $H_2$ on Pd(111) and Pd(110). *Physical Review B* **72**(12), 125411, 2005.

[31] H. F. Busnengo, A. Salin, and W. Dong. Representation of the 6D potential energy surface for a diatomic molecule near a solid surface. *Journal of Chemical Physics* **112**(17), pp. 7641–7651, 2000.

[32] R. A. Olsen, H. F. Busnengo, A. Salin, M. F. Somers, G. J. Kroes, and E. J. Baerends. Constructing accurate potential energy surfaces for a diatomic molecule interacting with a solid surface: $H_2$+Pt(111) and $H_2$+Cu(100). *Journal of Chemical Physics* **116**(9), pp. 3841–3855, 2002.

[33] M. Dion, H. Rydberg, E. Schröder, D. C. Langreth, and B. I. Lundqvist. Van der Waals density functional for general geometries. *Physical Review Letters* **92**(24), 246401, 2004.

[34] K. Lee, E. D. Murray, L. Kong, B. I. Lundqvist, and D. C. Langreth. Higher-accuracy van der Waals density functional. *Physical Review B* **82**(8), 081101, 2010.

[35] J. Zheng, Y. Zhao, and D. G. Truhlar. The DBH24/08 database and its use to assess electronic structure model chemistries for chemical reaction barrier heights. *Journal of Chemical Theory and Computation* **5**(4), pp. 808–821, 2009.

[36] K. Yang, J. Zheng, Y. Zhao, and D. G. Truhlar. Tests of the RPBE, revPBE, $\tau$-HCTHhyb, $\omega$B97X-D, and MOHLYP density functional approximations and 29 others against representative databases for diverse bond energies and barrier heights in catalysis. *Journal of Chemical Physics* **132**(16), 164117, 2010.

[37] R. Peverati and D. G. Truhlar. Quest for a universal density functional: the accuracy of density functionals across a broad spectrum of databases in chemistry and physics. *Philosophical Transactions of the Royal Society of London A* **372**(2011), 20120476, 2014.

[38] R. Peverati and D. G. Truhlar. M11-L: A local density functional that provides improved accuracy for electronic structure calculations in chemistry and physics. *Journal of Physical Chemistry Letters* **3**(1), pp. 117–124, 2012.

[39] R. Peverati and D. G. Truhlar. An improved and broadly accurate local approximation to the exchange-correlation density functional: the MN12-L functional for electronic structure calculations in chemistry and physics. *Physical Chemistry Chemical Physics* **14**(38), pp. 13171–13174, 2012.

[40] H. S. Yu, X. He, and D. G. Truhlar. MN15-L: a new local exchange–correlation functional for Kohn–Sham density functional theory with broad accuracy for atoms, molecules, and solids. *Journal of Chemical Theory and Computation* **12**(3), pp. 1280–1293, 2016.

[41] Y. Y. Chuang, M. L. Radhakrishnan, P. L. Fast, C. J. Cramer, and D. G. Truhlar. Direct dynamics for free radical kinetics in solution: solvent effect on the rate constant for the reaction of methanol with atomic hydrogen. *Journal of Physical Chemistry A* **103**(25), pp. 4893–4909, 1999.

[42] L. Sementa, M. Wijzenbroek, B. J. van Kolck, M. F. Somers, A. Al-Halabi, H. F. Busnengo, R. A. Olsen, G. J. Kroes, M. Rutkowski, C. Thewes, N. F. Kleimeier, and H. Zacharias. Reactive scattering of $H_2$ from Cu(100): comparison of dynamics calculations based on the specific reaction parameter approach to density functional theory with experiment. *Journal of Chemical Physics* **138**(4), 044708, 2013.

[43] A. Tkatchenko, L. Romaner, O. T. Hofmann, E. Zojer, C. Ambrosch-Draxl, and M. Scheffler. Van der Waals interactions between organic adsorbates and at organic/inorganic interfaces. *MRS Bulletin* **35**(6), pp. 435–442, 2010.

[44] S. Grimme. Density functional theory with London dispersion corrections. *Wiley Interdisciplinary Reviews: Computational Molecular Science* **1**(2), pp. 211–228, 2011.

[45] J. Klimeš and A. Michaelides. Perspective: Advances and challenges in treating van der Waals dispersion forces in density functional theory. *Journal of Chemical Physics* **137**(12), 120901, 2012.

[46] J. P. P. Ramalho, J. R. B. Gomes, and F. Illas. Accounting for van der Waals interactions between adsorbates and surfaces in density functional theory based calculations: selected examples. *RSC Advances* **3**(32), pp. 13085–13100, 2013.

[47] K. Berland, V. R. Cooper, K. Lee, E. Schröder, T. Thonhauser, P. Hyldgaard, and B. I. Lundqvist. van der Waals forces in density functional theory: a review of the vdW-DF method. *Reports on Progress in Physics* **78**(6), 066501, 2015.

[48] S. Grimme, J. Antony, S. Ehrlich, and H. Krieg. A consistent and accurate *ab initio* parameterization of density functional dispersion correction (DFT-D) for the 94 elements H-Pu. *Journal of Chemical Physics* **132**(15), 154104, 2010.

[49] A. Tkatchenko and M. Scheffler. Accurate molecular van der Waals interactions from ground-state electron density and free-atom reference data. *Physical Review Letters* **102**(7), 073005, 2009.

[50] J. Klimeš, D. R. Bowler, and A. Michaelides. Chemical accuracy for the van der Waals density functional. *Journal of Physics: Condensed Matter* **22**(2), 022201, 2010.

[51] J. Klimeš, D. R. Bowler, and A. Michaelides. Van der Waals density functionals applied to solids. *Physical Review B* **83**(19), 195131, 2011.

[52] V. R. Cooper. Van der Waals density functional: An appropriate exchange functional. *Physical Review B* **81**(16), 161104(R), 2010.

[53] K. Berland and P. Hyldgaard. Exchange functional that tests the robustness of the plasmon description of the van der Waals density functional. *Physical Review B* **89**(3), 035412, 2014.

[54] W. Liu, J. Carrasco, B. Santra, A. Michaelides, M. Scheffler, and A. Tkatchenko. Benzene adsorbed on metals: concerted effect of covalency and van der Waals bonding. *Physical Review B* **86**(24), 245405, 2012.

[55] H. Yildirim, T. Greber, and A. Kara. Trends in adsorption characteristics of benzene on transition metal surfaces: role of surface chemistry and van der Waals interactions. *Journal of Physical Chemistry C* **117**(40), pp. 20572–20583, 2013.

[56] J. Carrasco, W. Liu, A. Michaelides, and A. Tkatchenko. Insight into the description of van der Waals forces for benzene adsorption on transition metal (111) surfaces. *Journal of Chemical Physics* **140**(8), 084704, 2014.

[57] L. Martin-Gondre, J. I. Juaristi, M. Blanco-Rey, R. Díez Muiño, and M. Alducin. Influence of the van der Waals interaction in the dissociation dynamics of $N_2$ on W(110) from first principles. *Journal of Chemical Physics* **142**(7), 074704, 2015.

[58] M. Born and R. Oppenheimer. Zur Quantentheorie der Molekeln. *Annalen der Physik* **389**(20), pp. 457–484, 1927.

[59] C. Díaz, R. A. Olsen, D. J. Auerbach, and G. J. Kroes. Six-dimensional dynamics study of reactive and non reactive scattering of $H_2$ from Cu(111) using a chemically accurate potential energy surface. *Physical Chemistry Chemical Physics* **12**(24), pp. 6499–6519, 2010.

[60] A. Mondal, M. Wijzenbroek, M. Bonfanti, C. Díaz, and G. J. Kroes. Thermal lattice expansion effect on reactive scattering of $H_2$ from Cu(111) at $T_s$ = 925 K. *Journal of Physical Chemistry A* **117**(36), pp. 8770–8781, 2013.

[61] D. A. McCormack and G. J. Kroes. Accuracy of trajectory methods for activated adsorption of $H_2$ on Cu(100). *Chemical Physics Letters* **296**(5–6), pp. 515–520, 1998.

[62] E. Pijper, M. F. Somers, G. J. Kroes, R. A. Olsen, E. J. Baerends, H. F. Busnengo, A. Salin, and D. Lemoine. Six-dimensional quantum dynamics of scattering of (v=0, j=0) $H_2$ from Pt(111): comparison to experiment and to classical dynamics results. *Chemical Physics Letters* **347**(4–6), pp. 277–284, 2001.

[63] J. Stoer and R. Bulirsch. *Introduction to numerical analysis*. New York: Springer, 1980.

[64] G. Kresse and J. Hafner. *Ab initio* molecular dynamics for liquid metals. *Physical Review B* **47**(1), pp. 558–561, 1993.

[65] G. Kresse and J. Furthmüller. Efficiency of *ab initio* total energy calculations for metals and semiconductors using a plane-wave basis set. *Computational Materials Science* **6**(1), pp. 15–50, 1996.

[66] G. Kresse and J. Furthmüller. Efficient iterative schemes for *ab initio* total-energy calculations using a plane-wave basis set. *Physical Review B* **54**(16), pp. 11169–11186, 1996.

[67] G. Kresse and D. Joubert. From ultrasoft pseudopotentials to the projector augmented-wave method. *Physical Review B* **59**(3), pp. 1758–1775, 1999.

[68] G. Kresse and J. Hafner. Norm-conserving and ultrasoft pseudopotentials for first-row and transition elements. *Journal of Physics: Condensed Matter* **6**(40), pp. 8245–8257, 1994.

[69] D. Vanderbilt. Soft self-consistent pseudopotentials in a generalized eigenvalue formalism. *Physical Review B* **41**(11), pp. 7892–7895, 1990.

[70] P. E. Blöchl. Projector augmented-wave method. *Physical Review B* **50**(24), pp. 17953–17979, 1994.

[71] G. Román-Pérez and J. M. Soler. Efficient implementation of a van der Waals density functional: application to double-wall carbon nanotubes. *Physical Review Letters* **103**(9), 096102, 2009.

[72] M. Luppi, R. A. Olsen, and E. J. Baerends. Six-dimensional potential energy surface for $H_2$ at Ru(0001). *Physical Chemistry Chemical Physics* **8**(6), pp. 688–696, 2006.

[73] H. A. Michelsen, C. T. Rettner, D. J. Auerbach, and R. N. Zare. Effect of rotation on the translational and vibrational energy dependence of the dissociative adsorption of $D_2$ on Cu(111). *Journal of Chemical Physics* **98**(10), pp. 8294–8307, 1993.

[74] G. Anger, A. Winkler, and K. D. Rendulic. Adsorption and desorption kinetics in the systems $H_2$/Cu(111), $H_2$/Cu(110) and $H_2$/Cu(100). *Surface Science* **220**(1), pp. 1–17, 1989.

[75] A. C. Luntz, J. K. Brown, and M. D. Williams. Molecular beam studies of $H_2$ and $D_2$ dissociative chemisorption on Pt(111). *Journal of Chemical Physics* **93**(7), pp. 5240–5246, 1990.

[76] I. M. N. Groot, H. Ueta, M. J. T. C. van der Niet, A. W. Kleyn, and L. B. F. Juurlink. Supersonic molecular beam studies of dissociative adsorption of $H_2$ on Ru(0001). *Journal of Chemical Physics* **127**(24), 244701, 2007.

[77] F. Nattino, A. Genova, M. Guijt, A. S. Muzas, C. Díaz, D. J. Auerbach, and G. J. Kroes. Dissociation and recombination of $D_2$ on Cu(111): *ab initio* molecular dynamics calculations and improved analysis of desorption experiments. *Journal of Chemical Physics* **141**(12), 124705, 2014.

[78] H. A. Michelsen, C. T. Rettner, and D. J. Auerbach. On the influence of surface temperature on adsorption and desorption in the $D_2$/Cu(111) system. *Surface Science* **272**(1–3), pp. 65–72, 1992.

[79] M. J. Murphy and A. Hodgson. Adsorption and desorption dynamics of $H_2$ and $D_2$ on Cu(111): the role of surface temperature and evidence for corrugation of the dissociation barrier. *Journal of Chemical Physics* **108**(10), pp. 4199–4211, 1998.

[80] H. Hou, S. J. Gulding, C. T. Rettner, A. M. Wodtke, and D. J. Auerbach. The stereodynamics of a gas-surface reaction. *Science* **277**(5322), pp. 80–82, 1997.

[81] J. Lesnik. Untersuchungen über Vorläuferadsorption an Übergangsmetallen und Übergangsmetallegierungen. PhD thesis. Technischen Universität Graz, 2001.

[82] M. Beutl, J. Lesnik, K. D. Rendulic, R. Hirschl, A. Eichler, G. Kresse, and J. Hafner. There is a true precursor for hydrogen adsorption after all: the system $H_2$/Pd(111) + subsurface V. *Chemical Physics Letters* **342**(5–6), pp. 473–478, 2001.

[83] C. T. Rettner and D. J. Auerbach. Search for oscillations in the translational energy dependence of the dissociation of $H_2$ on Pd(100). *Chemical Physics Letters* **253**(3–4), pp. 236–240, 1996.

[84] K. D. Rendulic, G. Anger, and A. Winkler. Wide range nozzle beam adsorption data for the systems $H_2$/nickel and $H_2$/Pd(100). *Surface Science* **208**(3), pp. 404–424, 1989.

[85] F. Nattino, F. Costanzo, and G. J. Kroes. $N_2$ dissociation on W(110): an *ab initio* molecular dynamics study on the effect of phonons. *Journal of Chemical Physics* **142**(10), 104702, 2015.

CHAPTER 7

# Ab initio molecular dynamics study of $D_2$ dissociation on CO-precovered Ru(0001)

This chapter is based on:

M. Wijzenbroek and G. J. Kroes. *Ab initio* molecular dynamics study of $D_2$ dissociation on CO-precovered Ru(0001). *Physical Chemistry Chemical Physics*, accepted for publication. 2016.

## Abstract

In dynamics calculations of $H_2$ dissociating on metal surfaces often clean, high-symmetry surfaces are used. Few such dynamics studies have been performed on surfaces with pre-adsorbed molecules, and even fewer studies also consider the motion of the surface and the adsorbate. In this study, the dissociation of $H_2$ on a carbon monoxide-covered Ru(0001) surface is considered. *Ab initio* molecular dynamics (AIMD) calculations are performed on this system using the PBE-vdW-DF2 functional, which accurately describes the reaction probability for $H_2$ dissociation on Ru(0001). Using this functional, the reaction probability of $H_2$ on the CO-covered Ru(0001) surface is found to be too low compared to experiments. This suggests that exchange–correlation functionals that can describe reaction of $H_2$ on a bare metal surface are not in general able to describe the reaction of $H_2$ on a CO-precovered surface of the same metal, with the same accuracy. It can however not be ruled out that the discrepancy between theory and experiment is partly due to an inhomogeneous coverage of the surface by CO in the experiments. The incorporation of the motion of the surface has only a small effect on the reaction probability. It is found that when including surface motion for this system, the size of the simulation cell can be important. Upon collision, a considerable amount of energy is transferred to the surface, causing the adsorbed CO molecules to move apart, which opens the surface for reaction. In order to obtain converged reaction probabilities with respect to the size of the simulation cell, at least a $3 \times 3$ simulation cell is needed, because in the smaller $\sqrt{3} \times \sqrt{3}$ cell the CO molecules cannot be pushed apart as only a single independent CO molecule is present, also leading to less energy exchange with the surface.


## 7.1 Introduction

In detailed dynamics simulations of hydrogen molecules reacting on metal surfaces often clean, high-symmetry surfaces are used.[1] Only few dynamics studies have been performed on surfaces which have been pre-covered with, for example, H atoms or CO molecules, and even

fewer studies have allowed the surface atoms and the pre-adsorbed atoms or molecules to move. Such studies have been performed for $H_2$ dissociation on various palladium surfaces decorated with H, S or Cl atoms.[2–7] No studies with a non-rigid surface have however been performed yet for the dissociation of $H_2$ or $D_2$ on a CO-covered surface, which are of interest because CO acts as a common poison for catalysts.

An example of such a system, for which sticking probabilities have been experimentally measured, is $D_2$ dissociation on a CO-covered Ru(0001) surface.[8] This system has already been studied with extensive density functional theory (DFT) calculations[9] and with dynamics calculations,[10] but in the dynamics calculations the CO and the surface atoms were fixed at their ideal lattice positions. Although no large surface temperature effects would be expected at the rather low experimental surface temperature ($T_s = 180\,K$[8]), it has not yet been tested whether or not allowing the surface atoms and CO molecules to move may improve the description of the process. In particular, a relevant question is whether or not the $D_2$ can exchange energy with the CO molecules. The masses of the $D_2$ and CO molecules match better than those of $D_2$ and Ru, suggesting energy exchange may play a large role in the dynamics, as the simple Baule model suggests that energy exchange becomes important if the masses of the projectile and the surface atoms match.[11,12] Finally, Zhao *et al.*[13] have studied co-adsorption of $H_2$ and CO on Ru(0001) with DFT, considering precoverages of Ru(0001) by CO other than the 1/3 monolayer (ML) precoverage considered here. With the RPBE functional used, they obtained reasonable agreement with ultrahigh vacuum experiments for their computed CO and $H_2$ desorption temperatures and patterns.

The underlying surface system (CO on Ru(0001)) has been the subject of many different studies in which, *e.g.*, CO adsorption and desorption, surface structures and vibrations have been studied, both from an experimental[14–39] and a theoretical[13,38–52] point of view. At different CO coverages, different surface structures are observed. For low coverages of up to 1/3 ML, CO molecules tend to adsorb on top sites.[15,16,43–45] For CO on Ru(0001), the CO molecules adsorb with an orientation perpendicular to the surface, with the C atom bonded to the surface.[14–18] One particularly well-studied system is 1/3 ML CO on Ru(0001) (for a com-

parison of experimental and theoretical data, see reference 9), which exhibits a $(\sqrt{3}\times\sqrt{3})$R30° geometry, which seems to be the best defined CO-covered Ru(0001) surface,[9,45] with the CO molecules occupying one in every three top sites. For this reason, and because previous theoretical studies[9,10] of $D_2$ dissociation on CO-covered Ru(0001) have also considered this particular coverage, the 1/3 ML case is considered in this study.

For $H_2$ and $D_2$ dissociation on a bare Ru(0001) surface, two DFT exchange–correlation (XC) functionals were found in chapter 4 that could describe the reaction probability well over the range of incidence energies for which experiments[53] are available. Previous calculations[54] showed that the reaction could not be well described by the PW91[55] (or the similar PBE[56]) and RPBE[57] XC functionals, which are commonly used for studies of molecules dissociating on metal surfaces. A mixture of these functionals allowed several experiments on $H_2$ dissociation on Cu(111) to be reproduced with chemical accuracy.[58] For $H_2$ dissociation on Ru(0001) however, these functionals yielded reaction probabilities that increased too quickly with increasing incidence energy. It was, for this system, found that using functionals with either vdW-DF[59] or vdW-DF2[60] correlation results in an improved agreement of the reaction probability with experiments.

The description of CO-covered surfaces with DFT has received a lot of attention. For example, the popular PW91, PBE and RPBE functionals fail to predict the correct adsorption site of the CO molecule on the Pt(111) surface.[61] Also for other surfaces (Cu(111) and Rh(111)) the wrong adsorption site preference is found,[42] giving rise to the "CO adsorption puzzle".[46] Using higher level electronic structure calculations, *e.g.*, hybrid functionals (B3LYP[46] and PBE0 and HSE03[62]), the random phase approximation (RPA),[63] the revTPSS meta-generalized gradient approximation (meta-GGA) functional[49] or vdW-DF functionals[64] partially or fully resolves this problem. For 1/3 ML CO-covered Ru(0001) the correct adsorption site (top) is already predicted at the generalized gradient approximation (GGA) level.[9]

In this chapter, *ab initio* molecular dynamics (AIMD) calculations are performed to describe $D_2$ dissociation on a 1/3 ML CO-covered Ru(0001) surface, to understand if allowing the CO molecules and the

surface atoms to move has effects on the dynamics. A second aspect, however, is the use of the XC functional. Dynamics calculations have previously been performed for $H_2$ dissociation on CO-covered Ru(0001) with the RPBE[57] functional.[10] This functional however yielded reaction probabilities that were too low compared to experiments that have been performed for this system.[8] Recently, two functionals have been identified using a specific reaction parameter (SRP)[58] approach that can accurately describe the dissociation of $H_2$ on a bare Ru(0001) surface, which is not possible with the RPBE functional (see also chapter 4). These functionals use either vdW-DF[59] or vdW-DF2[60] correlation. An interesting question is whether these functionals can also properly describe $H_2$ dissociation on a CO-covered Ru(0001) surface.[65] For the present study one of the two candidate SRP functionals for $H_2$ dissociation on Ru(0001), the PBE-vdW-DF2 functional, is taken.

In section 7.2 the methods used are described, starting with the dynamical model in section 7.2.1. Initial and analysis conditions are described in section 7.2.2 and the computational details in section 7.2.3. In section 7.3 the results are presented and discussed, starting with properties of the surface in section 7.3.1. The molecule–surface interaction is explored in section 7.3.2. The reaction probability, its comparison to experiments as well as differences between the results obtained with different unit cell sizes are discussed in section 7.3.3. Finally, in section 7.4 the conclusions are given.

## 7.2 Methods

### 7.2.1 Dynamical model

In all calculations the Born–Oppenheimer[66] approximation is used. Two types of calculations are performed: calculations in which the surface atoms are allowed to move at the experimental surface temperature ($T_s = 180\,\mathrm{K}$), and calculations in which the surface atoms are frozen at their ideal lattice positions. The forces and energies needed for the dynamics were determined "on the fly" from DFT[67,68] calculations. For the DFT calculations the PBE-vdW-DF2[56,60] functional was used, which was in chapter 4 found to be able to describe the dissociation of $H_2$ and

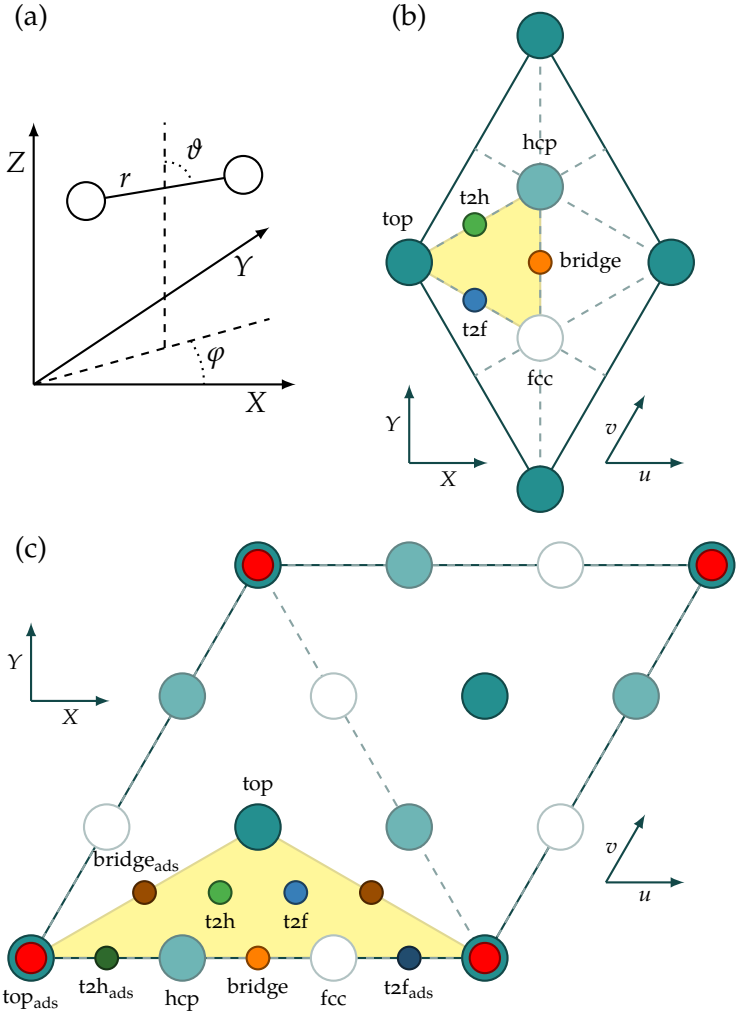


**FIGURE 7.1** (a) The center of mass coordinate system used to describe the coordinates of the $H_2$ molecule. (b) The surface unit cell considered for the $H_2$/Ru(0001) system. (c) The $\sqrt{3} \times \sqrt{3}$ surface unit cell considered for the $H_2$/CO+Ru(0001) system. The diagonal of the $\sqrt{3} \times \sqrt{3}$ unit cell coincides with one of the lattice vectors of the $3 \times 3$ cell. In (b) and (c), several sites which are commonly considered are indicated. The subscript "ads" in (c) is used to indicate which site is nearest the adsorbed CO, for sites that are, due to addition of CO, no longer symmetry equivalent.

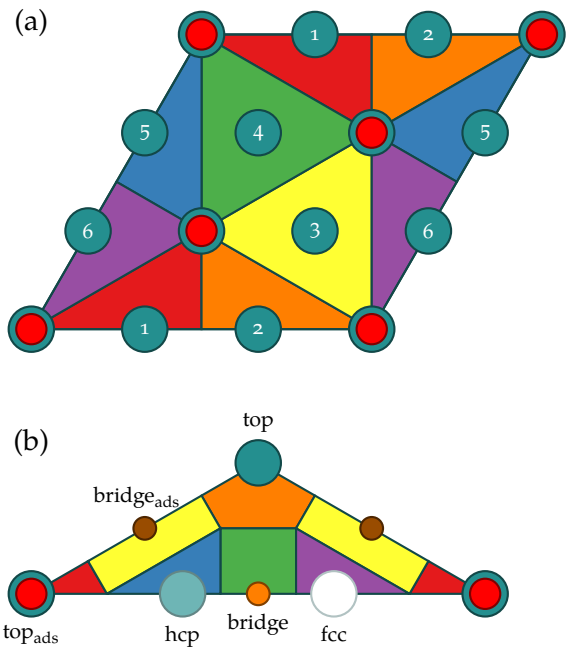


**Figure 7.2** (a) The six triangles spanned by the CO molecules for the $3 \times 3$ cell. Each triangle has three CO molecules that can move independently. (b) The bins used to compute site-specific properties. The sites giving names to the bins have been indicated (see also figure 7.1(c)).

$D_2$ on Ru(0001) rather accurately.

In the dynamics calculations for $T_s = 180\,\mathrm{K}$, the motion of all atoms of the $D_2$ molecule and the CO-covered Ru(0001) slab is taken into account, except for the bottom layer of the Ru(0001) slab, which remains fixed during the dynamics. For the ideal lattice calculations, the whole slab, including the layer of CO molecules, remains fixed during the dynamics and only the $D_2$ molecule is allowed to move. Calculations were done both using a $\sqrt{3} \times \sqrt{3}$ and a $3 \times 3$ cell, but for the ideal lattice calculations only a $\sqrt{3} \times \sqrt{3}$ cell was used. In figure 7.1 the coordinate system that is used to describe the location of the $H_2$ molecule, the surface unit cell for bare Ru(0001), and the $\sqrt{3} \times \sqrt{3}$ surface unit cell of 1/3 ML CO-covered Ru(0001) are shown. It is noted that if the surface atoms are allowed to move, the molecule–surface distance $Z$ is generally ill defined. Throughout this chapter the convention is used that the highest atom

that is part of the slab (including the adsorbate; for the CO-covered surface this is therefore generally an oxygen atom of a CO molecule on the surface) determines the location for $Z = 0$ Å. Negative $Z$ values thus correspond to the $H_2$ molecule being in the CO layer of the slab.

In figure 7.2 two schemes used for analysis are shown. In figure 7.2(a), the six triangles that are spanned by the CO molecules in a $3 \times 3$ cell are shown. These triangles are used to analyse the amount of freedom a molecule has to dissociate on different parts of a slab at a finite surface temperature. Each triangle has three CO molecules at the corners of the triangle that are, to a large extent, free to move relative to the surface. This is in contrast to the $\sqrt{3} \times \sqrt{3}$ cell, in which only one single independent CO is present. In figure 7.2(b), the bins used to obtain site-specific properties are shown. The names of the bins are derived from the site that is located at the center of the bins in the ideal, static surface.

In the dynamics, the equations of motion are integrated using the leapfrog propagator with a time step of 1 fs for the slab equilibrations, and a time step of 0.5 fs, 0.25 fs or 0.125 fs for ($v = 0$), ($v = 1$) and ($v \geq 2$) $D_2$, respectively.

### 7.2.2 Initial and analysis conditions

Quasi-classical dynamics calculations are performed, in which zero-point energy (ZPE) is imparted to the $D_2$ initially. The initial rovibrational energy that is put into the $D_2$ molecule is determined by the Fourier grid Hamiltonian method.[69] An ensemble of $D_2$ molecules in various rovibrational states and with various translational energies corresponding to the experimental distribution in the molecular beam is considered. This procedure, including the parameters used for these distributions, is the same as used for the $H_2$ dissociation on Ru(0001) calculations of chapter 4.

The $H_2$ molecule is initially placed at $Z = 6.5$ Å. The molecule is considered to have scattered if $Z > 4.0$ Å with a momentum vector away from the surface. The molecule is considered to have dissociated if $r > 2.0$ Å. Molecules that have neither reacted nor dissociated after 1 ps (2 ps for the highest energy point), are considered to have scattered.

To generate the initial conditions of the slab and CO molecules, several steps are performed. First, the bulk lattice constants $a$ and $c$ for Ru are determined by relaxing a HCP unit cell with two atoms. No thermal expansion is taken into account, as Ru at $T_s = 180$ K is very similar to Ru at $T_s = 0$ K (from 0 K to 180 K, the $a$ and $c$ lattice constants grow by 0.05% and 0.08%, respectively).[70] The ideal slab geometry is then determined by allowing all atoms of a CO-covered slab, except the bottom layer, to relax in the $z$ direction. Vibrational frequencies are then determined for each of the atoms that are allowed to move in the slab, while keeping the other atoms fixed. These vibrational frequencies are then used to initialize random displacements for the atoms of the slab. Initial velocities for the surface atoms are taken from a Maxwell–Boltzmann distribution. For the $\sqrt{3} \times \sqrt{3}$ cell, 50 randomly determined configurations are taken. Each of these 50 snapshots is propagated for in total 4.0 ps with a time step of 1.0 fs. During the first 1.0 ps velocities are rescaled every 5 (first 0.5 ps) and 50 (second 0.5 ps) time steps. After the velocity rescaling, the calculation proceeds in the $NVE$ ensemble, of which the first 0.5 ps is discarded. Initial conditions for the slab and CO molecules are then randomly selected from the remaining 2.5 ps, giving in total $125 \times 10^3$ possible sets of initial conditions spread over the different slabs. For the $3 \times 3$ cell, the same procedure is used, except that only 20 slabs are propagated due to the increased size of the simulation cell.

### 7.2.3 Computational details

The electronic structure calculations were done with version 5.2.12 of the VASP[71–74] software package. The standard[74] projector augmented wave (PAW)[75] potentials were used. The non-local vdW-DF2 correlation functional in VASP is evaluated within the scheme of Román-Pérez and Soler.[76]

To speed up convergence, first order Methfessel–Paxton[77] smearing was used with a smearing width of 0.1 eV. For the bulk calculation, a $20 \times 20 \times 20$ Γ-centered $k$-point grid was used with a plane wave cutoff of 500 eV. For all other calculations, a $9 \times 9 \times 1$ Γ-centered (shifted Monkhorst–Pack[78]) $k$-point mesh was used for calculations with the $\sqrt{3} \times \sqrt{3}$ unit cell, while a $5 \times 5 \times 1$ Γ-centered $k$-point mesh was used for

the 3 × 3 cell. A plane wave cutoff of 400 eV was used. For both cells a vacuum of 13 Å was chosen to separate different images of the slab. In all cases a five layered ruthenium slab was considered, with either one or three CO molecules adsorbed on one side, for the $\sqrt{3} \times \sqrt{3}$ and 3 × 3 cells, respectively. Convergence tests for the potential energy suggest that the error introduced due to the basis set size, $k$-point integration and the number of Ru layers is less than 30 meV. Tests with CO molecules adsorbed on both sides of the slab suggest barrier heights may be decreased by at most about 20 meV.

To obtain accurate statistics, 500 trajectories are computed for two energy points of interest on the reaction probability curve. Only for the highest energy point with the $\sqrt{3}\times\sqrt{3}$ cell for $T_s = 180$ K, 1000 trajectories are computed. Throughout this chapter, observables are often denoted by $O \pm \sigma$, where $\sigma$ is an approximation of the statistical errors due to the limited number of trajectories, and is approximated by $\sigma = s/\sqrt{nN}$, where $s$ is the sample standard deviation, $N$ the number of trajectories and $n$ the number of samples per trajectory. For reaction probabilities, $\sigma = \sqrt{P_r \cdot (1 - P_r)}/\sqrt{N}$, where $P_r$ is the computed reaction probability.

## 7.3 Results and discussion

### 7.3.1 Properties and dynamics of the CO-covered surface

The adsorption energies (defined as $E_{ads} = E_{CO} + E_{Ru} - E_{CO/Ru}$) for CO above a five layer Ru slab on the top and hcp sites are found to be 1.91 eV and 1.65 eV, respectively. These numbers match quite well to the adsorption energies computed by Groot *et al.*[9] and the top site adsorption energy is in good agreement with the measured adsorption energy of Pfnür and Menzel[23] for 1/3 ML (1.81 eV), but less so with the adsorption energy from an earlier study (1.66 eV) by the same authors[24] and the experimental value reported by Abild-Pedersen and Andersson[48] (1.49 ± 0.22 eV). It is noted that it is not clear how this value was determined (multiple experiments were cited) and at which coverage, which should be important: Pfnür and Menzel[23] found the adsorption energy to depend on the CO coverage of the surface.

In table 7.1 several geometrical parameters of the 1/3 ML CO-

**Table 7.1** Several geometrical parameters obtained with dynamics calculations on the CO-covered Ru(0001) surface. The meaning of the symbols is explained in the text. The values for $D_2$ dissociation correspond to averages over the (whole) computed trajectories for $E_{trans} = 0.466\,eV$.

| Property | Relaxed | $\sqrt{3}\times\sqrt{3}$ | (+ $D_2$) | $3\times3$ | (+ $D_2$) | Experiment |
|---|---|---|---|---|---|---|
| $\langle\sigma_O\rangle$ (Å) | 0 | 0.337 | 0.425 | 0.341 | 0.567 | — |
| $\langle\sigma_C\rangle$ (Å) | 0 | 0.216 | 0.270 | 0.214 | 0.347 | — |
| $\langle\sigma_{CO}\rangle$ (Å) | 0 | 0.278 | 0.351 | 0.280 | 0.468 | — |
| $\langle\sigma_O^{\parallel}\rangle$ (Å) | 0 | 0.330 | 0.414 | 0.335 | 0.559 | $0.5 \pm 0.1$[16] |
| $\langle\sigma_C^{\parallel}\rangle$ (Å) | 0 | 0.207 | 0.257 | 0.206 | 0.339 | $0.3 \pm 0.1$[16] |
| $\langle\sigma_O^{\perp}\rangle$ (Å) | 0 | 0.061 | 0.093 | 0.058 | 0.096 | 0.1[16] |
| $\langle\sigma_C^{\perp}\rangle$ (Å) | 0 | 0.056 | 0.077 | 0.055 | 0.071 | 0.1[16] |
| $\langle\vartheta_{C-O}\rangle$ (°) | 0 | 7.7 | 9.4 | 7.9 | 11.1 | — |
| $\langle\vartheta_{Ru-O}\rangle$ (°) | 0 | 5.6 | 7.0 | 5.7 | 9.2 | — |
| $\langle d_{1-2}\rangle$ (Å) | 2.137 | 2.139 | 2.134 | 2.139 | 2.137 | 2.094[79] |
| $\langle d_{prot}\rangle$ (Å) | 0.184 | 0.165 | 0.147 | 0.169 | 0.164 | $0.07 \pm 0.03$[27] |
| $\langle r_{Ru-C}\rangle$ (Å) | 1.915 | 1.920 | 1.918 | 1.920 | 1.923 | $1.93 \pm 0.04$[27] |
| $\langle r_{C-O}\rangle$ (Å) | 1.165 | 1.166 | 1.167 | 1.166 | 1.167 | $1.10 \pm 0.05$[27] |

covered Ru(0001) surface are shown, comparing the small and large simulation cells with and without the $D_2$ molecule impinging on the surface. All properties are ensemble averages, which in the context of the present calculations means that averages are taken over, if applicable, one or more occurrences in the unit cell and the different trajectories that were performed. Several types of properties are considered: average root mean square displacements ($\sigma_x$) of atoms ($x = C, O$) or the CO center of mass ($x = CO$) with respect to its position in the case of the ideal lattice, the parallel ($\sigma_x^{\parallel}$) or perpendicular ($\sigma_x^{\perp}$) components of the average root mean square displacements, the angle of a vector from atom $a$ to $b$ with respect to the surface normal ($\vartheta_{a-b}$), the first interlayer spacing ($d_{1-2}$, average distance between the two topmost Ru layers of the surface), the protrusion of the Ru atom directly below the CO molecule with respect to the other Ru atoms in that layer ($d_{prot}$), and bond lengths ($r_{a-b}$) between atoms $a$ and $b$. Many of these parameters

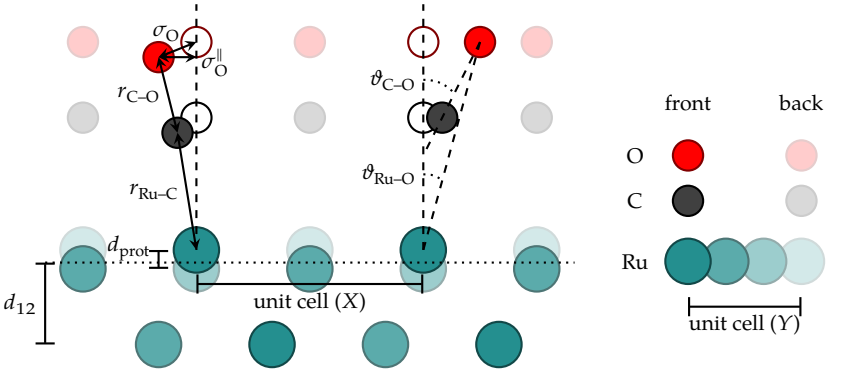


**Figure 7.3** Schematic side view (left) of the 1/3 ML CO-covered Ru(0001) surface. The shown view is along the $Y$-axis for the $\sqrt{3} \times \sqrt{3}$ cell of figure 7.1(c), starting at the bottom (the $U$ or $X$-axis). The frontmost two CO molecules have been displaced from their ideal positions (open circles). The geometrical parameters of table 7.1 are indicated and are explained in more detail in the text. Atoms that are further away are indicated by faded circles (see right figure).

are also shown in figure 7.3. In table 7.1, with a subscript Ru the Ru atom immediately below a C or O atom of a CO molecule is meant. The results for the cases with the $D_2$ molecule impinging on the surface are discussed in section 7.3.3; for the case without the $D_2$ molecule the results are discussed below.

The distance between the topmost ruthenium atom and the C atom, as well as the distance between the C and O atoms, has been measured by Michalk *et al.*[15] and Over *et al.*[27] The values found here for all cases (1.92 Å for the $r_{Ru-C}$ distance and 1.17 Å for $r_{C-O}$) match quite well to the experimental values by Over *et al.* ($1.93 \pm 0.04$ Å and $1.10 \pm 0.05$ Å, respectively) and Michalk *et al.* ($2.00 \pm 0.10$ Å and $1.10 \pm 0.10$ Å, respectively), although the computed C–O distance is a bit on the long side. The root mean square displacement of the C and O atoms has been measured by Gierer *et al.*[16] and Over *et al.*[27,28] The computed displacements are in fair agreement with the results of the latest experiment[16] ($0.5 \pm 0.1$ Å for $\sigma_O^{\parallel}$ at $T_s = 150$ K and $0.3 \pm 0.1$ Å for $\sigma_C^{\parallel}$). The protrusion of the Ru atom to which the CO is attached with respect to the other atoms in the layer is somewhat larger than the experimental value ($0.07 \pm 0.03$ Å) by Over *et al.*[27] The contraction of the distance between

the first and second layer is about 1.5% compared to the computed bulk interlayer spacing (2.169 Å), which is a bit smaller than the value for the bare Ru(0001) surface with the DFT functional used (3.3%). At $T_s$ = 300 K, Baddorf *et al.*[79] measured the contraction of the distance between the first and second layer to be 2.2 ± 0.4%, corresponding to a first interlayer spacing of about 2.094 Å. Finally, the results are overall in good agreement with DFT studies[9,45] in which the RPBE functional was used.

Another interesting property concerns the motion of CO with respect to the surface. From the C and O displacements given above, it is clear that although the molecule has some freedom to move, it does not readily move to the next top site (about 2.7 Å away). The fact that the displacement of the CO center of mass ($\sigma_{CO}$) closely matches the weighted average of the displacements of the individual C and O displacements, as well as that the Ru–C and C–O distances remain similar during the dynamics as in the static surface case, suggests that the molecules behave in a way similar to that proposed by Gierer *et al.*[16]: the CO molecule tilts with respect to the topmost Ru atom, keeping the topmost Ru to which the CO is adsorbed, and the C and O atoms approximately on a line. Tilt angles of the line connecting the two atoms with respect to the surface normal ($\vartheta_{C-O}$ and $\vartheta_{Ru-O}$) have been computed. $\vartheta_{Ru-O}$ is slightly smaller (by about 2°) than $\vartheta_{C-O}$, suggesting that the C atom is on average not displaced far enough for the Ru, C and O atoms to be on a line. Although the tilt angles are not large, the tilting of the CO molecules may nonetheless have an effect on the $H_2$ dissociation dynamics. A small decrease in reactivity might be expected, because more of the surface is "screened" by the CO for the impinging $D_2$ molecules.

### 7.3.2 The molecule–surface interaction

In figure 7.4 contour plots of the PES for $H_2$ dissociation on an ideal 1/3 ML CO-covered Ru(0001) surface ($\sqrt{3} \times \sqrt{3}$ cell) are shown for dissociation above various sites and orientations with $\vartheta = 90°$. It is clear that near a CO-covered Ru atom it is rather unfavourable for the $H_2$ molecule to dissociate, although for dissociation above hcp or bridge$_{ads}$ nonetheless a barrier and an exit channel is found. In contrast, for the cases where the $H_2$ molecule is near a Ru atom without an adsorbed

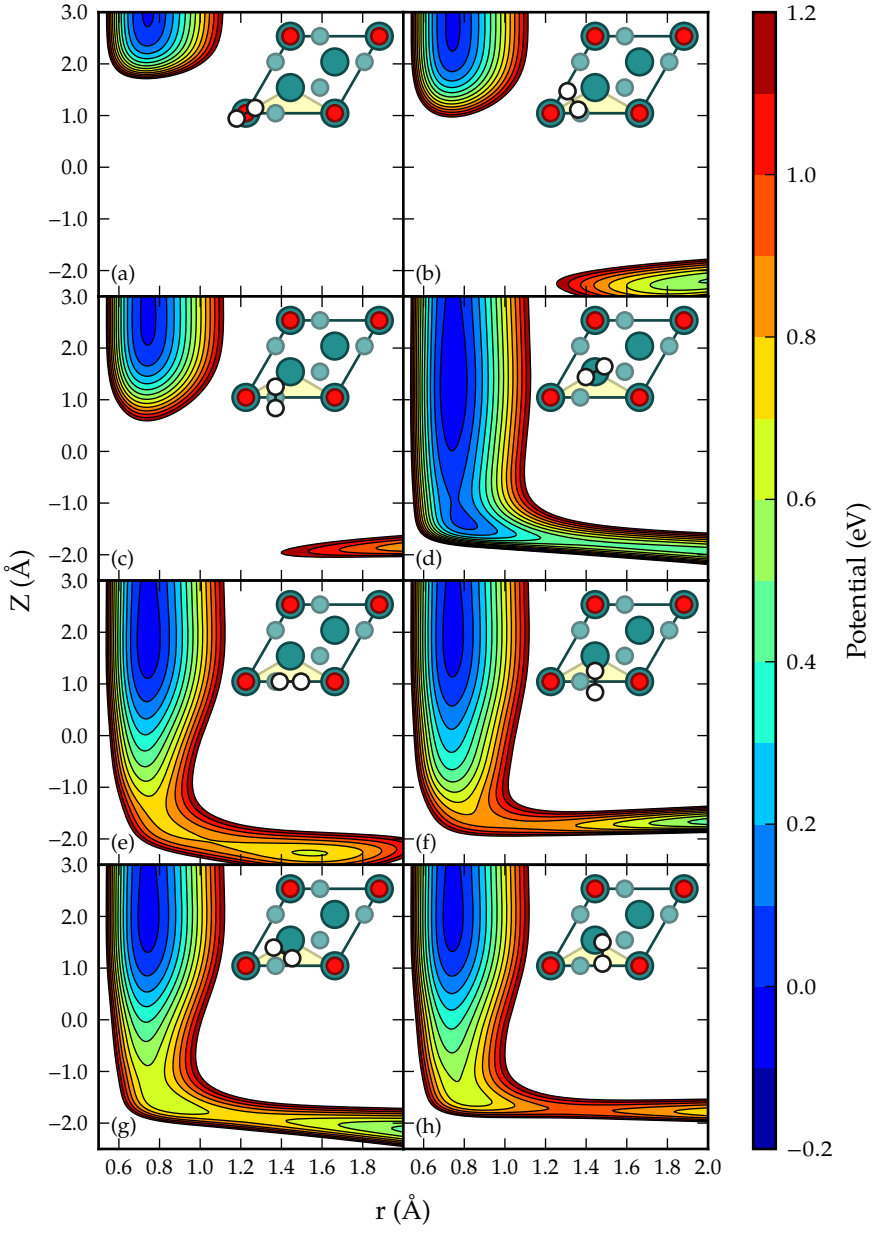


**Figure 7.4** The $(r, Z)$ dependence of the PES for $H_2$ dissociating on 1/3 ML CO-covered Ru(0001) above several different sites and orientations ($\vartheta = 90°$). (a) $\text{top}_{\text{ads}}$ ($\varphi = 0°$), (b) $\text{bridge}_{\text{ads}}$ ($\varphi = 120°$), (c) hcp ($\varphi = 90°$), (d) top ($\varphi = 0°$), (e) bridge ($\varphi = 0°$), (f) bridge ($\varphi = 90°$), (g) t2h ($\varphi = 150°$), (h) t2f ($\varphi = 90°$).

**Table 7.2** Barrier heights and positions for several dissociation geometries for $H_2$ dissociation on bare and 1/3 ML CO-covered Ru(0001). For all dissociation geometries $\vartheta = 90°$. The notation *a*-to-*b* corresponds to dissociation above the *a* site with the H atoms moving towards the next nearest *b* site. If this notation is ambiguous, the geometry according to figure 7.1(c) is given. The dissociation geometries also considered in figure 7.4 are indicated with the letter of the panel they are shown in. Values for the bare Ru(0001) surface from the PBE-vdW-DF2 PES described in chapter 4. RPBE barrier heights from reference 9.

| Site | Surface | $r_b$ (Å) | $Z_b$ (Å) | $E_b$ (eV) | $E_b^{\mathrm{RPBE}}$ (eV) |
|---|---|---|---|---|---|
| top-to-bridge | bare Ru(0001) | 0.751 | 2.605 | 0.004 | |
| — on $\mathrm{top_{ads}}$ (a) | CO/Ru(0001) | — | — | — | |
| — on top (d) | CO/Ru(0001) | 0.754 | −0.971 | 0.095 | 0.30 |
| bridge-to-hollow | bare Ru(0001) | 0.796 | 1.858 | 0.276 | |
| — on $\mathrm{bridge_{ads}}$ (b) | CO/Ru(0001) | 0.773 | −0.350 | 4.347 | |
| — on bridge (e) | CO/Ru(0001) | 1.059 | −2.050 | 0.799 | 0.85 |
| t2h-to-fcc | bare Ru(0001) | 0.771 | 2.139 | 0.115 | |
| — on $\mathrm{t2h_{ads}}$ | CO/Ru(0001) | — | — | — | |
| — on t2h (g) | CO/Ru(0001) | 1.225 | −1.887 | 0.739 | |
| t2f-to-t2f | bare Ru(0001) | 1.292 | 1.552 | 0.312 | |
| — t2f($\varphi = 90°$) (h) | CO/Ru(0001) | 1.312 | −1.737 | 0.923 | 0.84 |
| — t2f($\varphi = 150°$) | CO/Ru(0001) | 0.747 | −1.032 | 0.684 | |
| hcp-to-t2f | bare Ru(0001) | 0.850 | 1.678 | 0.430 | |
| — hcp($\varphi = 30°$) | CO/Ru(0001) | 0.721 | −0.538 | 2.807 | |
| — hcp($\varphi = 90°$) (c) | CO/Ru(0001) | 0.741 | −0.470 | 2.389 | |

CO molecule, dissociation is much more favourable. For all cases in figure 7.4 where a full elbow is shown, late barriers are found. For dissociation directly above the Ru atom without an adsorbed CO molecule, additionally an early barrier and a well are found. This is in general agreement with previous results for the RPBE functional.[9] For bridge-to-hollow dissociation (figure 7.4(e)), however, Groot *et al.* found an early barrier, while here a later barrier is obtained with the use of the PBE-vdW-DF2 functional. For t2f ($\varphi = 90°$) (figure 7.4(h)), only a late barrier is found, whereas previously also an early barrier was found for a geometry, t2f ($\varphi = 88°$), which is close to the one considered here.

In table 7.2 barrier heights and positions for dissociation of $H_2$ on an ideal 1/3 ML CO-covered Ru(0001) surface ($\sqrt{3} \times \sqrt{3}$ cell) are compared to those for dissociation of $H_2$ on an ideal, bare Ru(0001) surface. In the case where one geometry for the bare Ru(0001) has multiple symmetry inequivalent geometries for the CO-covered surface due to the addition of CO, both are given. The subscript "ads" refers to the site which is closest to the adsorbed CO molecule (see also figure 7.1). Note that Groot *et al.*[9] only considered the sites furthest away from the CO in their analysis (*i.e.*, the ones here denoted without subscript "ads"). Similar barrier heights are obtained for the fcc and t2f site as for the hcp and t2h site, respectively, and as such, values for a particular orientation are only given for either hcp (t2h) or fcc (t2f). It is clear that for all configurations that are considered the barrier height is increased relative to the bare Ru(0001), and in some cases a particular dissociation geometry even becomes non-dissociative (*i.e.*, no transition state could be found). This is in general agreement with findings obtained using the RPBE functional.[9] The computed barrier heights are in good agreement with previously obtained values[9] with the RPBE functional, except for the top-to-bridge barrier. For this geometry, the PBE-vdW-DF2 functional predicts a barrier height that is 0.20 eV lower than the RPBE barrier height. Note that the barrier referred to is for passage to a local molecular chemisorption minimum, see figure 7.4(d). Sites close to the CO molecule show either a very high barrier ($> 2$ eV) or no barrier at all.

The results obtained with the PBE-vdW-DF2 functional are at least in qualitative agreement with the results obtained with the RPBE functional.[9] As the dissociation barriers near $\text{top}_{\text{ads}}$ are very high, it is clear that the $H_2$ molecule is repelled by the adsorbed CO molecule and dissociation can therefore only occur in the center of the triangles shown in figure 7.2(a), *i.e.*, close to the bare top site. As $Z_b$ near the top site is $\approx -2$ Å, it is clear that the $H_2$ molecule needs to move into the layer of CO molecules, and if needed push the CO molecules aside, in order to be able to dissociate.

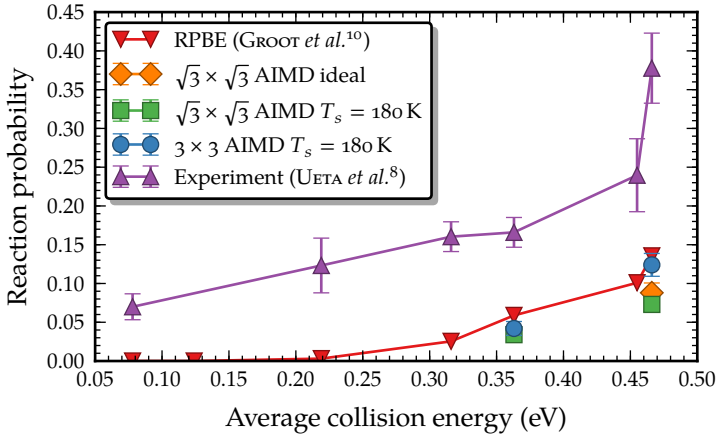


**Figure 7.5** Reaction probabilities as a function of average collision energy computed with several methods compared to experiment.[8] Results obtained with the RPBE[57] functional by Groot *et al.*[10] are also shown.

### 7.3.3 Reaction probability and energy exchange

In figure 7.5 the reaction probability is shown as a function of average collision energy as computed using a rigid, ideal $\sqrt{3} \times \sqrt{3}$ cell, and using $\sqrt{3} \times \sqrt{3}$ and $3 \times 3$ simulation cells at $T_s = 180\,\mathrm{K}$. For comparison, the experimental data by Ueta *et al.*[8] and the previous results using the RPBE[57] functional by Groot *et al.*,[9] which were obtained with the use of a rigid, ideal $\sqrt{3} \times \sqrt{3}$ cell in the DFT calculations, are also shown.

It is clear that the PBE-vdW-DF2 reaction probabilities are too low compared to experiment, which was also the case for the previously computed RPBE reaction probabilities.[9] The PBE-vdW-DF2 reaction probabilities are even lower than the RPBE reaction probabilities. The reaction probability computed with a frozen ideal surface matches closely to, or is even slightly larger than, the reaction probability computed with the $\sqrt{3} \times \sqrt{3}$ cell for $T_s = 180\,\mathrm{K}$. The reaction probabilities computed for $T_s = 180\,\mathrm{K}$ are greater if the $3 \times 3$ simulation cell is used, this result being statistically significant for $E_{\mathrm{trans}} = 0.466\,\mathrm{eV}$. At this incidence energy, the reaction probability for the $3 \times 3$ cell is higher by about 0.05 compared to the $\sqrt{3} \times \sqrt{3}$ cell.

It is not fully understood why a disagreement between theory and

experiment remains. As surface temperature is taken into account here, it seems likely that the disagreement of the PBE-vdW-DF2 reaction probabilities for $T_s = 180$ K with experiment is due to the XC functional not being good enough, even though this functional works well for $H_2$ dissociation on bare Ru(0001), as shown in chapter 4. Another possible cause for the discrepancy between theory and experiments concerns the coverage of Ru(0001) by CO in the experiment. To obtain the 1/3 ML CO-covered Ru(0001) system, which should correspond to the simple $\sqrt{3}\times\sqrt{3}$ system studied here,[15,19,21,22] the experiments worked with a system exhibiting half the measured saturation coverage.[8] The assumption has been that this should correspond to the 1/3 ML covered surface, because the saturation coverage is experimentally known to be 2/3 ML.[35] If the saturation coverage achieved by Ueta *et al.* however was somehow less than 2/3 ML, this could explain the observed discrepancy with experiment at least in part. Specifically, on average the coverage should then be less than 1/3 ML in the molecular beam experiment, and that should make the measured reactivity higher than the one calculated here. This could be aggravated by inhomogeneity effects, as this could give rise to the formation of islands[21] with the 1/3 ML $\sqrt{3} \times \sqrt{3}$ coverage considered here and areas with a much lower coverage, which should exhibit a much greater reactivity. It would therefore be useful if the experiments could be repeated with the accompanying use of low-energy electron diffraction (LEED) to ascertain the surface coverage pattern used in the experiments indeed corresponds to the $\sqrt{3}\times\sqrt{3}$ pattern considered here, to rule out this source of error.

The remainder of this section will focus on the effects motion of the surface has on the reaction probability. Possible reasons for why the reaction probability of $D_2$ on a thermal slab might be slightly smaller than the reaction probability of $D_2$ on a frozen ideal slab, as found with the $\sqrt{3}\times\sqrt{3}$ cell, are that the CO molecules and the Ru(0001) surface act as an energy sink, causing the $D_2$ to lose energy it could otherwise have used to overcome the barrier to dissociation, and that slightly less of the surface might be available because the CO molecule is, on average, slightly tilted in the dynamics. From the present results, it is not clear how important these effects are.

With respect to the difference between the smaller and larger simu-

**Table 7.3** For all AIMD calculations, the average initial translational energy of the molecules that go on to react, along with the reaction probability for that calculation.

| Energy | Cell model | $\langle E_{\text{trans}} \rangle_{\text{react}}$ (eV) | $P_r$ |
|---|---|---|---|
| 0.363 eV | $(\sqrt{3} \times \sqrt{3})$ 180 K | $0.415 \pm 0.015$ | $0.034 \pm 0.008$ |
| | $(3 \times 3)$ 180 K | $0.452 \pm 0.028$ | $0.042 \pm 0.009$ |
| 0.466 eV | $(\sqrt{3} \times \sqrt{3})$ ideal | $0.607 \pm 0.020$ | $0.088 \pm 0.013$ |
| | $(\sqrt{3} \times \sqrt{3})$ 180 K | $0.585 \pm 0.016$ | $0.073 \pm 0.008$ |
| | $(3 \times 3)$ 180 K | $0.576 \pm 0.020$ | $0.124 \pm 0.015$ |

lation cell, it is not immediately apparent what could be the cause. Possible causes could be extra dynamical effects due to the presence of multiple independent CO molecules, such as extra possibilities for energy exchange, but also small differences in DFT parameters (a smaller $k$-grid was used for the $3 \times 3$ calculations) might play a role. These two effects are discussed below. As is shown below, the larger reactivity obtained with the $3\times3$ cell is probably due to the $D_2$ exchanging energy with three independent CO molecules, which allows the nearby CO molecules to move apart, so that the reactive Ru(0001) surface becomes exposed.

Convergence tests have been carried out on the $k$-point grid used for the DFT calculations. From these convergence tests, it is clear that the $H_2$/CO+Ru(0001) interaction is described accurately, the largest observed difference between the $\sqrt{3} \times \sqrt{3}$ cell and the $3 \times 3$ cell being about 34 meV. Although this number is not small on the scale of the differences (the relative displacement on the energy scale of the two $T_s = 180$ K reaction probability curves is estimated to be in the range of $50 - 100$ meV), it cannot explain the whole difference. Also, the maximum observed energy difference was in the opposite direction to that which would be expected to explain the difference in reactivity (the potential near the surface was higher for the $3 \times 3$ cell rather than lower, which decreases reactivity instead of increasing it). It therefore seems unlikely that small differences in the DFT parameters can explain the observed differences for the two simulation cells.

In table 7.3 the average initial translational energy of the molecules that go on to react is shown for all AIMD calculations, together with

the reaction probability for each calculation. It is clear that for the different simulation cell models the average initial translational energy of the dissociating molecules is the same, at least insofar as the error due to sampling is concerned. This suggests that the "effective" barriers to dissociation are the same for all different simulation cell sizes and thus that differences between the models are not due to static effects (*i.e.*, due to the barrier to dissociation being different for different sizes of the simulation cell).

In table 7.1 several geometrical properties are given of the surface, with $D_2$ (the dynamics done to determine the reaction probability) and without $D_2$ (the dynamics of the slab used to generate initial conditions). In section 7.3.1 the results without $D_2$ were discussed. The results with $D_2$, and the comparison to the results without $D_2$, are discussed here. The numbers in table 7.1 correspond to averages from the trajectories beginning with the $D_2$ molecule in the gas phase, for the case that $D_2$ is present. As such, these parameters do not straightforwardly correspond to a physically measurable situation, and these parameters are only used to compare to the (in principle measurable) parameters for the case without $D_2$. For both the $\sqrt{3} \times \sqrt{3}$ and the $3 \times 3$ cell, the mean square displacement of the C and O atoms is increased markedly compared to the case without $D_2$, and even more so for the $3 \times 3$ cell than for the $\sqrt{3} \times \sqrt{3}$ cell. This occurs for both the parallel and perpendicular components of the displacements, but mostly for the parallel component. Intriguingly, for the perpendicular component, little or no difference is found between the $\sqrt{3} \times \sqrt{3}$ and the $3 \times 3$ cells, whereas the parallel component does show a difference. Furthermore, the average tilt angles of the CO with respect to the surface are also increased. This means that the geometry of the CO-covered Ru(0001) surface is altered by the impinging $D_2$ molecules, and more so for the $3 \times 3$ cell than for the $\sqrt{3} \times \sqrt{3}$ cell. As energy in $D_2$ can be exchanged with the surface to alter the geometry of the CO-covered surface, this in turn suggests that more energy is exchanged with the surface for the $3 \times 3$ cell than for the $\sqrt{3} \times \sqrt{3}$ cell. In particular, the O atom moves most, with the C atom moving less, as also indicated by the increased tilt angles. The other parameters, *i.e.*, the interlayer spacing, the protrusion of the topmost Ru atom, the Ru–C and C–O bond lengths are all not much influenced

**Table 7.4** Amount of energy exchanged with the surface in collisions of $D_2$ with the CO-covered Ru(0001) surface, for cases which result in scattering. Direct trajectories make only a single rebound.

| Energy | $\sqrt{3} \times \sqrt{3}$ cell (eV) | $3 \times 3$ cell (eV) |
|---|---|---|
| 0.363 eV | $0.080 \pm 0.003$ | $0.191 \pm 0.005$ |
| — direct only | $0.077 \pm 0.003$ | $0.187 \pm 0.005$ |
| — indirect only | $0.106 \pm 0.013$ | $0.225 \pm 0.018$ |
| 0.466 eV | $0.105 \pm 0.002$ | $0.263 \pm 0.007$ |
| — direct only | $0.104 \pm 0.002$ | $0.258 \pm 0.008$ |
| — indirect only | $0.119 \pm 0.010$ | $0.278 \pm 0.014$ |

by the impinging $D_2$ molecule. These results therefore indicate that energy can be exchanged between $D_2$ and the CO molecules, and not so much with the Ru(0001) surface.

In table 7.4 the amount of energy exchange of the molecule with the surface is shown for scattered trajectories, which is defined as the total energy lost to the surface by the $D_2$ molecule at $t = t_{\text{final}}$ compared to $t = 0$. The results have also been split into direct (single rebound) and indirect (multiple rebounds) scattering. It is clear that the amount of energy exchanged in the larger simulation cell is significantly larger than that for the smaller simulation cell, by about a factor 2.5 for the higher incidence energy and slightly less for the lower incidence energy. The number of atoms has increased by a factor 3 on going from the smaller to the larger cell, which suggests that, for the atoms with which energy is exchanged, also energy is exchanged with molecules that would correspond to mirror images in the $\sqrt{3} \times \sqrt{3}$ cell, but are independent in the $3 \times 3$ cell. For indirect scattering, slightly more energy is exchanged than is the case for direct scattering.

Intriguingly, a considerable amount of energy is transferred to the surface for both simulation cell sizes. It is rather remarkable that in the case of the $3 \times 3$ cell the amount of energy that is exchanged is over half the amount of initial translational energy, in particular if this is compared to the amount for the $\sqrt{3} \times \sqrt{3}$ cell. A likely explanation for this discrepancy seems to be that the $D_2$ molecule deposits energy into the CO molecule(s). It is interesting to see that in spite of the large energy

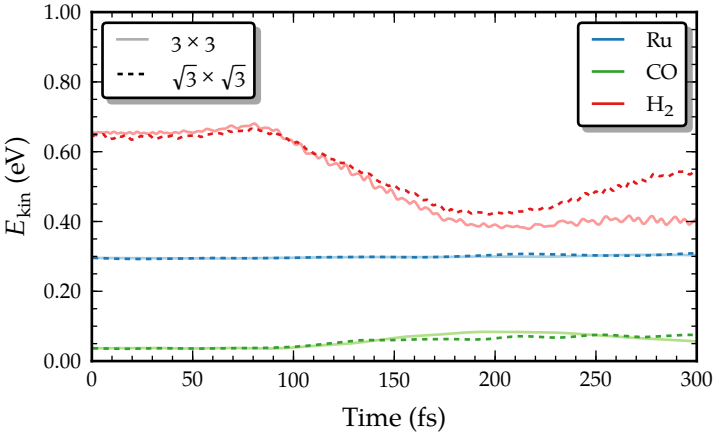


**Figure 7.6** Time evolution of the kinetic energy of the ruthenium slab, the CO molecules and $H_2$ molecule, averaged over all trajectories with $t_{final} > 300$ fs, for the $\sqrt{3}\times\sqrt{3}$ and $3\times3$ cells. The energies for the CO and Ru atoms have been normalized to the amount present in the $\sqrt{3}\times\sqrt{3}$ cell.

transfer to the CO molecule(s) the reaction probability of the ideal and the $T_s = 180$ K surface do not differ much. This suggests that the energy transfer is at least partly compensated by new reaction pathways becoming available.

To better understand to what part of the surface the energy is lost, in figure 7.6 the time evolution of the kinetic energy of the ruthenium slab, the CO molecules and the $H_2$ molecule, averaged over all trajectories with $t_{final} > 300$ fs, is shown. The kinetic energies of the CO molecules and Ru atoms for the $3 \times 3$ cell have been divided by three to account for the increase in the number of atoms in the $3 \times 3$ cell compared to the $\sqrt{3} \times \sqrt{3}$ cell. It is clear that the amount of kinetic energy that is transferred to the Ru atoms is rather small, while the amount of kinetic energy that is transferred to the CO molecules is larger. No large differences are observed between the smaller and larger cell. These results therefore show that energy is indeed exchanged with the, in the $3 \times 3$ cell, independent images, and, in particular, with the CO molecules.

Further information about the differences between the $\sqrt{3} \times \sqrt{3}$ and $3 \times 3$ cell can be found by binning the energy that is exchanged with the

**Table 7.5** Amount of energy exchanged with the surface in collisions of $D_2$ with the CO-covered Ru(0001) surface, binned with respect to the impact site.

| Energy | Site | $\sqrt{3}\times\sqrt{3}$ cell (eV) | $3\times3$ cell (eV) |
|---|---|---|---|
| 0.363 eV | $top_{ads}$ | $0.102 \pm 0.008$ | $0.104 \pm 0.009$ |
| | top | $0.056 \pm 0.007$ | $0.203 \pm 0.013$ |
| | $bridge_{ads}$ | $0.100 \pm 0.005$ | $0.173 \pm 0.009$ |
| | bridge | $0.057 \pm 0.004$ | $0.255 \pm 0.013$ |
| | hcp/fcc | $0.080 \pm 0.005$ | $0.215 \pm 0.010$ |
| 0.466 eV | $top_{ads}$ | $0.167 \pm 0.009$ | $0.178 \pm 0.012$ |
| | top | $0.066 \pm 0.005$ | $0.269 \pm 0.017$ |
| | $bridge_{ads}$ | $0.111 \pm 0.003$ | $0.222 \pm 0.011$ |
| | bridge | $0.095 \pm 0.007$ | $0.329 \pm 0.014$ |
| | hcp/fcc | $0.099 \pm 0.004$ | $0.295 \pm 0.013$ |

surface with respect to the impact site of the molecule. The results of such an analysis are given in table 7.5 and the bins that have been used are indicated in figure 7.2(b). For all sites that are considered, except the $top_{ads}$ site, and both incidence energies, the amount of energy exchange is larger for the $3\times3$ cell than for the $\sqrt{3}\times\sqrt{3}$ cell. For the $top_{ads}$ site however, the amount of energy exchange is, to within the statistical errors indicated, the same for both simulation cells. As the $top_{ads}$ site corresponds to the $D_2$ molecule colliding directly on top of the CO molecule, this difference is not surprising, because the next CO molecule is $\sqrt{3}$ times the Ru–Ru distance away, which for the present case is 4.77 Å. The molecule thus exchanges energy with only a single CO molecule, and predominantly energy in motion in the $Z$ direction, as it is a head-on collision and the molecule initially only has momentum in $Z$. For all other sites, the interpretation is that the molecule will go in between the CO molecules, which means that the $D_2$ molecule may be able to exchange energy with up to three nearest CO molecules. In this case, energy exchange will mostly involve motion in the $U$ and $V$ directions, as the $D_2$ molecule collides with the CO molecule(s) more from the side. As in the $\sqrt{3}\times\sqrt{3}$ cell only a single CO molecule is present the $D_2$ molecule pushes against its mirror images in such a way that the forces parallel to the surface partially cancel each other. As in the $3\times3$ cell

three independent CO molecules are present for similarly small $D_2$–CO distances projected on the surface (see figure 7.2(a)), such a cancellation of forces does not occur and energy can be exchanged with all of the three independent CO molecules without forces between CO and $D_2$ being partly cancelled through the imposed periodicity, explaining the larger energy exchange.

If energy is exchanged between the $D_2$ and CO in the $U$ and $V$ directions, the CO will move along the surface, but in case of the $\sqrt{3} \times \sqrt{3}$ cell the entire layer moves, as only a single independent CO molecule is present. In case of the $3 \times 3$ cell however, the three independent CO molecules may move apart. This can be analysed by tracking the size of the 2D triangles that are spanned by the CO molecules (six for the $3 \times 3$ cell, see also figure 7.2(a)). In table 7.6 the size of the surface triangle in which the $D_2$ is initially located ($t = 0$) is shown for the first and final time step of both reactive and non-reactive trajectories, with the corners of the triangle attached to either the C or the O atoms. For both non-reactive and reactive trajectories, and for both the C and O triangles, the size of the surface triangle in which the $D_2$ is initially located grows during the dynamics, from a value essentially equal to that of an ideal triangle size to a value which is in the range of about 15% to 30% larger, *i.e.*, the CO layer locally "opens" due to the impinging $D_2$ molecule pushing the CO molecules aside. The O triangles are larger than the C triangles, suggesting that the molecules, apart from being pushed away, are also tilted away to make room for $D_2$. As the initial triangle size is slightly larger for dissociative trajectories than for scattered trajectories, an additional effect appears to be that in the $3 \times 3$ CO-covered surface the $D_2$ molecule can find spots where the CO molecules have already moved apart a bit, which opens the surface to reaction. It should, however, be stressed that such an effect is small and not fully established at present due to the limited statistics of the dynamics calculations. The main established mechanism therefore is the CO layer opening effect due to the impinging $D_2$ molecule pushing the CO molecules away.

The difference between the reaction probability of the $3 \times 3$ and the $\sqrt{3} \times \sqrt{3}$ cells can thus be explained mainly from the amount of energy exchanged between the $D_2$ molecule and the surface, and in particular energy transferred to motion of CO molecules parallel to the surface.

| Energy | $\Delta_C$ (Å²) | | $\Delta_O$ (Å²) | |
|---|---|---|---|---|
| | $t = 0$ | $t = t_{final}$ | $t = 0$ | $t = t_{final}$ |
| 0.363 eV | $9.92 \pm 0.03$ | $11.29 \pm 0.08$ | $10.04 \pm 0.05$ | $12.32 \pm 0.13$ |
| — scattering | $9.91 \pm 0.03$ | $11.26 \pm 0.08$ | $10.03 \pm 0.05$ | $12.29 \pm 0.14$ |
| — dissociation | $9.97 \pm 0.13$ | $11.92 \pm 0.18$ | $10.22 \pm 0.27$ | $12.75 \pm 0.30$ |
| 0.466 eV | $9.85 \pm 0.03$ | $11.56 \pm 0.08$ | $9.94 \pm 0.05$ | $12.67 \pm 0.14$ |
| — scattering | $9.83 \pm 0.03$ | $11.45 \pm 0.09$ | $9.90 \pm 0.05$ | $12.61 \pm 0.16$ |
| — dissociation | $10.03 \pm 0.09$ | $12.26 \pm 0.17$ | $10.21 \pm 0.15$ | $13.05 \pm 0.30$ |
| ideal | 9.85 | — | 9.85 | — |

**Table 7.6** Size of the surface triangle (see figure 7.2(a)) in which the $D_2$ is initially located for $D_2$ scattering or dissociation on the CO-covered Ru(0001) surface. $t_{final}$ is taken to be the first time step for which the analysis conditions are met.





CHAPTER 7

Ab initio molecular dynamics study of $D_2$ dissociation on CO-precovered Ru(0001)

Significantly more energy is exchanged between the molecule and the CO overlayer for the $3 \times 3$ cell than for the $\sqrt{3} \times \sqrt{3}$ cell. As a result of this, the CO molecules can move away from one another in the $3 \times 3$ cell. Only in the $3 \times 3$ cell (three) independent CO molecules are present. These independent CO molecules can move apart, leaving more space, and therefore more favourable pathways to reaction, for the molecule.

An interesting open question is whether or not further increasing the size of the simulation cell could result in further changes in the reaction probability. As the spacing between different CO molecules is rather large (the diagonal of the HCP(0001) unit cell which, for this system, is 4.77 Å), it seems likely that the $D_2$ molecule cannot influence the motion of the next nearest neighbour CO molecule, meaning CO molecules further away than the three making up the triangle in which it lands (see figure 7.2). It is therefore not expected that increasing the size of the simulation cell further will dramatically change the reaction probability.

Even though the PBE-vdW-DF2 functional used here describes the reaction of $H_2$ and $D_2$ on bare Ru(0001) rather well (chapter 4), it severely underestimates the reactivity of $D_2$ on CO-covered Ru(0001). The PBE-vdW-DF2 functional may be described as a candidate SRP XC functional for $H_2$/Ru(0001) (it described the dissociation of $H_2$ and $D_2$ quite well, but its validity for other (diffraction) experiments was not established). The present study suggests that a XC functional that gives a good description of $H_2$ reacting on a bare metal surface may not necessarily work for the same metal, but with the surface poisoned by CO. Additional studies on other $H_2$–metal surface and $H_2$–CO pre-covered metal surface systems are needed to establish whether this finding is general to these systems and what causes the problem noted.

## 7.4 Conclusions

The dissociation of $D_2$ on 1/3 ML CO-covered Ru(0001) has been studied with quasi-classical AIMD calculations using the PBE-vdW-DF2 functional. The PBE-vdW-DF2 functional gives a reasonable description of the structure of the CO-covered surface, both compared to experimental data and compared to previous theoretical studies. The

molecule–surface interaction of $D_2$ with the CO-covered Ru(0001) surface is mostly in agreement with a previous study[9] where the RPBE functional was used, but some qualitative as well as quantitative differences are found.

The reaction probabilities computed with the AIMD method are not in agreement with experimental data, as the computed reaction probabilities are too low. The reaction probabilities are however in reasonable agreement with the previous RPBE results using a frozen ideal surface model, although the values reported here are still slightly lower. The discrepancy with experimental data is assigned to the functional which is used here not working well enough for this system, in spite of the fact that it works well for $H_2$ dissociation on bare Ru(0001). For the higher investigated incidence energy ($E_{\text{trans}} = 0.466\,\text{eV}$), the reaction probability for the $3 \times 3$ cell is somewhat higher (by about 0.05) than for the $\sqrt{3} \times \sqrt{3}$ cell.

The reaction probability for $D_2$ on a $T_s = 180\,\text{K}$ slab is overall similar to the reaction probability for $D_2$ on an ideal slab. This arises due to a balance between opposing factors. The $D_2$ molecule loses a rather large amount of energy to the surface. In this way the impinging $D_2$ molecules can push aside the CO molecule(s). Although the resulting energy loss leads to a decrease in reaction, as this energy cannot be used to overcome the barrier to reaction, the displacement of CO molecules leads to new reactive pathways opening up. The CO molecules in a $T_s = 180\,\text{K}$ slab are additionally slightly tilted, whereas they are upright in the ideal slab, which may lead to a decrease of reactivity, although the size of this effect is not clear from the present results.

The difference between the reaction probabilities obtained for the higher incidence energy for the $\sqrt{3} \times \sqrt{3}$ and the $3 \times 3$ cells can be explained by the number of independently moving CO molecules present in the cell. For the $3 \times 3$ cell, the $D_2$ molecule can exchange energy with up to three independent CO molecules, allowing the CO layer of the surface to open up locally. For the $\sqrt{3} \times \sqrt{3}$ cell only a single independent CO molecule is present, which leads to some of the forces working on the C and O atoms to be cancelled out due to the $D_2$ molecule pushing different mirror images of these atoms in opposing directions. As a result, the $D_2$ molecule exchanges less energy with the surface and cannot

displace the CO molecules far enough for dissociation to become more effective.

## References


[1] G. J. Kroes and C. Díaz. Quantum and classical dynamics of reactive scattering of $H_2$ from metal surfaces. Accepted to *Chemical Society Reviews*. doi: 10.1039/C5CS00336A. 2016.

[2] A. Gross and A. Dianat. Hydrogen dissociation dynamics on precovered Pd surfaces: Langmuir is still right. *Physical Review Letters* **98**(20), 206107, 2007.

[3] A. Lozano, A. Gross, and H. F. Busnengo. Adsorption dynamics of $H_2$ on Pd(100) from first principles. *Physical Chemistry Chemical Physics* **11**(27), pp. 5814–5822, 2009.

[4] A. Gross. *Ab initio* molecular dynamics simulations of the adsorption of $H_2$ on palladium surfaces. *ChemPhysChem* **11**(7), pp. 1374–1381, 2010.

[5] A. Lozano, A. Gross, and H. F. Busnengo. Molecular dynamics study of $H_2$ dissociation on H-covered Pd(100). *Physical Review B* **81**(12), 121402, 2010.

[6] A. Gross. Coverage effects in the adsorption of $H_2$ on Pd(100) studied by *ab initio* molecular dynamics simulations. *Journal of Chemical Physics* **135**(17), 174707, 2011.

[7] A. Gross. *Ab initio* molecular dynamics study of $H_2$ adsorption on sulfur- and chlorine-covered Pd(100). *Surface Science* **608**, pp. 249–254, 2013.

[8] H. Ueta, I. M. N. Groot, M. A. Gleeson, S. Stolte, G. C. McBane, L. B. F. Juurlink, and A. W. Kleyn. CO blocking of $D_2$ dissociative adsorption on Ru(0001). *ChemPhysChem* **9**(16), pp. 2372–2378, 2008.

[9] I. M. N. Groot, J. C. Juanes-Marcos, R. A. Olsen, and G. J. Kroes. A theoretical study of $H_2$ dissociation on $(\sqrt{3}x\sqrt{3})R30^\circ$ CO/Ru(0001). *Journal of Chemical Physics* **132**(14), 144704, 2010.

[10] I. M. N. Groot, J. C. Juanes-Marcos, C. Díaz, M. F. Somers, R. A. Olsen, and G. J. Kroes. Dynamics of dissociative adsorption of hydrogen on a CO-precovered Ru(0001) surface: a comparison of theoretical and experimental results. *Physical Chemistry Chemical Physics* **12**(6), pp. 1331–1340, 2010.

[11] B. Baule. Theoretische Behandlung der Erscheinungen in verdünnten Gasen. *Annalen der Physik* **349**(9), pp. 145–176, 1914.

[12] A. Gross. *Theoretical Surface Science*. Berlin: Springer, 2003.

[13] P. Zhao, Y. He, D. B. Cao, X. Wen, H. Xiang, Y. W. Li, J. Wang, and H. Jiao. High coverage adsorption and co-adsorption of CO and $H_2$ on Ru(0001) from DFT and thermodynamics. *Physical Chemistry Chemical Physics* **17**(29), pp. 19446–19456, 2015.

[14] J. C. Fuggle, T. E. Madey, M. Steinkilberg, and D. Menzel. Photoelectron spectroscopic studies of adsorption of CO and oxygen on Ru(001). *Surface Science* **52**(3), pp. 521–541, 1975.

[15] G. Michalk, W. Moritz, H. Pfnür, and D. Menzel. A LEED determination of the structures of Ru(001) and of CO/Ru(001)–$\sqrt{3} \times \sqrt{3}$R30°. *Surface Science* **129**(1), pp. 92–106, 1983.

[16] M. Gierer, H. Bludau, H. Over, and G. Ertl. The bending mode vibration of CO on Ru(0001) studied with low-energy electron-diffraction. *Surface Science* **346**(1–3), pp. 64–72, 1996.

[17] J. C. Fuggle, M. Steinkilberg, and D. Menzel. Angular dependence of UV photoemission spectra from clean Ru(001) and from adsorbed oxygen and CO. *Chemical Physics* **11**(2), pp. 307–317, 1975.

[18] T. E. Madey. The geometry of CO on Ru(001): Evidence for bending vibrations in adsorbed molecules. *Surface Science* **79**(2), pp. 575–588, 1979.

[19] E. D. Williams and W. H. Weinberg. Geometric structure of carbon monoxide chemisorbed on the ruthenium (001) surface at low temperatures. *Surface Science* **82**(1), pp. 93–101, 1979.

[20] H. Pfnür, D. Menzel, F. M. Hoffmann, A. Ortega, and A. M. Bradshaw. High resolution vibrational spectroscopy of CO on Ru(001): The importance of lateral interactions. *Surface Science* **93**(2–3), pp. 431–452, 1980.

[21] H. Pfnür and D. Menzel. Lateral interactions for CO/Ru(001): order-disorder transitions of the $\sqrt{3}$ structure. *Surface Science* **148**(2–3), pp. 411–438, 1984.

[22] H. Pfnür and H. J. Heier. Order-disorder phenomena in the system CO/Ru(001). *Berichte der Bunsengesellschaft für physikalische Chemie* **90**(3), pp. 272–277, 1986.

[23] H. Pfnür and D. Menzel. The influence of adsorbate interactions on kinetics and equilibrium for CO on Ru(001). I. Adsorption kinetics. *Journal of Chemical Physics* **79**(5), pp. 2400–2410, 1983.

[24] H. Pfnür, P. Feulner, H. A. Engelhardt, and D. Menzel. An example of "fast" desorption: anomalously high pre-exponentials for CO desorption from Ru(001). *Chemical Physics Letters* **59**(3), pp. 481–486, 1978.

[25] H. Pfnür, P. Feulner, and D. Menzel. The influence of adsorbate interactions on kinetics and equilibrium for CO on Ru(001). II. Desorption kinetics and equilibrium. *Journal of Chemical Physics* **79**(9), pp. 4613–4623, 1983.

[26] J. Braun, K. L. Kostov, G. Witte, and C. Woll. CO overlayers on Ru(0001) studied by helium atom scattering: structure, dynamics, and the influence of coadsorbed H and O. *Journal of Chemical Physics* **106**(19), pp. 8262–8273, 1997.

[27] H. Over, W. Moritz, and G. Ertl. Anisotropic atomic motions in structural analysis by low energy electron diffraction. *Physical Review Letters* **70**(3), pp. 315–318, 1993.

[28] H. Over, M. Gierer, H. Bludau, and G. Ertl. Anisotropic thermal displacements of adsorbed atoms and molecules on surfaces studied by low-energy electron diffraction. *Physical Review B* **52**(23), pp. 16812–16829, 1995.

[29] M. Bonn, S. Funk, Ch. Hess, D. N. Denzler, C. Stampfl, M. Scheffler, M. Wolf, and G. Ertl. Phonon- versus electron-mediated desorption and oxidation of CO on Ru(0001). *Science* **285**(5430), pp. 1042–1045, 1999.

[30] L. Diekhöner, H. Mortensen, A. Baurichter, and A. C. Luntz. Laser assisted associative desorption of $N_2$ and CO from Ru(0001). *Journal of Chemical Physics* **115**(7), pp. 3356–3373, 2001.

[31] J. Gladh, T. Hansson, and H. Öström. Electron- and phonon-coupling in femtosecond laser-induced desorption of CO from Ru(0001). *Surface Science* **615**, pp. 65–71, 2013.

[32] C. Hess, S. Funk, M. Bonn, D. N. Denzler, M. Wolf, and G. Ertl. Femtosecond dynamics of chemical reactions at surfaces. *Applied Physics A* **71**(5), pp. 477–483, 2000.

[33] P. Jakob. Fermi resonance distortion of the Ru–CO stretching mode of CO adsorbed on Ru(001). *Journal of Chemical Physics* **108**(12), pp. 5035–5043, 1998.

[34] K. L. Kostov, H. Rauscher, and D. Menzel. Adsorption of CO on oxygen-covered Ru(001). *Surface Science* **278**(1–2), pp. 62–86, 1992.

[35] D. E. Starr and H. Bluhm. CO adsorption and dissociation on Ru(0001) at elevated pressures. *Surface Science* **608**, pp. 241–248, 2013.

[36] S. Wagner, H. Öström, A. Kaebe, M. Krenz, M. Wolf, A. C. Luntz, and C. Frischkorn. Activated associative desorption of C + O → CO from Ru(001) induced by femtosecond laser pulses. *New Journal of Physics* **10**(12), 125031, 2008.

[37] S. Wurm, P. Feulner, and D. Menzel. Extremely high vibrational excitation of CO molecules desorbed from transition metal surfaces by electron impact. *Physical Review Letters* **74**(13), pp. 2591–2594, 1995.

[38] H. Öström, H. Öberg, H. Xin, J. LaRue, M. Beye, M. Dell'Angela, J. Gladh, M. L. Ng, J. A. Sellberg, S. Kaya, G. Mercurio, D. Nordlund, M. Hantschmann, F. Hieke, D. Kühn, W. F. Schlotter, G. L. Dakovski, J. J. Turner, M. P. Minitti, A. Mitra, S. P. Moeller, A. Föhlisch, M. Wolf, W. Wurth, M. Persson, J. K. Nørskov, F. Abild-Pedersen, H. Ogasawara, L. G. M. Pettersson, and A. Nilsson. Probing the transition state region in catalytic CO oxidation on Ru. *Science* **347**(6225), pp. 978–982, 2015.

[39] M. Dell'Angela, T. Anniyev, M. Beye, R. Coffee, A. Föhlisch, J. Gladh, T. Katayama, S. Kaya, O. Krupin, J. LaRue, A. Møgelhøj, D. Nordlund, J. K. Nørskov, H. Öberg, H. Ogasawara, H. Öström, L. G. M. Pettersson, W. F. Schlotter, J. A. Sellberg, F. Sorgenfrei, J. J. Turner, M. Wolf, W. Wurth, and A. Nilsson. Real-time observation of surface bond breaking with an X-ray laser. *Science* **339**(6125), pp. 1302–1305, 2013.

[40] I. M. Ciobica and R. A. van Santen. Carbon monoxide dissociation on planar and stepped Ru(0001) surfaces. *Journal of Physical Chemistry B* **107**(16), pp. 3808–3812, 2003.

[41] I. M. Ciobica, A. W. Kleyn, and R. A. van Santen. Adsorption and coadsorption of CO and H on ruthenium surfaces. *Journal of Physical Chemistry B* **107**(1), pp. 164–172, 2003.

[42] M. Gajdos, A. Eichler, and J. Hafner. CO adsorption on close-packed transition and noble metal surfaces: trends from *ab initio* calculations. *Journal of Physics: Condensed Matter* **16**(8), pp. 1141–1164, 2004.

[43] J. J. Mortensen, Y. Morikawa, B. Hammer, and J. K. Nørskov. A comparison of $N_2$ and CO adsorption on Ru(001). *Zeitschrift für Physikalische Chemie* **198**(1–2), pp. 113–122, 1997.

[44] C. Stampfl and M. Scheffler. Energy barriers and chemical properties in the coadsorption of carbon monoxide and oxygen on Ru(0001). *Physical Review B* **65**(15), 155417, 2002.

[45] J. S. McEwen and A. Eichler. Phase diagram and adsorption-desorption kinetics of CO on Ru(0001) from first principles. *Journal of Chemical Physics* **126**(9), 094701, 2007.

[46] A. Stroppa and G. Kresse. The shortcomings of semi-local and hybrid functionals: what we can learn from surface science studies. *New Journal of Physics* **10**(6), 063020, 2008.

[47] B. Hammer, Y. Morikawa, and J. K. Nørskov. CO chemisorption at metal surfaces and overlayers. *Physical Review Letters* **76**(12), pp. 2141–2144, 1996.

[48] F. Abild-Pedersen and M. P. Andersson. CO adsorption energies on metals with correction for high coordination adsorption sites – a density functional study. *Surface Science* **601**(7), pp. 1747–1753, 2007.

[49] J. Sun, M. Marsman, A. Ruzsinszky, G. Kresse, and J. P. Perdew. Improved lattice constants, surface energies, and CO desorption energies from a semilocal density functional. *Physical Review B* **83**(12), 121410(R), 2011.

[50] C. Corriol, G. R. Darling, S. Holloway, I. Andrianov, T. Klamroth, and P. Saalfrank. Vibrational heating in electron stimulated desorption of CO from transition metals: a classical mechanics analysis. *Surface Science* **528**(1–3), pp. 27–34, 2003.

[51] C. Corriol, G. R. Darling, S. Holloway, W. Brenig, I. Andrianov, T. Klamroth, and P. Saalfrank. Theory of electron stimulated desorption and dissociation of CO at transition metals. *Journal of Chemical Physics* **117**(9), pp. 4489–4498, 2002.

[52] G. Füchsel, J. C. Tremblay, and P. Saalfrank. A six-dimensional potential energy surface for Ru(0001)(2×2):CO. *Journal of Chemical Physics* **141**(9), 094704, 2014.

[53] I. M. N. Groot, H. Ueta, M. J. T. C. van der Niet, A. W. Kleyn, and L. B. F. Juurlink. Supersonic molecular beam studies of dissociative adsorption of $H_2$ on Ru(0001). *Journal of Chemical Physics* **127**(24), 244701, 2007.

[54] P. Nieto, D. Farías, R. Miranda, M. Luppi, E. J. Baerends, M. F. Somers, M. J. T. C. van der Niet, R. A. Olsen, and G. J. Kroes. Diffractive and reactive scattering of $H_2$ from Ru(0001): experimental and theoretical study. *Physical Chemistry Chemical Physics* **13**(18), pp. 8583–8597, 2011.

[55] J. P. Perdew, J. A. Chevary, S. H. Vosko, K. A. Jackson, M. R. Pederson, D. J. Singh, and C. Fiolhais. Atoms, molecules, solids, and surfaces: applications of the generalized gradient approximation for exchange and correlation. *Physical Review B* **46**(11), pp. 6671–6687, 1992.

[56] J. P. Perdew, K. Burke, and M. Ernzerhof. Generalized gradient approximation made simple. *Physical Review Letters* **77**(18), pp. 3865–3868, 1996.

[57] B. Hammer, L. B. Hansen, and J. K. Nørskov. Improved adsorption energetics within density-functional theory using revised Perdew-Burke-Ernzerhof functionals. *Physical Review B* **59**(11), pp. 7413–7421, 1999.

[58] C. Díaz, E. Pijper, R. A. Olsen, H. F. Busnengo, D. J. Auerbach, and G. J. Kroes. Chemically accurate simulation of a prototypical surface reaction: $H_2$ dissociation on Cu(111). *Science* **326**(5954), pp. 832–834, 2009.

[59] M. Dion, H. Rydberg, E. Schröder, D. C. Langreth, and B. I. Lundqvist. Van der Waals density functional for general geometries. *Physical Review Letters* **92**(24), 246401, 2004.

[60] K. Lee, E. D. Murray, L. Kong, B. I. Lundqvist, and D. C. Langreth. Higher-accuracy van der Waals density functional. *Physical Review B* **82**(8), 081101, 2010.

[61] P. J. Feibelman, B. Hammer, J. K. Nørskov, F. Wagner, M. Scheffler, R. Stumpf, R. Watwe, and J. Dumesic. The CO/Pt(111) puzzle. *Journal of Physical Chemistry B* **105**(18), pp. 4018–4025, 2001.

[62] A. Stroppa, K. Termentzidis, J. Paier, G. Kresse, and J. Hafner. CO adsorption on metal surfaces: a hybrid functional study with plane-wave basis set. *Physical Review B* **76**(19), 195440, 2007.

[63] L. Schimka, J. Harl, A. Stroppa, A. Grüneis, M. Marsman, F. Mittendorfer, and G. Kresse. Accurate surface and adsorption energies from many-body perturbation theory. *Nature Materials* **9**(9), pp. 741–744, 2010.

[64] P. Lazić, M. Alaei, N. Atodiresei, V. Caciuc, R. Brako, and S. Blügel. Density functional theory with nonlocal correlation: a key to the solution of the CO adsorption puzzle. *Physical Review B* **81**(4), 045401, 2010.

[65] G. J. Kroes. Towards chemically accurate simulation of molecule-surface reactions. *Physical Chemistry Chemical Physics* **14**(43), pp. 14966–14981, 2012.

[66] M. Born and R. Oppenheimer. Zur Quantentheorie der Molekeln. *Annalen der Physik* **389**(20), pp. 457–484, 1927.

[67] W. Kohn and L. J. Sham. Self-consistent equations including exchange and correlation effects. *Physical Review* **140**(4A), A1133–A1138, 1965.

[68] P. Hohenberg and W. Kohn. Inhomogeneous electron gas. *Physical Review* **136**(3B), B864–B871, 1964.

[69] C. C. Marston and G. G. Balint-Kurti. The Fourier grid Hamiltonian method for bound state eigenvalues and eigenfunctions. *Journal of Chemical Physics* **91**(6), pp. 3571–3576, 1989.

[70] J. W. Arblaster. Crystallographic properties of ruthenium. *Platinum Metals Review* **56**(3), pp. 181–189, 2013.

[71] G. Kresse and J. Hafner. *Ab initio* molecular dynamics for liquid metals. *Physical Review B* **47**(1), pp. 558–561, 1993.

[72] G. Kresse and J. Furthmüller. Efficiency of *ab initio* total energy calculations for metals and semiconductors using a plane-wave basis set. *Computational Materials Science* **6**(1), pp. 15–50, 1996.

[73] G. Kresse and J. Furthmüller. Efficient iterative schemes for *ab initio* total-energy calculations using a plane-wave basis set. *Physical Review B* **54**(16), pp. 11169–11186, 1996.

[74] G. Kresse and D. Joubert. From ultrasoft pseudopotentials to the projector augmented-wave method. *Physical Review B* **59**(3), pp. 1758–1775, 1999.

[75] P. E. Blöchl. Projector augmented-wave method. *Physical Review B* **50**(24), pp. 17953–17979, 1994.

[76] G. Román-Pérez and J. M. Soler. Efficient implementation of a van der Waals density functional: application to double-wall carbon nanotubes. *Physical Review Letters* **103**(9), 096102, 2009.

[77] M. Methfessel and A. T. Paxton. High-precision sampling for Brillouin-zone integration in metals. *Physical Review B* **40**(6), pp. 3616–3621, 1989.

[78] H. J. Monkhorst and J. D. Pack. Special points for Brillouin-zone integrations. *Physical Review B* **13**(12), pp. 5188–5192, 1976.

[79] A. P. Baddorf, V. Jahns, D. M. Zehner, H. Zajonz, and D. Gibbs. Relaxation and thermal expansion of Ru(0001) between 300 and 1870 K and the influence of hydrogen. *Surface Science* **498**(1–2), pp. 74–82, 2002.

# Samenvatting

Veel chemische en fysische processen, zowel in industriële en alledaagse toepassingen, gebeuren aan een oppervlak. Een belangrijke toepassing van reacties van moleculen op oppervlakken is katalyse: het oppervlak verlaagt de barrière tot reactie, zodat moleculen door te adsorberen op het oppervlak kunnen reageren. Omdat dergelijke processen vaak erg complex zijn, mede doordat bijvoorbeeld het oppervlak niet goed gekarakteriseerd is, of doordat het oppervlak vervuild is met al aanwezige atomen of moleculen, is het vaak niet duidelijk waarom een bepaald proces wel of niet plaatsvindt. Vaak worden bij studies aan molecuul–oppervlak reacties daarom dus schone, goed gedefiniëerde oppervlakken gebruikt.

Voordat chemie kan plaatsvinden op het oppervlak, moet het oppervlak eerst bedekt worden met een reactant, wat bereikt wordt door adsorptie. Een bekend adsorptiemechanisme is dissociatieve chemisorptie. Bij dit mechanisme wordt een chemische binding in een aankomend molecuul gebroken, waarna beide fragmenten van het molecuul een nieuwe binding vorming met het oppervlak. Dit type reactie is in veel molecuul–oppervlak reacties een elementaire reactiestap en kan ook de snelheidsbepalende stap zijn, zoals bijvoorbeeld het geval is bij het Haber–Bosch proces, waarin ammonia gemaakt wordt. Hierin is de dissociatieve chemisorptie van $N_2$ de snelheidsbepalende stap. Dissociatieve chemisorptie is daarom een interessant proces om te bestuderen.

Een bijzonder interessante molecuul–oppervlak reactie om te bestuderen is de dissociatieve chemisorptie van waterstof op een metaaloppervlak. Omdat waterstof een homonucleair tweeatomig molecuul is en H het lichtste atoom is, is het het simpelste systeem waarin dissociatieve chemisorptie kan plaatsvinden. Ook speelt de beweging van op-

pervlakteatomen door de excitatie van fononen en electron–gat-paren waarschijnlijk geen belangrijke rol bij de dissociatieve chemisorptie van waterstof. Door deze effecten te verwaarlozen is het potentiële energie-oppervlak slechts zes-dimensionaal, waardoor het mogelijk is om zowel (quasi-)klassieke dynamica als quantumdynamica te doen.

Er worden in berekeningen aan waterstofdissociatie op metaaloppervlakken vaak een aantal benaderingen gemaakt. Ten eerste wordt aangenomen dat de oppervlakteatomen vast staan op hun ideale roosterposities. Ten tweede worden electron–gat-paar excitaties verwaarloosd. Als laatste wordt voor het uitrekenen van het potentiële energie-oppervlak vaak dichtheidsfunctionaaltheorie (DFT) gebruikt met een benaderende uitdrukking voor de exchange–correlatie energie.

Het hoofddoel van dit proefschrift is om een verbeterde beschrijving van $H_2$ dissociatie op metaaloppervlakken te leveren, en om beter te begrijpen wanneer en waarom gemaakte benaderingen in deze berekeningen falen. In dit proefschrift worden berekeningen aan waterstofdissociatie op metaaloppervlakken besproken, waarbij voornamelijk het effect van de gekozen exchange–correlatie functionaal op dynamische eigenschappen wordt beschouwd, maar ook oppervlaktetemperatuureffecten worden besproken.

Zo wordt in **hoofdstuk 3** een model ontwikkeld om oppervlaktetemperatuureffecten te beschrijven voor de dissociatie van $H_2$ en $D_2$ op Cu(111). In dit model is, in tegenstelling tot eerder ontwikkelde modellen zoals de (aangepaste) *surface oscillator* modellen, het doel niet om energieoverdracht te beschrijven, waarvan verwacht wordt dat het maar een kleine bijdrage aan de dynamica levert door het grote verschil in massa tussen $H_2$ en Cu, maar om te beschrijven hoe het oppervlak meer "gerimpeld" raakt door de verplaatsing van Cu atomen ten opzichte van hun ideale roosterposities bij een bepaalde oppervlaketetemperatuur $T_s$. In het ontwikkelde statische corrugatiemodel wordt een paarpotentiaal gebruikt om de potentiaal te corrigeren voor de verplaatsing van oppervlakteatomen. In een dergelijk model is het niet mogelijk om energie uit te wisselen tussen het waterstof en het oppervlak. De verbreding die gevonden is in experimenten van de reactiewaarschijnlijkheid als een functie van de invalsenergie, wordt primair toegeschreven aan de verplaatsing van oppervlakteatomen en kan in ieder geval semi-

kwantitatief worden beschreven. De *rotational quadrupole alignment parameter* wordt verlaagd, waardoor een betere overeenstemming met experimenten ontstaat. Bij lage oppervlaktetemperaturen, zoals $T_s = 120$ K, welke gebruikt is in moleculaire bundel-experimenten, worden geen grote verschillen gevonden met berekeningen waarbij een ideaal statisch oppervlak gebruikt is.

In **hoofdstuk 4** worden verscheidene exchange–correlatie functionalen getest voor toepasbaarheid op de dissociatie van waterstof op Ru(0001), om te zien of een functionaal gevonden kan worden die zowel de afhankelijkheid van reactie van de invalsenergie als de diffractiekansen goed beschrijft. Het is voor dit systeem bekend dat de energetische corrugatie sterk afhangt van welke exchange–correlatie functionaal gebruikt wordt. Als een exchange–correlatie functionaal gebruikt wordt waarin vdW-DF of vdW-DF2 correlatie van de Rutgers–Chalmers groep gebruikt wordt, heeft het potentiële energieoppervlak een hogere energetische corrugatie voor een bepaalde laagste barrièrehoogte dan de puur semi-lokale exchange–correlatie functionalen die zijn getest. Door deze hogere energetische corrugatie zijn de reactiewaarschijnlijkheidscurves breder voor deze functionalen en dus in betere overeenstemming met de breedte van de experimentele reactiewaarschijnlijkheidscurve. De revTPSS meta-GGA functionaal geeft geen grote verbetering ten opzichte van de "standaard" GGA functionalen, bijvoorbeeld die met PBE correlatie, maar de meta-GGA geeft wel roosterconstantes die goed in overeenstemming zijn met experimenten, in tegenstelling tot de standaard GGA functionalen. De PBE-vdW-DF2 functionaal, waarin PBE exchange gecombineerd is met vdW-DF2 correlatie, en de PBE:RPBE(50:50)-vdW-DF functionaal, waarin 50% PBE en 50% RPBE exchange gecombineerd zijn met vdW-DF correlatie, geven allebei een goede overeenstemming met de experimentele reactiewaarschijnlijkheden. Deze functionalen geven echter geen goede overeenstemming voor diffractie, omdat de berekende diffractiewaarschijnlijkheden te groot zijn in vergelijking met de experimentele waarden. Waarom dit het geval is is niet duidelijk. Het kan gerelateerd zijn aan de Debye–Waller extrapolatie, welke gedaan wordt door experimentatoren om de diffractiewaarschijnlijkheden in te schatten voor een 0 K oppervlak. Het is niet duidelijk of deze extrapolatie goed werkt voor dit systeem.

In **hoofdstuk 5** worden vier exchange–correlatie functionalen getest op het beschrijven van de dissociatie van $H_2$ op Pd(111), om te bepalen of een specifieke reactie parameter (SRP) functionaal gevonden kan worden voor dit systeem. Een vergelijking met experimentele data wordt bemoeilijkt door de hoeveelheid beschikbare experimentele data, omdat drie verschillende moleculaire bundel experimenten zijn uitgevoerd en alle drie een ander resultaat laten zien. Er wordt aangenomen dat het laatste experiment in tijd het meest betrouwbaar is. De PBE-vdW-DF functionaal geeft een goede overeenstemming met de experimenteel vastgestelde reactiewaarschijnlijkheden bij invalsenergieën groter dan 125 meV. Bij lagere energieën kan noch quantum noch quasi-klassieke dynamica de experimentele reactiewaarschijnlijkheden reproduceren, omdat de omslag van reactiewaarschijnlijkheden bij lage invalsenergieën niet optreedt. De overeenstemming met de experimentele toestandsopgeloste reactiewaarschijnlijkheden, welke zijn gemeten voor invalsenergieën kleiner dan 125 meV, is ook niet goed omdat ook hier geen omslag gevonden wordt. De overeenstemming tussen quantum and quasi-klassieke dynamica is echter in het algemeen wel goed. Een reden voor het ontbreken van de omslag in de reactiewaarschijnlijkheden kan zijn dat er te weinig paden zijn waarbij dissociatie zonder barrière kan optreden. Het is ook mogelijk dat het niet meenemen van energieoverdracht tussen het molecuul en het oppervlak in het dynamische model verantwoordelijk is voor de slechte overeenstemming met experiment. Berekeningen elders in de literatuur aan het $H_2$/Pd(111) systeem suggereren dat bij lage botsingsenergieën energieoverdracht naar het oppervlak kan leiden tot *trapping*, wat op zijn beurt weer leidt tot meer reactie.

In **hoofdstuk 6** worden de optPBE-vdW-DF en SRP48 functionalen vergeleken met elkaar voor wat betreft de toepassing op de dissociatie van $H_2$ en $D_2$ op Cu(111), Cu(100), Pt(111) en Ru(0001), om te kijken of functionalen met vdW-DF correlatie in principe een verbeterde beschrijving van $H_2$ dissociatie op metaaloppervlakken kunnen geven dan "gewone" GGA functionalen. De potentiële energieoppervlakken voor de verschillende systemen zijn kwalitatief gelijk voor de optPBE-vdW-DF functionaal en de SRP48 functionaal. De potentiaal als een functie van de molecuul–oppervlak afstand $Z$ stijgt sneller voor de optPBE-vdW-DF

functionaal dan voor de SRP48 functionaal. Beide functionalen geven een goede beschrijving voor dynamische eigenschappen zoals reactiewaarschijnlijkheden, alhoewel de optPBE-vdW-DF functionaal een betere algemene beschrijving geeft. Reactiewaarschijnlijkheden voor $D_2$ dissociatie op Ru(0001) en Pt(111) berekend met de optPBE-vdW-DF functionaal stijgen minder snel met de invalsenergie dan die berekend met de SRP48 functionaal, waardoor een betere overeenstemming met experiment ontstaat. De *vibrational efficacy* voor $H_2$ dissociatie op Cu(111) is een beetje groter bij berekeningen met de optPBE-vdW-DF functionaal. De afhankelijkheid van reactie van het initiële rotationele quantumgetal $J$ is verschillend voor de twee functionalen: de optPBE-vdW-DF functionaal voorspelt dat reactie niet of nauwelijks afhangt van $J$ voor lage $J$, maar de SRP48 functionaal laat een grotere afhankelijkheid zien van $J$ (reactie neemt toe met $J$ ook bij kleine $J$, wat in tegenstelling is met experiment). De berekende *rotational quadrupole alignment parameters* zijn lager voor SRP48, wat overeenkomt met de hogere reactiewaarschijnlijkheden die met deze functionaal berekend zijn. De optPBE-vdW-DF functionaal geeft in het algemeen resultaten die beter in overeenstemming zijn met experiment dan de SRP48 functionaal.

In **hoofdstuk 7** wordt de dissociatie van $D_2$ op een met CO moleculen bedekt Ru(0001) oppervlak bestudeerd. Voor dit systeem wordt de *ab initio* moleculaire dynamica (AIMD) methode gebruikt met de PBE-vdW-DF2 functionaal om de beweging van de CO moleculen en de ruthenium oppervlakteatomen mee te nemen in de dynamica. Twee verschillende formaten simulatiecel worden beschouwd: een 3×3 cel en een kleinere $\sqrt{3} \times \sqrt{3}$ cel. De reactiewaarschijnlijkheid bij $E_{\text{trans}} = 0.466\,\text{eV}$ is ongeveer 0.05 hoger voor de $3 \times 3$ simulatiecel dan voor de kleinere cel. De berekende reactiewaarschijnlijkheden zijn niet in overeenstemming met de experimentele reactiewaarschijnlijkheden. Aangezien een functionaal is gebruikt die goed werkte voor $H_2$ dissociatie op Ru(0001), suggereert dit dat een functionaal die voor een dergelijk systeem goed werkt niet noodzakelijkerwijs ook goed werkt voor $H_2$ dissociatie op een CO-bedekt oppervlak van hetzelfde metaal. De reactiewaarschijnlijkheden verkregen met de PBE-vdW-DF2 functionaal zijn in goede overeenstemming met in het verleden berekende reactiewaarschijnlijkheden met de RPBE functionaal, waarbij geen beweging van het oppervlak

mee was genomen. Er worden geen grote verschillen gevonden voor de reactiewaarschijnlijkheid tussen een ideaal CO/Ru(0001) oppervlak en een 180 K oppervlak. Ondanks dat wordt er wel een grote hoeveelheid energie overgedragen aan de CO moleculen, en deze hoeveelheid hangt af van het formaat van de gekozen simulatiecel. Bij $E_{\text{trans}} = 0.466\,\text{eV}$, wordt $0.105 \pm 0.002\,\text{eV}$ overgedragen voor een $\sqrt{3} \times \sqrt{3}$ simulatiecel, terwijl $0.263 \pm 0.007\,\text{eV}$ wordt overgedragen aan de CO moleculen en het oppervlak voor een $3 \times 3$ simulatiecel. Energieoverdracht gebeurt voornamelijk in de laterale vrijheidsgraden van het CO molecuul. Energieoverdracht waarbij beweging loodrecht op het oppervlak betrokken is, gebeurt vooral wanneer een $D_2$ molecuul frontaal botst op een CO molecuul, en is niet afhankelijk van het formaat van de simulatiecel. Omdat het $D_2$ molecuul zich kan begeven in de CO laag, wordt het verschil in energieoverdracht voor de laterale vrijheidsgraden veroorzaakt doordat het $D_2$ molecuul tegen spiegelbeelden van het CO molecuul aandrukt op een zodanige wijze dat de krachten werkend op de CO moleculen gedeeltelijk opgeheven worden in kleinere simulatiecellen. Dit zorgt voor een verminderde hoeveelheid energieuitwisseling met het oppervlak en de CO moleculen. De energie die wordt uitgewisseld met de CO moleculen zorgt ervoor dat deze zich uit elkaar bewegen, waardoor het oppervlak lokaal "geopend" wordt, wat reactie van $D_2$ bevordert.

# Curriculum vitae

Mark Wijzenbroek is geboren op 14 mei 1988 te Vlaardingen. In 2006 heeft hij zijn gymnasiumdiploma behaald aan het Groen van Prinsterer-lyceum, tevens te Vlaardingen. In datzelfde jaar is hij begonnen aan de bachelorstudie "Molecular Science and Technology" aan de Universiteit Leiden en de TU Delft. Na deze studie in 2009 met succes te hebben afgerond, is hij aan de masterstudie "Chemistry" aan de Universiteit Leiden begonnen. Als onderdeel van deze studie heeft hij een onderzoeksstage gedaan bij de Theoretische Chemie groep van prof. dr. Geert-Jan Kroes, waar hij begeleid is door dr. Mark F. Somers. Eind 2011 heeft hij zijn masterstudie afgerond, waarna hij in 2012 is begonnen als promovendus in dezelfde onderzoeksgroep.

# List of publications

- M. Wijzenbroek and M. F. Somers. Static surface temperature effects on the dissociation of $H_2$ and $D_2$ on Cu(111). *Journal of Chemical Physics* **137**(5), 054703, 2012.
- J. M. Boereboom, M. Wijzenbroek, M. F. Somers, and G. J. Kroes. Towards a specific reaction parameter density functional for reactive scattering of $H_2$ from Pd(111). *Journal of Chemical Physics* **139**(24), 244707, 2013.
- A. Mondal, M. Wijzenbroek, M. Bonfanti, C. Díaz, and G. J. Kroes. Thermal lattice expansion effect on reactive scattering of $H_2$ from Cu(111) at $T_s$ = 925 K. *Journal of Physical Chemistry A* **117**(36), pp. 8770–8781, 2013.
- L. Sementa, M. Wijzenbroek, B. J. van Kolck, M. F. Somers, A. Al-Halabi, H. F. Busnengo, R. A. Olsen, G. J. Kroes, M. Rutkowski, C. Thewes, N. F. Kleimeier, and H. Zacharias. Reactive scattering of $H_2$ from Cu(100): comparison of dynamics calculations based on the specific reaction parameter approach to density functional theory with experiment. *Journal of Chemical Physics* **138**(4), 044708, 2013.
- M. Wijzenbroek and G. J. Kroes. The effect of the exchange-correlation functional on $H_2$ dissociation on Ru(0001). *Journal of Chemical Physics* **140**(8), 084702, 2014.
- M. Wijzenbroek, D. M. Klein, B. Smits, M. F. Somers, and G. J. Kroes. Performance of a non-local van der Waals density functional on the dissociation of $H_2$ on metal surfaces. *Journal of Physical Chemistry A* **119**(50), pp. 12146–12158, 2015.

- M. Wijzenbroek and G. J. Kroes. *Ab initio* molecular dynamics study of $D_2$ dissociation on CO-precovered Ru(0001). *Physical Chemistry Chemical Physics*, accepted for publication. 2016.